Piezoelectric Micromachined Ultrasound Transducers for Medical Imaging

by

Derrick R. Chou

Department of Biomedical Engineering
Duke University

Date:_____

Approved:

_____
Olaf T. von Ramm, Supervisor

_____
Robert E. Kielb

_____
Joseph A. Kisslo

_____
Stephen W. Smith

_____
Patrick D. Wolf

Dissertation submitted in partial fulfillment of
the requirements for the degree of Doctor of Philosophy
in the Department of Biomedical Engineering
in the Graduate School of
Duke University

2011

ABSTRACT

Piezoelectric Micromachined Ultrasound Transducers for Medical Imaging

by

Derrick R. Chou

Department of Biomedical Engineering
Duke University

Date:_____

Approved:

_____
Olaf T. von Ramm, Supervisor

_____
Robert E. Kielb

_____
Joseph A. Kisslo

_____
Stephen W. Smith

_____
Patrick D. Wolf

An abstract of a dissertation submitted in partial fulfillment of
the requirements for the degree of Doctor of Philosophy
in the Department of Biomedical Engineering
in the Graduate School of
Duke University

2011

Copyright © 2011 by Derrick R. Chou
All rights reserved except the rights granted by the
Creative Commons Attribution / Non-commercial License

Abstract

Piezoelectric micromachined ultrasound transducer (pMUT) two-dimensional (2D) arrays have been proposed as an alternative to conventional bulk-PZT thickness-mode transducers for high frequency, forward-looking, catheter-based ultrasound imaging of the cardiovascular system. The appeal of pMUTs is based on several key advantages over conventional transducer technologies, including high operational frequencies, small element size, and low cost due to their microelectromechanical system (MEMS) silicon-based fabrication. While previous studies have demonstrated acoustic performance characteristics suitable for ultrasound image formation, pulse-echo B-mode imaging of tissue and tissue-like phantoms using 2D pMUT arrays small enough for forward-looking catheter-based applications have been demonstrated only at Duke University [1-3].

Having demonstrated the suitability of 2D pMUT arrays for tissue imaging, an important step is to demonstrate effective design control. The frequency of operation is a fundamental component of transducer design. Previous modeling efforts for pMUT vibration have used classical/Kirchoff thin plate theory (CPT) or Mindlin thick plate theory, however pMUTs with geometric dimensions similar to those explored here, have not been modeled with experimental comparison to physical devices.

It is hypothesized that the frequency of vibration of pMUTs can be predictively modeled based on experimental data from various pMUT configurations. Experimental frequency results were acquired and used to develop an empirical model based on a modified Mindlin thick plate theory. This dissertation presents the development of the frequency design theory culminating in a set of predictive design equations for the

frequency of vibration of 2D pMUT arrays aimed at improving their use in high-frequency, forward-looking, catheter-based ultrasound imaging applications.

Acknowledgements

Many, many thanks to my wife, Sarah, for her love, patience, and unending support throughout my graduate career.

Thanks to my family for their support and encouragement throughout my academic career. To my parents, Gene and J.J. Chou, and my sister, Alison, I would not be where I am today without you.

I am very appreciative of the advice and guidance provided by the members of my committee. Thank you for your time, energy, and patience.

Thank you to my lab mates, Scott Dianis and Cooper Moore, for being a part of this journey with me and aiding my experimental efforts when needed.

I am truly grateful for the advice and technical expertise offered by John Castellucci in overcoming the many experimental and analytical challenges faced throughout the duration of my research efforts.

I would also like to acknowledge the substantial contributions of Dr. David Dausch and our collaborators at RTI, International for their financial support and through whom we would not have had the high quality devices to work with had they not been made available to us in our collaborative effort. Thank you so much for the time, energy, and advice shared with me throughout the design, fabrication, and experimental process.

Finally, I thank my advisor, Dr. Olaf von Ramm, for his support, advice, and the opportunity to conduct research in such a fruitful and enjoyable environment. The journey and the finish would not have been possible without your wisdom, guidance, and mentorship.

Contents

Abstract **iv**

Acknowledgements **vi**

List of Tables **xiii**

List of Figures **xv**

1 Introduction **1**

1.1 Introduction……. 1

1.2 Hypothesis……... 2

2 Background **4**

2.1 Introduction……. 4

2.2 Ultrasound Fundamentals…… 4

2.3 Ultrasound Echo Imaging…… 5

2.3.1 Phased Array Imaging…… 6

2.4 Volumetric Imaging…… 9

2.5 Imaging Considerations in 2D Array Design……. 10

2.5.1 Imaging Resolution……... 10

2.5.2 2D Array Design Considerations……...12

2.6 Ultrasound Transducers……... 14

2.6.1 The Piezoelectric Effect and Piezoelectric Materials…… 14

2.6.2 Thickness-mode Ultrasound Transducers……. 15

2.6.3 Micromachined Ultrasound Transducers (MUTs)…… 16

2.6.3.1 Capacitive Micromachined Ultrasound Transducers (pMUTs)…… 17

2.6.3.2 Piezoelectric Micromachined Ultrasound Transducers (pMUTs)… 19

3 2D pMUT Arrays – 5x5 and 9x9 22

3.1 Introduction…… 22

3.2 pMUT Structure & Operation…… 23

3.2.1 Principle of pMUT flexure…… 23

3.2.2 pMUT Structure and Fabrication……...24

3.2.3 pMUT Flexure Mode Operation……....25

3.3 2D 5x5 and 9x9 pMUT Array Design……27

3.4 2D pMUT Array Experimental Results……..29

3.4.1 Electrical Properties……...29

3.4.2 Transmit Properties……... 31

3.4.3 Receive Properties……38

3.4.4 Receive Biasing……45

3.4.5 Pulse-Echo Performance……... 47

3.5 Summary…… 50

4 2D pMUT Arrays – 14x14 53

4.1 Introduction…… 53

4.2 14x14 2D pMUT Design……53

4.3 14x14 2D pMUT Array Experimental Measurements……... 55

4.3.1 Single Element Impedance Analyzer Frequency Response……..56

4.3.2 Single Element Transmit Response……...57

4.3.3 Single Element Receive Response…… 61

4.3.4 Single Element Pulse-Echo Response……...65

4.3.5 14x14 2D Array Pulse-Echo Imaging……... 70

4.4 14x14 2D Array Summary of Results…… 74

5 Visualization of PMUT Flexure Using Optical Vibrometry 76

5.1 Introduction…… 76

5.2 Experimental Methods – Optical Vibrometry…… 76

5.3 Experimental Results……..78

5.3.1 pMUT Displacement…… 78

5.3.2 Visualization of Vibrational Mode Shapes……80

5.3.3 Vibrational Dimensions……88

5.3.4 Element Crosstalk and Coupling……... 89

5.3.5 Air vs. Water Loading……... 91

5.4 Summary…… 95

6 Analytical Methods: Plate Vibration 98

6.1 Introduction…… 98

6.2 Plate Vibration – Classical Plate Theory……98

6.2.1 Frequency of Vibration under Classical Plate Theory…….. 99

6.3 Plate Vibration – Thick Plate Theory……....103

6.3.1 Plate Theories Applied to MUTs……104

6.3.2 Vibrational Frequencies of Rectangular Mindlin Plates…….… 106

6.4 Other Considerations to the Vibration of Plates……... 109

6.4.1 Effective Plate Flexural Rigidity for Multilayer Laminated Structures…….. 109

6.4.1.1 Isostress "Law of Mixtures" …….. 110

6.4.1.2 Muralt Layer-wise Composite Modulus……. 111

6.4.1.3 Pister & Dong Layer-wise Composite Modulus……. 112

6.4.2 Effect of Water-loading on Plate Vibration…… 113

6.4.3 Effect of Compliant Edge Support…….. 114

7 Analysis of Results and Development of a pMUT Frequency Theory 118

7.1 Introduction…….. 118

7.2 pMUT Mechanical Properties…….. 120

7.2.1 Material Properties of Constituent Layers……...120

7.2.2 Composite Density…….. 121

7.2.3 Composite Modulus…… 121

7.3 Resonant Oscillation in Pulse-Echo Configuration…….. 124

7.3.1 Measurement of the Resonant Oscillation……...125

7.3.2 Propagation of the Resonant Oscillation……. 125

7.3.3 Coupling and Crosstalk of the Resonant Oscillation……...127

7.3.4 Effect of Air vs. Water Loading on Resonant Oscillation……...128

7.3.5 Effect of Resonant Oscillation on Imaging Performance……131

7.3.6 Relevance of Resonant Oscillation in pMUT Vibrational Theory……..132

7.4 Summary of pMUT Measured Frequencies……. 133

7.5 Mindlin Thick Plate Theory Applied to pMUT Free Resonant Vibration……... 138

7.5.1 Conventional CPT & Mindlin Plate Theories Applied to pMUT $f_{res,air}$……...138

7.5.2 Generalized Analytical Method using pMUT $f_{res,air}$…… 140

7.5.3 Calculation of E_{comp} using Idealized Boundary Conditions…….144

7.5.4 Calculation of λ^2 from Resonant Frequencies…….147

7.5.5 Compliant Support in pMUT Vibration……...153

7.5.6 Modified Mindlin Plate Theory with Compliant Support for pMUT Vibrational Frequencies…….. 160

7.5.7 Application of the Modified pMUT Frequency Theory to New Devices…... 164

7.6 Summary……...171

8 pMUT Frequency Theory for Imaging Applications 173

8.1 Introduction…….. 173

8.2 Effect of Water Loading on pMUT Vibrational Frequency……. 174

8.3 Optimal Acoustic Receive Frequencies for Imaging……... 178

8.4 Optimal Acoustic Transmit Frequencies for Imaging…….. 184

8.5 Higher Order Modes……. 190

8.6 Summary…….. 194

9 Discussion 197

9.1 Application of the pMUT Frequency Theory……... 197

9.1.1 Transducer Design - Balancing Frequency, Efficiency, Sensitivity, and Physical Dimensions……... 197

9.1.2 Limitations of the pMUT Frequency Theory…….. 200

9.2 Future Work……. 202

9.2.1 Measuring Composite E_{PMUT} or E_{PZT}……... 202

9.2.2 Broader Range of Device Dimensions…… 202

9.2.3 Optical Vibrometry……..203

9.2.4 Limiting Resonant Oscillation……203

9.3 Conclusions…….. 204

A Vibration of Strings, Bars, and Plates 206

A.1 Vibration of Strings and Thin Bars…….. 206

A.1.1 Transverse Wave Equation for a String……...206

A.1.2 Longitudinal Wave Equation for a String or Thin Bar……207

A.2 Vibration of Bars…….. 207

A.2.1 Bending Waves in a Bar…….. 208

A.2.2 Boundary Conditions for a Bar……... 210

A.2.3 Rotary Inertia and Shear Deformation in Thick Bars……. 211

A.3 Vibration of Rectangular Plates – Thin Plates……. 212

A.3.1 Waves in a Thin Plate……..212

A.3.2 Equation of Motion for a Thin Plate……... 212

A.3.3 Boundary Conditions……...214

A.3.4 Plates with Elastic Support……..215

A.3.5 Frequency of Vibration Under Classical Plate Theory……... 215

A.4 Vibration of Rectangular Plates – Thick Plates……216

A.4.1 Equation of Motion for a Thick Plate……..216

A.4.2 Vibrational Frequencies of Rectangular Mindlin Plates……. 217

Bibliography **219**

Biography **225**

List of Tables

3.1 PZT film and DRIE etch dimensions and thicknesses for 5x5 2D pMUT arrays.... 27

3.2 PZT film and DRIE etch dimensions and thicknesses for 9x9 2D pMUT arrays.... 28

3.3 Electrical properties of 5x5 pMUTs – single element capacitance and frequencies from impedance analyzer ……..……..... 30

3.4 Transmit frequency, transmit output pressure, and transmit efficiency for 5x5 pMUT 2D arrays at 3.0cyc, 25-30V_{tx}……..... 32

3.5 Measured receive properties of 5x5 pMUT 2D arrays. Receive frequency, pressure sensitivity, and -6dB bandwidth for 1- and 3-cycle pulses…… 40

4.1 14x14 2D pMUT array device specifications …….. 55

4.2 Impedance analyzer frequencies for 14x14 2D pMUT array single elements……. 57

4.3 Measured transmit properties of 14x14 pMUTs. Transmit frequency, pressure, efficiency, and -6dB bandwidth (3- and 1-cycle) …….....….. 58

4.4 Measured receive properties of 14x14 pMUTs. Receive frequency, sensitivity, and -6dB bandwidth (3- and 1-cycle)……... 62

4.5 14x14 pMUT single element pulse-echo signal frequency, amplitude, and insertion loss at 30$V_{tx\text{-}pp}$ and 60$V_{tx\text{-}pp}$…… 66

5.1 Comparison of air- and water-loaded frequencies from optical, electrical, and acoustic measurement……... 85

6.1 Reference λ^2 values for CCCC rectangular Kirchoff plate (CPT)…… 102

7.1 Bulk material properties for constituent materials in pMUTs……..... 120

7.2 Calculated composite Young's modulus for pMUT device types using Muralt and Pister & Dong's layer-wise methods……... 122

7.3 Frequencies of pulse-echo persistent oscillation and optimal pulse-echo signal….. 129

7.4 Persistent oscillation amplitudes in air and water for 14x14 pMUT single elements at 30$V_{pp\text{-}tx}$……... 131

7.5 Frequencies measured using electrical, optical, and acoustic methods for 5x5 and 14x14 2D pMUT arrays under air and water loading……... 134

7.6 Theoretical fit values for Wg 5x5 pMUT fundamental resonant free vibration frequencies in air……... 143

7.7 Calculated composite Young's moduli from curve-fitting method…….. 145

7.8 R^2 values calculated from λ^2 ratio residuals for different compliance models ...…. 159

7.9 R^2 values of modified Mindlin frequency parameters with compliant support for pMUTs using linear, quadratic, piece-wise, and group-wise compliance models... 162

7.10 R^2 values of modified Mindlin frequency theory with compliant support for pMUTs using linear, quadratic, piece-wise, and group-wise compliance models... 164

7.11 Dimensions and resonant frequencies for A- and C-series devices…….. 165

7.12 R^2 from fit residuals, λ^2_{eff} curves, and frequency theory curves for A- and C-series pMUTs using linear, quadratic, piece-wise, and group-wise compliance models... 171

8.1 Statistics for calculated percent decrease in frequency due to water loading for pMUT device structures…… 175

8.2 Calculated frequency factors for single-sided water loading in the vibration of A- and Wg-series devices…….. 176

8.3 Acoustic receive frequencies (f_{rx}) compared to calculated water-loaded resonant frequencies ($f^{t*}_{res,H2O}$) for A- and Wg-series devices. observed f_{rx} and $f^{t*}_{res,H2O}$ are provided…….. 179

8.4 R^2 values for theoretical and observed receive frequencies for Wg- and A-series devices…….. 184

8.5 Calculated optimal acoustic transmit frequencies in water (compliance-modified Mindlin frequencies with water loading) compared to observed values…….. 185

8.6 Percent difference between calculated optimal acoustic transmit frequencies in water (compliance-modified Mindlin frequencies with water loading) compared and observed values…….. 187

8.7 R^2 values for theoretical and observed transmit frequencies for Wg- and A-series devices…….. 190

8.8 Calculated higher-order frequencies for Wg8 B200 device specifications under air- and water-loading……... 193

8.9 Theoretical Mindlin frequencies for 1-3 and 3-1 modes in comparison to observed acoustic transmit frequencies…… 193

List of Figures

2.1 Transmit pulse formation from a phased array……. 7

2.2 Reception of echoes from a phased array……. 8

2.3 B-mode scanning and display……... 9

3.1 Piezoelectric unimorph deformation under application of an electric field……. 23

3.2 Cut-through diagram of pMUT laminate structure with component layers……. 24

3.3 Top-down diagram of pMUT structure with positioning of the cavity, PZT, and electrode…… 25

3.4 Flextensional mode of operation for pMUTs. Applied bipolar voltage cycle, ferroelectric hysteresis loop, and mechanical displacement as a function of input voltage……... 26

3.5 Photo of 9x9 2D pMUT array with 50µm membranes showing bottom ground grid and signal traces running to periphery of device……... 28

3.6 5x5 pMUT single element impedance phase vs. frequency for representative arrays of varying size in air……... 31

3.7 Representative 1.0-cycle transmit pulse from Wg8 75µm element with FFT…….. 33

3.8 Frequency vs. etched cavity length for 5x5 pMUT array elements…….. 34

3.9 Transmit pressure and field efficiencies of pMUT elements driven at 25-30V_{pp} for t_{PZT} of 1-2 µm and t_{Si} of 5, 10, and 15 µm……... 35

3.10 pMUT transmit efficiency vs. applied transmit excitation voltage for Wg9 B7550 array element at 8.6MHz, 3.0 or 3.5 cycles…….. 36

3.11 Angular response of representative 75µm and 200µm single elements in transmit into hydrophone…… 37

3.12 5x5 pMUT 2D array f_{rx} vs. L_{etch} for devices of varying thickness…… 42

3.13 Average single element receive sensitivity for 5x5 pMUT arrays……... 43

3.14 Rx pressure sensitivity (mV/kPa) vs. peak-to-peak voltage amplitude of biasing cycle for different cycle lengths…… 47

3.15 Pulse-echo response at 8.4 MHz and FFT bandwidth for a 75 µm pMUT single element with t_{PZT}=1 µm and t_{Si}=10 µm using 0.5 cycle, 4.2MHz, 27.6 V_{pp} pulse… 49

3.16 Calculated single element pulse-echo insertion loss for a 65µm 9x9 array element. Pulse-echo signal from aluminum block target with 3.5 cycle transmit at 2.2cm range using 25 elements in transmit and receive…….. 50

4.1 14x14 2D pMUT array with 75µm membranes with 150µm element pitch……... 54

4.2 14x14 pMUT single element impedance phase vs. frequency for arrays of varying size……... 56

4.3 A1_2D_75_175_9 single element transmit pulse waveform into pressure-calibrated hydrophone @ 5.6MHz, 1.5cyc, $60V_{tx}$. Range = 20mm……. 58

4.4 FFT of A1_2D_75_175_9 single element transmit pulse waveform @ 5.6MHz, $60V_{tx}$ – 3.5 and 1.5 cycles. Range = 20mm……. 59

4.5 Transmit frequency and efficiency for 14x14 2D pMUT array single elements vs. etched length……. 60

4.6 Single element Tx angular response into hydrophone for center element in a 14x14 2D pMUT array @ 5.6MHz ($2.8MHz_{in}$), $30.9V_{tx}$, 3.0 cycles, 20mm range.. 61

4.7 Receive frequency and sensitivity for 14x14 pMUT array single elements vs. etched length……. 63

4.8 A1_2D_175_9 single element receive pulse waveform with transmit from 5.0MHz piston @ 5.2MHz, 100kPa. Range = 100mm…… 64

4.9 A1_2D_175_9 single element receive pulse waveform FFT with transmit from 5.0MHz piston @ 5.2MHz, 100kPa. Range = 100mm…… 64

4.10 Single-element pulse-echo waveform off of Al block reflector at a range of 20mm driven with 3.5 cycles at 5.6MHz and $50V_{tx}$……. 66

4.11 FFT of single-element pulse-echo waveform off of Al block reflector at a range of 20mm driven with 3.5 cycles at 5.6MHz and $50V_{tx}$……. 67

4.12 A representative waveform of the persistent oscillation on the pMUTs in pulse-echo configuration in water…….. 69

4.13 B-mode of 5 nylon strings at 2.5mm spacing in deionized water using A1_2D_75_150 device @ $25V_{dc}$ (~$40V_{tx}$), $3.13MHz_{in}$, 2.5 cycles. …… 70

4.14 B-mode images of targets from a tissue-mimicking small-parts phantom – resolution, range, and 4mm anechoic cyst targets using A1 75µm devices at $25V_{dc}$ (~$40V_{tx}$), 2.5 cycles, 2.78 or $3.13MHz_{in}$..... 71

4.15 B-modes of human carotid artery and internal jugular vein - during and after the Valsalva maneuver. Images acquired using A1_2D_175_9 14x14 pMUT array... 73

5.1 Displacement vs. time of 2D pMUT array in air @ f_{in}=3.0MHz, 3.0cyc, 22.7V_{tx}, f=6.75MHz…… 79

5.2 Displacement vs. time of 2D pMUT array in air @ f_{in}=2.8MHz, 3.0cyc, 22.7V_{tx}, f=5.7MHz with 6.75MHz ringdown……. 79

5.3 FFT spectra of displacement waveforms of A1_2D_175_9 2D pMUT array @ 3.0cyc, 22.7V_{tx} at multiple input frequencies in air…….. 80

5.4 Surface displacement mode shape of a 75µm element from a 14x14 2D pMUT array driven at 3.0 cycle, 3.0MHz, 22.7V_{tx}. 6.75MHz mode in air and 5.28MHz mode in water…… 81

5.5 Surface displacement mode shapes of a 200µm pMUT element in air at showing different modes of operation. 5x5 2D pMUT array driven at 3.0 cycle, 3.2MHz, 22.7V_{tx}……... 82

5.6 Surface displacement mode shapes of a 200µm pMUT element in water at showing different modes of operation. 5x5 2D pMUT array driven at 3.0 cycle, 3.2MHz, 22.7V_{tx}……... 84

5.7 FFT of Wg8 200µm and A1_2D 75µm single element vibration in air from on optical measurement at 3.2MHz and 2.8MHz, respectively…… 87

5.8 Profile of surface displacement and measurement of displacement along length and width dimensions of a 75µm pMUT element for 6.75MHz band in FFT…….. 89

5.9 Visualization of vibration of a driven element and the subsequent motion of adjacent elements which were not electrically actuated indicating coupling of neighboring elements…… 90

5.10 FFT plot of A1_2D_175 in air and water driven at 3.0 cycles, 22.7V_{tx} at various f_{in} - air (2.8MHz_{in}, 3.0MHz_{in}) and water (2.8MHz_{in})…… 91

5.11 FFT plot of A1_2D_175 array (2.8MHz_{in}) vs. Wg8B200100 array (3.2MHz_{in})….. 93

5.12 Vibration of a 200µm pMUT element in air in the 5.8-6.6MHz band showing higher-order 3-1 mode of operation. 5x5 2D pMUT array driven at 3.0 cyc, 3.2MHz, 22.7V_{tx}……... 94

6.1 λ^2 values for SSSS and CCCC rectangular Mindlin plates……... 108

6.2 Virtual mass function f for rectangular plates used in calculation of correction factor for water-loaded frequency……. 114

6.3 Frequency correction for compliant support in a cantilever beam……... 115

7.1 Pulse-echo (V_{pe}) and persistent oscillation (V_{osc}) amplitude as a function of the applied transmit frequency for a representative 14x14 array (A1_2D_175_9) at $30V_{pp\text{-}tx}$ with the reflecting target at 10mm range……. 127

7.2 FFTs and a representative waveform of the persistent, non-propagating oscillation on the pMUTs in pulse-echo configuration in air and water…….. 130

7.3 Measured pMUT resonant frequencies, $f_{res,air}$, compared to conventional plate theory frequencies calculated using devices of the same structure, plotted against device etched cavity length. CPT and Mindlin plate theories are considered with simply-supported and fully clamped BCs……. 139

7.4 Mindlin-compensation of the resonant free vibration under air loading for 5x5 pMUT array devices. (a) Uncompensated thickness-normalized frequency vs. etched length. (b) Ratio of CPT to Mindlin λ^2 applied as Mindlin-compensation factors (c) Mindlin-compensated thickness-normalized frequency vs. etched length…… 141

7.5 Curve-fitting to the Mindlin-compensated resonant free vibration frequencies under air loading for 5x5 pMUT array devices.……..... 142

7.6 Fundamental mode λ^2 vs. *L/t* for Wg-series 5x5 pMUTs grouped by device size. λ^2 calculated from the measured resonant frequencies of pMUT plotted against CPT and Mindlin theories with CCCC and SSSS boundary conditions……... 149

7.7 Interpolation of the aspect ratios of Wg-series devices for use in theoretical calculations……... 150

7.8 Fundamental mode λ^2 vs. *L/t* for Wg-series 5x5 pMUTs. λ^2 calculated from the measured resonant frequencies of pMUT plotted against CPT and Mindlin theories with CCCC and SSSS boundary conditions. Plate theory λ^2's include interpolation based on variable pMUT *L/W* aspect ratios……. 151

7.9 λ^2 vs. *L/t* for Wg-series 5x5 and A-series 14x14 pMUTs. λ^2 calculated from the measured resonant frequencies of pMUT plotted against CPT and Mindlin theories with CCCC and SSSS boundary conditions. Plate theory λ^2's shown are calculated using Wg14 thickness and include interpolation based on variable pMUT *L/W* aspect ratios……... 152

7.10 λ^2 ratio ($\lambda^2_{eff}/\lambda^2_{theory}$) vs. non-dimensional t/L for Wg-series 5x5 arrays. Effective frequency parameter calculated from measured resonant frequencies, theoretical frequency parameters determined from Mindlin theory for a CCCC plate…….. 155

7.11 Fitting of λ^2 ratio ($\lambda^2_{eff}/\lambda^2_{theory}$) vs. non-dimensional t/L for Wg-series 5x5 arrays by four different methods – linear fit, linear fit by device thickness groups, quadratic fit, piece-wise linear fit……. 156

7.12 Modeled effective pMUT frequency parameter (λ^2_{pmut}) curves and observed pMUT data vs *L/t* for Wg-series devices…….. 161

7.13 Frequency curves vs. etched length for theoretical Mindlin plates with compliant support modeled after Wg-series devices……. 162

7.14 Frequency curves vs. *L/t* for theoretical Mindlin plates with compliant support modeled after Wg-series devices…….. 163

7.15 Calculated λ^2 ratios from A- and C-series device frequencies plotted as a function of relative thickness *t/L*……. 166

7.16 λ^2 vs. *L/t* for A- and C-series devices……... 168

7.17 A- and C-series observed frequencies and pMUT frequency curves based on Mindlin plates with compliant support vs device length…….. 169

7.18 A- and C-series observed frequencies and pMUT frequency curves based on Mindlin plates with compliant support vs. device length/Si thickness……. 170

8.1 Theoretical and observed optimal acoustic receive frequencies in water for imaging applications. Theoretical f^t_{rx} calculated using quadratic, piece-wise, and group-wise compliance models…… 183

8.2 Theoretical and observed optimal acoustic transmit frequencies in water for imaging applications. Theoretical f^t_{tx} calculated using quadratic, piece-wise, and group-wise compliance models…… 189

9.1 f_{rx} and f_{tx} frequency curves for multiple thicknesses with AR=1.25, t_{PZT}=1μm, W_{PZT}=W_{etch}*1.05, L_{PZT}=L_{etch}*0.85…….. 199

Chapter 1

Introduction

1.1 Introduction

Real-time 3D ultrasound imaging has become widespread in clinical use. At the heart of any medical ultrasound imaging system is the transducer. While the transducer is by no means the only important component of an ultrasound scanner, advances in imaging technology have often been linked with innovations in transducer design.

The use of piezoelectric micromachined ultrasound transducer (pMUT) two-dimensional (2D) arrays for minimally-invasive, catheter-based imaging of the cardiovascular system has been proposed based on several key advantages over conventional transducer technologies, including high operational frequencies, small element size, and low cost due to their microelectromechanical system (MEMS) silicon-based fabrication. pMUTs utilize a thin PZT film unimorph plate to achieve acoustic transmission and reception. Development of pMUTs has demonstrated acoustic performance characteristics suitable for ultrasound image formation, however B-modes of tissue or tissue-like phantoms using 2D pMUT arrays small enough for forward-looking catheter-based applications have been demonstrated only at Duke University [1-3].

Having demonstrated the suitability of 2D pMUT arrays for tissue imaging, an important step is to demonstrate effective design control. The frequency of operation is a fundamental component of transducer design. For pMUTs, numerous geometric and material factors influence the frequency of operation. This thesis focuses on determining

the predominant factors that affect frequency and modeling their effects using various theoretical principles. Many of the reported modeling efforts for pMUT vibration have used classical/Kirchoff thin plate theory (CPT) or Mindlin thick plate theory, however pMUTs with the geometric dimensions similar to those explored here, suitable for forward-looking cather-based imaging, have not been modeled with comparison to physical devices. The principles of plate theory, fundamental and higher-order modes, compliant boundary conditions, and water-loading have been explored extensively in the analytical modeling efforts of this dissertation using frequency data collected from physical devices. This dissertation presents the development of a frequency design theory culminating in a set of predictive design equations for the frequency of vibration of 2D pMUT arrays aimed at improving their use in high-frequency, forward-looking, catheter-based ultrasound imaging applications.

1.2 Hypothesis

The pMUT arrays designed and produced at Research Triangle Institute, International in collaboration with Duke University have been shown to be suitable for image formation in tissue and tissue-like media. However, their operation has not been described by a quantitative theory. Experimental pMUT frequency results were acquired and used to develop an empirical model based on Mindlin thick plate theory.

The overall hypothesis is that *the frequency of vibration of pMUTs can be predictively modeled based on experimental data from various pMUT configurations*. In proving this primary hypothesis, the following points will be demonstrated.

First, the results of this research will show that the fundamental frequency of resonant vibration can be measured in both air and water using electrical, acoustic, and optical methods. The experimental results will be presented in the context of transducer characterization for the purpose of demonstrating that pMUT 2D arrays can be used for medical imaging applications.

Second, it will be demonstrated that the measured fundamental resonant frequencies can be modeled using a modified Mindlin plate theory taking into account the effect of relative thickness-dependent compliant support.

Third, it will be shown that optimal acoustic transmit frequencies for imaging can be modeled using confined vibrational dimensions based on the forced nature of acoustic transmission. Optimal acoustic receive frequencies will be shown to be modeled using the full device dimensions due to the free nature of acoustic reception.

Finally, the overall hypothesis that the frequency of vibration of pMUTs can be predictively modeled using a modified Mindlin plate theory will be tested by applying the theory to pMUT devices not included in its development. These frequencies will be shown to be well-described by the frequency theory, demonstrating use of the theory for predictive frequency design.

Chapter 2

Background

2.1 Introduction

The primary objective of this work is to quantitatively describe the frequency of vibration of piezoelectric micromachined ultrasound transducers (pMUTs) for ultrasound imaging applications. The application of a predictive frequency theory will enable the design optimization of pMUT transducer arrays used for catheter-based volumetric imaging using 2D arrays as an end goal. This chapter presents the basic principles of ultrasound imaging and ultrasound transducers capable of real-time 3D volumetric imaging.

2.2 Ultrasound Fundamentals

Ultrasound is a medical imaging modality which utilizes acoustic waves for image formation. The fundamental principles of ultrasound are quite similar to sonar. The typical ultrasound system operates in a pulse-echo mode in which an acoustic wave is transmitted and images are formed from the sound reflected back to the receiver. The transmitted acoustic pulse is generated by the excitation of transducer elements with an electrical signal. The ultrasound transducer, often a piezoelectric device, provides a mechanical response to the electrical excitation which can be coupled to transmit into a medium like water or tissue. The reflected echoes subsequently cause mechanical

displacement of the transducer elements which generate an electrical signal which is used to form the ultrasound image.

The reflection of sound is the basis by which targets in the field can be detected by an ultrasound system. Acoustic energy is reflected wherever changes in acoustic impedance occur. Acoustic impedance, Z, describes the relationship between the acoustic pressure, p, and the particle velocity, u, in a given medium through the relation $Z = p/u$. Acoustic impedance for a medium is dependent on the local volume density, ρ_0, and the speed of sound, c, and can be calculated using the relation $Z = \rho_0 c$. Materials of differing density and acoustic velocity will have different acoustic impedances. Acoustic impedance mismatches occur at boundaries between different material types and sound is reflected from these boundaries. The amount of acoustic energy that is reflected is dependent on the magnitude of the acoustic impedance mismatch. For planar boundaries between structures larger than one wavelength, λ, the amplitude of the reflected sound from the boundary relative to the incident sound is given by the reflection coefficient, R, given by

$$R = \frac{Z_2 - Z_1}{Z_2 + Z_1} \tag{2.1}$$

where Z_1 and Z_2 are the acoustic impedance of the two media forming the boundary.

For biomedical ultrasound, reflections from the boundaries between tissue structures can be used to visualize structures for a wide range of medical applications.

2.3 Ultrasound Echo Imaging

Acoustic reflections from boundaries of impedance change are used to form ultrasound images. Filtering and envelope detection are used to extract echo amplitudes

and remove the ultrasound carrier frequency. Several different scanning and display modes are used to present echo information. A-mode (amplitude mode) scans plot the amplitude of the received echoes from a single scan direction as a function of range [4]. In M-mode (motion mode) scans, the echo amplitudes along a single direction are used to modulate the pixel brightness and are plotted as a function of range on a vertical line of the display. Subsequent acquisitions are displayed adjacent to the previous line, thus providing a time progression of the received echoes in an M-mode scan [4].

Brightness mode (B-mode) imaging utilizes the principles of an A-mode scan, acquiring echo amplitudes along multiple scan directions, displaying them as a two-dimensional (2D) cross-section image (Figure 2.3). Early B-mode imaging was accomplished by mechanically translating or rotating the ultrasound transducer to achieve the required sweep through multiple scan directions. Current conventional ultrasound systems now employ transducer arrays and electronic beam steering to perform B-mode scanning. The transducers presented in this dissertation make use of electronic beam steering using a 2D matrix phased array.

2.3.1 Phased Array Imaging

Conventional ultrasound imaging scanners use a transducer composed of a linear or two-dimensional array of elements to produce a focused acoustic pulse and receive the resulting echoes. Focusing and steering of the acoustic energy is accomplished by phasing or applying time delays to the transducer elements [5, 6]. Figure 2.1 illustrates the general principles of transmit phasing using a linear array of 7 elements. A transmit

voltage excitation pattern *T* is applied to the transducer elements *E* at the desired operating frequency, typically at or near the center frequency of the transducer.

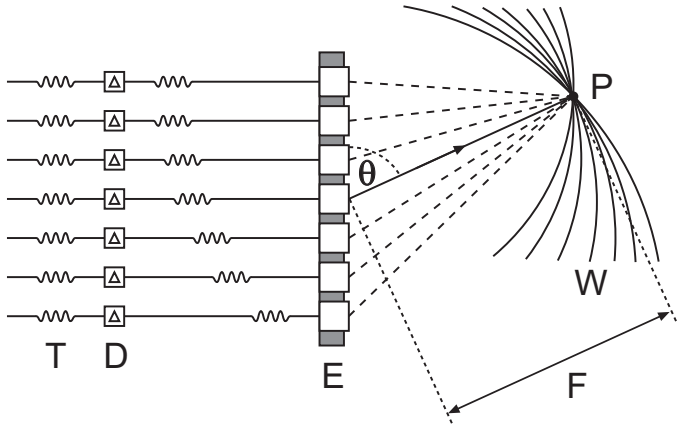

Figure 2.1: Transmit pulse formation from a phased array.

Delays *D* are applied to the excitation pattern to control the timing of the element excitation based on the steering angle θ and focal distance *F*. Acoustic wavefronts *W* propagate into the medium and sum coherently at focal point *P*. A large portion of the acoustic energy travels along a path defined by the vector from the center of the transducer through the focal point. The acoustic pulse propagating along this path forms the transmit beam.

The process for receiving on a phased array is similar, illustrated in Figure 2.2. Acoustic wavefronts *W* reflected from the target at point *P* arrive at the transducer elements *E*, inducing received signal voltages, *R*, corresponding to their arrival times. The received waveforms are time-shifted through delays *D*. The time-delayed waveforms are summed to form the receive signal, *S*. The receive delays are determined from the desired steering angle and focal distance. Beamforming by application of the receive delay profile provides a method of preferentially receiving echoes along the

receive beam. The summed receive signal corresponding to a single transmit beam as a function of range forms a scanline [5].

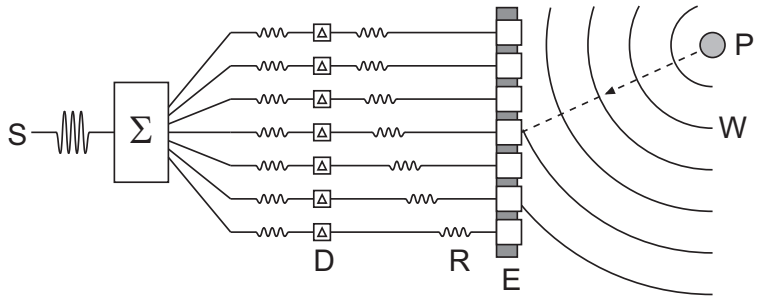

Figure 2.2: Reception of echoes from a phased array.

The resolution of the ultrasound image is dependent on the characteristics of the transmit and receive beams. In transmit, the focus of the transmit beam is fixed as the acoustic energy launched from the transducer cannot be changed after it begins traveling in the medium. However, the focus of the receive beam can be changed in time as the echoes are received. Dynamic receive focusing is achieved by adjusting the receive focus as reflected echoes from deeper targets are received [7, 8]. This dynamic adjustment maintains an optimal focus of the received echoes and improves the overall resolution and image quality.

The formation of a B-mode image is accomplished by steering the transmit beam through a range of angles. Envelope detection is employed to remove the carrier frequency from the received scanlines. The scanline data is then displayed by mapping brightness values corresponding to the magnitude of the echoes received as a function of range via scan conversion. The brightness data is mapped to the display along the angle of the scanline [9] as shown in Figure 2.3.

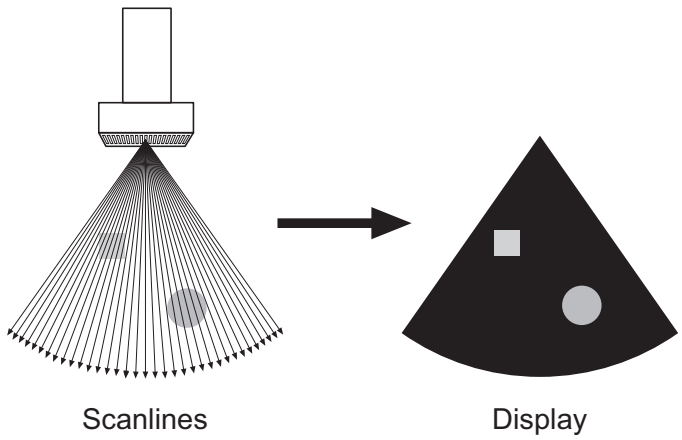

Figure 2.3: B-mode scanning and display.

2.4 Volumetric Imaging

Linear arrays can only steer an ultrasound beam in the azimuth direction. The resulting B-scans thus only capture a 2D cross-section of a three-dimensional (3D) field. This limitation can become problematic in practice. Alignment of the 2D imaging plane can be difficult when the interrogation of a specific anatomical structure is desired, particularly when the structure has a complex 3D shape. Target motion also introduces difficulty in 2D tomographic imaging. Out-of-plane motion can result in changes in shape or disappearance of the target from the B-mode image. If multiple images of an anatomical structure are required, particularly over an extended period of time, duplication of the image plane can be challenging.

The use of 3D or volumetric imaging to acquire a 3D volume of data instead of just a 2D slice addresses these limitations. Early volumetric imaging was accomplished by the mechanical translation or rotation of a linear array [10-12]. The 2D planes acquired over the course of the mechanical sweep could then be reconstructed by a computer to form a

volume of data. With a volume of data, the entire 3D volume and be rendered, or a 2D plane in any orientation can be calculated and rendered individually.

Mechanical steering of a linear array introduces a number of significant limitations. Mechanical movement of a linear array to interrogate a volume slows the image acquisition rate to a degree at which subject and operator motion become problematic. Linear arrays also have a fixed elevation focus which results in suboptimal volume resolution outside of this focus and mismatch between the elevation and azimuth resolutions.

Electronic beam steering can be accomplished using a 2D grid of piezoelectric elements, called a 2D or matrix array. The phase delay steering described in section §2.3.1 for a linear array can be extended to the case of a matrix array, allowing beam steering in both elevation and azimuth [13]. Electronic beam steering with a 2D matrix array eliminates many of the problems introduced by mechanically moving components and improves the overall volume resolution by providing better control of the elevation focus.

2.5 Imaging Considerations in 2D Array Design

2.5.1 Imaging Resolution

The spatial resolution of an imaging system is commonly defined as the minimum separation required to differentiate two identical point targets (the Rayleigh resolution limit). As a diffraction-limited coherent imaging modality, ultrasound utilizes the wave

properties of sound for imaging. Spatial resolution depends on how tightly the sound can be focused. Focusing is determined by the interference pattern between sound waves.

In pulsed operation, the axial resolution is dependent on the length of the pulsed waveform. The axial resolution can be approximated as half the length of the transmitted pulse, expressed as

$$Axial\ Resolution \approx \frac{N\lambda}{2} \tag{2.2}$$

where N is the number of cycles in the pulse and λ is the wavelength.

The angular response at the focus of the transducer can be approximated by taking the spatial Fourier transform of the transducer aperture. For a rectangular aperture, the lateral resolution is given by

$$Lateral\ Resolution \approx \frac{\lambda z}{D} \tag{2.3}$$

where λ is the wavelength, z is the focal distance, and D is the width of the aperture. The lateral resolution can also be expressed as an angular resolution given by

$$Angular\ Resolution \approx \sin^{-1}\left(\frac{\lambda}{D}\right) \tag{2.4}$$

The lateral resolutions given above in Equations 2.3 and 2.4 are for on-axis focus. Steering of the focal point off-axis effectively reduces the apparent transducer aperture by the cosine of the steering angle, reducing the lateral resolution. Lateral resolution is thus non-constant, changing as a function of depth and steering angle.

In phased array imaging, the differences between axial and lateral resolution given above reveal non-uniform spatial resolution.

2.5.2 2D Array Design Considerations

Several other key considerations play into the design of 2D arrays. The physical dimensions of 2D array elements and their spatial distribution within the array affect their performance in significant ways, particularly in the beam pattern produced by the transducer.

The pressure wave propagating from the face of an unfocused transducer generally maintains the approximate lateral dimensions of the transducer for a certain distance, but natural divergence begins to spread the beam at larger distances. In the region near the transducer (the "near field"), the beam has many amplitude and phase irregularities arising from the interference between the contributions of waves from different parts of the transducer face whereas in the region further from the transducer (the "far field"), the beam profile is much more uniform and well-behaved. By solving for the radiation pattern from an ultrasound transducer, the transition distance between the near- and far-field regions can be determined for a rectangular aperture to be

$$z_R = \frac{a^2}{\lambda} = \frac{D^2}{4\lambda} \tag{2.5}$$

where λ is the wavelength, D is the full lateral dimension of the aperture, and a is half of the lateral dimension of the aperture. Within this transition distance, the pressure amplitude from a transmitting transducer aperture is oscillatory and difficult to characterize. However, the transition distance identifies the point where the last on-axis maximum occurs, and the resultant pressure amplitude beyond this point is no longer oscillatory, behaving as a slowly decreasing (~1/z) field. Beyond the transition distance,

the attenuation of the pressure field with distance is much more predictable and more easily characterized.

The relative spacing and size of individual elements in a 2D array also influences the beam pattern of a transducer. Segmentation of the transducer into an array of elements introduces complexity in the radiation pattern. The appearance of reduced-amplitude images of the main beam, known as grating lobes, can be introduced as a result of the spacing between individual elements. The angles at which the grating lobes appear are those for which the path length difference between rays from neighboring elements is equal to an integer number of wavelengths. At these angles, constructive interference occurs and some power is radiated in those directions. The grating lobe angles are then given by

$$\phi_g = \sin^{-1}\left(\frac{n\lambda}{s}\right) \qquad n = \pm 1, \pm 2, \ldots \tag{2.6}$$

where s is the center-to-center distance, or pitch, of neighboring elements. There will be as many grating lobe orders in the beam pattern as the number of solutions of Equation 2.6 that fall within $\pm 90^{\circ}$. In an image, grating lobes produce multiple responses from a single object, confusing the interpretation of object position. For a transducer with one grating lobe on each side of the main beam, an on-axis target will present with apparent, or phantom, objects off-axis at ϕ_g on either side of the image of the actual object. Grating lobes can be avoided by controlling the spacing of individual elements, decreasing s enough to force all solutions of ϕ_g to fall beyond $\pm 90^{\circ}$.

The proximity between individual elements can also influence coupling or crosstalk between them through mechanical or electrical means. Mechanical waves and

deformations in one element may result in a mechanical or electrical response of neighboring piezoelectric elements. Electrical traces, leads, pads or other structures in close proximity may lead to the induction of electrical signals in neighboring elements. Coupling and crosstalk can introduce confusion in the interpretation of electrical response from received pressures or result in the unintentional propagation of transmitted pressure waves from separate, distinct elements, possibly reducing the angular response of the elements. Both effects can result in a reduction of image quality or reliability. The effects of coupling and crosstalk can be minimized by taking measures to mechanically and electrically isolate individual elements within the array.

2.6 Ultrasound Transducers

2.6.1 The Piezoelectric Effect and Piezoelectric Materials

Numerous physical principles and techniques have been employed for use in the generation and reception of ultrasound, but none have been utilized as extensively for use in medical devices as those based on the piezoelectric effect [14, 15]. The piezoelectric effect describes the ability of materials to develop electric displacement as a result of an applied mechanical stress [16]. Similarly, the inverse piezoelectric effect describes a deformation of the material under an applied electric field. This coupling of mechanical and electrical energy by these piezoelectric materials is a result of their crystal structure. While the unit cells of the piezoelectric crystals do not possess a net dipole moment, when the lattice is stressed, the asymmetry of the crystal structure causes the

displacement of the center of charge in the unit cell. This displacement of charge yields a net electric field in the material.

A special class of piezoelectric materials called ferroelectrics, or piezoelectric ceramics, are organized in regions of randomly oriented dipole moments. By applying an external electric field at elevated temperatures (100-200°C), these domains tend towards alignment in the direction of the electric field. This process is referred to as "poling," used to increase the piezoelectric properties of the material.

Among all ferroelectric materials, the most widely used in ultrasound imaging is lead zirconate titanate, or PZT. The unit cell structure of PZT is similar to a simple cubic crystal. However, below the transition temperature, the lead, zirconium, and titanium ions are displaced with respect to the O_2 ions. This displacement is what causes the strong internal dipole moment responsible for the exceptional ferroelectric properties of PZT.

2.6.2 Thickness-mode Ultrasound Transducers

Many transducer designs have been formulated to provide optimal characteristics for different applications. At the core of many of these designs are the basic principles derived from the classical thickness-mode bulk PZT transducer [15]. The classic piston transducer is based on a PZT bulk ceramic plate or disc on which electrodes are laid and poled in the thickness direction to operate as a thickness mode, or extensional mode, resonator. The resonance frequency of the transducer is governed by the thickness of the PZT. The fundamental resonance mode exists when the thickness of the PZT is equal to half the wavelength such that

$$l = \frac{\lambda}{2} \ , \ f = \frac{c}{2l} \tag{2.7}$$

While there are many advantages to these thickness mode transducers, they can be limited in performance, particularly bandwidth, due to the large acoustic impedance mismatch between the PZT (34 MRayls) and the surrounding medium such as water or air (1.5 MRayls for water, 340 Rayls for air). Backing and quarter-wavelength matching layers can be used to help to overcome this problem, but these solutions can be limited by the availability of appropriate matching layer materials and the challenging construction of thinner matching layers as transducer frequencies increase. Such fabrication limitations are of considerable concern, particularly in applications such as 3D volumetric ultrasound where 2D arrays with a large number of closely spaced elements are employed. Even with current dicing and cabling capabilities, these arrays can be difficult and expensive to fabricate.

Commercial side-looking catheters utilizing thickness-mode linear arrays have already been brought to market (eg. Acuson Acunav 7.0MHz catheter, Siemens [17]. Bulk PZT 2D arrays for forward-looking applications have been demonstrated in the literature [18-22] with up to 97 channels operating at 10.0MHz. However, restrictions on kerf size, the complexity of interconnect, limited element survival through fabrication, and potentially high production costs present significant challenges for forward-looking, thickness-mode 2D arrays for catheter-based imaging.

2.6.3 Micromachined Ultrasound Transducers (MUTs)

Micromachined ultrasound transducers (MUTs) are an alternative to traditional PZT

bulk ceramic arrays, particularly for 2D arrays. The use of microelectromechanical (MEMS) devices in ultrasound transducer design is an approach to achieving ultrasound generation and detection while overcoming some of the shortcomings of traditional bulk PZT arrays, particularly for forward-looking catheter-based imaging applications. Such limitations include manufacturable element size for high-density 2D arrays for high-frequency imaging, high element impedance, and large-volume production costs, yielding an advantage to MUT technologies.

MEMS devices are fabricated using well-established semiconductor manufacturing processes, which provide a reliable, cost-effective approach for large volume production of high density 2D arrays with very small form factor. MUT devices can even be constructed to interface directly with on-chip integrated circuits for signal processing [23-27]. Several methods of achieving ultrasound transduction using microelectromechanical (MEMS) devices have been realized. The two predominant approaches are capacitive micromachined ultrasound transducers (cMUTs) and piezoelectric micromachined ultrasound transducers (pMUTs), the latter being the focus of this dissertation.

2.6.3.1 Capacitive Micromachined Ultrasound Transducers (cMUTs)

Capacitive MUTs (cMUTs) operate based on electrostatic transduction [28, 29] rather than piezoactuation. In cMUTs, a membrane is suspended above the fixed substrate, forming a parallel plate capacitor with plate dimensions on the order of 10s of micrometers and gap distances of 10s to 100s of nanometers.

Motion of the flexural membrane during transmit is provided by electrostatic attraction between the oppositely charged plates, and the opposing restoring force

provided by the stiffness of the membrane. In receive, the incident acoustic pressure causes deflection of the membrane which leads to changes in element capacitance. If the element has a fixed charge placed on it, the changing capacitance will result in a variable voltage. This measurable voltage change is the received signal used to form ultrasound images.

The primary performance advantage of cMUTs is high bandwidth, often in excess of 100%. Limitations include lower sensitivity and penetration depth compared to conventional PZT transducers. Typically, a large DC voltage bias of up to 200V must be applied across the membranes during operation which may be problematic for catheter-based applications and even for external contact transducers.

Different cMUT structures are also often required for ultrasound generation and detection – a large gap size during transmission to permit large deformations of the membrane and a small gap size in receive to increase sensitivity. Arrays consisting of both transmit- and receive-dedicated cMUT membranes are required to balance the performance trade-offs between the two element types. The lack of efficient dual-purpose cMUTs places limitations on the size and layout of cMUT arrays.

For high-frequency transducers capable of delivering output pressures suitable for imaging applications, multiple membranes are often used in concert to form a single array element. Often, such necessities limit cMUT use to linear arrays as 2D arrays do not allow sufficient space for numerous membranes per 2D array element that would produce sufficient output, receive sensitively, and fit within the element pitch constraints of a high-frequency 2D transducer array.

Numerous efforts to produce cMUT arrays are ongoing at the time of this writing, though a large number of images presented in the literature are produced using linear [28, 30] and 2D [29] arrays much too large for catheter-based imaging applications.

Of the images presented using arrays suitable for forward-looking catheter probes, 1D arrays operating at 9.2MHz have been demonstrated [31], but 2D and ring arrays have only been shown to operate at lower frequencies (<5MHz) [25, 32, 33] or require target insonification using a separate PZT transducer in order to form the ultrasound image.

2.6.3.2 Piezoelectric Micromachined Ultrasound Transducers (pMUTs)

Piezoelectric micromachined ultrasound transducer (pMUT) two-dimensional (2D) arrays have been proposed as an alternative to conventional bulk-PZT thickness-mode transducers for high frequency, forward-looking, catheter-based ultrasound imaging of the cardiovascular system. The appeal of pMUTs is based on several key advantages over conventional transducer technologies, including high operational frequencies (>20MHz), small element size, and low cost due to their MEMS-based fabrication.

To date, several studies have produced limited results with pMUT devices [34-47]. Few groups have studied pMUTs of the dimensions suitable for high-frequency catheter-based imaging, and fewer still have fabricated physical devices for experimentation. Often, reported pMUT research efforts culminate with only models or simulation of device operation [37, 47]. Even among those with fabricated devices, the device structures and dimensions vary greatly. Circular [36, 40-44] and long, thin rectangular structures [34, 38, 39] are favored for their reduced modeling complexity due to geometrical symmetries or assumptions. Among the studies implementing the square or near-square elements

required for dense 2D arrays, most are too large (>100μm) for high frequency (>10) applications.

While previous studies have demonstrated acoustic performance characteristics suitable for ultrasound image formation, pulse-echo B-mode imaging of tissue and tissue-like phantoms using 2D pMUT arrays with dimensions small enough for forward-looking catheter-based applications have been demonstrated only at Duke University [1-3].

The pMUT arrays designed and produced at Research Triangle Institute, International (Research Triangle Park, NC) in collaboration with Duke University have been acoustically characterized and shown to be suitable for image formation in tissue and tissue-like media. An important step is to demonstrate effective design control. The frequency of operation is a fundamental component of transducer design. Numerous geometric and material factors influence the frequency of pMUT operation. While a wide range of operating frequencies have been demonstrated, the device dimensions and other design factors have been selected largely on an ad-hoc basis. Quantitative description and predictive equations for the frequency of operation are necessary for the continued study of pMUT 2D arrays.

Previous modeling efforts for pMUT vibration have used classical/Kirchoff thin plate theory (CPT) or Mindlin thick plate theory, however pMUTs with the geometric dimensions similar to those explored here, suitable for forward-looking catheter-based imaging, have not been modeled with comparison to physical devices.

Experimental pMUT frequency results were acquired and used to develop an empirical model based on Mindlin thick plate theory. The principles of plate theory, fundamental and higher-order modes, compliant boundary conditions, and water-loading

have been explored extensively through analytical modeling efforts using frequency data collected from physical devices. This dissertation presents the development of a frequency design theory culminating in a set of predictive design equations for the frequency of vibration of 2D pMUT arrays aimed at improving their use in high-frequency, forward-looking, catheter-based ultrasound imaging applications.

Chapter 3

2D pMUT Arrays – 5x5 and 9x9

3.1 Introduction

The initial pMUT devices tested consisted of membranes in 5x5 and 9x9 2D matrix arrays. These devices were test arrays intended to encompass a wide range of structural dimensions, demonstrating the acoustic properties of devices with sizes and thicknesses suitable for catheter-based imaging applications. With only 25 or 81 2D array elements, the element count and aperture size were suitable for demonstrating the possibility of phased array image formation with 2D pMUT arrays, but are limited in both resolution and overall transmit pressure output. Larger 14x14 arrays are presented in Chapter 4, designed using the information gained through study of the 5x5 and 9x9 arrays to optimize imaging properties for array sizes more suitable for image formation.

The experimental methods, results, and observations presented in this chapter will focus on the relationship between device structure and acoustic properties for 5x5 and 9x9 2D array devices. A brief overview of pMUT structure and flexure is provided. The acoustic properties investigated will include transmit and receive frequencies, bandwidth, angular response, transmit pressure output and efficiency, receive sensitivity, and pulse-echo insertion loss.

3.2 pMUT Structure & Operation

3.2.1 Principle of pMUT Flexure

PMUTs are an implementation of the piezoelectric unimorph which employs the combination of the actuation and sensing properties of piezoactive materials with the mechanical advantage provided by a coupled cantilever or membrane.

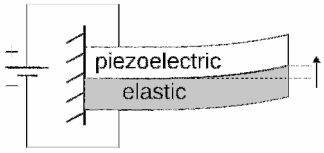

Figure 3.1: Illustration of piezoelectric unimorph deformation under application of an electric field.

A basic piezoelectric unimorph consists of an active layer mechanically coupled to a non-active layer as shown in Figure 3.1. The application of an electric field across the piezoactive layer induces a deformation of that layer due to lateral strain, causing a bending displacement in the coupled cantilever. Similarly, a flexural displacement of the cantilever causes a deformation of the coupled piezoactive layer, inducing an electric field which can be detected.

In pMUTs, the cantilever is extended to form an enclosed membrane spanning a cavity below with an electroded thin-film PZT layer above. The coupled membrane layer provides a mechanical advantage many times that of the deformation of the PZT alone.

3.2.2 pMUT Structure and Fabrication

The structure of a pMUT element consists of a flexible piezoelectric membrane over a cavity which deforms mechanically with applied electrical stimulation. An electroded PZT film is deposited using a spin-coating process onto a silicon/silicon oxide (Si/SiO_2) substrate. The PZT film and electrode layers are photolithographically patterned and etched to form a two-dimensional array of elements. A cavity in the bulk silicon behind each element is etched using a deep reactive ion etch (DRIE) process. Figure 3.2 illustrates the basic structure of a pMUT element.

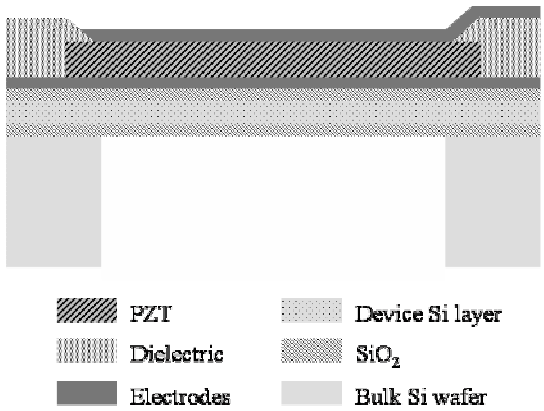

Figure 3.2: Cut-through diagram of pMUT laminate structure with component layers.

For these pMUT devices, the cavity, PZT film layer, and electrodes are positioned in the conformation shown in Figure 3.3. The cavity is shorter in one dimension than the other and undercuts the PZT film layer by several micrometers. In the longer dimension, the cavity extends beyond the dimensions of the PZT film.

Typical PZT film dimensions range from 40-215μm and DRIE etch dimensions range from 25-250μm. PZT film thicknesses are between 1.0-2.0μm while $Si/Si/O_2$ thicknesses are between 2.5-16.0μm yielding total device thicknesses between 5.5-19.0μm.

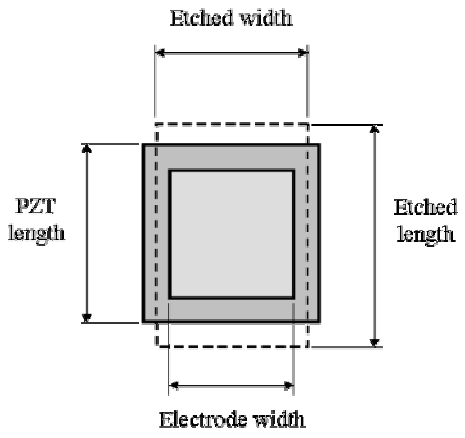

Figure 3.3: Top-down diagram of pMUT structure shown with positioning of the cavity, PZT, and electrode.

3.2.3 pMUT Flexure Mode Operation

Flexure mode operation is a unique method for electromechanical transduction that is significantly different and less understood than conventional thickness mode operation used in bulk ceramic transducers. Ceramic thickness-mode transducers are poled in the thickness direction and operate below the coercive voltage of the PZT material, whereas pMUT devices operate by applying a bipolar signal at voltage levels above the coercive voltage in order to induce 90° domain switching in the PZT film [48]. This causes flextensional motion of the membrane to generate acoustic transmit output from the device. Figure 3.4 illustrates the flexure mode of operation of the pMUT membrane through an applied bipolar voltage cycle [1].

A result of this flextensional mode of operation with bipolar drive is the production of two electromechanical displacement cycles for every voltage cycle applied. The membrane position is driven primarily by expansion and contraction of the PZT film in the lateral direction (parallel to the membrane surface). Because the pMUT is a

unimorph structure, when the PZT film attempts to contract in the lateral direction due to a net domain alignment in the thickness direction, the membrane flexes downward.

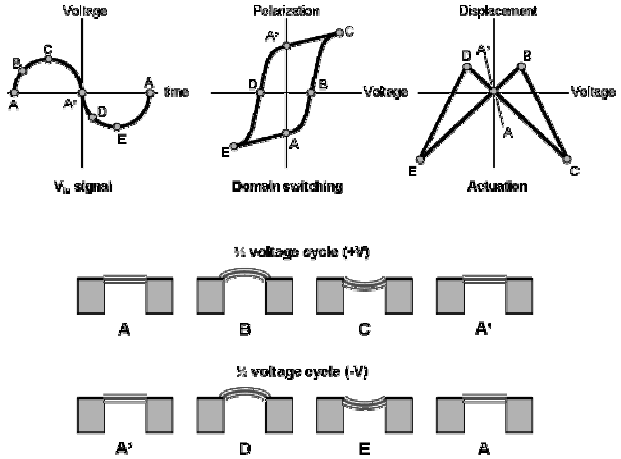

Figure 3.4: Flextensional mode of operation for pMUTs. (Top-left) Applied bipolar voltage cycle, (top-center) ferroelectric hysteresis loop (indicating domain switching), and (top-right) mechanical displacement as a function of input voltage. (Bottom) Diagram of membrane displacement through a full bipolar voltage cycle. Points A and A' refer to 0V applied, points B and D refer to the coercive voltage, and points C and E refer to maximum applied voltage.

In contrast, when the PZT attempts to expand in the lateral direction due to 90° domain reorientation at the coercive voltage, the membrane flexes upward. Furthermore, the same movement occurs for both signs of polarization. This frequency doubling effect has been observed in flextensional bulk ceramic unimorph actuators [48]. One applied sine wave cycle with frequency f_{in} will displace the pMUT membrane as shown in Figure 3.4 producing two flexure cycles. Therefore, the transmit frequency, f_{out}, will be twice the input frequency ($f_{out} = 2f_{in}$) when the pMUT operates in this vibrational mode.

3.3 2D 5x5 and 9x9 pMUT Array Design

The PZT film dimensions ranged from 59-217µm and DRIE etch dimensions ranged from 39-250µm. PZT film thicknesses were between 1.0-2.0µm while $Si/Si/O_2$ thicknesses were between 5.0-16.0µm yielding total device thicknesses (including electrode and thermal layers) between 8.0-19.0µm. Device specifications for 5x5 and 9x9 wafers are provided in Table 3.1 and 3.2.

Table 3.1: PZT film and DRIE etch dimensions and thicknesses for 5x5 2D pMUT arrays. Total device thickness includes electrode and thermal layer contribution.

Wafer	Si/SiO_2 membrane thickness (um)	PZT thickness (um)	Total device thickness* (um)	Nominal Size	DRIE Width (um)	DRIE Length (um)	PZT Width (um)	PZT Length (um)
Wg5	5.0	1.1	8.0	50	40	66	64	60
(5x5)				75	71	100	91	86
				100	99	129	113	110
				200	194	249	217	214
Wg6	5.0	2.0	8.9	50	39	64	62	57
(5x5)				75	70	100	88	84
				100	99	128	111	108
				200	197	246	213	211
Wg8	11.0	1.0	13.0	50	43	69	64	59
(5x5)				75	70	101	90	86
				100	95	126	110	107
				200	193	243	215	213
Wg9	11.0	2.0	13.9	50	42	65	62	58
(5x5)				75	70	101	86	81
				100	96	125	113	108
				200	195	243	215	212
Wg12	16.0	1.0	18.0	50	39	65	64	59
(5x5)				75	69	100	88	85
				100	95	125	113	109
				200	191	241	214	212
Wg14	16.0	2.0	18.9	50	38	65	68	64
(5x5)				75	66	96	92	89
				100	90	122	114	110
				200	187	238	217	214

Table 3.2: PZT film and DRIE etch dimensions and thicknesses for 9x9 2D pMUT arrays. Total device thickness includes electrode and thermal layer contribution.

Wafer	Si/SiO_2 membrane thickness (um)	PZT thickness (um)	Total device thickness* (um)	Nominal Size	DRIE Width (um)	DRIE Length (um)	PZT Width (um)	PZT Length (um)
L2	6.0	1.2	8.1	65	61	84	75	73
(9x9)				75	69	95	87	83
L6	6.0	2.0	8.9	50	38	58	68	64
(9x9)				65	58	78	84	80
				75	71	96	93	89
				100	95	125	118	114
				150	148	177	166	162
L8	11.0	1.2	13.1	65	59	83	78	74
(9x9)				75	66	94	88	84
L11	11.0	2.0	13.9	50	64	82	64	59
(9x9)				65	70	88	--	--
				75	77	100	90	85
				100	98	127	113	107

Signal traces from the top electrodes run between the membranes to signal pads along the periphery of the device which are wirebonded to pin pads of the CPG18421 ceramic package (Spectrum Semiconductor Materials, Inc). The bottom ground electrodes of the device are arranged as an interconnected grid with traces running to large ground pads at the corners of each device as shown in Figure 3.5.

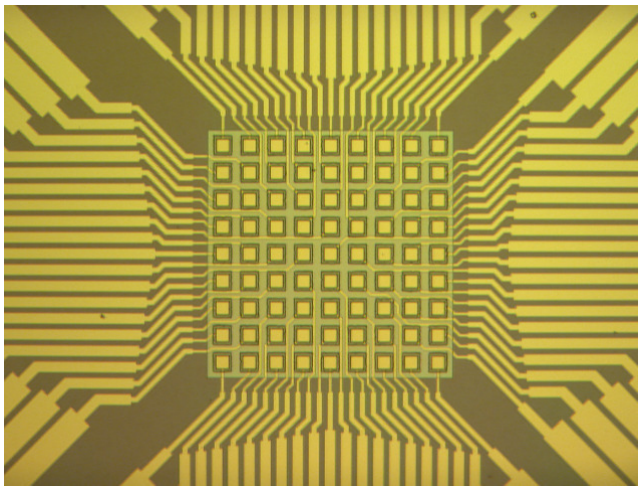

Figure 3.5: Photo of 9x9 2D pMUT array with 50µm membranes showing bottom ground grid and signal traces running to periphery of device.

These earliest pMUT 2D array prototypes covered a wide range of membrane areas and thicknesses in order to capture a broad set of operational parameters.

3.4 2D pMUT Array Experimental Results

Acoustic properties were measured in a water tank filled with de-ionized water to prevent electrical shorting on the transducer face. Unless otherwise specified, the pMUT 2D arrays were held in custom holder into which the pMUT ceramic package could be placed with access to the package pins on the back while the device face was submerged in water. The holder was fixed to a custom mount which allowed it to be held in place on a ring stand. The holder was lowered into the water tank far enough to submerge the face of the array while a receiving hydrophone, transmitting piston, or pulse-echo target was positioned using the XYZ-translation system on the water tank.

3.4.1 Electrical Properties

Measured single element capacitance for the 5x5 2D pMUT arrays are provided in Table 3.3.

An impedance analyzer (HP4194) was used to identify resonant frequencies in the electrical response of single pMUT elements in air. Due to the low impedance of the elements, the magnitude plot does not show measurable change. However, the phase of the impedance is more sensitive to changes in the frequency response. Deformation of

the membrane during vibration causes a change in phase of the impedance, with the greatest change at or near the resonant frequency.

Table 3.3: Electrical properties of 5x5 pMUTs – single element capacitance and frequencies from impedance analyzer.

Device	t_{Si} (μm)	t_{PZT} (μm)	t_{dev} (μm)	W_{etch} (μm)	L_{etch} (μm)	f_{imp} (MHz)	C (pF)
Wg5 B5050_100A	6.0	1.1	8.0	40	66	12.70	42.3
Wg6 B5050_100C	6.0	2.0	8.9	39	64	13.70	30.1
Wg8 B5050_100D	11.0	1.0	13.0	43	69	10.65	46.1
Wg9 B5050_100	11.0	2.0	13.9	42	65	12.78	27.9
Wg12 B5050_100B	16.0	1.0	18.0	39	65	13.45	43.7
Wg14 B5050_100	16.0	2.0	18.9	38	65	--	32.5
Wg5 B7550_100A	6.0	1.1	8.0	71	100	8.86	77.8
Wg6 B7550_84A	6.0	2.0	8.9	70	100	10.00	46.3
Wg8 B7550_100C	11.0	1.0	13.0	70	101	9.11	91.0
Wg9 B7550_100D	11.0	2.0	13.9	70	101	8.70	51.0
Wg12 B7550_100A	16.0	1.0	18.0	69	100	9.75	81.4
Wg12 B7550_100B	16.0	1.0	18.0	69	100	9.65	81.4
Wg14 B7550_100A	16.0	2.0	18.9	66	96	10.90	47.8
Wg5 B10050_100A	6.0	1.1	8.0	99	129	5.03	121.0
Wg6 B10050_100C	6.0	2.0	8.9	99	128	5.83	75.7
Wg8 B10050_100A	11.0	1.0	13.0	95	126	4.14	122.6
Wg9 B10050_100C	11.0	2.0	13.9	96	125	4.45	74.4
Wg12 B10050_100A	16.0	1.0	18.0	95	125	--	122.2
Wg14 B10050_100A	16.0	2.0	18.9	90	122	6.07	72.9
Wg5 B200100_100D	6.0	1.1	8.0	194	249	1.19	444.6
Wg6 B200100_100B	6.0	2.0	8.9	197	246	1.39	270.0
Wg8 B200100_100A	11.0	1.0	13.0	193	243	1.86	448.2
Wg9 B200100_100C	11.0	2.0	13.9	195	243	1.84	213.1
Wg12 B200100_100B	16.0	1.0	18.0	191	241	2.49	481.0
Wg14 B200100_100D	16.0	2.0	18.9	187	238	2.44	254.0

Figure 3.6 shows the phase of the impedance vs. frequency for representative elements from devices of varying size in air. The frequency at which the impedance phase peaks indicates the fundamental resonant frequency of the pMUT membrane.

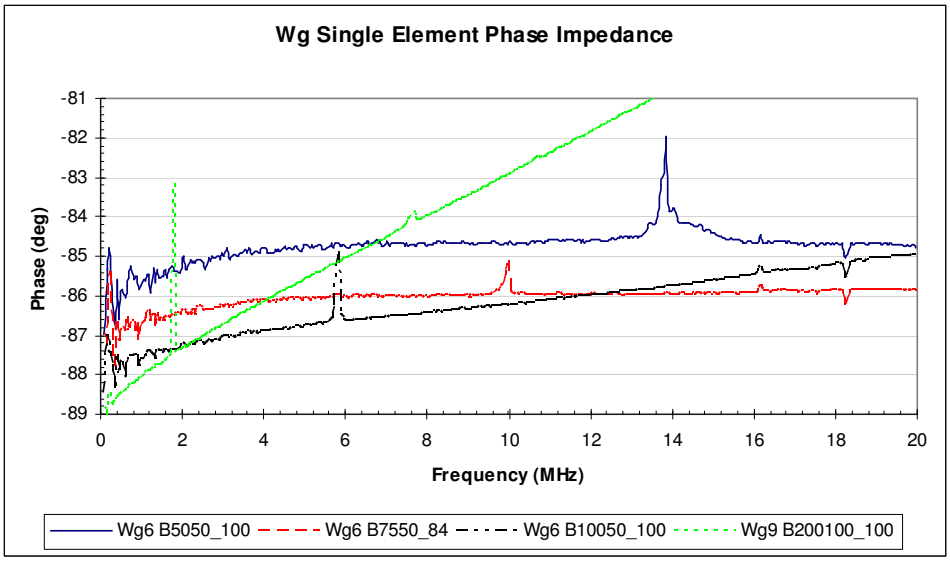

Figure 3.6: 5x5 pMUT single element impedance phase vs. frequency for representative arrays of varying size in air.

3.4.2 Transmit Properties

The frequency and sensitivity of the pMUTs in transmit were measured at a range of 20mm using a pressure calibrated, wide-bandwidth hydrophone (Onda Corp., SEA GL-0200) with an integrated preamplifier. The hydrophone was clamped to an X, Y, Z manual translation system and submerged in the water tank. The hydrophone was then moved to a position 2cm below the pMUT array and peaked to the highest transmit amplitude from the center element of the array. All measurements in transmit were then made from this position. The hydrophone output was passed through a low-noise, wideband variable gain signal amplifier (custom boxed AD600 with transmit protection) set at 66dB gain.

The pMUT devices were placed in a custom holder above a water tank filled with deionized water. The pMUT elements were driven with a 3.0 cycle sine wave burst from a function generator (Agilent 33250A) through a 50dB power amplifier (ENI Model

325LA). For initial comparisons, all pMUT elements regardless of PZT film thickness were operated at approximately the same applied voltage of 25-30V peak-to-peak (V_{pp}). A digitizing oscilloscope (Tektronix TDS 754A) was used to measure the amplitude and center frequency of the signal amplifier output. A 10x oscilloscope probe (TEK P6139A, 8.0pF, 10MΩ) was used to measure the voltage output from the power amplifier at the pMUT elements.

Table 3.4: Transmit frequency, transmit output pressure, and transmit efficiency for 5x5 pMUT 2D arrays at 3.0cyc, 25-30V_{tx}.

Device	t_{Si} (µm)	t_{PZT} (µm)	t_{dev} (µm)	W_{etch} (µm)	L_{etch} (µm)	f_{tx} (MHz)	P_{tx} (kPa)	Tx Eff. (Pa/V)
Wg5 B5050_100A	6.0	1.1	8.0	40	66	10.90	4.1	155.7
Wg6 B5050_100C	6.0	2.0	8.9	39	64	11.90	2.7	105.3
Wg8 B5050_100D	11.0	1.0	13.0	43	69	11.00	4.8	174.6
Wg9 B5050_100	11.0	2.0	13.9	42	65	12.60	3.9	145.6
Wg12 B5050_100B	16.0	1.0	18.0	39	65	13.20	1.0	36.1
Wg14 B5050_100	16.0	2.0	18.9	38	65	13.60	0.6	22.6
Wg5 B7550_100A	6.0	1.1	8.0	71	100	7.70	3.5	129.7
Wg6 B7550_84A	6.0	2.0	8.9	70	100	8.20	2.1	76.4
Wg8 B7550_100C	11.0	1.0	13.0	70	101	8.40	4.5	168.4
Wg9 B7550_100D	11.0	2.0	13.9	70	101	8.60	3.8	138.3
Wg12 B7550_100A	16.0	1.0	18.0	69	100	9.10	4.5	173.6
Wg12 B7550_100B	16.0	1.0	18.0	69	100	9.05	4.5	173.6
Wg14 B7550_100A	16.0	2.0	18.9	66	96	8.60	1.3	50.8
Wg5 B10050_100A	6.0	1.1	8.0	99	129	4.30	1.8	60.8
Wg6 B10050_100C	6.0	2.0	8.9	99	128	5.20	1.8	60.9
Wg8 B10050_100A	11.0	1.0	13.0	95	126	5.10	2.8	102.7
Wg9 B10050_100C	11.0	2.0	13.9	96	125	4.80	2.2	88.1
Wg12 B10050_100A	16.0	1.0	18.0	95	125	6.20	3.5	133.9
Wg14 B10050_100A	16.0	2.0	18.9	90	122	6.40	1.9	66.7
Wg5 B200100_100D	6.0	1.1	8.0	194	249	3.80	3.7	147.2
Wg6 B200100_100B	6.0	2.0	8.9	197	246	4.30	2.8	117.6
Wg8 B200100_100A	11.0	1.0	13.0	193	243	6.50	4.7	240.3
Wg9 B200100_100C	11.0	2.0	13.9	195	243	6.80	3.8	154.0
Wg12 B200100_100B	16.0	1.0	18.0	191	241	8.40	2.4	134.9
Wg14 B200100_100D	16.0	2.0	18.9	187	238	8.60	2.2	95.4

Measured values for the transmit frequency, transmit pressure output, and transmit efficiency (mV received on hydrophone/pMUT drive V) are listed in Table 3.4 for 5x5

2D pMUT arrays with element widths ranging from 50µm – 200µm and element pitch ranging between 100µm – 300µm.

A 1.0-cycle transmit pulse measured using the hydrophone for a single element from a representative 5x5 pMUT array is shown in Figure 3.7 along with its FFT showing a -6dB bandwidth of 56%.

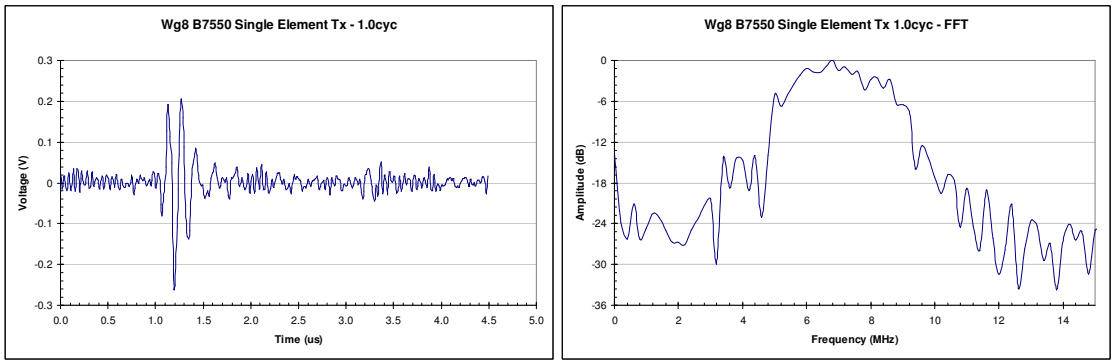

Figure 3.7: Representative 1.0-cycle transmit pulse (left) from Wg8 75µm element with FFT (right).

The measured operating frequency for each device was determined by selecting the frequency of maximum output pressure from the array elements as measured by the calibrated hydrophone. Frequencies fell between 3.8 – 13.6 MHz, depending on the element width and the membrane thickness. In general, smaller element width and higher membrane thickness yielded higher transmit frequencies. Figure 3.8 shows the frequency as a function of pMUT element etched length for each pMUT construction.

We observe that elements with lengths falling in the 50µm – 150µm range exhibit a linear decrease in frequency as element length increases, regardless of the thicknesses of the PZT and Si layers. This follows the expected trend for vibrational plates. As the resonant dimension of vibration increases, the wavelength supported by the structure increases, and frequency decreases. However, for the larger elements with 250µm etched

length, we observe that the frequency is greater than expected for a structure of this size, suggesting that these devices operate in a higher order mode than the smaller elements.

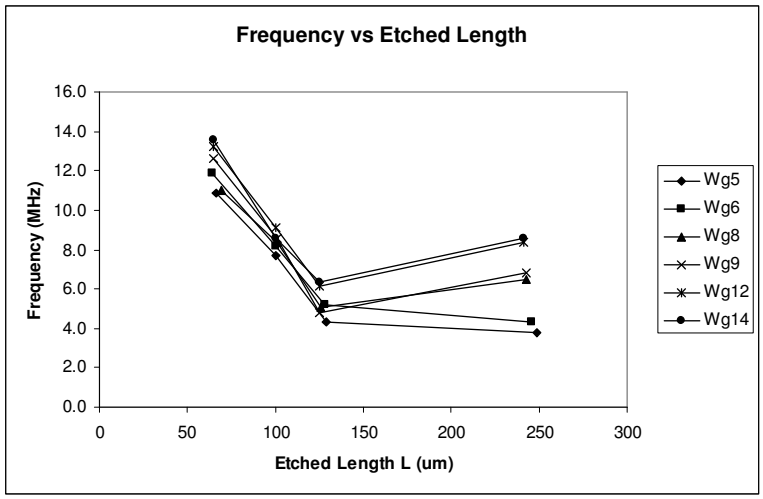

Figure 3.8: Frequency vs. etched cavity length for 5x5 pMUT array elements.

We observe that there exists a frequency dependence on the construction of the elements for these large elements. The Si thickness appears to change the frequency, with an increase in the Si layer giving an increase in frequency. Additionally, we observe that for thicker PZT (Wg6, Wg9, Wg14), the frequency is higher than for the devices with the same Si thickness but thinner PZT film (Wg5, Wg8, Wg12, respectively).

In order to correlate the transmit properties of elements with different PZT thicknesses, transmit pressure efficiency was calculated as a ratio of pressure received at the calibrated hydrophone, P_{gl}, to the transmit excitation voltage applied to the element, V_{Tx}. Transmit pressure field efficiency was calculated as a ratio of pressure received at the calibrated hydrophone, P_{gl}, to the electric field applied to the element, $E_{Tx}= V_{Tx}/t_{PZT}$.

Figure 3.9 shows the transmit efficiencies for pMUT single elements in relation to element size (given here by the length of the etched cavity) for devices with different

PZT and Si thicknesses. For devices with 5µm and 10µm Si thickness, we observe that elements with thicker PZT films provided higher pressure output per unit electric field applied and, excluding the larger 200µm elements, smaller elements yield a higher transmit efficiency. Note that with thicker PZT devices, higher voltages are required to achieve the same electric field in the PZT. For several devices, the transmit pressure field efficiency advantage for thicker PZT is marginal and may be outweighed by other considerations, particularly receive sensitivity (discussed in a later section).

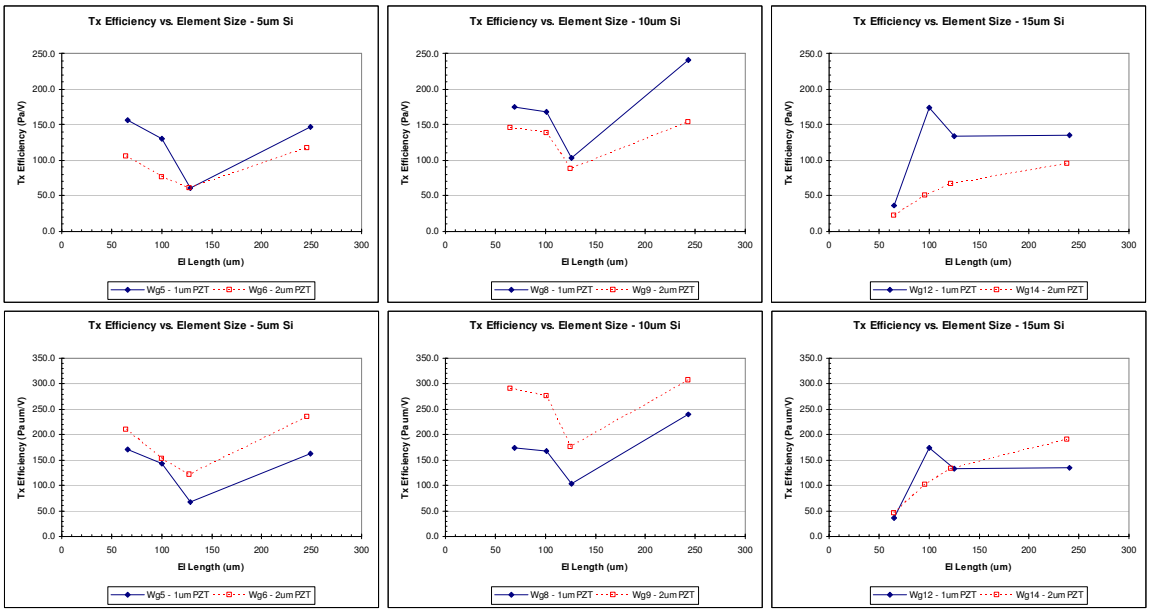

Figure 3.9: Transmit pressure and field efficiencies of pMUT elements driven at 25-30V_{pp} for PZT thicknesses of 1 and 2 µm and device silicon thicknesses of (left) 5 µm, (center) 10 µm and (right) 15 µm. Transmit pressure efficiency (top row) was calculated as pressure received at the hydrophone divided by applied voltage. Transmit pressure field efficiency (bottom row) was calculated as pressure received at the hydrophone divided by applied field (V_{tx}/t_{PZT}).

The increase in the transmit efficiency of the large 200µm elements suggests that these devices may be operating in a different vibrational mode. We also observe that an increase from 5µm to 10µm in Si thickness yields an increase in transmit efficiency, but

increasing the Si thickness (and thus, the membrane stiffness) further to 15µm causes a dampening of the device's ability to transmit. This dampening is particularly great for smaller elements where the width to thickness ratio of the membranes is smaller and an increase in stiffness may have a greater effect.

Increased applied voltage also increases transmit efficiency and output pressure. The transmit pressure efficiency of a single pMUT element was measured for transmit excitation voltages in the range $5V_{pp} – 70V_{pp}$. Figure 3.10 shows the transmit pressure efficiency measured in Pa/V and transmit pressure for a single Wg9 B7550 array element (75µm element width, 2µm PZT thickness, 10µm Si thickness). Transmitted pressure was measured using the pressure-calibrated SEA GL-0200 hydrophone.

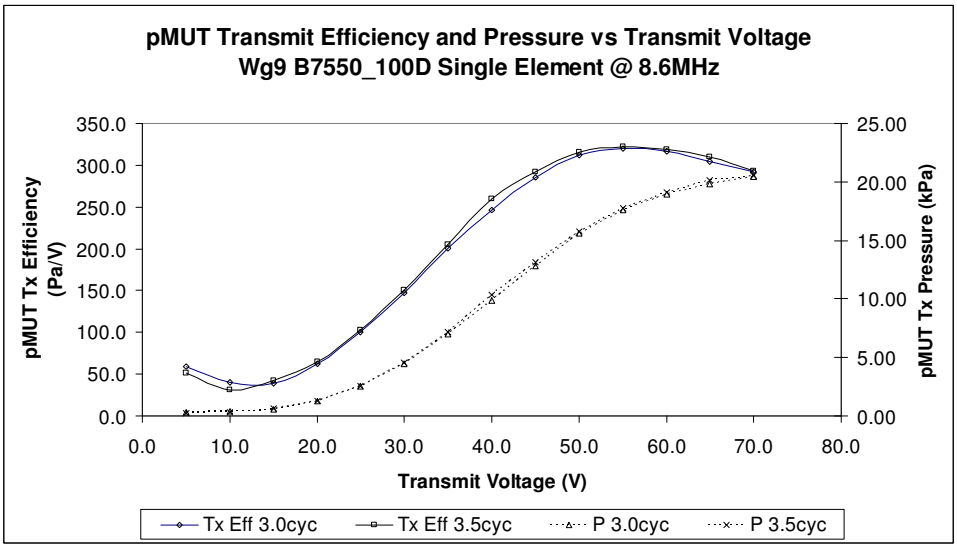

Figure 3.10: pMUT transmit efficiency vs. applied transmit excitation voltage for Wg9 B7550 array element with PZT film thickness of 2µm and 10µm Si thickness at 8.6MHz, 3.0 or 3.5 cycles. Transmit efficiency calculated as Tx pressure/applied voltage (Pa/V) where Tx pressure is measured using a pressure calibrated hydrophone.

At a distance of 20mm from the pMUT array, transmit efficiencies up to 322 Pa/V have been observed, with pressure output as high as 20.5 kPa.

Because the pMUTs operate in a flextensional mode (above the coercive voltage) that employs 90° domain switching in the PZT film, the polarization and displacement of the pMUT membrane is nonlinear with respect to the applied voltage beyond the coercive voltage [48]. Therefore, the acoustic transmit output can be increased nonlinearly by increasing voltage above the coercive voltage until the polarization becomes saturated.

The angular response in transmit was measured by translating the hydrophone linearly in elevation and azimuth with amplitudes measured at regular intervals. Signal amplitude in relative dB plotted vs. angle for representative 75µm and 20µm elements are shown in Figure 3.11. Both elevation and azimuth are shown to be in good agreement as expected for devices with near-uniform dimensions.

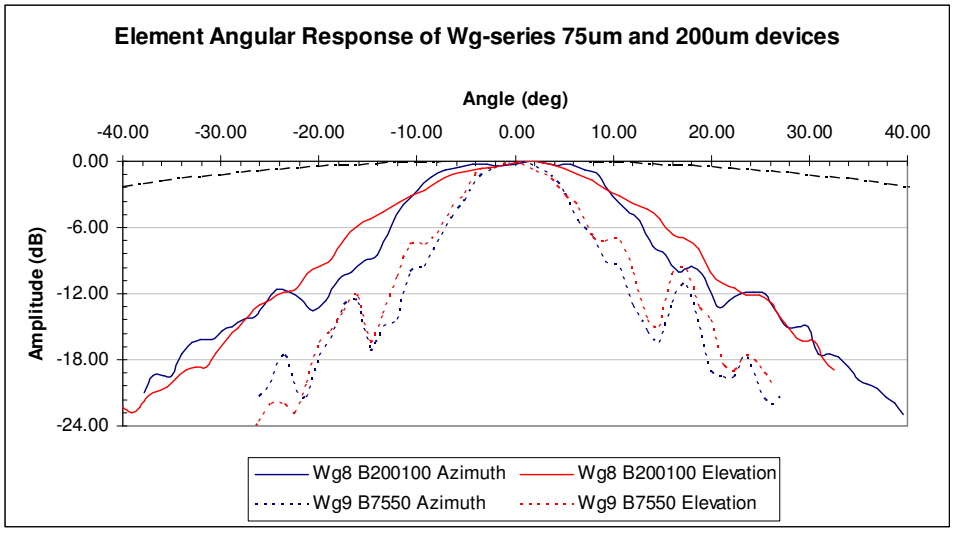

Figure 3.11: Angular response of representative 75µm and 200µm single elements in transmit into hydrophone. Measured data as labeled, *cos(θ)* shown in black for reference.

The 200mm device has a -6dB half-angle of 12.7° in azimuth and 16.0° in elevation. The smaller 75µm device shows a surprisingly narrower angular response, with a -6dB half-angle of about 7.8° in both directions. Both devices have a narrower response than

both an idealized point source, which would have a nearly flat angular response, and an idealized small element (with size small compared to the wavelength) which would experience a decrease proportional to the cosine of the angle to the aperture (-6dB half-angle = 60°). The narrow angular response for both devices indicates that coupling/crosstalk may induce adjacent elements to vibrate, causing an effective aperture larger than expected to be formed by multiple elements.

3.4.3 Receive Properties

Characterization of the frequency response of pMUTs in receive was performed by providing an acoustic pulse from a piston transducer and receiving with a pMUT array element in a water tank filled with deionized water. The pMUT was held in the custom holder while the piston was moved to a position that peaked receive amplitude of the pMUT using the X,Y,Z translation stage. The piston was driven with the output of the Agilent function generator alone or with the addition of the 50dB power amplifier.

The wide range of frequencies in receive required the use numerous pistons to provide acoustic input for the pMUTs. Panametrics 5.0, 7.5, and 10MHz pistons were pressure-calibrated to produce 100kPa using the GL-0200 hydrophone. The pMUT array was then substituted in place of the hydrophone and the received signal was recorded. The piston transmit frequency was swept across a range to determine the optimal receive frequency, determined by identifying the frequency at which the pMUT element was most sensitive. In a passive receive mode, the pMUT element output was amplified with the AD600 signal amplifier with the output measured on an oscilloscope.

The receive sensitivity was calculated as the peak-to-peak received signal amplitude on the pMUT (corrected for the gain of the AD600 amplifier) divided by the piston pressure output (roughly 100kPa). Receive bandwidth was measured for 1- and 3-cycle piston output by taking the -6dB bandwidth from the FFT of the received signal.

Receive frequency, sensitivity, and bandwidths for the 5x5 2D pMUT arrays are provided in Table 3.5. For 100µm and 200µm devices, multiple receive frequencies are observed. The lower frequencies tend to have higher receive sensitivities and bandwidths than the higher frequencies. The low frequencies are expected to be fundamental mode while the higher frequencies are higher-order modes.

Figure 3.12 provides the receive frequencies plotted against element size for each device type. Transmit frequencies are also provided for comparison. The receive frequencies, in general, are lower than the transmit frequencies for the same device, with the deviation increasing as element size increased. Increases in PZT or Si thickness was associated with higher receive frequency.

The measured receive frequencies in water were typically within 10% of the measured transmit frequencies in water, particularly for the 50µm and 75µm devices. However, multiple frequency peaks were observed in the receive response of the 100µm and 200µm devices.

Table 3.5: Measured receive properties of 5x5 pMUT 2D arrays. Receive frequency, pressure sensitivity, and -6dB bandwidth for 1- and 3-cycle pulses. Impedance analyzer and transmit frequencies provided for comparison.

Device	t_{dev} (µm)	W_{etch} (µm)	L_{etch} (µm)	$f_{imp.\ an.}$ (MHz)	f_{tx} (MHz)	f_{rx} (MHz)	Rx Sens (µV/kPa)	3cyc -6dB BW (%)	1cyc -6dB BW (%)
Wg5 B5050_100A	8.0	40	66	12.7	10.90	10.98	14.02	17.3%	20.0%
Wg6 B5050_100C	8.9	39	64	13.7	11.90	12.11	13.67	9.1%	9.1%
Wg8 B5050_100D	13.0	43	69	10.65	11.00	11.07	9.69	16.2%	18.9%
Wg9 B5050_100	13.9	42	65	12.78	12.60	11.96	5.85	19.2%	22.5%
Wg12 B5050_100B	18.0	39	65	13.45	13.20	12.96	1.80	21.2%	23.1%
Wg14 B5050_100	18.9	38	65	--	13.60	13.31	1.24	12.0%	13.2%
Wg5 B7550_100A	8.0	71	100	8.86	7.70	7.28	23.55	19.6%	19.9%
Wg6 B7550_84A	8.9	70	100	10	8.20	7.56	21.00	14.7%	15.5%
Wg8 B7550_100C	13.0	70	101	9.11	8.40	7.78	14.62	25.6%	37.8%
Wg9 B7550_100D	13.9	70	101	8.7	8.60	7.31	16.74	15.8%	14.4%
Wg12 B7550_100A	18.0	69	100	9.75	9.10	8.21	3.61	24.1%	24.9%
Wg12 B7550_100B	18.0	69	100	9.65	9.05	8.19	9.22	23.2%	24.0%
Wg14 B7550_100A	18.9	66	96	10.9	8.60	8.56	4.13	14.0%	14.0%
Wg5 B10050_100A	8.0	99	129	5.03	4.30	3.94	60.53	25.8%	32.0%
Wg6 B10050_100C	8.9	99	128	5.83	5.20	4.61	51.17	24.4%	26.5%
Wg8 B10050_100A	13.0	95	126	4.14	5.10	4.13	63.61	28.8%	42.7%
Wg9 B10050_100C	13.9	96	125	4.45	4.80	4.10	61.03	31.0%	46.3%
Wg12 B10050_100A	18.0	95	125	--	6.20	4.73	5.25	23.4%	25.1%
Wg14 B10050_100A	18.9	90	122	6.07	6.40	4.92	10.40	22.9%	23.5%
Wg5 B10050_100A	8.0	99	129	--	--	3.32	100.98	--	--
Wg6 B10050_100C	8.9	99	128	--	--	3.94	57.31	--	--
Wg8 B10050_100A	13.0	95	126	--	--	2.92	99.00	--	--
Wg9 B10050_100C	13.9	96	125	--	--	3.23	96.16	--	--
Wg12 B10050_100A	18.0	95	125	--	--	3.80	8.05	--	--
Wg14 B10050_100A	18.9	90	122	--	--	4.16	17.26	--	--
Wg5 B200100_100D	8.0	194	249	--	3.80	2.57 / 3.60	13.74	27.6%/---	34.4%/---
Wg6 B200100_100B	8.9	197	246	--	4.30	4.52	37.63	11.6%	12.9%
Wg8 B200100_100A	13.0	193	243	--	6.50	6.01	28.89	24.5%	25.8%
Wg9 B200100_100C	13.9	195	243	--	6.80	6.20	27.24	21.8%	23.7%
Wg12 B200100_100B	18.0	191	241	--	8.40	--	--	--	--
Wg14 B200100_100D	18.9	187	238	--	8.60	--	--	--	--
Wg5 B200100_100D	8.0	194	249	1.19	--	0.7 / 1.4	12.51	--	--
Wg6 B200100_100B	8.9	197	246	1.39	--	0.8 / 1.1	22.13	--	--
Wg8 B200100_100A	13.0	193	243	1.86	--	1.10 / 1.52	38.98	---/33.3%	---/45.3%
Wg9 B200100_100C	13.9	195	243	1.84	--	1.10 / 1.51	49.38	---/29.3%	---/34.0%
Wg12 B200100_100B	18.0	191	241	2.49	--	1.98	37.38	34.5%	49.5%
Wg14 B200100_100D	18.9	187	238	2.44	--	2.05	58.76	31.0%	48.0%

For the 100μm devices, one frequency close to that of the transmit response was observable (8 – 23% lower than f_{tx}) with the deviation from f_{tx} increasing as the Si thickness increased. A second frequency was observed between 23-35% below f_{tx}. The ratio between these two observed frequencies in receive for the 100μm devices is between 1.17-1.41, which is close to the aspect ratio (etched length/width) of the devices, 1.29-1.36. The two frequencies observed are likely attributed to the superposition of frequencies supported along either length or width dimension. Their appearance in the response of the 100μm devices may be the result of the convergence of the two frequencies as the aspect ratio approaches 1.0 (a square plate). The smaller devices are more bar-like, with larger *L:W* aspect ratios, which would result in a larger separation between frequencies supported along device dimensions.

The aspect ratio of the 200μm devices is even lower (1.25-1.28) possibly providing even stronger coupling of the two modes simultaneously. We observe that the 200mm devices with 5μm and 10μm Si exhibit several receive frequency peaks. These multiple frequency peaks are associated with numerous higher-order modes of vibration. From optical vibrometry measurements, there is strong evidence that shows that the lowest receive frequencies are correlated with a fundamental mode of vibration. The highest receive frequencies close to the transmit frequencies are a 3-1 mode while the intermediate frequencies are associated with fundamental-type modes with slightly smaller size constraints defined by geometric features of the device, such as the active PZT area. Images of these modes are shown in the optical vibrometry results. Further analysis of these frequency modes is discussed in a later chapter.

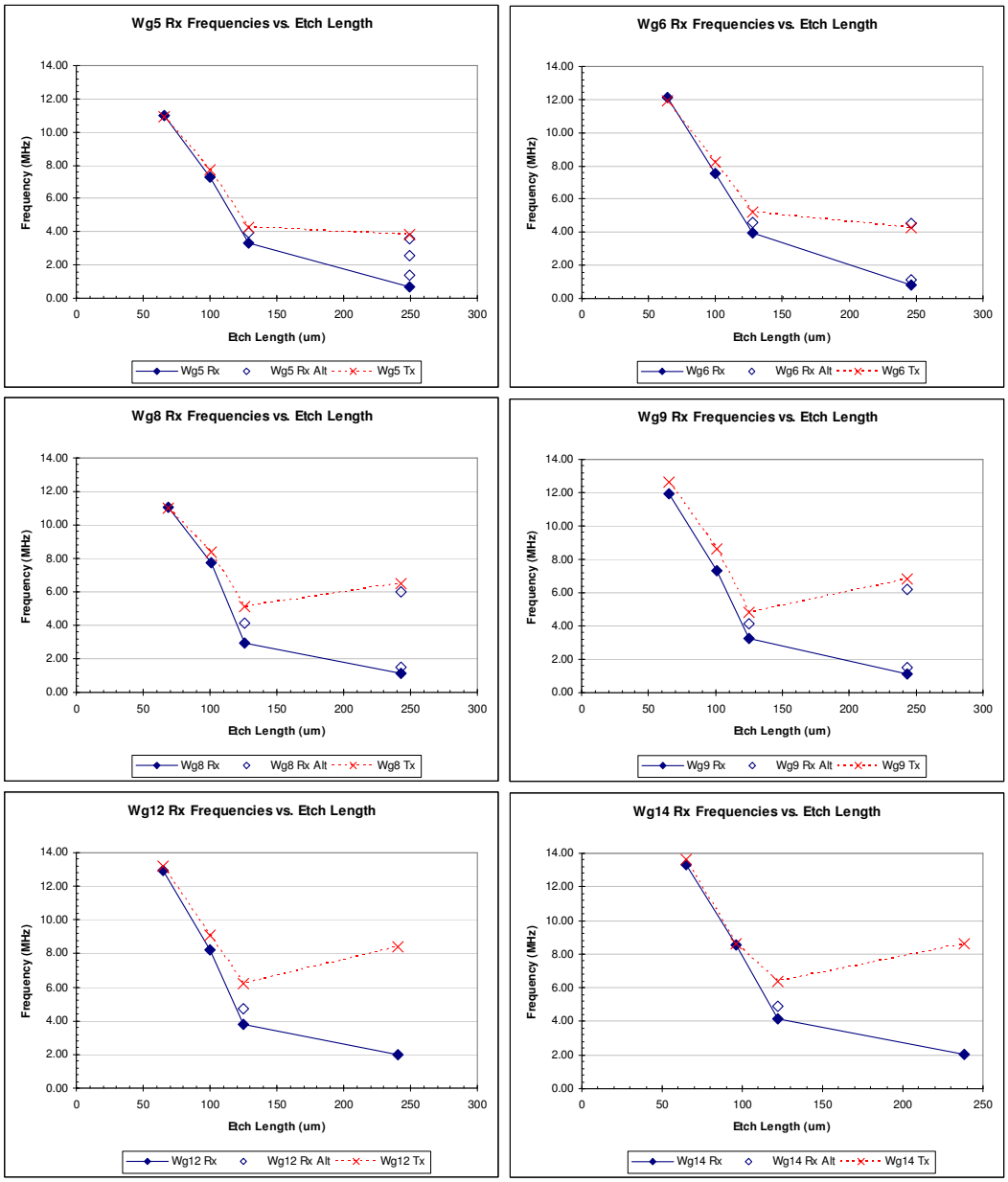

Figure 3.12: 5x5 pMUT 2D array f_{rx} vs. L_{etch} for devices of varying thickness. Solid plot designates the lowest f_{rx} mode. Hollowed points denote higher-mode f_{rx}. Measured f_{tx} (dotted) are provided for comparison.

The receive sensitivity for the lowest frequency mode of single elements of varying size and thickness is plotted in Figure 3.13.

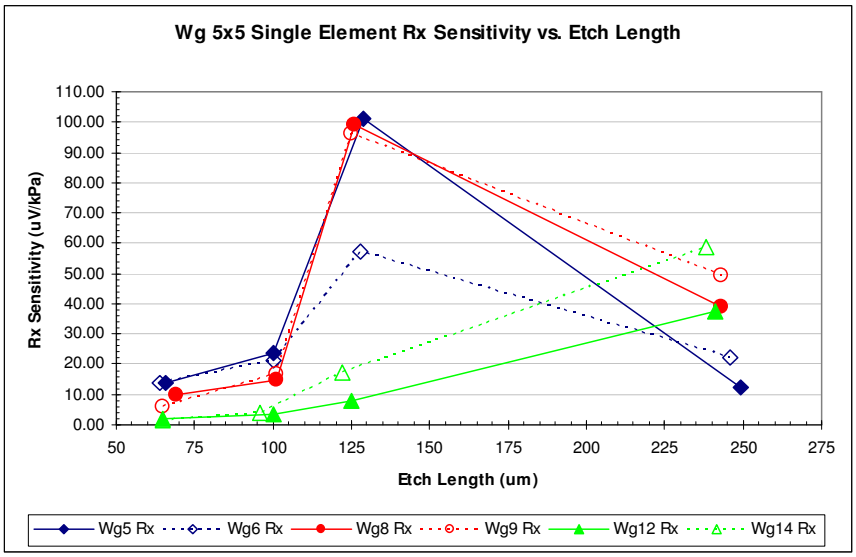

Figure 3.13: Average single element receive sensitivity for 5x5 pMUT arrays. Solid lines denote 1µm PZT, dotted lines denote 2µm PZT.

Receive sensitivity is expected to increase with larger membrane area which is shown to be the trend for the measured response of devices smaller than 125µm in length. The 200µm membranes (250µm etch length) exhibited lower sensitivity than the 100µm membranes for devices with 5µm and 10µm Si. This decrease in sensitivity may be associated with the existence of multiple higher-order frequency modes mentioned previously which would diminish the received signal amplitude due to the multi-modal displacement of the device surface. Note, also, that the lowest frequency mode for the 200µm devices with 5µm and 10µm Si were very narrow-band, ringing for a long duration, much more so than any of the other frequency modes. The relative plate thickness to the lateral span (length) of the devices will be shown later to play a significant role in operating frequency.

Of critical importance in the discussion of pMUT receive performance is the highly dependent response to the application of electrical stimulation that significantly affects

the receive sensitivity, termed "biasing." The amplitude response of the pMUTs in receive varies greatly in a passive unbiased state, both temporally and between elements in the same array.

To improve the consistency in receive sensitivity across an array, a partial-cycle biasing pulse may be applied to the pMUT element using a single channel from a T5 [49] transmit board. The biasing pulse is delivered synchronously with the signal driving the piston. Care must be taken in selecting the measurement range to allow time for the AD600 boxed amplifier to recover from the biasing pulse before the arrival of the acoustic pulse from the piston. The protection circuit of the AD600 amplifier can be modified to minimize the recovery time of the amplifier greatly while losing only 2-4dB gain. However, connection of the T5 Tx board (even when inactive) loads the pMUT in receive enough to diminish the receive signal amplitude by as much as 8-10dB for some devices, which is not ideal for frequency characterization of the pMUTs as the signal levels are already very small. The loss due to loading is typically recoverable for most devices from the sensitivity increase found in active biasing, however, some devices are more susceptible to loading and less responsive to the effects of active biasing.

In imaging applications where connection of transmit and receive components are both necessary and unavoidable, pulse-biasing provides both consistency across an array and improved sensitivity in this configuration. A more detailed investigation on the effect of active biasing is discussed below.

3.4.4 Receive Biasing

The receive biasing of pMUTs has been demonstrated by providing an extra electrical voltage to the element prior to reception. It is unclear at this time how this biasing occurs in the piezoelectric film. Increases in receive sensitivity on the pMUTs have been observed with the application of DC voltages as well as partial-cycle transmit pulses.

As a receive-only device, a pMUT element may be biased with a DC voltage in the range of -5V to 5V and possibly higher. The applied DC voltage that will result in the maximum receive sensitivity was found to be unpredictable. The DC biasing voltage does not appear to depend on element size, thickness, or position in the array, and DC biasing has been observed to decrease the receive sensitivity of the pMUTs in some cases.

The use of a partial-cycle transmit excitation pulse to gain a receive sensitivity advantage over full-cycle transmit excitation has been demonstrated in both water tank experiments and pulse-echo image acquisition using the T5 scanner.

In water tank experiments, a partial-cycle biasing pulse may be applied to the pMUT element using a single channel from a T5 transmit board. The biasing pulse is delivered synchronously with the signal driving the transmit device (piston in Rx-only mode or pMUT element in pulse-echo mode) to ensure that the received pressure arrives following the biasing excitation. Partial-cycle biasing is achieved on the T5 transmit board by changing the digital transmit excitation pattern to include additional positive or negative excitation components. The possible partial-cycle timing patterns are limited by the internal clock of the pattern generator used to control the T5 transmit board (10ns in the water tank experiments). Thus, the transmit excitation pattern can be changed by adding additional positive or negative excitation in 10ns increments. For example, a 5.0MHz,

1.0-cycle transmit excitation pattern would include a 10-clock-cycle loop with positive excitation and a 10-clock-cycle loop with negative excitation. A 1.5-cycle transmit excitation pattern would include another 10-clock-cycle loop with positive excitation while a 1.25-cycle transmit excitation pattern would include only an additional 5-clock-cycle loop.

Shown in Figure 3.14 is a plot of the receive pressure sensitivity for bias cycles amplitudes between $5V_{pp}$ – $50V_{pp}$ for 3.00, 3.25, 3.50, 3.75, and 4.00 cycle biasing pulses. The 3.25 and 3.50 cycle biasing pulses provide a receive sensitivity advantage over both full-cycle pulses (3.0 and 4.0 cycles) and a 3.75 cycle pulse. Biasing with partial-cycle pulses may leave the PZT film of the device in a polarization state that yields greater sensitivity in the receive mode. The biasing advantage of some partial cycle pulses over others may indicate that the device's polarization and displacement curves display a preference for either a positive or negative poled state. Then, for certain cases, the voltage that the partial-pulse cycle leaves may maximize the polarization, thus optimizing the receive sensitivity.

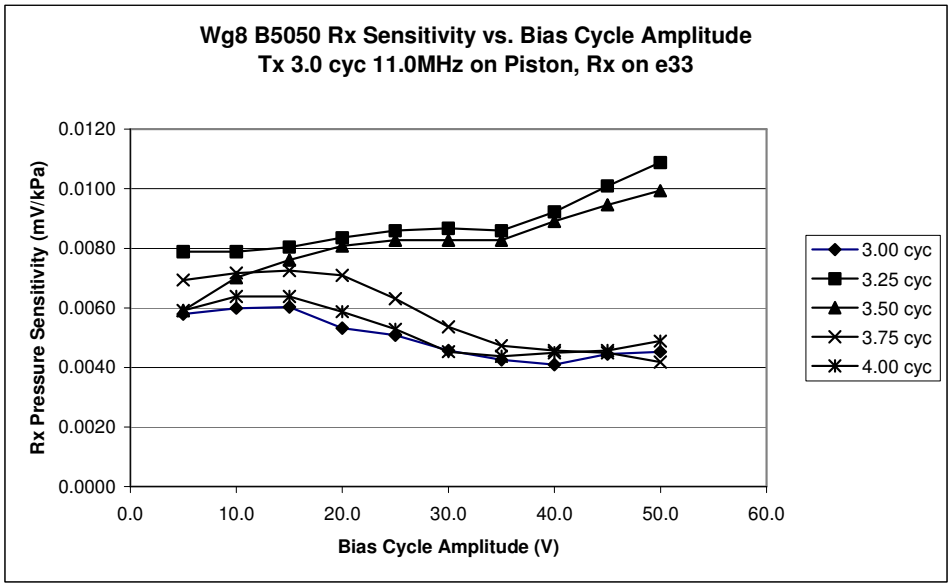

Figure 3.14: Rx pressure sensitivity (mV/kPa) vs. peak-to-peak voltage amplitude of biasing cycle for different cycle lengths.

The pMUT arrays also carry some memory of the biasing mode last applied to them even after the biasing stimulus has been removed. The extent of this memory effect has not been studied in depth, but they have been observed to remain in a biased state after the input has been removed on the scale of hours.

Acoustic measurement with a pressure-calibrated hydrophone showed that the partial-cycle excitation on the pMUT did not produce any significant change in the transmit pressure output from the device, indicating that the biasing advantage is a receive effect.

3.4.5 Pulse-Echo Performance

Pulse-echo measurements were made using an aluminum block target in both the water tank and on the Duke T5 phased array scanner. The scanner was used primarily for 100µm and 200µm element arrays or when it was necessary to join multiple elements for

increased Tx or Rx efficiency. The higher capacitance of these larger single or grouped elements resulted in oscillations between the power amplifier and the pMUT array in the bench-top water tank testing configuration.

In water tank experiments, the Tx pulse from the power amplifier was passed through a transmit protection circuit to decouple the power amplifier used in transmit from the receive amplifier during receive and to limit the current into the pMUT element during the high-voltage transmit excitation cycle. After the protection circuit, the transmit excitation signal was delivered to the pMUT element(s). The receive amplifier was then connected to the receive element(s), and the output of the amplifier was measured using an oscilloscope.

For pulse-echo measurements on the T5 scanner, the pMUT was positioned over an aluminum block target at 20mm range in deionized water and held in a custom breakout board to facilitate connection to the T5 system. The transmit frequency, number of pulse cycles, and active elements were then designated in software. The RF sum was then measured using an oscilloscope. Figure 3.15 shows the pulse-echo response of a single 75µm pMUT element (Wg8 B7550) at 8.4MHz with a 27.6V_{tx}, 0.5-cycle transmit excitation pulse. The -6dB bandwidth for this array was 57%.

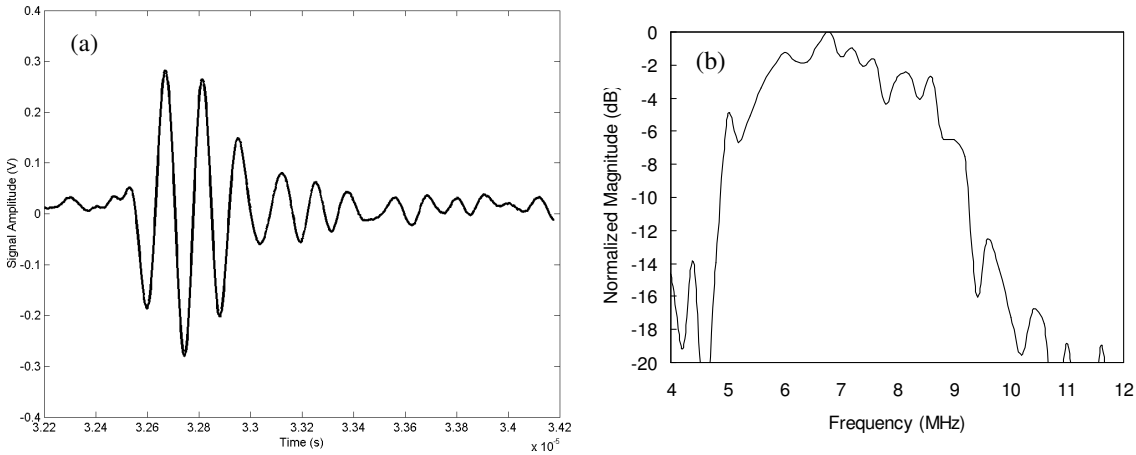

Figure 3.15: (a) Pulse-echo response at 8.4 MHz and (b) FFT bandwidth for a 75 µm pMUT single element with 1 µm PZT thickness and 10 µm silicon thickness driven with a 0.5 cycle, 4.2MHz, 27.6 V_{pp} pulse.

To obtain a value for the pulse-echo insertion loss, multiple Tx elements were required to produce sufficient pressures that could be measured with the pMUT elements in receive. The bench water tank setup was used for this measurement as the T5 scanner receive amplifier gain was indeterminate. A grouping of 25 adjacent elements of a 9x9 array electrically shorted to form one large element. An L6-65 array (65µm element width, 2µm PZT thickness, 5µm Si thickness) was used for this measurement. All 25 elements were used to transmit a 3.5 cycle, 8.8MHz or 8.4MHz signal with peak-to-peak transmit excitation voltage in the range of $30V_{pp} – 60V_{pp}$. The resulting pulse-echo off of the aluminum block target was received on all 25 elements and amplified using the AD600 signal amplifier. The single element pulse-echo insertion loss was then calculated from the 25-element signal by dividing the signal by a factor of 25^2=625 to compensate for the use of 25 elements in transmit and 25 elements in receive, adjusting for the gain of the receive signal amplifier, and dividing by the transmit excitation voltage. Figure 3.16 shows the calculated single element pulse-echo insertion loss

acquired using this method. At $60V_{tx}$, the calculated single element pulse-echo insertion loss at 8.8MHz was -93.1dB. The advantage of this measurement method is that each element that is used in receive is biased with a partial-cycle transmit excitation pulse. However, this calculation assumes a linear process when transmitting and receiving with multiple elements.

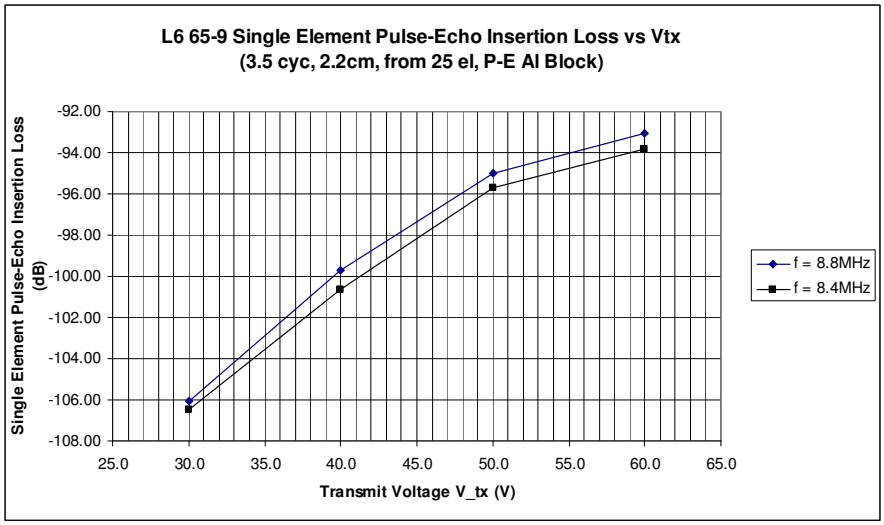

Figure 3.16: Calculated single element pulse-echo insertion loss for a 65µm 9x9 array element. Pulse-echo signal from aluminum block target with 3.5 cycle transmit at a 2.2cm range. 25 elements used in transmit and receive. Single element insertion loss calculated from scaled 25 element pulse echo.

3.5 Summary

Electrical characterization of the 5x5 2D pMUT arrays using an impedance analyzer demonstrated a method of measuring the resonant vibrational frequencies in air, with frequency decreasing with increased element size. Measured element capacitance was consistent with expected values based on device construction.

Characterization of the 5x5 2D pMUT arrays in transmit, receive and pulse-echo has demonstrated promising results for imaging applications. Transmit pressure output up to

20.5 kPa and transmit efficiencies up to 322 Pa/V for 75µm single elements at 20mm range were observed, with up to 56% bandwidth for a 3-cycle truncated sinusoidal pulse.

Transmit frequency decreased with increased element lateral dimension and decreased membrane thickness. Elements with 50µm – 150µm etch length exhibit a linear decrease in frequency as element length increases, regardless of the thicknesses of the PZT and Si layers as expected for vibrational plates. However, for the larger elements with 250µm etched length, we observe that the frequency is greater than we expect for a structure of this size, suggesting operation in a higher mode. The large 200µm elements exhibit a frequency dependence on the element thickness. An increase in the Si layer results in an increase in frequency while thicker PZT yields higher frequencies than devices with the same Si thickness but thinner PZT film. Elements with thicker PZT film also provided higher pressure output per unit electric field applied with smaller elements yielding a higher transmit efficiency with the exception of the 200µm devices operating in a higher order mode.

Receive sensitivities were observed up to 101µV/kPa, increasing as element surface increased and generally decreasing with element thickness. Receive bandwidth for 1-cycle pulse was observed up to 48%. Receive frequency decreased with increased element lateral dimension and decreased element thickness. Receive frequencies were also, in general, lower than the transmit frequencies for the same device. Multiple frequency peaks were observed in the receive response of the 100µm and 200µm devices.

Receive biasing was also investigated. Application of a DC bias voltage resulted in uncertain changes in receive sensitivity independent of element size, thickness or position in the array. Application of partial-cycle transmit excitation pulse biasing was shown to

produce consistent change in receive sensitivity, though the degree of change varied marginally from element to element. Various partial-cycle transmit patterns were considered, with 3.25- and 3.5-cycles producing the greatest sensitivity at high transmit excitation voltage amplitudes. However, care must be taken in the application of partial-cycle biasing as in some cases a decrease in sensitivity was observed for some patterns between different device constructions. Bias characterization should be performed for each device to determine the optimal transmit excitation waveform for pulse-echo operation.

Pulse-echo characterization showed an insertion loss of up to -93.1dB (rel. V/V_{tx}) in a full-array pulse-echo experiment with an assumption of linear transmit and receive response for multiple elements. Pulse-echo bandwidth for a 0.5-cycle transmit was measured to be 57%.

Chapter 4

2D pMUT Arrays – 14x14

4.1 Introduction

Larger 14x14 pMUT arrays were constructed in a subsequent iteration of pMUT 2D devices. The larger arrays were fabricated to demonstrate that the acoustic performance observed in the 5x5 and 9x9 arrays could be scaled up to arrays large enough for imaging.

Additionally, the larger arrays offer an opportunity to focus on the smaller device dimensions that yielded more optimal frequencies and sensitivities for imaging as shown in the testing of 5x5 arrays. Device dimensions were chosen to be equivalent to or smaller than the nominal 75μm 5x5 devices to ensure fundamental mode operation at frequencies sufficient for catheter-based imaging. The range of device dimensions was extended to even smaller membranes than those available with 5x5 arrays. Device thicknesses were chosen to be <12μm for Si/SiO_2 and <1.2μm for PZT based on evidence of decreased sensitivity in thicker devices among 5x5 test arrays.

4.2 14x14 2D pMUT Design

The pMUT 14x14 2D arrays used in this research were similar in structure to the 2D 5x5 and 9x9 arrays discussed previously. pMUT membranes were aligned in a 14x14 evenly-spaced grid over a ground grid or plane. The ground node was connected to the ceramic package ground via traces to the corners of the wafer which were wirebonded to

the package ground plane. Signal traces were routed from signal pads on the periphery of the wafer to individual elements. The device signal pads were wirebonded to the package pads of the CPG22414 ceramic package (Spectrum Semiconductor Materials, Inc.).

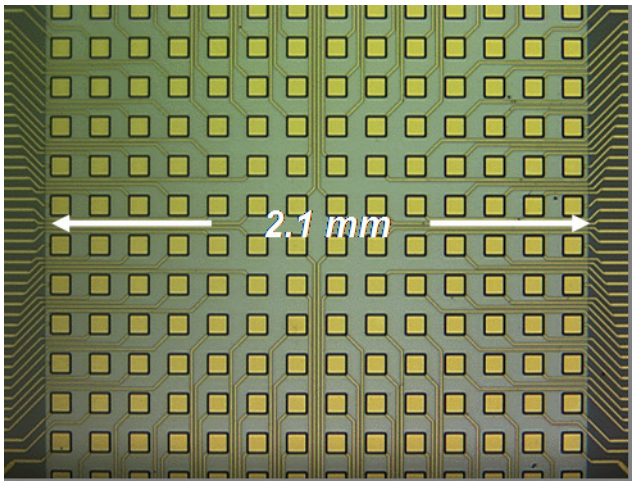

Figure 4.1: 14x14 2D pMUT array with 75µm membranes with 150µm element pitch. Total width and height of active array area is 2.1mm.

Membrane dimensions were targeted for 75µm devices in the first run of devices (wafers A1-A6) and were varied between 40µm and 75µm for a wider range of frequencies in the second run (wafers A11-A16). The PZT film layer was 1.2µm for all 14x14 devices, with 6.0µm Si/SiO_2 wafers A1-A6 and 6.5µm and 12.0µm in wafers A11-A16. Device specifications including target PZT film and DRIE etch dimensions as well as measured dimensions from test structures on the array are provided in Table 4.1.

Estimated frequencies are provided for all devices based on a simple resonator model using the long etch dimension as the resonator length. Measured operating transmit frequencies are provided, when available, as the peak transmit frequency measured into a hydrophone. Note that not all devices were packaged for testing. Only devices from

wafers A1, A2, and A6 with 75µm elements and wafer A11 with 40, 50, 65, and 75µm elements were packaged and tested.

Table 4.1: 14x14 2D pMUT array device specifications with estimated and measured frequencies provided when available.

Wafer	Device	t_{PZT} (um)	t_{Si} (um)	t_{dev} (um)	PZT width (um)	PZT height (um)	DRIE width (um)	DRIE height (um)	Est. Freq. (MHz)	Meas. Tx Freq. (MHz)
A1	75	1.2	6.0	8.13	82	86	103	78	6.0	5.4-6.2
A2	75	1.2	6.0	8.13	84	88	96	65	7.0	6.2-7.4
A11	75	1.2	6.5	8.63	83	87	104	72	6.0	4.2
A11	65	1.2	6.5	8.63	73	76	91	63	8.0	7.0-7.8
A11	50	1.2	6.5	8.63	58	62	77	50	9.0	9.4
A11	40	1.2	6.5	8.63	47	52	64	39	12.0	13.0

All 14x14 2D pMUT arrays were constructed with center-to-center element pitch of 150µm or 175µm for 75µm membrane devices, 150µm for 65µm devices, 100µm for 50µm devices, and 90µm for 40µm devices. Devices from A1-A6 were grounded with a bottom ground grid. Devices A11-A16 had either a grid or plane bottom grounding configuration.

Element capacitances were measured to be 22-58pF per element for 40-75µm arrays.

4.3 14x14 2D pMUT Array Experimental Measurements

Acoustic properties were measured in a water tank filled with de-ionized water to prevent electrical shorting on the transducer face. Unless otherwise specified, the pMUT 2D arrays were held in the ZIF socket of a custom breakout board which aids in connection to the T5 system. Individual elements could also be probed from the back side of the connector board. The board was fixed to a custom mount which allowed it to be held in

place on a ring stand. The board was lowered into the water tank far enough to submerge the face of the array while a receiving hydrophone, transmitting piston, or pulse-echo target was positioned using the XYZ-translation system on the water tank.

4.3.1 Single Element Impedance Analyzer Frequency Response

The HP4194 impedance analyzer was used to identify resonant frequencies in the electrical response of single pMUT elements in air. Figure 4.2 shows the phase of the impedance vs. frequency.

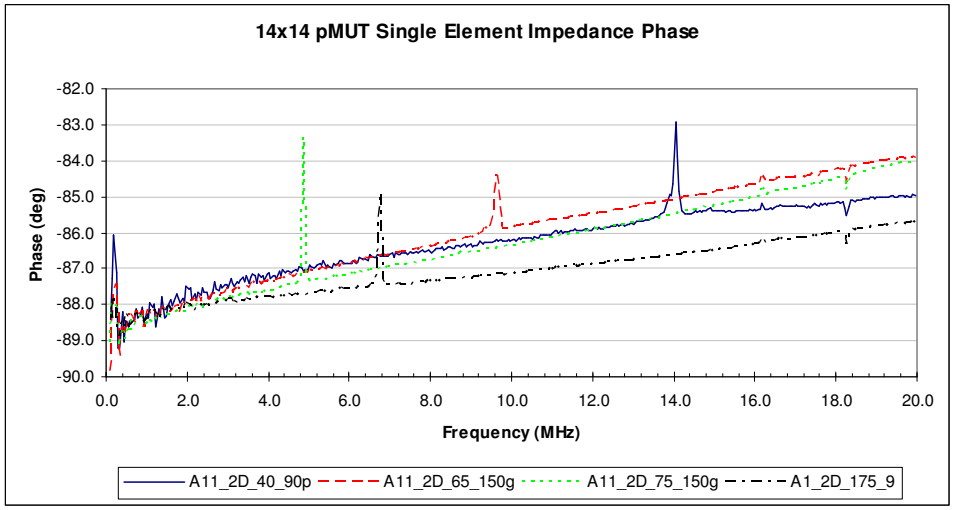

Figure 4.2: 14x14 pMUT single element impedance phase vs. frequency for representative arrays of varying size.

The frequency at which the impedance phase peaks indicates the fundamental resonant frequency of the pMUT membrane. This impedance change can be used as an electrical measurement of the resonant frequency to complement the acoustic measurements. Measured resonance frequencies from the phase of the impedance are provided in Table 4.2.

Table 4.2: Impedance analyzer frequencies for 14x14 2D pMUT array single elements. (Phase peak amplitudes for device A11_2D_50_100p_1 were very low, only a few were elements measurable).

Device	t_{Si} (um)	t_{PZT} (um)	t_{dev} (um)	W_{etch} (um)	L_{etch} (um)	$f_{imp\ an}$ (MHz)
A11_2D_40_90p_1	6.5	1.2	8.6	39	64	14.00
A11_2D_50_100p_1	6.5	1.2	8.6	50	77	6.10 *
A11_2D_65_150g_1	6.5	1.2	8.6	63	91	8.65
A11_2D_65_150p_1	6.5	1.2	8.6	63	91	9.50
A11_2D_75_150g_1	6.5	1.2	8.6	72	104	4.80
A11_2D_75_150p_1	6.5	1.2	8.6	72	104	4.90
A1_2D_175_9 (75µm)	6.0	1.2	8.1	78	103	6.76
A1_2D_150_12 (75 µm)	6.0	1.2	8.1	78	103	6.82
A2_2D_175_12 (75 µm)	6.0	1.2	8.1	65	96	8.00

Comparison of electrical frequency response will be shown in a later chapter to be in excellent agreement with optical vibrometry results. Unfortunately, attempts to observe the effect of loading on the array with water or other media were unsuccessful as the vibration was likely dampened enough to bring any phase change in the impedance down below the sensitivity of the analyzer.

4.3.2 Single Element Transmit Response

The single element transmit response was measured into a pressure-calibrated hydrophone at a range of 20mm. The peak operational frequency was determined by sweeping the input frequency while keeping the transmit voltage at a constant $30V_{tx\text{-}pp}$, recording the frequency at which the peak-to-peak voltage measured on the hydrophone was greatest. Output pressure at the GL0200 hydrophone was determined using the pressure-voltage calibration documentation. Transmit pressure efficiency was calculated as the output pressure divided by the high-amplitude transmit voltage (approx. $30V_{pp}$). The -6dB bandwidth was determined from the FFT of the 1- and 3-cycle transmit

excitation pulses. These properties for A1, A2, and A11 devices of varying size are shown in Table 4.3.

Table 4.3: Measured transmit properties of 14x14 pMUTs. Transmit frequency, pressure, efficiency, and -6dB bandwidth (3- and 1-cycle pulses when available).

Device	t_{Si} (um)	t_{PZT} (um)	t_{dev} (um)	W_{etch} (um)	L_{etch} (um)	f_{tx} (MHz)	P_{gl} (kPa)	Tx Effic. (Pa/V)	-6dB %BW (3cyc)	-6dB %BW (1cyc)
A11_2D_40_90p_1	6.5	1.2	8.6	39	64	13.00	4.70	156.76	7.45	7.84
A11_2D_50_100p_1	6.5	1.2	8.6	50	77	9.40	2.82	93.90	18.00	--
A11_2D_65_150g_1	6.5	1.2	8.6	63	91	7.70	5.05	168.43	9.93	10.60
A11_2D_65_150p_1	6.5	1.2	8.6	63	91	7.00	4.65	155.16	15.30	17.52
A11_2D_75_150g_1	6.5	1.2	8.6	72	104	4.20	2.76	91.88	--	--
A11_2D_75_150p_1	6.5	1.2	8.6	72	104	4.20	2.45	81.67	--	--
A1_2D_175_9	6.0	1.2	8.1	78	103	5.40	7.38	219.8	13.33	20.95
A2_2D_175_12	6.0	1.2	8.1	65	96	6.20	6.14	190.8	12.86	16.86
A1_2D_150_12	6.0	1.2	8.1	78	103	5.60	6.21	185.8	14.41	--

The input excitation waveform was typically a high-voltage 3.0-cycle truncated sine wave produced from a function generator through a 50dB power amplifier (ENI). Figure 4.3 shows a typical single-element transmit output waveform from a 14x14 2D array element measured with the hydrophone.

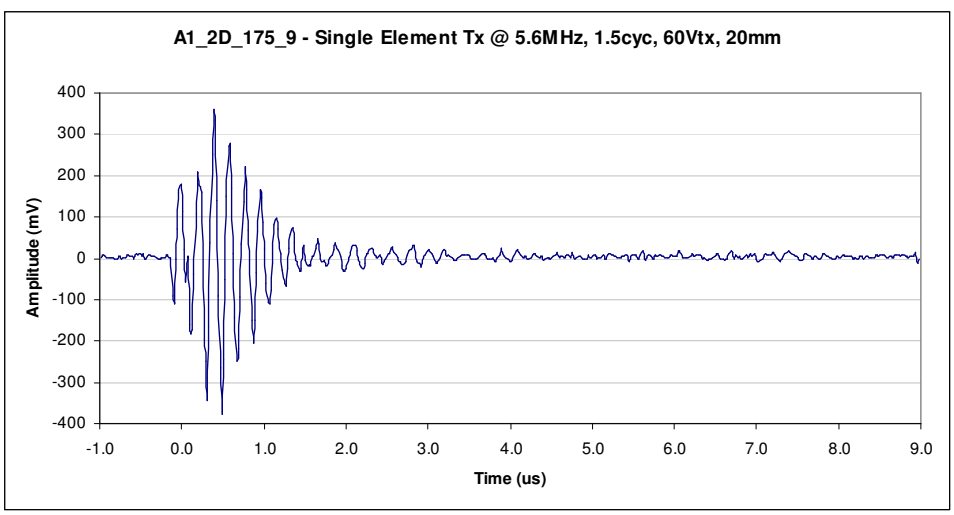

Figure 4.3: A1_2D_75_175_9 single element transmit pulse waveform into pressure-calibrated hydrophone @ 5.6MHz, 1.5cyc, 60V_{tx}. Range = 20mm, amplitude shown includes gain of AD600 small-signal amplifier.

The transmit output pressures for an 14x14 75µm device at 20mm were measured up to 7.4 kPa and transmit efficiencies up to 220 Pa/V were observed. The transmit bandwidth was taken from the Fourier transform of the 1.5- and 3.5-cycle transmit waveforms. The FFT of both waveforms are shown in Figure 4.4.

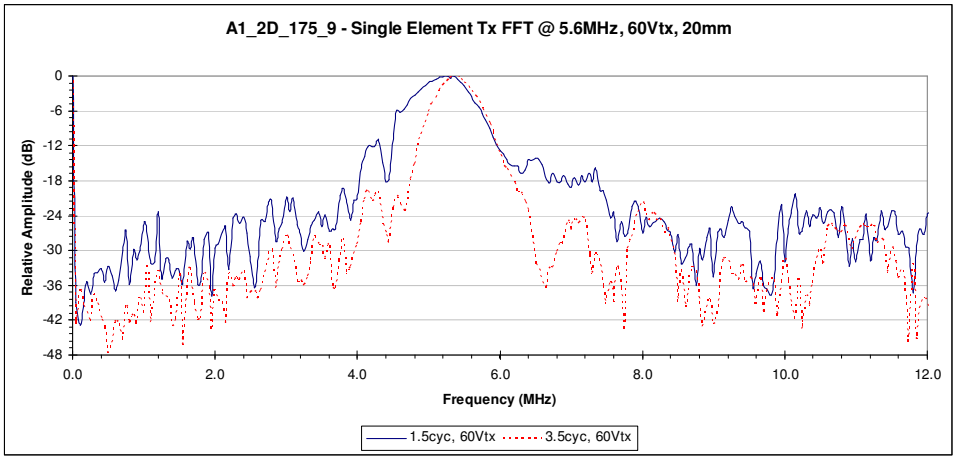

Figure 4.4: FFT of A1_2D_75_175_9 single element transmit pulse waveform @ 5.6MHz, 60V_{tx} – 3.5 and 1.5 cycles. Range = 20mm.

The -6dB bandwidth is 21.3% for 1.5-cycle transmit and 14.8% for 3.5-cycle transmit.

The transmit frequencies and single-element efficiencies for all 14x14 2D arrays are plotted against the etched length in Fig. 4.5. As the device thicknesses remain relatively constant for all 14x14 devices, plots are left without normalizing to non-dimensional L/t or t/L for this set of data.

The frequency decreases with increased etched length as expected. The transmit efficiency for A1 75um, A2 75um, and A11 40µm and 65µm devices is roughly two times larger than for the A11 50µm and 75µm devices. We note that the A11 50µm and 75µm devices produced poor image quality which may be due in part to low transmit

pressure output. The cause of the low transmit efficiency for these devices is currently unknown, possibly the result of process or material variability in fabrication.

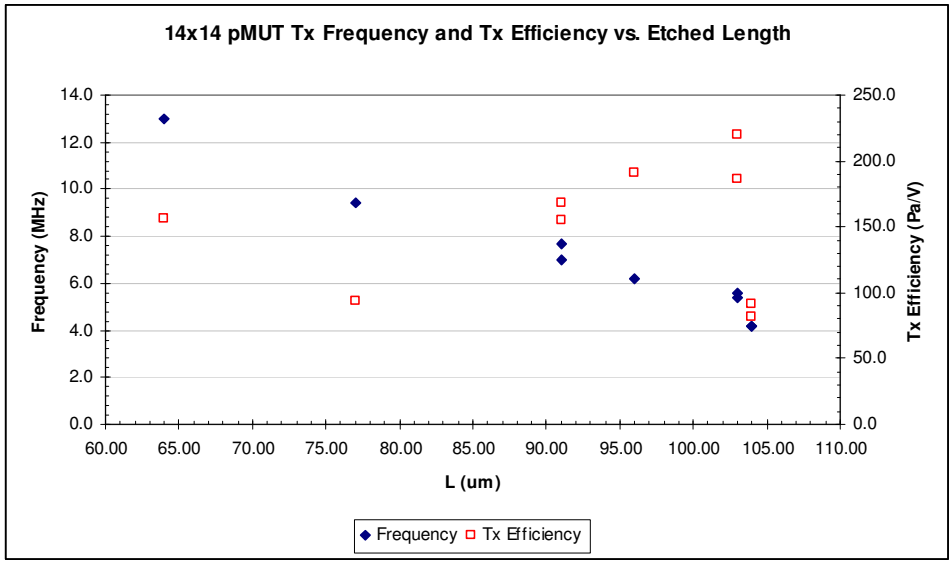

Figure 4.5: Transmit frequency and efficiency for 14x14 2D pMUT array single elements vs. etched length.

The angular response of a single 2D array element was measured by translating the pressure-calibrated hydrophone along the elevation and azimuth directions at a specified range. Figure 4.6 shows the angular response for 75µm element driven at 5.6MHz, 30.9V_{tx}, and 3.0 cycles at 20mm range.

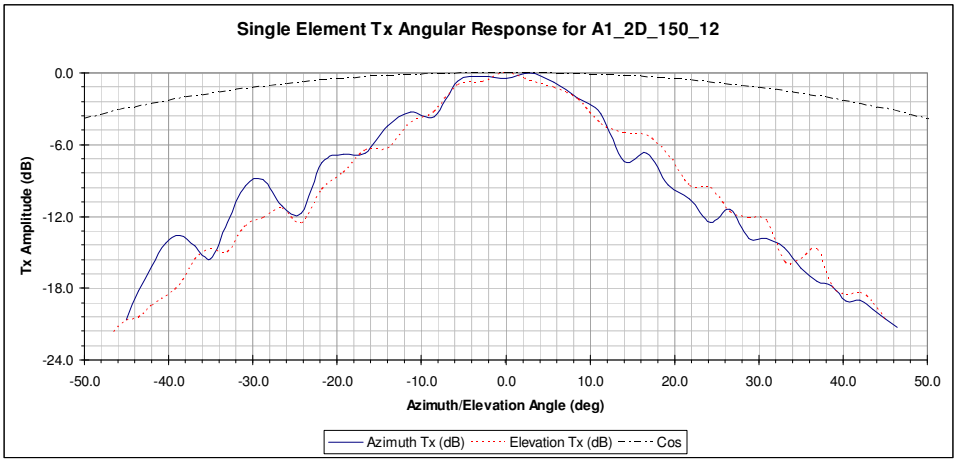

Figure 4.6: Single element Tx angular response into hydrophone for center element in a 14x14 2D pMUT array @ 5.6MHz (2.8MHz$_{in}$), 30.9V$_{tx}$, 3.0 cycles, 20mm range. *cos(θ)* shown for reference.

The -6dB half angle is between 13° - 18° in both elevation and azimuth.

The overall transmit response of the 14x14 2D array elements is consistent with the properties measured in the 5x5 and 9x9 devices.

4.3.3 Single Element Receive Response

Characterization of the frequency response of pMUTs in receive was performed by providing an acoustic pulse from a piston transducer and receiving with the pMUT array element in a water tank filled with deionized water. The pMUT was held in the custom holder while the piston was moved to a position that peaked receive amplitude of the pMUT using the X,Y,Z translation stage. The piston was driven with the output of the Agilent function generator alone or with the addition of the 50dB power amplifier.

The wide range of frequencies in receive required the use numerous pistons for transmit. Panametrics 5.0, 7.5, and 10MHz pistons were pressure-calibrated to produce 100kPa using the GL-0200 hydrophone. The pMUT array was then substituted in place

of the hydrophone and the received signal was recorded. The range for Rx characterization was chosen to be 100mm due to the aperture size of the pistons used. This range accommodates the focus of the f=100, 10MHz piston and is sufficiently far enough to lie beyond the transition point of the other pistons.

The piston transmit frequency was swept across a range to determine the resonant frequency, determined by identifying the frequency at which the pMUT element was most sensitive. In a passive receive mode, the pMUT element output was amplified using the AD600 signal amplifier with the output measured on an oscilloscope.

Table 4.4: Measured receive properties of 14x14 pMUTs. Receive frequency, sensitivity, and -6dB bandwidth (3- and 1-cycle pulses).

Device	t_{Si} (um)	t_{PZT} (um)	t_{dev} (um)	W_{etch} (um)	L_{etch} (um)	f_{rx} (MHz)	V_{rx} (mV)	Rx Sens. (uV/kPa)	-6dB %BW (3 cyc)	-6dB %BW (1 cyc)
A11_2D_40_90p_1	6.5	1.2	8.6	39	64	12.75	0.3	6.1	15.0	16.9
A11_2D_50_100p_1	6.5	1.2	8.6	50	77	10.00	0.2	3.7	31.0	39.5
A11_2D_65_150g_1	6.5	1.2	8.6	63	91	7.51	1.1	16.6	11.3	11.7
A11_2D_65_150p_1	6.5	1.2	8.6	63	91	6.91	1.2	17.8	12.3	12.6
A11_2D_75_150g_1	6.5	1.2	8.6	72	104	3.88	3.6	51.8	26.9	36.7
A11_2D_75_150p_1	6.5	1.2	8.6	72	104	3.89	3.9	56.2	30.0	47.4
A1_2D_175_9	6.0	1.2	8.1	78	103	5.17	2.6	38.5	29.1	35.0
A2_2D_175_12	6.0	1.2	8.1	65	96	6.14	2.6	33.9	18.0	25.4
A1_2D_150_12	6.0	1.2	8.1	78	103	5.40	2.8	41.0	22.8	25.9

The receive frequency, sensitivity, and -6dB bandwidths are provided in Table 4.4. The sensitivity was calculated as the peak-to-peak amplitude of the received signal voltage divided by the measured pressure incident on the pMUT. The bandwidth was determined from the FFT of the received waveform for 1- and 3-cycle pulses.

The receive frequencies and single element sensitivities of the 14x14 2D pMUT arrays are plotted against the etched length in Figure 4.7.

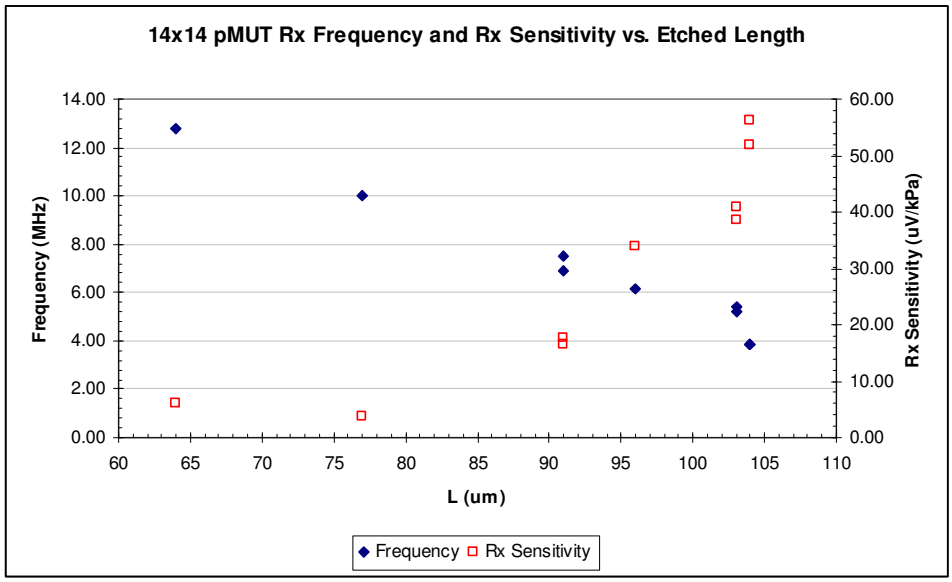

Figure 4.7: Receive frequency and sensitivity for 14x14 pMUT array single elements vs. etched length.

The frequency decreases with increased etched length as expected. The sensitivity increases as the length (and subsequently the overall membrane and active PZT area) increases as expected.

Receive waveforms and FFTs for 1- and 3-cycle pulses are shown in Figures 4.8 and 4.9 for a typical 14x14 array element.

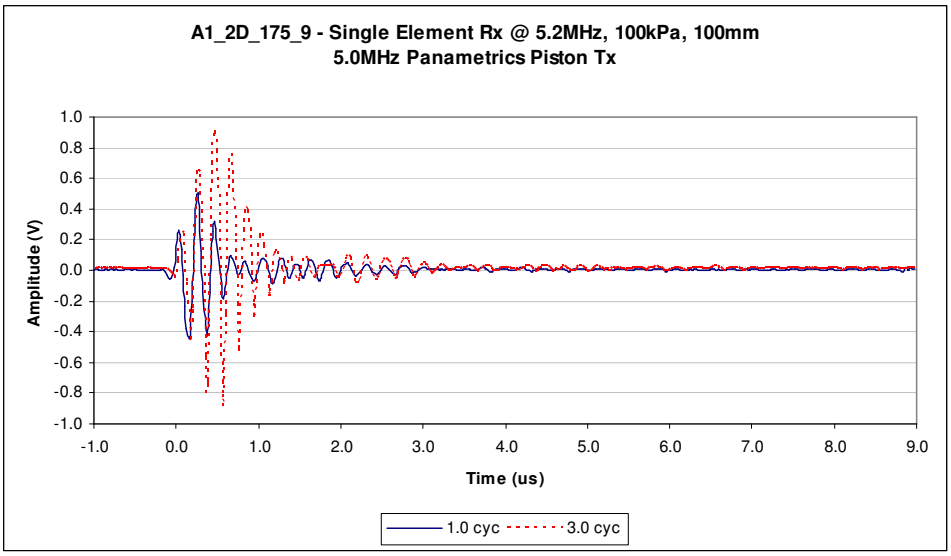

Figure 4.8: A1_2D_175_9 single element receive pulse waveform with transmit from 5.0MHz piston @ 5.2MHz, 100kPa. Range = 100mm. Shown with GL0200 amplifier gain.

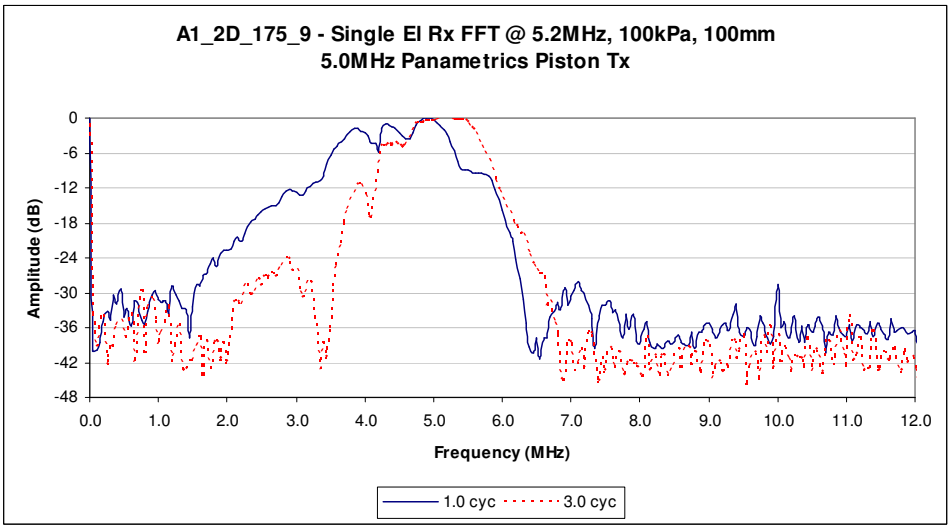

Figure 4.9: A1_2D_175_9 single element receive pulse waveform FFT with transmit from 5.0MHz piston @ 5.2MHz, 100kPa. Range = 100mm.

The overall receive response of the 14x14 2D array elements is consistent with the properties measured in the 5x5 and 9x9 devices.

4.3.4 Single Element Pulse-Echo Response

The pulse-echo response of the 14x14 2D array elements was performed by transmitting a 3.5 cycle pulse on a single element of the array at transmit voltage amplitudes between 30-60V_{tx} using a T5 system transmitter board. The high-voltage transmit pulse was delivered to the package pin of the single array element.

An aluminum block reflector was placed at a range of 10 or 20mm from the transducer. The pulse-echo signal off the aluminum block was measured from the package pin of the pMUT element with an oscilloscope through the AD600 boxed signal amplifier.

The range was chosen to be sufficiently far into the far-field of the element aperture as well as the whole-array aperture. It was also necessary to choose a range far enough to allow for the recovery of the receive amplifier after the high-voltage transmit pulse, at least 12μs with the current receive amplifier configuration.

The pMUT array was held in the custom breakout board which allowed for 2 degrees of freedom of angular rotation while the aluminum block could be positioned in the third rotational dimension while also being translated linearly with the XYZ-translation system on the water tank.

The transmit excitation frequency, array position, and rotation were peaked to obtain the highest peak-to-peak signal amplitude. Measured pulse-echo signal frequencies, amplitudes, and insertion loss are given in Table 4.5 for A1 and A2 14x14 arrays at 30$V_{tx\text{-}pp}$ and 60$V_{tx\text{-}pp}$ with the reflector placed at a range of 10mm. Transmit efficiency and receive sensitivity are used to calculate an expected insertion loss, not including

reflection, attenuation, and other propagation effects which likely accounts for the 10-15dB difference observed.

Table 4.5: 14x14 pMUT single element pulse-echo signal frequency, amplitude, and insertion loss at $30V_{tx\text{-}pp}$ and $60V_{tx\text{-}pp}$. Transmit efficiency, receive sensitivity, and associated calculated insertion loss included for comparison.

Device	t_{dev} (um)	W_{etch} (um)	L_{etch} (um)	V_{tx} (V)	PE Pulse Freq (MHz)	V_{PE} (mV)	PE Ins. Loss (dB rel. V/V)	Tx Effic. (Pa/V)	Rx Sens. (µV/kPa)	Calc. Tx/Rx Ins Loss (dB rel V/V)
A1_2D_175_9	8.1	78	103	30.0	5.60	60.0	-115.6	219.78	38.5	-101.4
A1_2D_150_12	8.1	78	103	30.0	5.65	65.0	-114.9	190.77	33.9	-103.8
A2_2D_175_12	8.1	65	96	30.0	6.00	48.0	-117.5	185.78	41.0	-102.4
A2_2D_150_9	8.1	65	96	30.0	7.00	45.0	-118.1	--	--	--
A2_2D_150_10	8.1	65	96	30.0	7.10	40.0	-119.1	--	--	--
A1_2D_175_9	8.1	78	103	60.0	5.60	118.0	-115.7	219.78	38.52	-101.4
A1_2D_150_12	8.1	78	103	60.0	5.65	108.0	-116.5	190.77	33.93	-103.8
A2_2D_175_12	8.1	65	96	60.0	6.00	66.0	-120.8	185.78	40.98	-102.4
A2_2D_150_9	8.1	65	96	60.0	7.00	65.0	-120.9	--	--	--
A2_2D_150_10	8.1	65	96	60.0	7.10	53.0	-122.7	--	--	--

Figure 4.10 shows a typical pulse-echo waveform from a single 2D array element driven with 3.5 cycles at 5.6MHz and $50V_{tx}$ with an Al block reflector placed at a range of 20mm.

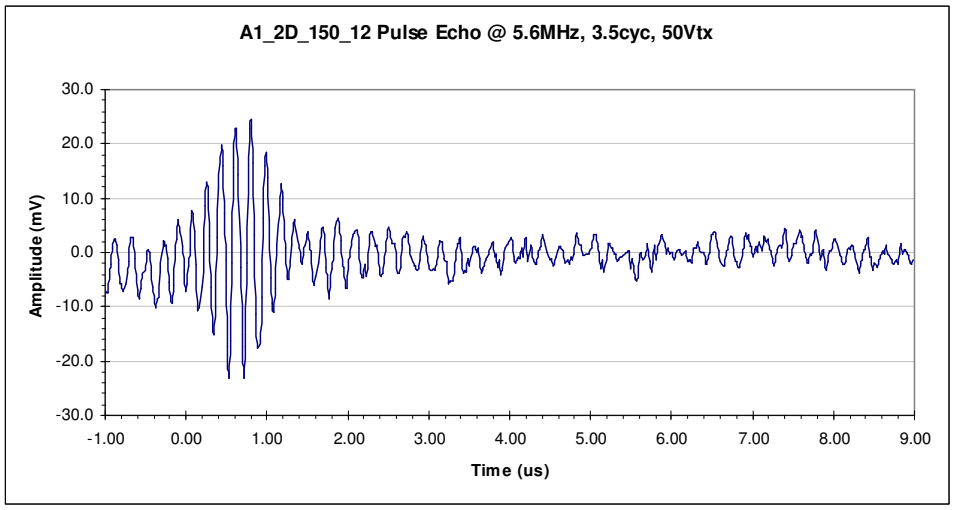

Figure 4.10: Single-element pulse-echo waveform off of Al block reflector at a range of 20mm driven with 3.5 cycles at 5.6MHz and $50V_{tx}$.

Performing a Fourier transform on the pulse-echo waveform, we find the 5.6MHz signal produces a peak with a -6dB bandwidth of 13.4% while an additional large peak occurs at 4.7MHz, as shown in Figure 4.11.

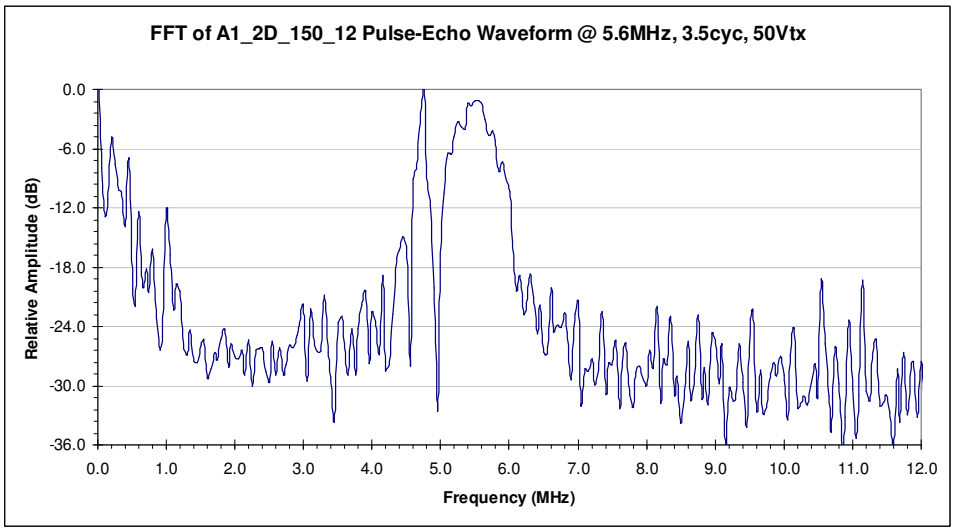

Figure 4.11: FFT of single-element pulse-echo waveform off of Al block reflector at a range of 20mm driven with 3.5 cycles at 5.6MHz and $50V_{tx}$.

The 4.7MHz peak is the result of a prolonged oscillation in the pulse-echo waveform which precedes the actual reflected pulse from the aluminum block target and remains unchanged when the reflecting target is translated in range or removed altogether. Similar prolonged oscillations were observed in the previous 5x5 2D arrays as well as 1D arrays from the same A1 wafer. Optical vibrometer measurements of a similar array (A1_2D_175_9) show 2 peaks in water, a 5.4MHz propagating mode and a smaller peak in the 3.8-4.7 MHz band (see §5.3). It is likely that the 4.7MHz peak observed here is the result of resonant oscillation within the structure caused by the high-voltage transmit pulse which persists for a duration long enough to be observed when the pulse-echo signal is expected. It is reasonable that the oscillations in the pulse-echo signal lasting up

to 30µs after the transmit pulse in these 2D arrays and up to 80µs in the 1D array measurements may be the result of the prolonged ringing observed in the optical vibrometry measurements.

Further investigation into the characteristics of this persistent oscillation based on electrical, acoustic, and optical measurements is detailed with the analysis of the frequency theory in Chapters 7 & 8. Pertinent information regarding the effect of the oscillation on the imaging properties of 2D pMUT arrays is summarized here.

This oscillation is shown to be the fundamental plate resonance of the pMUT membrane. It is capable of propagation, but in imaging applications the amplitude remains lower than the transmitted pulse, appearing as a lower-frequency "ringy" tail after the short-cycle transmit pulse. Imaging applications require operation off-resonance in order to maintain a wide-band (short duration) pulse. The transmit efficiency, receive sensitivity, and overall pulse-echo insertion loss is comparable at the oscillation frequency rather than the identified optimal operating frequency, but the tradeoff for short pulse length and wide bandwidth outweighs any marginal gains in operating at the fundamental oscillation frequency.

Much of the resonant oscillation energy stays within the device silicon. Neighboring elements show high sensitivity at this frequency and experience significant crosstalk within the array, observed both electrically and optically. Vibration experienced on all neighboring elements is shown to be solely the result of vibration of the transmitting element.

The duration and amplitude of the resonant oscillation (up to 30us) varies between devices. However, the oscillation amplitude following transmit excitation is significant

enough to reach measurable levels through the receive amplifier, obscuring reflected echoes from even hard targets within the duration of the oscillation (up to 2-3cm). In some devices, the persistent resonant oscillation amplitude has been measured to be greater than 7mV, much larger than the expected signal amplitude from reflective targets and large enough to saturate the receive amplifier. A representative waveform from a 75µm element is shown in Figure 4.12 which includes recovery of the receive amplifier.

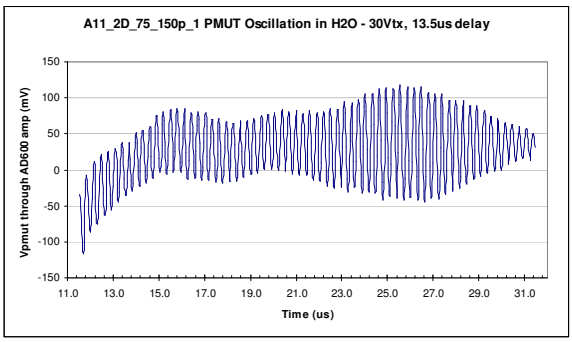

Figure 4.12: A representative waveform of the persistent oscillation on the pMUTs in pulse-echo configuration in water.

Referencing the time-domain oscillation observed in the optical vibrometry results, the timing of resonant oscillation waveform shown falls well within the duration of the surface displacement measured using optical methods.

The amplitude of the persistent oscillation across devices also provides indication of imaging performance. Devices that exhibited particularly high oscillation amplitudes were notably poorer in imaging performance with much lower signal to noise and an inability to resolve targets close to the transducer (within 3cm).

4.3.5 14x14 2D Array Pulse-Echo Imaging

Pulse-echo images were acquired with the 14x14 pMUT 2D arrays using the Duke T5 phased array scanner. B-mode images of string targets, tissue phantoms, and in vivo tissue structures were obtained.

A B-mode image of string targets at 2.5mm spacing using a representative 2D array (A1_2D_150_12) is shown in Figure 4.13.

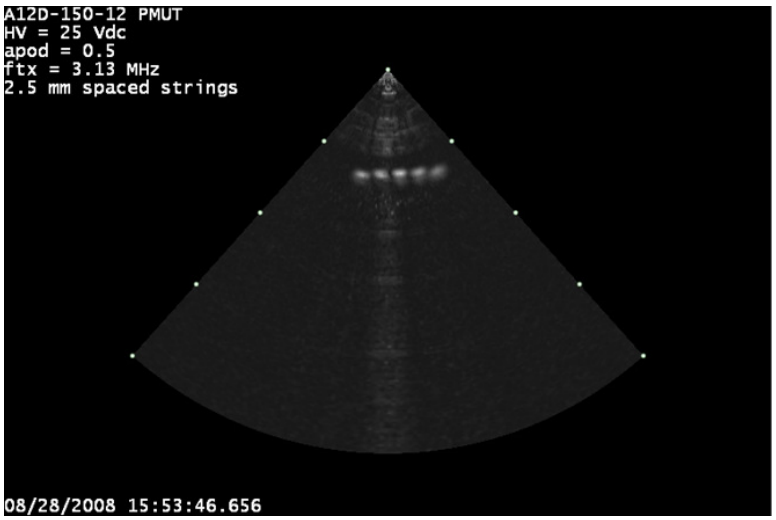

Figure 4.13: B-mode of 5 nylon strings at 2.5mm spacing in deionized water using A1_2D_75_150 device @ $25V_{dc}$ (~$40V_{tx}$), $3.13MHz_{in}$, 2.5 cycles.

The expected lateral and axial resolution for this device at 12mm range for a 2.5 cycle, 6.2MHz pulse is 1.44mm and 0.30mm, respectively. The 2.5mm space strings shown are easily resolved by the array.

B-mode images were also acquired of the tissue-mimicking small parts phantom (Gammex/RMI 404 LE), shown in Figure 4.14. These images were acquired using A1 75µm devices with 2.78MHz or 3.13MHz, $40V_{tx}$, 2.5cyc transmit and 4.5-6.5MHz or 5.25-7.5MHz bandpass filters to reduce noise.

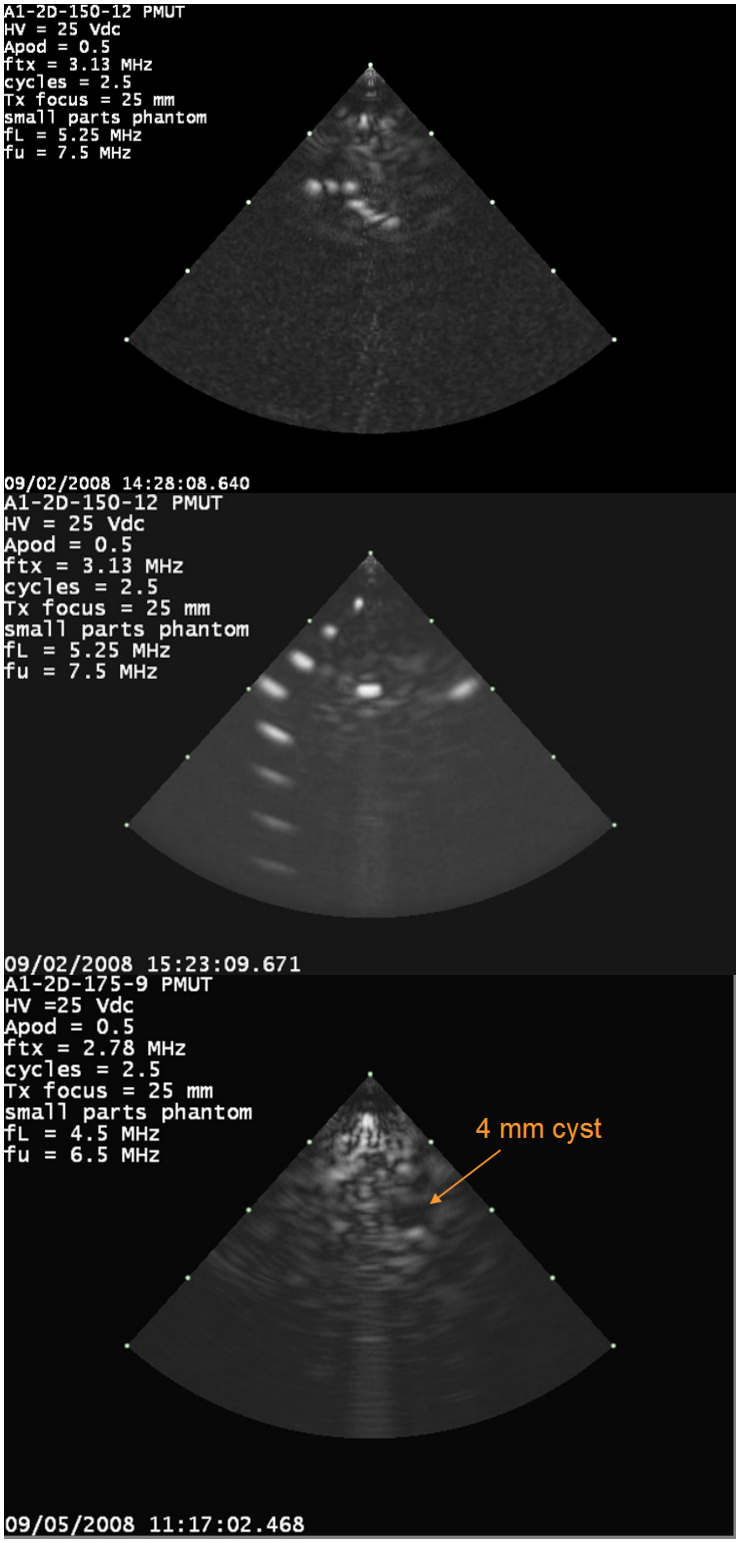

Figure 4.14: B-mode images of targets from a tissue-mimicking small-parts phantom – (top) resolution target, (middle) range targets, (bottom) 4mm anechoic cyst. Acquired using A1 75µm devices @ $25V_{dc}$ (~$40V_{tx}$), 2.5 cycles, 2.78 or $3.13MHz_{in}$ (as noted).

The tissue phantom has an attenuation of 0.5 dB/cm/MHz with 100μm diameter nylon targets at spacings of 0.5 – 2 mm as well as 1-4mm anechoic cyst targets. B-mode images of lateral resolution and range targets show the resolution and penetration of the array. The 1 and 2mm spaced targets can be resolved while the 0.5mm spaced targets cannot, as expected at 15mm range. The 14x14 pMUT array demonstrates pulse-echo penetration up to 4cm. The 4cm anechoic cyst is also resolvable at 2cm range.

In vivo B-mode images of a human carotid artery and jugular vein were obtained using a 14x14 2D 75μm array with the Duke T5 scanner. The images shown in Figure 4.15 were acquired using a 2.5 cycle pulse at f_{in} = 2.78MHz and $V_{tx} = 25V_{dc} = 40V_{pp}$ with a 4.5-6.5MHz bandpass filter for noise reduction.

The carotid artery and jugular vein were identified by performing the Valsalva maneuver (forced exhalation against a closed airway) which reduces venous return to the heart as the intrathoracic pressure increases, leaving more blood pooled in the peripheral venous system which, in turn, causes the veins to distend to accommodate the increased volume.

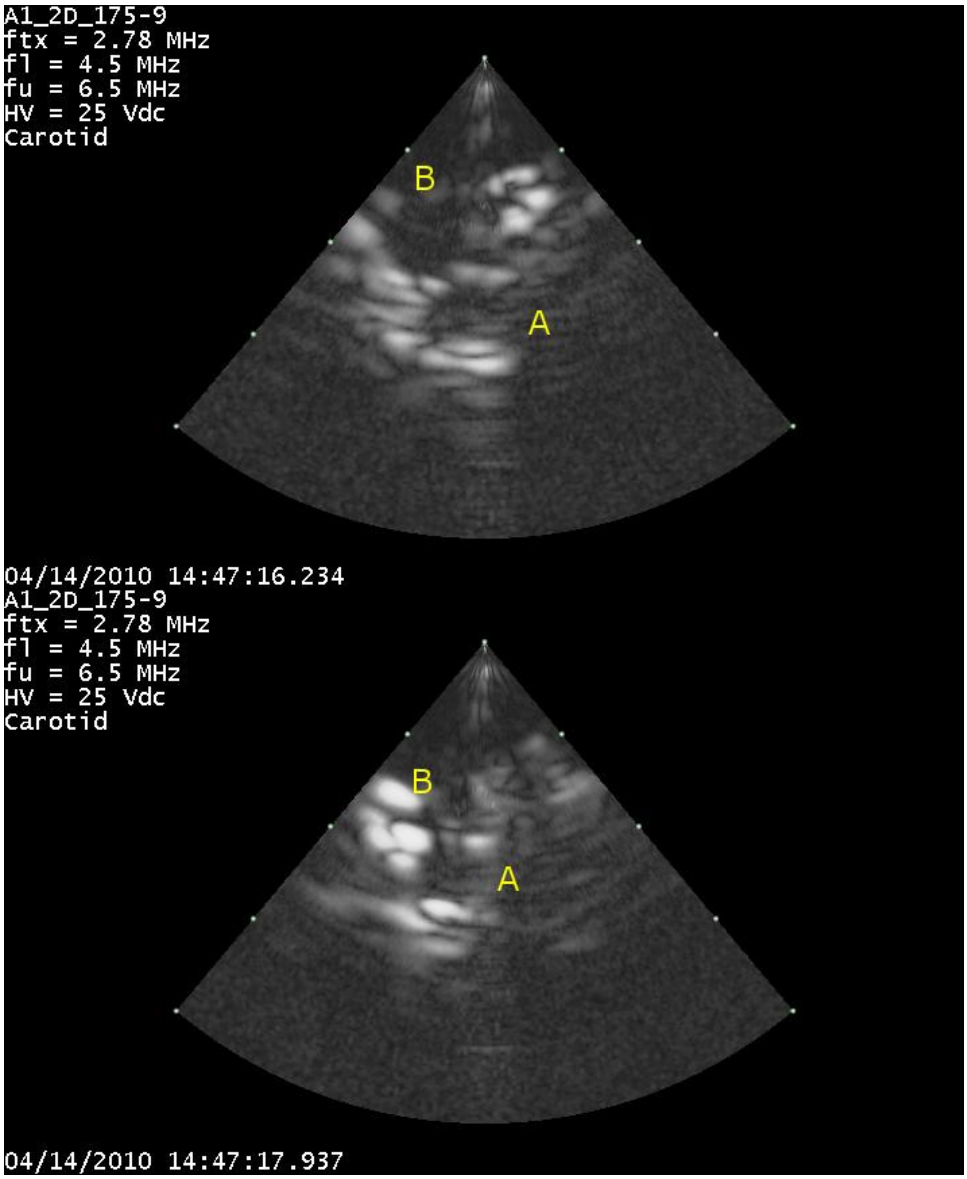

Figure 4.15: B-modes of human carotid artery (A) and internal jugular vein (B) - during (top) and after (bottom) the Valsalva maneuver. Images acquired using A1_2D_175_9 14x14 pMUT array. Note that the jugular vein distends as the Valsalva maneuver increases chest pressure, reducing venous return to the heart, increasing the volume of blood pooled in the peripheral venous system.

The tissue structures are readily identifiable in the images, representing some of the first-ever reported B-mode images of in vivo tissue structures using 2D pMUT arrays.

4.4 14x14 2D Array Summary of Results

Electrical characterization of the 14x14 2D pMUT arrays using an impedance analyzer showed resonance frequencies in air consistent with those measured using optical vibrometry methods, with frequency decreasing with increased element size.

Characterization of the 14x14 2D pMUT arrays in transmit, receive and pulse-echo has demonstrated performance consistent with 5x5 arrays. Transmit and receive frequencies for devices of similar size and thickness were in line with those observed with 5x5 devices.

Transmit pressure output up to 7.4 kPa and transmit efficiencies up to 220 Pa/V for 75µm single elements at 20mm range were observed, with up to 21% bandwidth for a 1-cycle truncated sinusoidal pulse. Transmit frequency decreased with increased element lateral dimension. Transmit efficiency was consistent with a slight increase with increased element size with the exception of the A11 50µm and 75µm devices which exhibited lower transmit output. The -6dB half angle for the transmit angular response is between 13° - 18° in both elevation and azimuth.

Receive sensitivities were observed up to 56µV/kPa, increasing as element surface increased. Receive bandwidth for 1-cycle pulse was observed up to 47%. Receive frequency decreased with increased element lateral dimension

Pulse-echo characterization showed insertion loss of up to -115dB (rel. V/V_{tx}). A significant persistent oscillation of roughly 15-20% lower frequency was also observed. Further experimentation showed that this persistent oscillation is non-propagating and remains within the device structure following high-voltage transmit pulse for up to 30µs,

long enough to disrupt received echoes returning from reflective targets up to 2cm in range. This oscillation was also observable in air, with frequencies mirroring the optical vibrometry and impedance analyzer frequencies in air very closely.

Pulse-echo B-mode images of string targets in water, a tissue-mimicking phantom, and in vivo tissue structures were obtained using the Duke T5 phased array imaging system. Imaging of resolution targets indicates operation consistent with expected performance. Range targets showed imaging penetration depth of up to 4cm. Imaging of the carotid artery and jugular vein during the Valsalva maneuver represent some of the first-ever B-mode images of in vivo tissue structures.

The experimental results obtained demonstrate that the acoustic performance observed in 5x5 and 9x9 2D pMUT arrays carries over and scales to arrays large enough for imaging, culminating in image acquisition of targets in the water tank, tissue-mimicking phantom, and in vivo tissue.

Chapter 5

Visualization of PMUT Flexure Using Optical Vibrometry

5.1 Introduction

Direct optical measurement of the pMUT elements in high-frequency vibration would serve as confirmation of fundamental mode operation for smaller elements and complex higher-order mode vibration of the larger elements. Some uncertainty also exists in the true vibrational dimensions of the devices. The fabrication tolerances of the DRIE process are currently unmeasurable without the use of destructive SEM sectioning. Inter-element interactions such as mechanical coupling or electrical cross-talk should also be discernable using optical methods.

5.2 Experimental Methods – Optical Vibrometry

A laser Doppler vibrometry system that is capable of the speed and resolution requirements necessary for this research is available commercially. The MSA-400 Micro System Analyzer from Polytec is used for precise 3D dynamic characterization of MEMS microstructures. The MSA-400 is capable of characterizing out-of-plane vibrations using laser Doppler vibrometry. The MSA-400-M2-20-D system can be used to make single-point displacement and self-referenced or differentially-referenced full-field vibration measurements of structures vibrating at frequencies up to 24MHz. Coupled with a 50x

microscope objective, the system achieves a lateral resolution of 0.85µm with a 180x134µm field of view.

A limited-use demonstration of a Polytec Micro System Analyzer (MSA-400-M2-20-D) scanning laser Doppler vibrometry system was arranged for the measurement of pMUTs 2D arrays.

The system was equipped with the high-speed controller for out-of-plane dynamic vibration measurement and analysis up to 24MHz. The demo system included 10x and 50x long-range microscope objectives.

Due to the time constraints of the limited-use demonstration, optical measurements were made of only two pMUT devices. The first was device A1_2D_175-9, a 14x14 2D array with 75µm nominal elements with 175µm center-to-center element spacing. The second was device Wg8 B200100_100C, a 5x5 2D array with 200µm nominal elements with 300µm center-to-center element spacing. Additionally, experimental measurements made for one device were not often reproduced for the other.

The pMUTs were held in a custom mount with a manual XY-translation stage which was fixed to the optical workstation. The vibrometer system was mounted on an active vibration-isolation table.

Single elements of the pMUT devices were driven using a 3.0 cycle truncated sine wave burst from a function generator (Agilent 33250A) through a 50dB power amplifier (ENI Model 325LA). All pMUT elements were operated at an applied voltage of approximately $30V_{tx\text{-}pp}$.

The MSA vibrometer offers an optical reflection image of the device surface over which a customizable measurement sample field is defined. The vibrometer utilizes a

low voltage reference signal to sync the displacement data between different measurement points. The function generator output was split off to provide this reference signal while the input to the ENI amplifier was attenuated using an attenuator box. This configuration was used instead of the internal sync of the function generator due to the amplitude requirements of the optical system reference signal.

Depending on the number of sample points, the total acquisition time for a full scan was typically under 7 minutes. Single point or scans with fewer sample points were typically acquired within a few seconds.

The pMUT devices were operated in air while water-loading was applied by placing a few drops of deionized water on the surface of the device.

5.3 Experimental Results

5.3.1 pMUT Displacement

The membrane displacement in air was measured as a function of time from a sample point in the center of the membrane. The transmit drive pulse provided was a 3.0 cycle truncated sinusoid at $22.7V_{tx}$ while the input frequency was varied between 2.8MHz and 3.0MHz. The measured displacement as a function of time for f_{in}=3.0MHz is shown in Figure 5.1 and for f_{in}=2.8MHz is shown in Figure 5.2.

From Figures 5.1 and 5.2, we observe that after an initial 3-5 cycles of oscillation at 2 times the input frequency in both plots (6.0MHz and 5.7MHz, respectively), an extended oscillation at 6.75MHz in both plots persists for up to 50μs after the initial transmit excitation. The peak-to-peak membrane displacement was measured to be 63nm at

3.0MHz$_{in}$ and 41nm at 2.8MHz$_{in}$. Both input waveforms were 3.0 cycles at 22.7V$_{tx}$. The duration of the extended oscillation suggests that the pMUT structure has a resonant peak at 6.75MHz under air loading. Thus the peak-to-peak membrane displacement could be greater than 63nm as the maximum membrane displacement is likely to occur when the device is driven at this frequency or with higher excitation amplitude at or above 30V$_{tx}$.

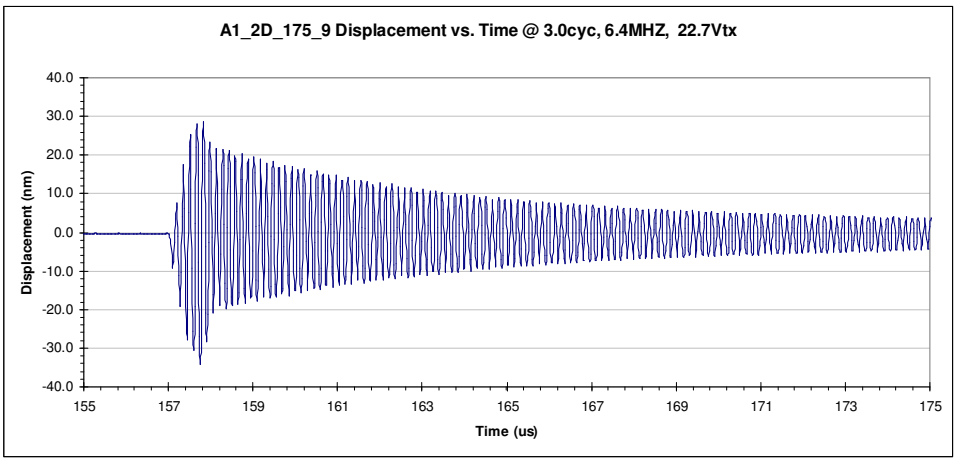

Figure 5.1: Displacement vs. time of 2D pMUT array in air @ f_{in}=3.0MHz, 3.0cyc, 22.7V$_{tx}$, f=6.75MHz.

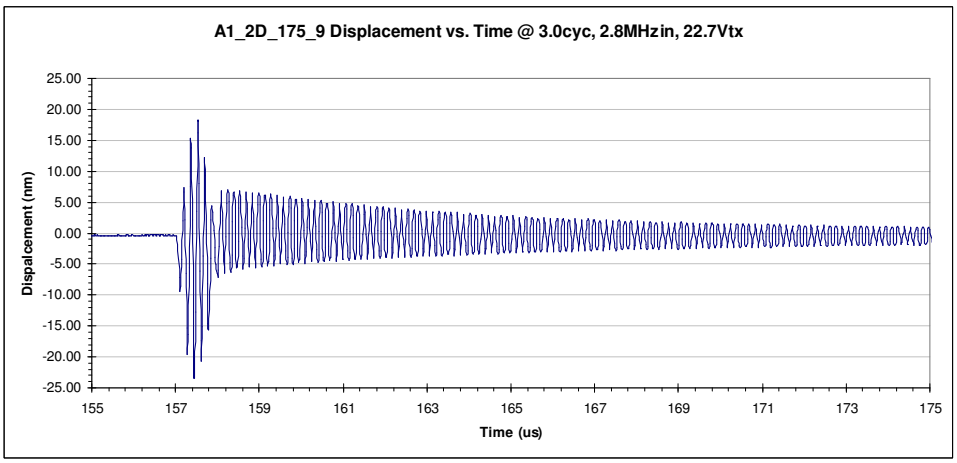

Figure 5.2: Displacement vs. time of 2D pMUT array in air @ f_{in}=2.8MHz, 3.0cyc, 22.7V$_{tx}$, f=5.7MHz with 6.75MHz ringdown.

The Fourier transform of both plots is given in Figure 5.3, which helps to highlight the frequency component in both waveforms, particularly the sharp resonant peak at 6.75MHz. From the FFT, we see that as the transmit frequency falls away from the peak resonance, the 6.75MHz peak decreases as energy is transferred into the 5.0-6.0MHz band, which correlates well with the decrease in amplitude of the 6.75MHz tail shown in the time-domain waveform.

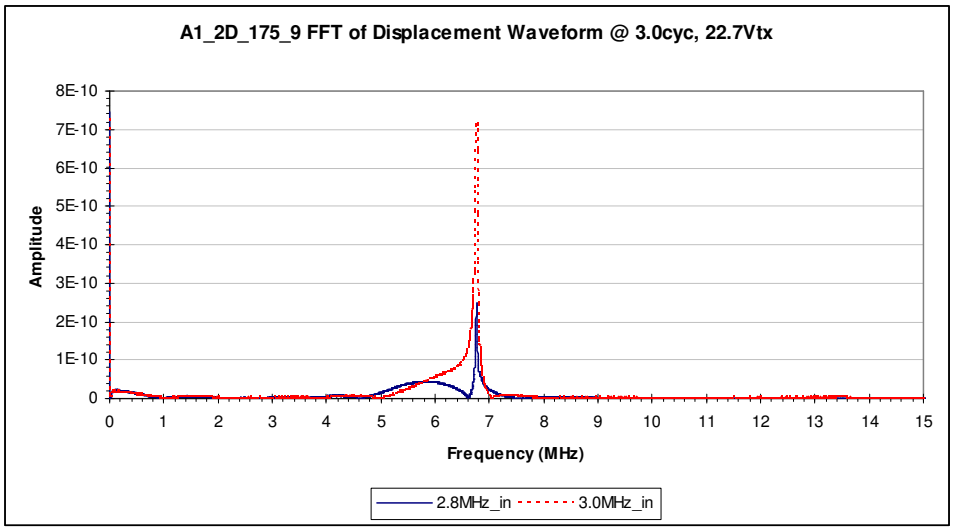

Figure 5.3: FFT spectra of displacement waveforms of A1_2D_175_9 2D pMUT array @ 3.0cyc, 22.7V_{tx} at multiple input frequencies in air.

That the membrane displacement in air oscillates at 6.75MHz for such a long duration is surprising, but reasonable, as the mechanical energy is not easily propagated into the air medium and remains within the pMUT structure.

5.3.2 Visualization of Vibrational Mode Shapes

The MSA-400 Micro System Analyzer was used to visualize the mode shapes of individual 75µm and 200µm pMUT elements in vibration. The 75µm elements were

observed to operate in a fundamental mode under both air- and water-loaded conditions (Figure 5.4). Surface displacement was observed over a larger area than expected indicating that our assumptions about the vibrational boundary conditions may be incorrect.

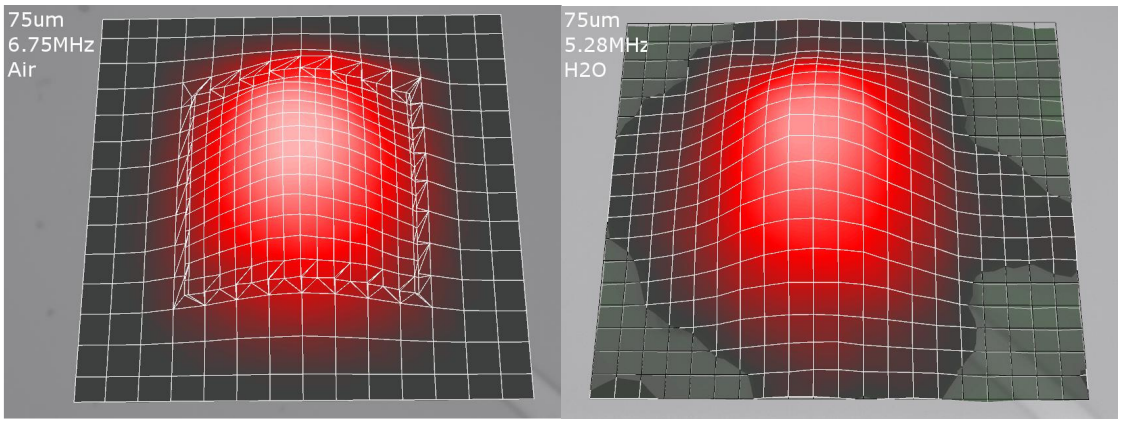

Figure 5.4: Surface displacement mode shape of a 75µm element from a 14x14 2D pMUT array driven at 3.0 cycle, 3.0MHz, 22.7V_{tx}. 6.75MHz mode in air (left) and 5.28MHz mode in water (right).

Visualization of the 200µm pMUT elements confirmed the hypothesis of higher order operation of these larger elements. Surface displacement modes in air and water are provided in Figure 5.5 and 5.6, respectively.

Fundamental mode vibration was observed at frequencies <2MHz in air, but additional peaks at 2.63, 5.47, 5.69, and 7.81 MHz in air revealed what appeared to be a complex combination of higher order vibrational modes which likely contribute to the higher frequency acoustic output of the larger devices observed in previous measurements.

The higher-order mode shapes shown in Figure 5.5 are typically classified by the number of half sine waves in each direction, given by an *m-n* notation where *m* and *n* specify the number of half-sine waves along the x- and y-axes, respectively.

Alternatively, the mode numbers can be determined by the number of nodal lines (lines which remains at rest while the other parts of the body are in a state of vibration) in each direction (not including one fixed edge), *m* and *n* then specifying the number of nodal lines parallel to the x- and y-axes, respectively.

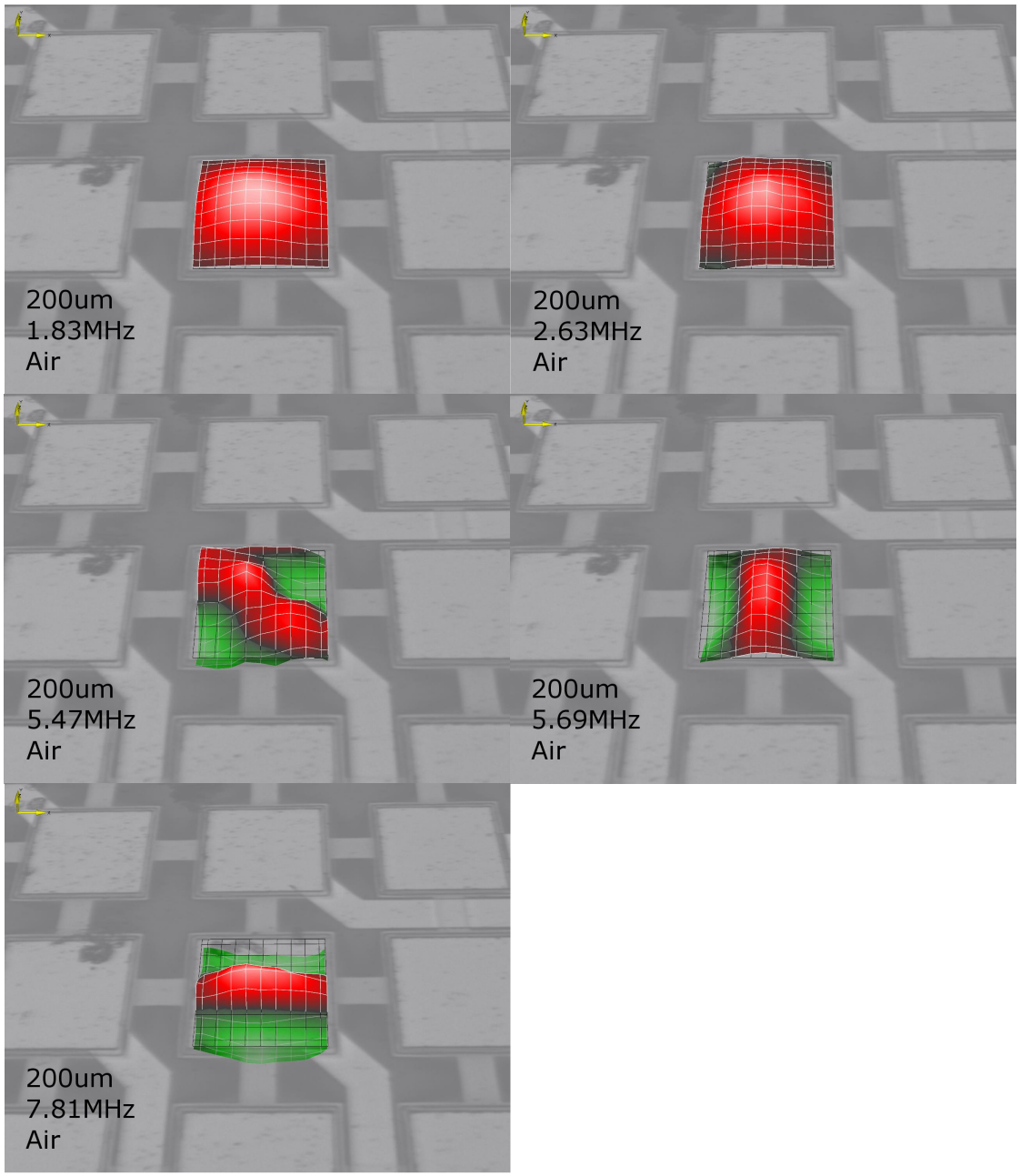

Figure 5.5: Surface displacement mode shapes of a 200µm pMUT element in air at showing different modes of operation. 5x5 2D pMUT array driven at 3.0 cycle, 3.2MHz, 22.7V_{tx}.

The fundamental mode, therefore, is given as the 1-1 mode. In Figure 5.5, the 5.7MHz component is the 1-3 mode while the 7.8MHz component is the 3-1 mode. The 5.5MHz component is likely a superposition of the 2-1 and 1-2 modes which can occur when the resonant frequencies supporting each mode are similar, which is often the case when the structure is square or near square.

The mode shape at the 2.63MHz frequency is notable in that the surface displacement is fundamental in shape but confined in lateral dimensions more than the 1.83MHz mode. The frequency of this mode is too low to be considered a 3-3 mode. Upon closer examination, it appears that dimensions of this 2.63MHz mode align more closely with the PZT film or metal electrode dimensions than the etched cavity below. Remembering that these optical measurements were performed by transmitting a high-voltage excitation across the electrodes sandwiching the active PZT, it is reasonable that the dimensions of the PZT layer provides an additional set of boundary conditions for some vibrational modes.

For the same device under water-loading, the mode shapes shown in Figure 5.6 exhibit similar characteristics as those in air, though the low sensitivity of the vibrometer through water limited observation of some of the modes under air-loading.

In water tank characterization of the transmit response of the 200μm devices, the peak transmit frequency was 6.5MHz with low pressure output observed at frequencies below 2MHz (§3.4.2). This indicates that the 1.16MHz fundamental is not an optimal propagating mode for large pMUT membranes. Rather, a contribution from a complex

combination of higher-order modes likely provides more optimal transmit propagation in water.

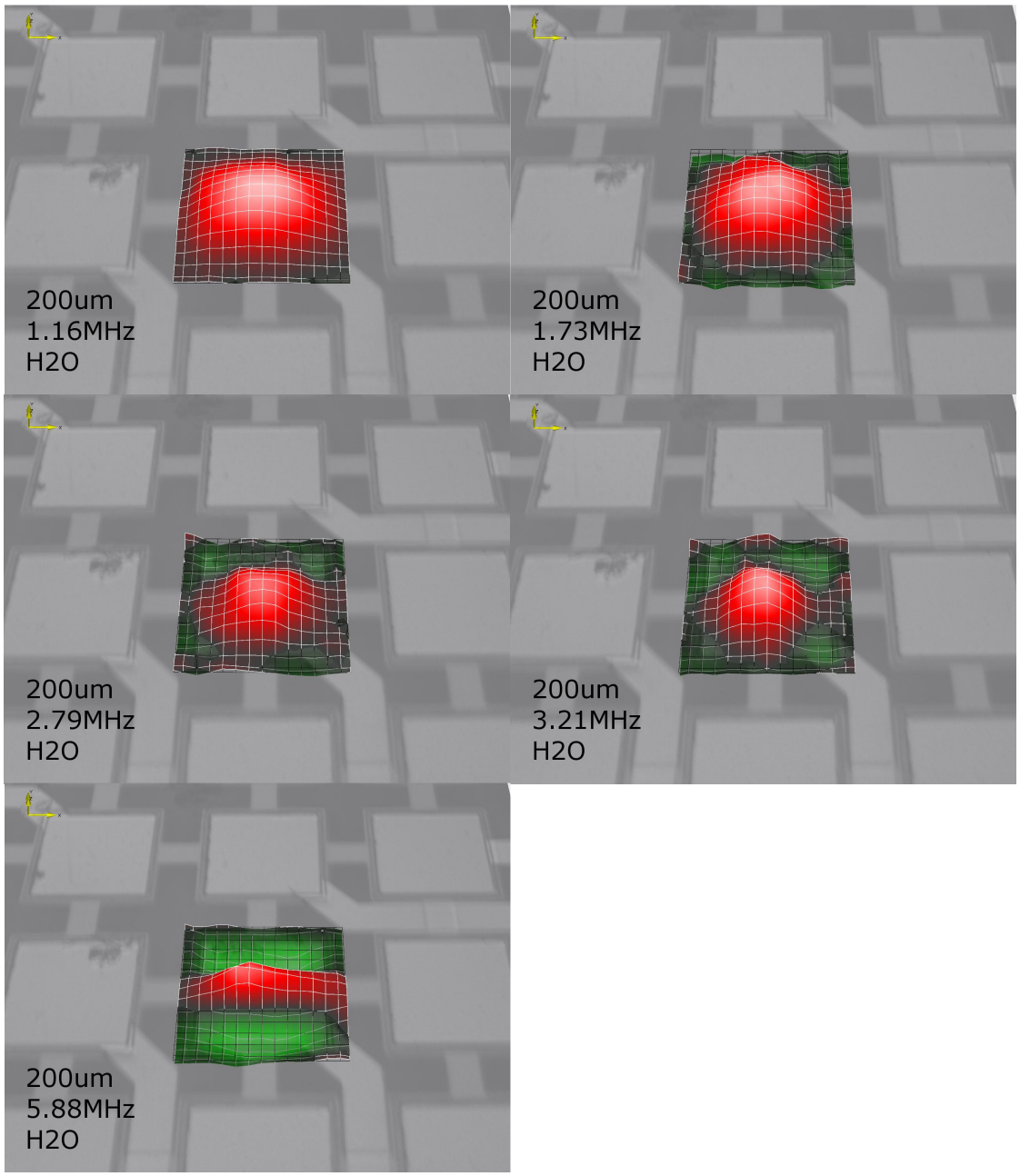

Figure 5.6: Surface displacement mode shapes of a 200µm pMUT element in water at showing different modes of operation. 5x5 2D pMUT array driven at 3.0 cycle, 3.2MHz, 22.7V_{tx}.

However, in measurements of the acoustic receive response, multiple frequencies were observed for this device. Frequency peaks at 1.10, 1.52, and 6.01MHz were observed in acoustic receive measurements (§3.4.3). The 1.10 and 1.52MHz are likely associated with the fundamental 1.16MHz and confined fundamental 1.73MHz frequency modes observed optically, while the 6.01MHz frequency measured in receive is likely associated with the 5.88MHz 3-1 mode measured optically. The optically measured frequency modes are summarized in Table 5.1 with electrically and acoustically measured frequencies for comparison.

Table 5.1: Comparison of air- and water-loaded frequencies from optical, electrical, and acoustic measurement. 1-1* designates confined fundamental modes.

						Air			H2O			
Device	**Mode**	**Etch W (um)**	**Etch L (um)**	**PZT W (um)**	**PZT L (um)**	**Imp An Freq (MHz)**	**PE Osc Freq (MHz)**	**Opt Vib Freq (MHz)**	**Tx Freq (MHz)**	**Rx Freq (MHz)**	**PE Osc Freq (MHz)**	**Opt Vib Freq (MHz)**
A1 75	1-1	78	103	86	82	6.76	6.80	6.75	5.40	5.17	4.45	5.28
Wg8 200	1-1	193	243	215	213	1.86	1.85	1.83	--	1.10	1.11	1.16
	1-1*					--	--	2.63	--	1.52	--	1.73 2.79 3.21
	2-1 1-2					--	--	5.47	--	--	--	--
	1-3					--	--	5.69	--	--	--	--
	3-1					--	--	7.81	6.50	6.01	--	5.88

While not all frequency modes are accounted for in Table 5.1, there is extremely strong correlation between the optically measured 1-1 frequency mode and both the resonant frequencies measured using the impedance analyzer and the resonant oscillation observed in pulse-echo measurements (both discussed in the experimental results section for each device). Based on these results, there is evidence that the fundamental 1-1 frequency mode for all devices can be determined using an impedance analyzer or measurement of the resonant oscillation in air or water in a pulse-echo configuration.

The acoustic transmit response has also been shown to be up to 10% higher than the receive response of the same vibrational mode. For large devices like the 200µm Wg8 device measured here, acoustic receive response in the 1-1 mode can be excited while the transmit response at these frequencies remains poor. As this 1-1 mode is the fundamental resonance frequency, the bandwidth is very narrow and associated pulse lengths are extremely long in duration. These characteristics prove to be detrimental to proper image acquisition and off-resonance operation may be more optimal for imaging applications. The confined 1-1 modes described previously may provide an acceptable off-resonance operating point. While the higher-order modes may provide adequate transmit and receive response, non-fundamental mode displacement of the element could lead to unusual angular response.

The amplitudes of the FFT frequency peaks provide insight into the relationship between the vibrational modes. Unfortunately, true FFT data was not obtained during the course of the demonstration for the 200µm device, and only screen captures of the acquisition window are available. FFTs for the Wg8 200µm device and A1 75µm device vibration in air are shown in Figure 5.7.

In the FFT for the A1 75µm device, two large peaks exist at 5.85MHz and 6.75MHz. The 6.75MHz is shown to be the true resonance frequency in air while the 5.85MHz component is a result of driving the pMUT off-resonance. FFTs for this device driven at 3.0MHz is shown in Figure 5.3 with a much larger 6.75MHz component and significantly diminished 5.85MHz content. Mode shapes for both of these frequency bands are 1-1 fundamental.

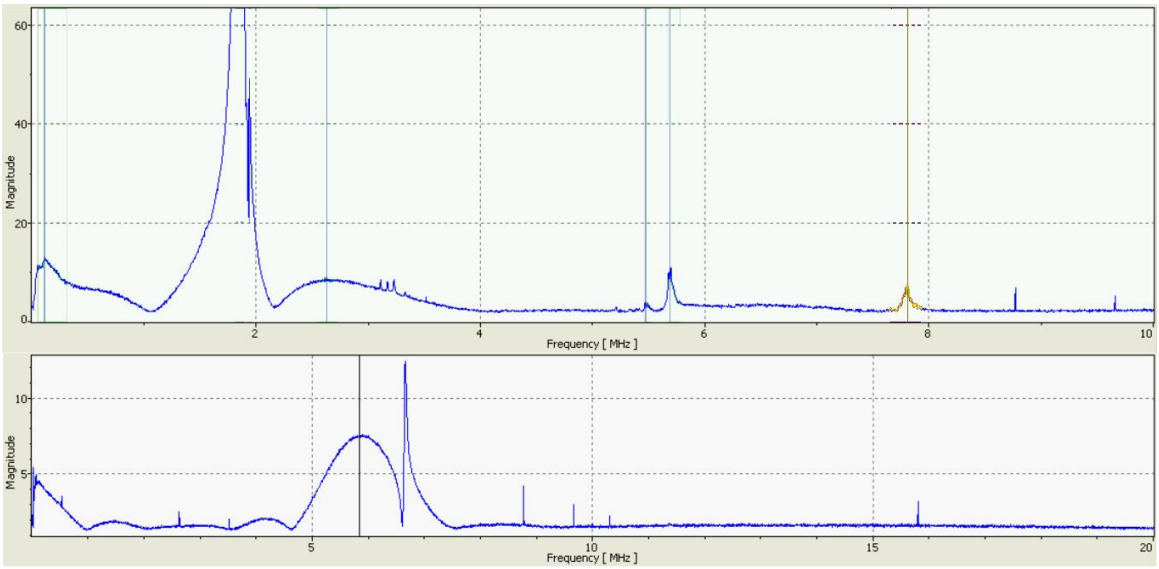

Figure 5.7: FFT of Wg8 200µm (top) and A1_2D 75µm (bottom) single element vibration in air based on optical measurement. Excitation frequencies were 3.2MHz and 2.8MHz, respectively.

In the FFT for the Wg8 200µm device, the peak in the 1.8MHz range (1-1 mode) is much larger than the frequency peaks centered at 2.63, 5.69, and 7.81MHz. Unfortunately, as the FFT for the water-loaded element were not obtained, it is unclear how the 1-1 mode was affected by loading and is thus difficult to discern why the 1-1 mode did not present an optimal propagating mode. There are indications that while the 1-1 mode in air showed more than 50x higher amplitude than the higher order modes, in water the relative amplitudes differed by less than 10x, though the 1-1 mode appears to maintain the highest amplitude. This significant reduction in relative amplitude of the fundamental mode from air- to water-loaded conditions was also observed in the 75µm device.

5.3.3 Vibrational Dimensions

Measurement of displacement across both axes of the 75μm elements (Fig. 5.8) revealed that the dimensions over which the pMUT vibrates may be up to 20% greater than the DRIE etch dimensions which may contribute significantly to the differences we observe between their theoretical and measured frequencies of operation.

The etch dimensions measured on test parts of the same specifications from the A1 wafer were measured to be 103μmx78μm. Measurement of the length dimensions between points of zero surface displacement yield possible vibrational dimensions of up to 115x93μm, an 11.7% increase in length and nearly a 19.2% increase in width.

The surface displacement profile also has a number of features which may correlate to components of the pMUT laminate structure. Etched hole and PZT film dimensions taken from test structures are shown as labeled in Figure 5.8. While the maximum resolution of the optical vibrometer is fine enough to provide sub-micron accuracy, the time constraints of the demonstration allotted only enough time to collect the displacement profile shown. Future vibrometry measurements would benefit from focusing on collecting a finer sampling of data points for greater accuracy in the identification of structural components and the measurement of vibrational dimensions.

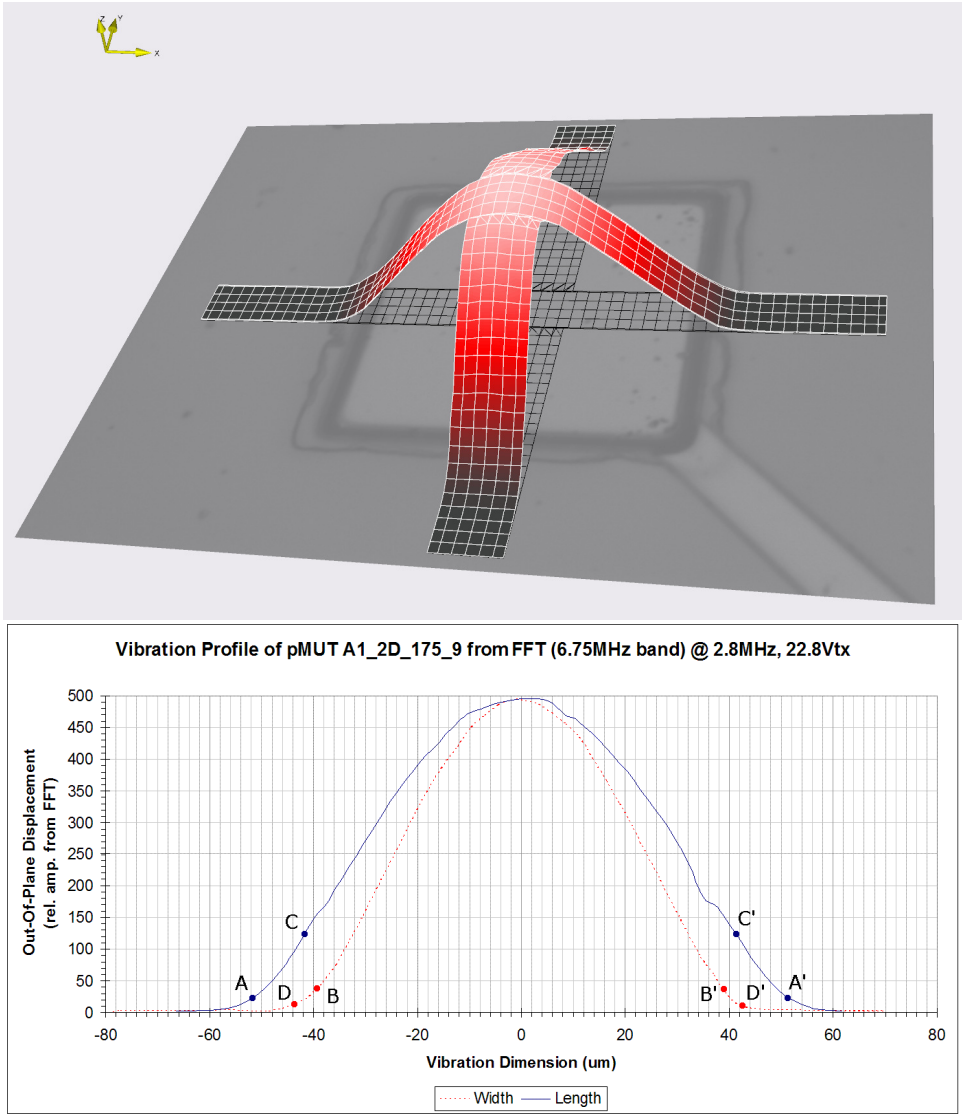

Figure 5.8: (Top) Profile of surface displacement in 6.75MHz band rendered in 3D overlaying reflected light microscopy image for registration. (Bottom) Measurement of displacement along length and width dimensions of a 75µm pMUT element for 6.75MHz band in FFT. Amplitude shown is relative amplitude from FFT (unspecified units). Labels specify approximate dimensions of elements of the membrane structure. A-A' and B-B' are the DRIE etched length and width, respectively. C-C' and D-D' are the PZT film dimensions.

5.3.4 Element Crosstalk and Coupling

In order to examine the effect of coupling and crosstalk among elements of the 2D arrays, the sample grid was extended to encompass multiple elements with a focus on

highlighting the displacement of surrounding membranes when a single element was excited. Figure 5.9 shows the rendered displacement in the peak 6.75MHz frequency band.

We observe significant evidence of coupling or crosstalk in the structure. We see that the excited element and its surrounding elements within the same column and row vibrate nearly 180° out-of-phase relative to one another. The relative peak displacement on the elements in the same column (above and below) and row (left and right) is approximately 34% and 24% of that on the excited element, respectively. The displacement of the element on a diagonal from the excited element is 16% of that of the excited element.

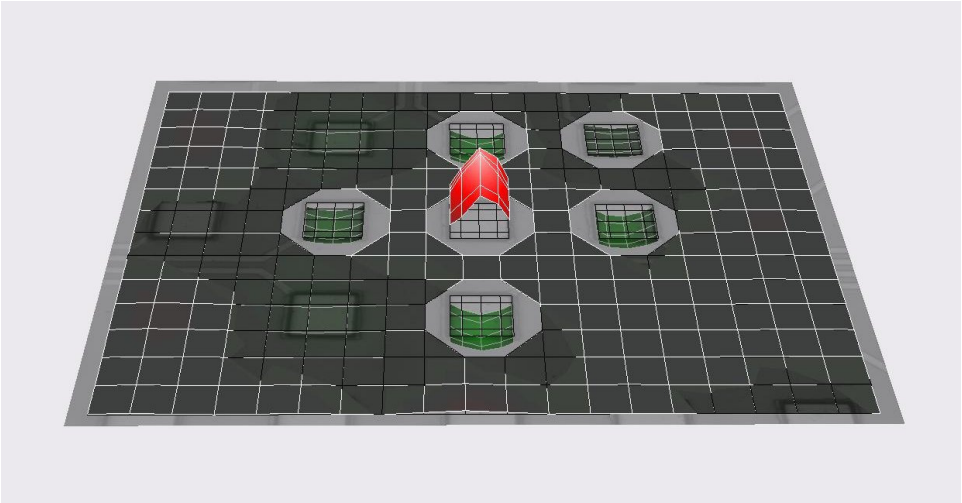

Figure 5.9: Visualization of vibration of a driven element (center) and the subsequent motion of adjacent elements which were not electrically actuated indicating coupling of neighboring elements.

We also observe that a very low amplitude, but measurable, displacement wave propagates along the bulk silicon outward from the excited element. This suggests that mechanical coupling through the inactive bulk silicon may contribute a pathway of acoustic energy transfer throughout the device structure.

The surrounding elements were not electrically isolated (grounded) in this measurement, which would help to determine the effect of electrical crosstalk between element signal pads and traces. A more focused investigation through optical methods should reveal a great deal more about the sources and pathways of coupling and crosstalk within the pMUT 2D array structure.

5.3.5 Air vs. Water Loading

Deionized water was placed on the pMUT surface and displacement measurements were made through the water droplet surface. This water droplet provides sufficient loading to dampen the pMUT vibration, shifting the 5.85MHz and 6.75MHz resonance peaks in air (the latter contributing to the long-duration oscillation) down to 5.4MHz in water for the A1_2D_175_9 device as shown in the FFTs provided in Figure 5.10.

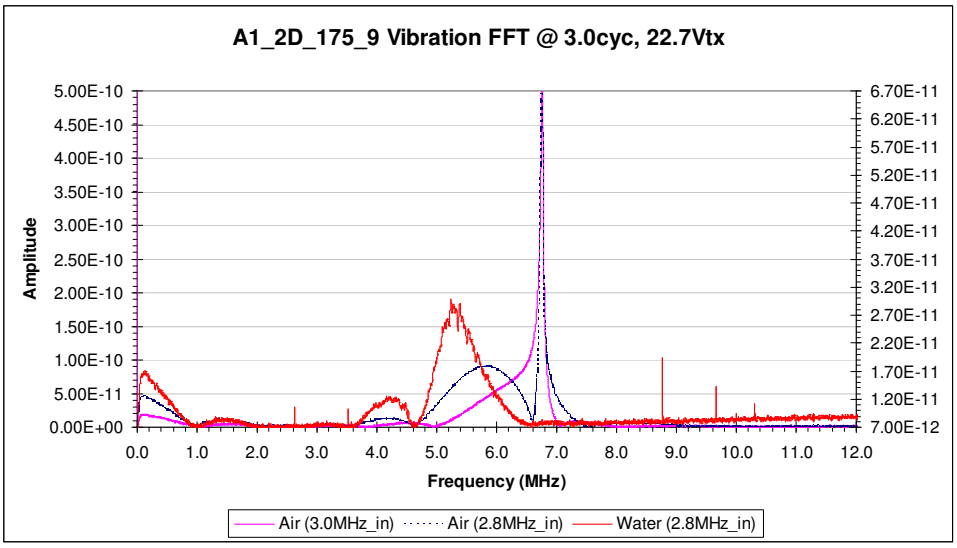

Figure 5.10: FFT plot of A1_2D_175 in air and water driven at 3.0 cycles, 22.7V_{tx} at various f_{in} - air (2.8MHz_{in}, 3.0MHz_{in}) and water (2.8MHz_{in}). Signal amplitude decreased significantly with water loading. Frequency dampening and downshift observed with water loading.

Note that the existence of 2 separate peaks at 5.85MHz and 6.75MHz in the FFT when driven at 2.8MHz is a result of the device being driven at a frequency away from resonance. The 6.75MHz appears to be the true resonant frequency while the peak at 5.85MHz is a result of the doubling of the 2.8MHz drive frequency.

We also note that the small 4.16MHz and 1.45MHz peaks remain unchanged in the FFTs when driven at 2.8MHz and are slightly higher in the FFT when driven at 3.0MHz.

Hydrophone measurements in the water tank showed the peak transmit frequency that propagates into the water is 5.4MHz. We suspect that this 5.4MHz propagating mode in water is the 6.75MHz resonant peak in air, shifted down to 5.4MHz due to the loading of the water. From visualizations of the surface displacement, both the 6.75MHz peak in air and the 5.4MHz peak in water are a fundamental 1-1 mode.

Unfortunately, the time-domain displacement waveform in water was not obtained so we are unable to determine if the 6.75MHz long-duration oscillation was reduced by the water loading. However, the width of the 5.4MHz peak in the FFT suggests that the pulse duration is likely shorter than the 6.75MHz oscillation.

Additionally, the effect of loading was measured for only 1 input frequency. Further characterization of the effect of water loading at other input frequencies would greatly increase our understanding of pMUT vibration. Comparison of optical vibrometry data with hydrophone pressure transmit measurements at numerous input frequencies could provide a wealth of information on the conditions under which pMUTs can be driven to maximize their transmit response.

Figure 5.11 shows the FFTs of both measured pMUT devices under water loading. The 75µm arrays were operated at 2.8MHz$_{in}$ while the 200µm arrays were operated at 3.2MHz$_{in}$.

The larger elements possess frequency peaks in the 5.8-6.6MHz and 2.8-3.4MHz bands and a sharp peak at 1.2MHz. The large 1.2MHz peak corresponds to a fundamental 1-1 mode shape from vibrational visualizations. However, the peak transmit frequency measured into a hydrophone was 6.4MHz.

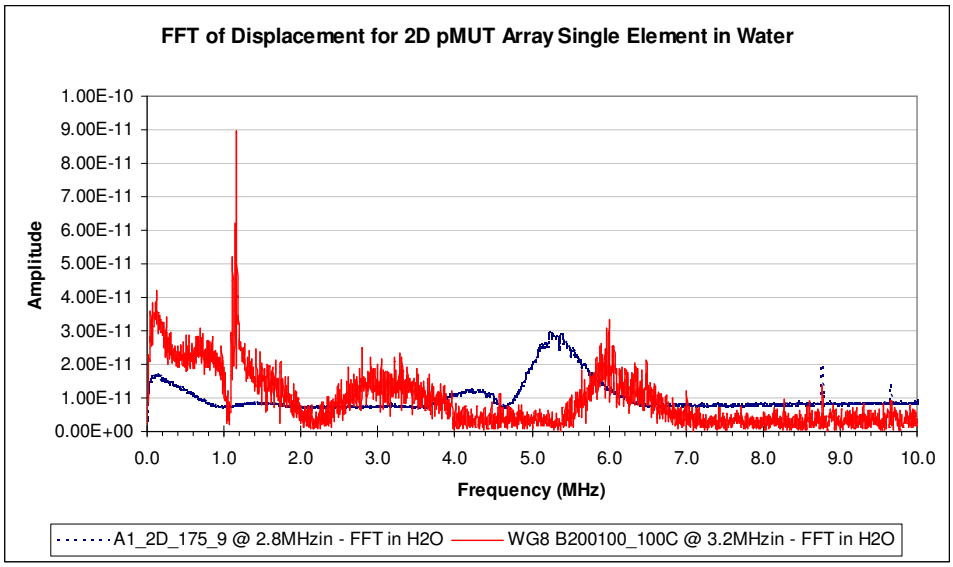

Figure 5.11: FFT plot of A1_2D_175 array (2.8MHz$_{in}$) vs. Wg8B200100 array (3.2MHz$_{in}$). Multiple frequency components observed for Wg8B200100, including a large peak at 1.2MHz.

Figure 5.12 shows a visualization of the mode shape in the 5.8-6.6MHz band where the 6.4MHz propagating frequency should fall.

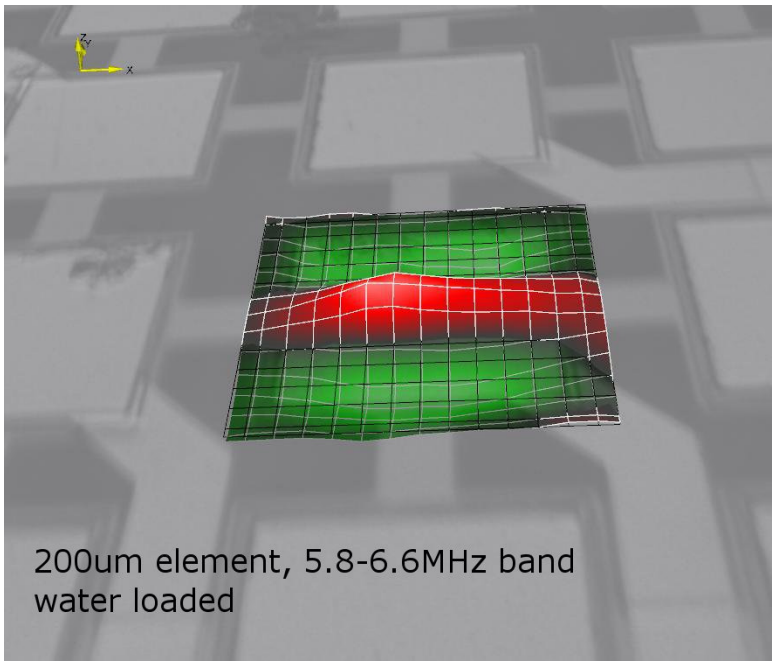

Figure 5.12: Vibration of a 200µm pMUT element in air in the 5.8-6.6MHz band showing the higher-order 3-1 mode of operation. Fundamental mode at 1.2MHz is not shown. 5x5 2D pMUT array driven at 3.0 cycle, 3.2MHz, 22.7V_{tx}.

Figure 5.12 indicates that the propagating mode of the large 200µm pMUTs is not a fundamental mode, but a higher order 3-1 mode shape. Note also that the mode shape of the 5.8-6.6MHz band in the water-loaded pMUT corresponds to the mode shape of the 7.8MHz component in the air-loaded condition, suggesting a down shift in frequency of this mode due to the loading of the water. Our current understanding of the basis for propagation in water to occur for the 3-1 mode rather than the fundamental 1-1 mode is incomplete and will likely require further testing and comparison between acoustic and optical vibrometry measurements.

5.4 Summary

Measurement of surface displacement showed peak-to-peak membrane displacement of up to 63nm in air for a 75µm device driven at $3.0MHz_{in}$. Under air loading, we also observed an extensive oscillating tail in the displacement waveform at 6.75MHz which was corroborated in the FFT. Greater surface displacement is likely achievable when driven at higher excitation amplitudes or at frequencies closer to $3.375MHz_{in}$ that will more effectively drive the 1-1 resonant mode.

Optical visualization of the mode shapes for devices of differing size showed 1-1 mode vibration for the 75µm and confirmed the operation of the larger 200µm pMUT elements in a combination of higher order modes. Fundamental 1-1, confined 1-1, 2-1/1-2, 1-3, and 3-1 modes were observed in the 200µm device in air. Fundamental 1-1, confined 1-1, and 3-1 modes were observed under water loading for this device. The sensitivity of the optical vibrometer through water limits observation of the other modes found under air-loading.

Comparing the frequencies from impedance analyzer measurements and pulse-echo oscillations observed in air and water within the structure of the pMUTs, 1-1 mode vibration was validated for these frequencies indicating that electrical and acoustic methods can be used to identify the highly resonant 1-1 mode. However, for imaging applications, driving off-resonance is likely to produce more optimal waveforms in terms of pulse duration and bandwidth.

From a comparison of acoustic measurements with optical vibrometry results, the 3-1 mode was identified as a more optimal propagating transmit mode for imaging

applications than the 1-1 mode for the large devices. Acoustic receive response of the 1-1 mode was approximately 30% more sensitive than the 3-1 mode, but pulse duration and bandwidth of the 3-1 mode produced better imaging waveforms.

The confined 1-1 mode for both devices indicate that the PZT film may provide an additional set of boundary conditions, particularly in transmit, which may result in the slightly higher transmit frequencies compared to receive frequencies measured acoustically.

The uncertainty surrounding the membrane vibrational dimensions and boundary conditions was confirmed with high resolution displacement profiles showing surface deformation over a greater area than expected. Measurement of the dimensions between points of zero surface displacement show an increase of up to 11.7% in length and 19.2% increase in width. Additional optical measurements are necessary to determine the extent of the geometric variation in devices of different size in order to draw further conclusions that could be broadly applied to the frequency theory.

Element crosstalk or coupling in the 2D array structure was also confirmed optically. Displacement of neighboring elements was shown to be as high as 34% when a transmit excitation waveform was applied across an adjacent element. The nature of this coupling, electrical or mechanical, was indeterminate during the short series of measurements taken. However, low amplitude displacement was observed in areas of the bulk silicon suggesting some mechanical propagation across boundaries previously considered to be isolated.

We have also shown that measurement of the pMUTs in vibration is possible under both air and water loading. The effect of air vs. water loading was explored and suggests

that the mechanical dampening of the vibrating structure may decrease the resonant frequency by nearly 1.4MHz for both device sizes.

Chapter 6

Analytical Methods: Plate Vibration

6.1 Introduction

The development of a pMUT frequency theory relies on the foundation of plate vibrational theory. This chapter presents the theoretical principles and equations that will be used in the analysis of measured pMUT frequencies and the development of the quantitative model to describe them. Both classical plate theory (CPT, or Kirchoff plate theory) for thin plates and Mindlin plate theory for moderately thick plates are used in the later analysis. An overview of both theories is provided in Appendix A, beginning with the equation of motion and leading to the frequency equations for each theory.

This chapter presents the general frequency equation for thin and thick plates as well as the methods used to calculate the frequency parameters for each theory.

6.2 Plate Vibration – Classical Plate Theory

The classical plate theory (CPT), or Kirchoff-Love theory, is an extension of Euler-Bernoulli beam theory with a number of notable assumptions, including

- the thickness of the plate does not change during deformation
- straight lines perpendicular to the midplane prior to deformation remain straight and normal to the midplane after deformation (plane sections remaining plane)

These assumptions are appropriate for the vibration of thin plates where the overall displacement is small compared to the thickness. The second stated assumption results in

zero transverse shear strain (transverse being the direction z in an xy-spanning plate) through the thickness of the plate.

6.2.1 Frequency of Vibration under Classical Plate Theory

The natural frequency of vibration for a thin, isotropic plate with dimensions a,b and thickness h is given as

$$\omega = \frac{\lambda^2}{a^2}\sqrt{\frac{D}{\rho h}} \tag{6.1}$$

where ρ is the volume density, λ^2 is the frequency parameter, and plate flexural rigidity D is given by

$$D = \frac{Eh^3}{12(1-v^2)} \tag{6.2}$$

where v is Poisson's ratio, E is Young's modulus. For clarity, we will set the dimensions of the plate along the coordinate axes x,y such that the edges of the plate are at $x=0$, $x=a$, $y=0$, and $y=b$. This will allow us to maintain consistency in establishing the positional relationship between plate dimensions, mode shapes, and non-uniform boundary conditions.

The frequency parameter, λ^2, also referred to as the plate eigenvalue, is determined in most cases by numerical analysis utilizing the plate deformation and boundary conditions. However, for the plate with simple support on all edges (SSSS), an exact solution exists in the form of

$$\lambda^2 = (m\pi)^2 + \left(\frac{n\pi}{\phi}\right)^2 \tag{6.3}$$

where m and n are the mode numbers along dimensions a,b and $\phi = b/a$. Reference tables for values of λ^2 for other simple boundary conditions have been derived and can be readily found in the literature. Combining Eqs. 6.1 and 6.3 then gives the frequency of vibration for SSSS rectangular plates as

$$\omega_{SSSS} = \left[\left(\frac{m\pi}{a}\right)^2 + \left(\frac{n\pi}{b}\right)^2\right]\sqrt{\frac{D}{\rho h}} \tag{6.4}$$

The use of the frequency parameter provides a fixed proportionality between the natural frequency and plate eigenvalue. This allows us to calculate plate frequencies for more challenging boundary conditions from the basic SSSS case using only the frequency parameter of the case of interest, as follows

$$f_i = \frac{\lambda_i^2}{\lambda_{ssss}^2} f_{ssss} \tag{6.5}$$

where f_i and λ_i^2 are values for the case of interest. Provided the frequency parameter can be obtained for the case of interest, the plate vibration frequency can thus be determined with ease.

Values for λ^2 for all boundary conditions are given over a range of aspect ratios $\phi = b/a$ and mode numbers m,n. It should be noted that the frequency parameters utilized in this thesis will assume $\phi\ (= b/a) > 1$, that is, the long edge of the plate falls parallel to the y-axis ($b>a$). For cases where $a>b$ a modified frequency parameter λ^{*2} can be used where

$$\lambda^{*2} = \left(\frac{m\pi}{\phi^*}\right)^2 + (n\pi)^2 \qquad \omega = \frac{\lambda^{*2}}{b^2}\sqrt{\frac{D}{\rho h}} \qquad \text{where } \phi^* = \frac{a}{b} \tag{6.6}$$

and $\lambda^{*2} = \lambda^2 \phi^2$. For the case of uniform boundary conditions or fundamental (m,n =1) frequencies this simple relationship is minor and the frequency parameter offsets the use of a or b in the calculation of the frequency. However, at higher order modes where $m \neq n$ and where boundary conditions are non-uniform, care must be taken in determining the mode shapes along each plate dimension and the selection of the appropriate frequency parameter. Confusion of these relationships may result in extreme differences in the calculated vibrational frequencies.

For the case of plates simply supported on two opposite sides and clamped on the other two sides (SCSC), Gorman[50] supplies a reference table (see Gorman, EV-2). For the fully clamped case (CCCC), Gorman utilizes the symmetry of the boundary problem and breaks the plate into quarter-plates, clamped on two adjacent sides and free or SS on the remaining two. The solutions are then derived for cases where the quarter-plate displacement is symmetric or antisymmetric about the midlines of the plate (the free or SS edges of the quarter-plate). For symmetric displacement about an edge, a free boundary condition is utilized on that edge. For antisymmetric displacement, a SS boundary condition is used.

Gorman's tables are divided into fully symmetric, symmetric-antisymmetric, and fully asymmetric mode cases. For the fully clamped plate, the symmetry of the problem allows for fully-symmetric and fully-antisymmetric modes to be calculated for all plates with aspect ratios $0.33 \leq \phi \leq 3.0$ using only λ^2 defined over $1.0 \leq \phi \leq 3.0$. For symmetric-asymmetric modes, Gorman provides tables for $1.0 \leq \phi \leq 3.0$ and $1.0 \leq \phi_I \leq 3.0$ where $\phi_I = 1/\phi$. Leissa [51] also provides an extensive table of frequency parameters for the fully clamped rectangular thin plate which can be used in conjunction with

Gorman's work for validation. Using these tables, all modes for fully clamped plates can be determined using interpolation to a high degree of accuracy for a wide range of width-length aspect ratios.

In the analysis presented in this thesis, reference tables for λ^2 are coded (up to 3,3 mode) in a lookup table, employing linear interpolation on the aspect ratio for a given *m,n* mode. Reference values taken from Gorman and Leissa for a rectangular CCCC thin plate with aspect ratio $\phi\,(=b/a)$ in the range 1.0-3.0 are provided in Table 6.1 up to 3,3 mode.

Table 6.1: Reference λ^2 values for CCCC rectangular Kirchoff plate (CPT).

λ^2 for Classical Plate Theory – CCCC								
$\phi = b/a = 1.00$					$\phi = 2.00$			
	n = 1	2	3			n = 1	2	3
m=1	35.99	73.39	131.6		m=1	24.58	31.83	44.7
2	73.39	108.2	165		2	63.98	71.08	83.27
3	131.6	165	220		3	87.25	116.4	123.2
$\phi = 1.25$					$\phi = 2.50$			
	1	2	3			1	2	3
1	29.89	52.51	89.25		1	23.52	27.81	35.42
2	68.51	89.35	124.3		2	63.08	67.39	74.78
3	127.5	139.2	181.3		3	61.49	79.76	101.36
$\phi = 1.50$					$\phi = 3.00$			
	1	2	3			1	2	3
1	27.01	41.7	66.52		1	23.06	25.86	30.72
2	66.13	79.81	100.8		2	62.64	65.52	70.44
3	125.3	138.6	144.2		3	47.96	60.32	75.04

The values given in Table 6.1 can be used with Eq. 6.1 to calculate frequencies for CCCC thin plates within the range of ϕ shown.

Frequencies for idealized SSSS and CCCC boundary conditions can thus be calculated using the methods described.

6.3 Plate Vibration – Thick Plate Theory

The classical plate theory is appropriate for the study of thin plates where the thickness is small compared to the surface dimensions and the deflection is small compared to the thickness. Plates considered thin typically have a span to thickness of 20:1 or more [52]. The CPT does not account for the inertia of the plate due to rotation or the additional plate flexibility from shear deformation. Both of these effects decrease the frequency of vibration. Thus, the frequencies from CPT are subsequently over-estimated for thick plates, particularly for higher order modes.

The pioneering study of thick plate vibration in the work of Mindlin [53, 54] provides a so-called first-order shear deformation theory for moderately thick plates in which rotary inertia was also considered. Mindlin's theory assumes a constant shear stress distribution through the thickness requiring a shear correction factor, κ; which compensates for errors resulting from the approximation made on the non-uniform distribution. Mindlin theory has been accepted to provide sufficient accuracy for plates with moderate thickness.

Various higher-order theories have since been proposed which achieve higher accuracy at the cost of much greater computational effort. Liew et al. [55] present an excellent review on the development of theories regarding thick plate vibration. As an example, a higher-order plate theory presented by Reddy et. al [56] provides frequency solutions requiring a great deal of computation but yielding less than 1.3% difference from Mindlin solutions for plates within the range of the pMUT geometries studied here. Consequently, the simplicity of Mindlin plate theory is much preferred for the study of pMUTs in this work over the minimal accuracy gained by using higher-order plate theories.

6.3.1 Plate Theories Applied to MUTs

The progress of MUT technologies has fueled the application of plate vibration theories toward their development for frequency control and optimization. The plate theories selected for modeling devices is highly dependent on the geometry and dimensions of the devices considered.

CPT is best used when the plate thickness is much smaller than the lateral dimensions due to some of the fundamental assumptions in the theory. Mindlin plate theory (second-order shear deformation) includes both shear rotary inertia and is better used for moderately thick plates. Higher-order plate theories and finite element analysis (FEA) are often used for greater accuracy at the expense of greater computational effort.

While portions of each of these theories are useful in contributing to the understanding of pMUT operation for the devices studied in this work, critical differences in the device geometries and dimensions limit their overall applicability to this work.

Circular plate theories are helpful in understanding the general effects of changing plate dimensions as well as the analysis of multilayered structures. However, many works simplify the derivations to a two-dimensional structure, making use of the radial symmetry present in circular structures [36, 40-44]. Overall, additional analysis is necessary to observe the effect of length and width dimensions of a rectangular plate.

Long, thin, rectangular structures are easily modeled using beam theory [38, 39] as the large length-width aspect ratio allows the much longer length dimension to be ignored in much of the frequency analysis. FEA has also been used for long, thin devices [34].

However, such a structure is more suited to 1D array applications and would be difficult to use in a 2D array configuration.

Models of square or near-square pMUT plates are the most relevant to the devices studied in this thesis. However, these models use devices larger than 100μm on a side. CPT is used for very thin plates (t<1.65μm) with FEA used for validation [37, 47] without comparison to physical devices. Models of thicker devices (8<t<40μm) used FEA to model vibration of 250x250μm plates [45]. Limitations in fabrication tolerances as well as increasing errors in the theoretical frequencies as device sizes decrease have left a void in the discussion of the operation of small, moderately thick, rectangular pMUTs.

The devices studied in this dissertation have lateral dimensions between 39-250μm and thicknesses between 5.6-18.9μm. With these smaller device sizes, the effect of transverse shear and rotational inertia increases as the thickness-span ratio increases. CPT begins to become inadequate in describing pMUT vibration while Mindlin plate theory is more appropriate for plates with moderate relative thickness. Unfortunately, Mindlin theory is applied rarely in the study of pMUT vibration, often disregarded in favor of FEA models. When Mindlin theory is applied, it is has been used in combination with CPT where thin plate theory is used for the first few mode orders and Mindlin theory is applied for higher-order modes where the shear and rotational inertia have a greater effect.

Outside of MUT applications, Mindlin theory has demonstrated high accuracy in modeling the vibration of plates with dimensions similar to the pMUTs studied here. Mindlin plate theory offers an excellent foundation from which to develop an analytical model for the vibration of small, moderately thick, rectangular pMUTs.

6.3.2 Vibrational Frequencies of Rectangular Mindlin Plates

Determination of the natural frequency of vibration for Mindlin plates is approached in a manner similar to classical plate theory as presented in Appendix A.3. For simply supported conditions, the frequency equation is

$$\frac{\rho^2 h^3}{12kG}\omega^4 - \omega^2\left[\rho h + \left\{\left(\frac{m\pi}{a}\right)^2 + \left(\frac{n\pi}{b}\right)^2\right\}\left(\frac{\rho}{kG}D + \frac{\rho h^3}{12}\right)\right] + D\left\{\left(\frac{m\pi}{a}\right)^2 + \left(\frac{n\pi}{b}\right)^2\right\}^2 = 0 \tag{6.7}$$

The classical plate theory frequency equation for simply supported rectangular plates can be recovered by setting $\frac{\rho h^3}{12}$ and $\frac{1}{kGh}$ to zero, yielding

$$\omega = \left[\left(\frac{m\pi}{a}\right)^2 + \left(\frac{n\pi}{b}\right)^2\right]\sqrt{\frac{D}{\rho h}} \tag{6.8}$$

Solutions to the Mindlin frequency equation for simply supported plates are found by determining the non-dimensional frequency parameter λ^2 given by Rao [57]

$$\lambda_{mn}^2 = \sqrt{\frac{1}{2}\left[\frac{k'}{s^4} + \Gamma_{mn}^2\left(\frac{m\pi}{s}\right)^2(1+k')\right] - \sqrt{\frac{1}{4}\left[\frac{k'}{s^4} + \Gamma_{mn}^2\left(\frac{m\pi}{s}\right)^2(1+k')\right]^2 - k'\left(\frac{m\pi}{s}\right)^4\Gamma_{mn}^4}} \tag{6.9}$$

where

$$s^2 = \frac{1}{12}\left(\frac{h}{a}\right)^2 \qquad x_{mn} = \left(\frac{m}{a}\right)\left(\frac{b}{n}\right) \qquad \Gamma_{mn}^2 = 1 + \frac{1}{x_{mn}^2}$$

$$k' = \frac{1}{2}k(1-\nu) \qquad k^2 = \frac{5}{6-\nu} \tag{6.10}$$

The natural frequency of vibration for mode *m,n* is then found by the relation

$$\omega = \frac{\lambda_{mn}^2}{a^2}\sqrt{\frac{D}{\rho h}} \tag{6.11}$$

Reddy et al. [56, 58] provide a transformation from Kirchoff to Mindlin theory

$$\omega_M^2 = \frac{6\kappa^2 G}{\rho h^2}\left\{\left[1+\frac{1}{12}\omega_K h^2\sqrt{\frac{\rho h}{D}}\left(1+\frac{2}{\kappa^2(1-\nu)}\right)\right]-\sqrt{\left[1+\frac{1}{12}\omega_K h^2\sqrt{\frac{\rho h}{D}}\left(1+\frac{2}{\kappa^2(1-\nu)}\right)\right]-\frac{\rho h^2}{3\kappa^2 G}\omega_K^2}\right\} \tag{6.12}$$

where ω_M is the Mindlin natural frequency, ω_K is the Kirchoff natural frequency. When rotary inertia is neglected, the frequency relationship simplifies to:

$$\hat{\omega}_M^2 = \frac{\omega_K^2}{1+\frac{\omega_K^2 h^2}{6(1-\nu)\kappa^2}\sqrt{\frac{\rho h}{D}}} \tag{6.13}$$

The difference between frequencies for simply supported rectangular Mindlin plates determined from Eq. 6.9 and 6.12 is <1.3% over the range of pMUT dimensions studied in this dissertation. The difference between solutions with and without rotational inertia (Eq. 6.12 and 6.13, respectively) is <0.64% difference over the range of pMUT dimensions studied in this work.

For plates with other simple boundary conditions, tables of frequency parameters, λ^2, can be found for plates with different width:length and thickness:length aspect ratios. They are applied in a manner similar to the classical plate theory solutions, making use of the fixed proportionality between frequencies and frequency parameters.

Liew et al. [59] present a comprehensive set of frequency parameters for Mindlin plates with thickness-length ratios up to 0.2 for a wide range of combinations of simple boundary conditions. Comparison to other published frequency parameters (when available) show excellent agreement (<0.1%). Numerous resources exist for thin plates

(t/L<0.01) for comparison at different width-length aspect ratios, including the works of Leissa [51] However, for moderately thick plates, few sources provide adequate frequency parameter tables encompassing the range of width-length and thickness-length aspect ratios covered by the pMUT devices studied in this work. Liew et al. is one of the few works providing adequate frequency parameter values within the range of interest for use here.

Reference frequency parameter values from Liew et al. are plotted against the thickness ratio (*t/L*) for SSSS and CCCC boundary conditions in Figure 6.1 to demonstrate the frequency decrease due to transverse shear and rotational inertia as the relative plate thickness increases.

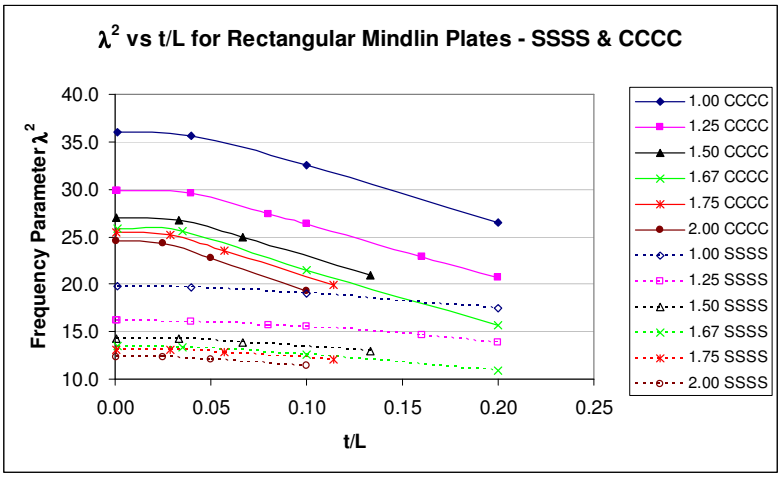

Figure 6.1: λ^2 values for SSSS and CCCC rectangular Mindlin plates. SSSS and CCCC comparison to scale.

Comparing the frequency parameters of both simply-supported and fully clamped plates, the transverse shear and rotational inertia are shown to contribute more greatly to decreasing the frequencies in clamped plates.

Xing and Liu [60] provides a set of closed form solutions for the frequency parameters of rectangular Mindlin plates under free vibration. However, a critical step in the usage of the closed form solution is left out, minimizing the applicability of the solutions for this work. A limited set of solutions presented in data tables are compared to the numerical analysis of Liew et al. Results from both methods in the limited data tables are in good agreement. If the missing steps in the solution set can be resolved, these closed form solutions would provide greater accuracy in the frequency parameters, becoming a valuable resource in the study of pMUT vibration.

6.4 Other Considerations to the Vibration of Plates

A number of other considerations to the theories regarding the vibration of plates are necessary for the study of pMUT vibration. The effect of multilayer laminated plate structure, loading by different media such as water, and compliant edge conditions should be considered in the discussion of pMUT vibration.

6.4.1 Effective Plate Flexural Rigidity for Multilayer Laminated Structures

The composite laminated structure of pMUTs introduces additional complexity into the application of plate dynamics theory to their vibrational analysis. Two approaches to reconciling this complexity are analytical and numerical methods. In the analytical approach, the composite is treated as a homogenous material with effective material properties calculated for the structure. Numerical methods similar to finite element analysis provides adequate accuracy at the cost of great computational effort and is best

used when a finite element approach to vibration analysis on the whole is used. As an analytical approach to the vibration analysis of plates is desired, analytical methods for an effective plate flexural rigidity are preferred.

In treating a layered structure as homogenous, three methods were considered for this investigation. The first is a "law of mixtures" volume fraction treatment while the other two are layer-wise theories. Layer-wise treatments of the composite modulus integrate through the thickness of the structure, accounting for the non-homogenous distribution of different material properties within the structure better than a "law of mixtures" treatment.

6.4.1.1 Isostress "Law of Mixtures"

The composite Young's modulus, E_{comp}, for a composite structure can be calculated as an isostress composite modulus given by

$$\frac{1}{E_{comp}} = \frac{v_1}{E_1} + \frac{v_2}{E_2} \tag{6.14}$$

where E_n is the Young's modulus for each component and v_n is the volume fraction for each layer. This composite modulus is adapted from that of fiber-reinforced composites in an isostress condition. By building up a composite modulus as we account for each layer serially, we arrive at a modulus for the whole pMUT membrane. For multi-layered composites, Eq. 6.14 may be extended to calculate the composite modulus as

$$\frac{1}{E_{comp}} = \sum_n \frac{v_n}{E_n} \tag{6.15}$$

where v_n is the volume fraction of each component.

The isostress modulus describes the condition in which each layer experiences equal force for all cross-sectional areas. For a multi-layer composite plate, a force normal to the surface of the plate yields an isostress condition.

The use of isostress calculations that flow from the "law of mixtures" (as applied in fiber-in-matrix composites) is acceptable for specimens under uniaxial stress [61], but may not be appropriate here.

6.4.1.2 Muralt Layer-wise Composite Modulus

Muralt et. al provide a model for clamped multi-layer plates applied to pMUTs [41] utilizing a layer-wise formulation of an effective plate flexural rigidity. With some minor modification in notation and simplification for the case of isotropic layers, the effective plate flexural rigidity for an *n*-layer plate is given by:

$$D_{eff} = \frac{1}{3}\sum_{n}\frac{E_n((h_n - z_s)^3 - (h_{n-1} - z_s)^3)}{(1 - v_n{}^2)} \tag{6.16}$$

with

$$z_s = \frac{1}{2}\frac{\sum E_n(h_n{}^2 - h_{n-1}{}^2)}{\sum E_n t_n} \tag{6.17}$$

where z denotes the height above the bottom plane of the plate, t_n is the thickness of the nth layer finishing at height $h_n = \sum_{k=1}^{n} t_k$, and E_n is the Young's modulus of the nth layer. The position z_s is the position of the neutral plane, assumed to be identical to the stress center. The use of the bottom of the plate as the $z=0$ reference position differs from other texts which use the position of the neutral plane as the reference point [62], but results in a more straightforward computation for non-symmetric laminate structures about the

neutral plane. The location of the neutral plane at $z=0$ is more suited for symmetric sandwich plates.

This D_{eff} can be used within the framework of plate vibration equations.

6.4.1.3 Pister & Dong Layer-wise Composite Modulus

Eccardt and Hansen [40] utilize an extension of Kirchoff thin-plate theory to handle multilayer laminated plates for modeling of cMUTs. They utilize an effective flexural rigidity, D_{eff}, for a multilayer structure defined by Pister and Dong [63] as

$$D_{eff} = \frac{AC - B^2}{A} \tag{6.18}$$

where

$$A = \sum_n Q_n (h_n - h_{n-1}) ,$$

$$B = \sum_n Q_n \frac{(h_n{}^2 - h_{n-1}{}^2)}{2} ,$$

$$C = \sum_n Q_n \frac{(h_n{}^3 - h_{n-1}{}^3)}{3} ,$$

$$\text{with} \quad Q_n = \frac{E_n}{1 - v_n^2} \tag{6.19}$$

Thus, analysis of thin multilayer plates can be conducted in an analogous manner to single-layer plates by substituting D_{eff} for flexural rigidity D in the Kirchoff thin-plate solutions provided the thicknesses and material properties (E_n and v_n) of each nth layer remains constant over the membrane width. The use of D_{eff} in Mindlin plate theory

should be applicable as well as the contributions of transverse shear and rotary inertia are accounted for in the frequency parameter.

6.4.2 Effect of Water-loading on Plate Vibration

The theoretical derivations considered in classical (Kirchoff) plate theory and higher-order plate theory (Mindlin) presented thus far have assumed vibration in a vacuum. Consideration of water-loading and its effect on vibrational frequency has been summarized by Leissa [51]. By Leissa's reference, a correction formula to account for the effects of water on one side of a rectangular plate for all boundary conditions has been provided by Greenspon [64, 65].

The frequency ratio of vibration in water vs. vacuum is given as

$$\frac{\omega}{\omega_0} = \sqrt{\frac{1}{1+\left(\frac{\gamma_w}{\gamma}\right)\left(\frac{b}{h}\right)\left(\frac{f}{2}\right)\left(\frac{A_{ij}^2}{B_{ij}}\right)}} \tag{6.20}$$

where ω is water-loaded frequency and ω_o is in vacuum, γ_w/γ is the dimensionless ratio of the mass density of water to that of the plate, f is a "virtual mass function" from Figure 6.2 (reproduced from Fig. 12.6 in Leissa). A and B are mode-dependent coefficients given for mode i-j in Table 12.3 of Leissa, dependent on CC or SS conditions. For mode 1-1, (A_{ij},B_{ij}) = (0.6904, 1) for CCCC and (0.4053,0.25) for the SSSS case.

Note that the virtual mass function approaches 1 for square plates and trends toward 0 as the plate appears more beam-like. Also, as the mass density of the plate increases, the frequency ratio approaches 1. As the span-thickness ratio (b/h) increases, the frequency

ratio decreases, indicating that plates that appear thinner compared to their lateral dimensions will be more greatly affected by the water load.

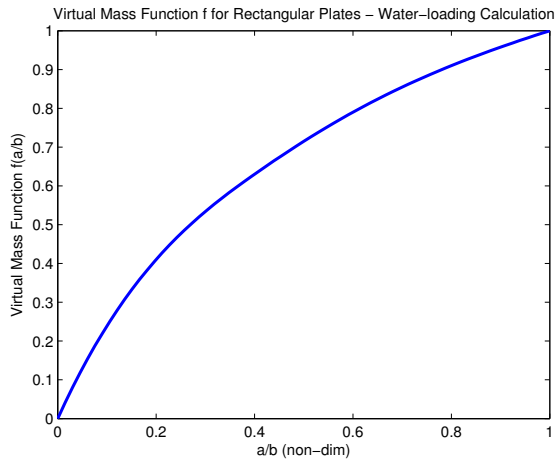

Figure 6.2: Virtual mass function f for rectangular plates used in calculation of correction factor for water-loaded frequency.

6.4.3 Effect of Compliant Edge Support

From the discussion of plate vibration, the boundary conditions have been shown to affect the natural frequency of vibration in a significant way. The idealized clamped and simply supported boundary conditions considered thus far have been idealized as rigid support. In the definitions for these boundary conditions described in a previous section, both support types were limited from transverse displacement, and for the clamped support, no velocity (transverse or rotational) is permitted at the boundary.

For the pMUT structures considered in this research, the plate boundaries are formed by the device silicon extending beyond the edges of the etched cavity. On some boundaries, some overlap of the PZT or metal layers occurs. Because the device silicon is elastic to some degree and not absolutely rigid as an idealized boundary would be, some consideration to the effect of compliance in the support must be considered.

Kobrinsky et al. [66] consider the compliance of boundaries of a beam supported on both ends. The compliance of the supports was shown to significantly affect the behavior of the beams and cannot be ignored. Several proposed approaches to include the compliance of supports are summarized. These include defining an effective length of the beam calibrated to experimental or FEM data, solving the complete beam and support structure using FEM, using correction factors in the analytical expressions, and modeling the supports as springs (transverse and rotational). For the analytical solutions desired in this research, effective geometric dimensions or correction factors are favored over the FEM approaches.

The effect of compliant support on the frequency of vibration of a structure is easily observed in the case of a cantilever beam [67]. The frequency of vibration measured for cantilevers with varying thickness-length ratios is shown in Fig. 6.3 as a ratio to the theoretical cantilever vibrational frequency with idealized rigid support, plotted against the thickness ratio.

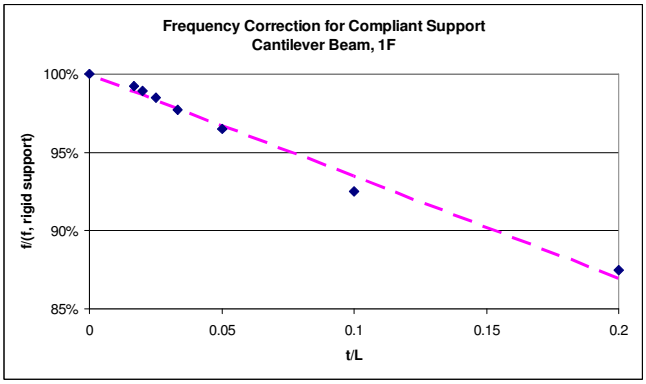

Figure 6.3: Frequency correction for compliant support in a cantilever beam.

A linear relationship exists as shown by the linear fit to the data such that

$$\frac{f}{f_{\text{rigid support}}} \approx 1.0 - 0.65\frac{t}{L}, \frac{t}{L} < 0.2 \tag{6.21}$$

where f is the measured frequency with support compliance, $f_{\text{rigid support}}$ is the theoretical frequency assuming rigid support, t is the thickness of the beam and L is the length. As the relative thickness of the beam increases with respect to its length, the contribution of support compliance in decreasing the vibrational frequency grows. This decrease occurs as a result of increased deformation at the edge. For a thin beam, the deformation profile at the edge remains relatively straight. However, as the beam thickness increases, the lateral deformation on both sides of the neutral plane increases in response to the material strain at the boundary. The additional deformation results in a decrease in the frequency of vibration in a manner similar to the contributions of shear and rotational forces in Mindlin theory.

The linear fit to the data provides a correction factor to the vibrational frequency for cantilevers. Similar correction factors exist for plate vibration, though the relationship may not be linear.

Xiang et al. [52] developed solutions for the free vibration of rectangular Mindlin plates with edges elastically restrained against transverse and rotational displacement. Numerical results were obtained to show the effects of elastic spring stiffness, relative thickness, and aspect ratio on the natural frequencies of flexural vibrations of rectangular Mindlin plates.

Gorman [68] utilized the superposition method to obtain frequency parameters for the free vibration of Mindlin plates on uniform elastic edge support. Frequency parameter

curves over a wide range of edge stiffness and thickness-span ratios (0.01 and 0.1) are shown for both square and near-square ($L/W = 1.5$) plates. Increases in edge stiffness constants increase the frequency parameter as expected,

Zhou [69] provides a set of static beam functions for rectangular Mindlin plates with uniform elastic (translational and/or rotational) edge constraints. The resulting frequency parameters from this model provided reasonable accuracy to other published data sets.

Xiang et al., Gorman, and Zhou's works showed the effect of elastic compliance in the boundary of Mindlin plates over a range of width-length and thickness-span aspect ratios. These models showed that the frequency parameters decrease as the thickness-span ratio increases (up to 0.2) as expected for Mindlin plates as the shear deformation and rotary inertia begin to contribute to a greater degree. While the overall frequency parameters are lower for low stiffness edge constraints, the decrease in the frequency parameter as the thickness-span increases is also shown to be more pronounced when the stiffness of the edge constraints is higher. The decrease in frequency parameter is also more pronounced at the higher order vibrational modes.

Chapter 7

Analysis of Results and Development of a pMUT Frequency Theory

7.1 Introduction

The ability to determine the fundamental frequency of vibration for an ultrasound transducer is paramount to optimizing the transducer design for selected applications. For theoretical calculations, the pMUT structure investigated here may be approximated as a rectangular laminated composite plate with mechanically bounded edge conditions.

This chapter will present the development of a pMUT frequency theory based on a modified Mindlin plate theory which accounts for *t/L*-dependent compliant edge support.

First, the individual and composite material properties of the pMUT structure will be considered. Uncertainty in the Young's modulus for the deposited PZT film requires evaluation over a range of values used in the literature with similar PZT films. Methods of calculating the composite density and Young's modulus will also be considered.

An analysis of the resonant oscillation frequencies observed in a pulse-echo configuration will show that this oscillation is a natural, free vibration of the plate structure with a fundamental 1-1 mode shape. The frequency will be shown to be poorly propagating into water, but that a downshift in frequency is observed under water-loading. Testing of separate elements in the array demonstrate that the vibrational energy crosses boundaries considered to be isolated by either mechanical coupling or electrical crosstalk. The oscillation frequencies are shown to be in excellent agreement with optical

vibrometry and electrical impedance results for a 1-1 mode. These fundamental resonant frequencies will be used to guide the modeling of pMUT vibration using plate theory.

A comparison to conventional CPT (classical thin-plate theory, also called Kirchoff plate theory) and Mindlin plate theories will demonstrate that the wide range of relative thicknesses for the pMUT devices studied requires consideration of the shear and rotational contributions addressed in Mindlin theory.

A generalized analytical method using the fundamental resonance frequencies in air will demonstrate adherence of the observed frequencies to the $f \propto t/L^2$ relationship when Mindlin-type effects are accounted for. Factoring out the t/L^2 term using a linear fitting method, the deviation of observed frequencies from the conventional plate theories with idealized BCs will be shown to result from a decreased effective Young's modulus, E_{eff}, or a decreased effective frequency parameter, λ_{eff}^2. The E_{eff} calculated from measured data will be shown to be unrealistic compared to known material properties. The frequency decrease resulting from lower λ_{eff}^2 will then be shown to be attributed to compliant support, modeled using curve-fitting methods.

The pMUT frequency theory will then be developed using the compliant support models as a modification to the Mindlin plate theory. Comparison to measured frequencies not included in the model development will demonstrate the predictive nature of the pMUT frequency theory for fundamental mode resonant vibration in air.

7.2 pMUT Mechanical Properties

The development of a plate vibration theory for pMUTs is highly dependent on the mechanical properties of the structure. Recalling from the Background, several approaches to MUT modeling treat the composite structure as a homogenous material with effective material properties calculated for the structure. For the rectangular laminated composite structure of the pMUTs under discussion, the material properties of the constituent layers will be similarly used to calculate composite plate properties used in the subsequent plate vibration theory.

The geometric parameters of the pMUT arrays used in both experimentation and theoretical calculations are given in the experimental results chapters for the corresponding devices.

7.2.1 Material Properties of Constituent Layers

The bulk material properties for constituent materials in the pMUT structure are listed in Table 7.1. [70]

Table 7.1: Bulk material properties for constituent materials in pMUT. (* highly process-dependent).

Material	E (Pa)	ρ (kg/m^3)	c (m/s)
Au	7.80_E10	19300	2010
PZT	1.00 - 8.60_E10*	7800	1132 - 2264
Pt	1.47_E11	21450	2618
SiO2	7.17_E10	2200	5709
Si	1.25_E11	2330	7325

The velocity, c, shown in Table 7.1 arrives from the relation $c=\sqrt{(E/\rho)}$. Note that the Young's modulus, E, for PZT is given as a range as it is highly process-dependent. The mechanical properties for deposited thin-films, in particular, differ greatly from the bulk

material. The Young's modulus for sol-gel deposited, circular thin-film (0.4-1.6μm) PZT measured using the wafer bulge technique [71] was calculated to be 10-40GPa. In comparison, the Young's modulus for bulk PZT was referenced to be 48-71GPa in the same reference. Models of pMUT vibration in the literature use E_{PZT} values of 80GPa [39], and 75.2GPa [45], 86.2GPa [47], and 75.7GPa [41]. Because E depends so heavily on the thickness and process of deposition and we have been yet unable to directly measure the modulus for the PZT films used in this research, our theoretical analysis must account for an unknown modulus value that falls in or near this range.

Suggested methods to measure the Young's modulus of PZT from thin cantilever and plate structures are provided in the Discussion (§9.2.1). Such structures created using the fabrication methods for pMUTs presented in this thesis are not currently available.

7.2.2 Composite Density

The composite membrane density was determined by calculation of the mass and volume for each layer in the laminate structure, and then summed to formulate values for the total mass and total volume of the pMUT element. The ρ_{tot} was then calculated as the total mass divided by the total volume. The layer width used for the volume calculations was the DRIE width for all layers as listed in Tables 3.1, 3.2, and 4.1. The layer lengths were used as listed for each material layer.

7.2.3 Composite Modulus

Three possible methods of calculating a composite modulus are given in the Analytical Methods (§6.4.1) – the isostress "law of mixtures," Muralt's layer-wise

method [41], and Pister & Dong's layer-wise method [63]. The isostress composite modulus is an adaptation from fiber-in-matrix type composites which Chou et al. [61] identify as applicable in small samples under uniaxial stress but inappropriate for the analysis of layered plates under flextensional vibration. The isostress composite modulus was not encountered in the MUT modeling literature while the two layer-wise theories were used or referenced specifically in the discussion of MUT vibration. The isostress composite method was subsequently abandoned in the analysis of pMUT vibration in this work.

Both layer-wise theories yield comparable composite moduli over the range of pMUT dimensions. Effective composite moduli for pMUT devices are calculated in Table 7.2 for Muralt and Pister & Dong's methods using E_{PZT} = 10, 40, and 86 GPa to encompass the Young's modulus values observed in the literature.

Table 7.2: Calculated composite Young's modulus for pMUT device types (based on layer thicknesses only) using Muralt (E_{Muralt}) and Pister & Dong's (E_{PD}) layer-wise methods. Calculations shown use E_{PZT} = 10, 40, and 86 GPa to encompass the range of values observed in pMUT-related literature.

			E_{PZT} =	10GPa	10GPa	40GPa	40GPa	86GPa	86GPa
Device	**t_{Si} (µm)**	**t_{PZT} (µm)**	**t_{dev} (µm)**	**E_{Muralt} (GPa)**	**E_{PD} (GPa)**	**E_{Muralt} (GPa)**	**E_{PD} (GPa)**	**E_{Muralt} (GPa)**	**E_{PD} (GPa)**
Wg5	6.0	1.1	8.03	97.67	92.89	102.66	99.71	110.35	109.29
Wg6	6.0	2.0	8.93	91.26	81.82	98.10	92.72	108.62	107.05
Wg8	11.0	1.0	12.93	103.22	101.13	107.45	106.15	113.98	113.51
Wg9	11.0	2.0	13.93	93.57	88.23	100.42	97.34	110.95	110.07
Wg12	16.0	1.0	17.93	107.23	106.03	110.78	110.03	116.25	115.98
Wg14	16.0	2.0	18.93	97.80	94.51	103.87	101.96	113.20	112.66
A1	6.0	1.2	8.13	96.71	91.41	101.97	98.74	110.08	108.96
A2	6.0	1.2	8.13	96.71	91.41	101.97	98.74	110.08	108.96
A11	6.5	1.2	8.63	96.96	92.04	102.25	99.26	110.41	109.37

Both layer-wise methods assume uniform layer thicknesses and are independent of plate lateral dimensions, utilizing only the component layer thicknesses in the calculation. Referring to the formulation presented in the Background, both methods are actually used

to calculate an effective plate flexural rigidity, D_{eff}, which is then converted to an effective Young's modulus, E_{eff}, through the relation $D_{eff} = \frac{E_{eff}\, h_{tot}^3}{12(1-\nu^2)}$ using the total plate thickness for h_{tot} and 0.3 for ν.

The percent difference between Muralt's and Pister & Dong's solutions for E_{PZT}=10GPa is <6% except Wg6 devices where the difference is 10.3%. The difference between the two methods decreases as the Young's modulus for the two primary layers (PZT and Si) become more similar. This difference likely arises from errors in locating the neutral axis in Muralt's method, while Pister & Dong's method does not require determination of the neutral axis. Note that the largest deviation between the two layer-wise methods occurs for the devices with the largest relative PZT thickness (to Si thickness). Pister & Dong's method was chosen for the development of the subsequent frequency theory for its straight-forward calculation and independence from determination of the neutral plane location.

Variation in the value chosen for E_{PZT} results in up to 23% difference in the calculated composite modulus between the maximum and minimum of the E_{PZT} range, though <16% is more typical. Suggested methods to measure the Young's modulus of the laminate using a composite cantilever beam or other structures under known load are discussed in §9.2.1. Unfortunately, the structures required to measure a composite modulus were unavailable at the time of this writing. A value of E_{PZT} = 10GPa was chosen for use in the subsequent analysis for consistency. However, measurement of the composite modulus for the structures and geometries studied in this work is highly suggested and would greatly contribute to the accuracy of the frequency theory.

The error introduced through the composite modulus is eventually diminished by the square root taken in the frequency calculation (Eq. 6.1 with 6.2), thus contributing less than 6% error in the frequency when choosing between the two methods and less than 12.5% over the range of E_{PZT} shown.

7.3 Resonant Oscillation in Pulse-Echo Configuration

A persistent oscillation was initially observed on the 14x14 pMUT arrays when a single element was connected in a pulse-echo configuration, with a high-voltage transmit waveform delivered with the receive amplifier connected to the same element. A short description of this oscillation was provided in the experimental methods section covering the single element pulse-echo response of the 14x14 2D pMUT array devices. Further characterization and analysis of the persistent oscillation was conducted on both the 14x14 and 5x5 2D array elements. Coupled with the results from optical vibrometry and electrical impedance analysis, the observations made indicate that the persistent oscillation is the fundamental (1-1) mode resonance remaining in the structure over a long duration in response to the high-voltage transmit waveform. The resonant oscillation is shown to be only weakly propagating into the medium, but contributing greatly to mechanical coupling or electrical crosstalk between elements within the array.

The straightforward acquisition of the frequency of the oscillation under both air and water loading presents an excellent method to determine the resonant response of the pMUT plate. This frequency will be useful in the subsequent development of the pMUT vibration theory.

7.3.1 Measurement of the Resonant Oscillation

Measurement and characterization of the resonant oscillation was initially performed on the A1_2D_150_12 array. The characterization was then extended to all the 14x14 2D pMUT arrays and later conducted on the 5x5 2D arrays. The extensive characterization of the oscillation using the A1_2D_150_12 array will be presented first, followed by observations from the rest of the 14x14 array devices. The resonant oscillation frequencies for 5x5 devices were collected similarly and are presented in the summary of measured vibrational frequencies in section §7.4.

Measurement of the frequency of the resonant oscillation is straightforward and can be determined using a Fourier transform of the electrical signal across the element shortly after the high-voltage transmit is applied. Typically, this should be done immediately following the recovery of the receive amplifier while the oscillation amplitude is still high, roughly 10-30μs after the transmit waveform has been applied.

Recalling from the single element pulse-echo characterization of the A1_2D_150_12 14x14 array in section §4.3.4, a large 4.7MHz peak was observed in the FFT of the pulse-echo signal. The 4.7MHz peak is the result of a prolonged oscillation in the pulse-echo waveform which precedes the actual reflected pulse from the aluminum block target and remains unchanged when the reflecting target is translated in range or removed altogether.

7.3.2 Propagation of the Resonant Oscillation

To discern whether the 4.7MHz oscillation is a propagating mode, the array was driven in a transmit-only configuration into the GL0200 hydrophone at the observed optimal operating frequency of 5.4MHz (which was determined based on both

quantitative measurement of the peak-to-peak amplitude and qualitative assessment of the waveform envelope). The frequency component in the 4.7MHz range was -21dB down from the 5.4MHz frequency component. This indicates that the 5.4MHz signal is propagated while the 4.7MHz oscillation propagates to a lesser degree (resulting in a "ringy" tail following the truncated sinusoid pulse) but largely remains in the structure.

Single elements were then driven at frequencies between 2.0-2.5MHz to excite the oscillation frequency rather than the observed optimal pulse-echo frequency in both transmit-only and pulse-echo configurations. Transmit-only measurements revealed an acceptable waveform with lower amplitude signal at this lower frequency while the pulse-echo measurements showed significantly decreased reflected pulse amplitude. This indicates that while 4.7MHz may be a frequency that these pMUTs can be driven to transmit at, it is not a frequency at which these elements transmit and receive in a pulse-echo configuration as effectively as they do at 5.6MHz.

Further testing in the pulse-echo mode while varying the driving frequency showed that decreasing the transmit frequency from 5.6MHz down to 4.5MHz resulted in a decrease in the reflected pulse amplitude by a factor of 2 while the amplitude of the persistent oscillation increased by a factor of 3. The change in pulse-echo signal and oscillation amplitudes as a function of frequency is shown for A1_2D_175_9 in Figure 7.1.

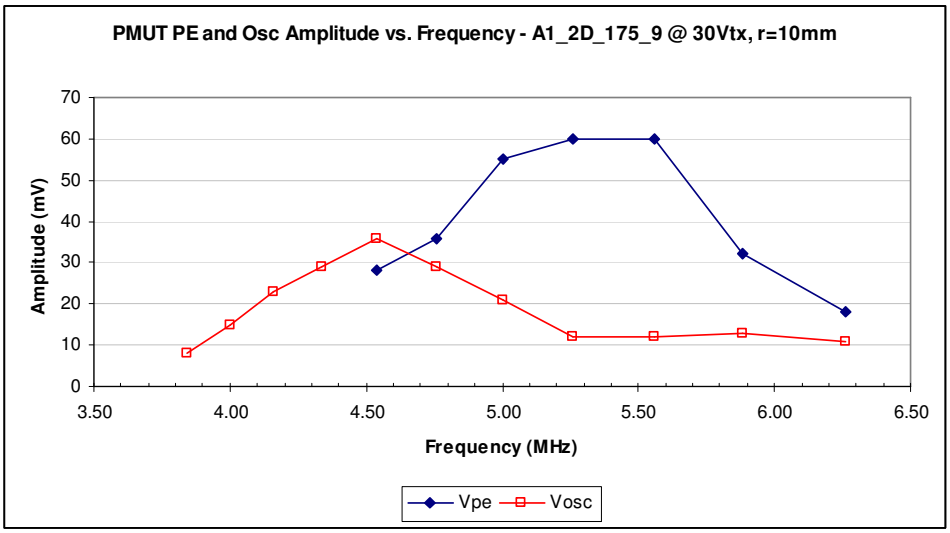

Figure 7.1: Pulse-echo (V_{pe}) and persistent oscillation (V_{osc}) amplitude as a function of the applied transmit frequency for a representative 14x14 array (A1_2D_175_9) at $30V_{pp-tx}$ with the reflecting target at 10mm range.

For this array (A1_2D_150_12), we recall that the peak transmit and receive frequencies are 5.6MHz and 5.4MHz, respectively. The pulse-echo measurements for the same device show that the optimal pulse-echo operating frequency is between 5.2-5.6MHz where the oscillation is minimized, with a 5:1 ratio of reflected pulse signal to persistent oscillation amplitude. At lower transmit frequencies, the signal:oscillation ratio decreases to 1:1.

7.3.3 Coupling and Crosstalk of the Resonant Oscillation

To determine whether the oscillation was contained within the device structure and how it might impact neighboring elements, a corner element was driven in transmit while the oscillation amplitude was measured on neighboring elements. The presence of measurable oscillation amplitude was observed on nearly all elements within the array.

The oscillation amplitude diminished as the distance between the two elements decreased, but measurable oscillation was observed as far as the opposing corner element.

Contact force was applied to the surface of the device on both the active device area and on the surrounding bulk silicon to dampen or augment the oscillation. Application of force on the bulk silicon did not result in measurable change in the oscillation amplitude. Application of force on the active device area resulted in significant change of the amplitude, typically decreasing but in some cases increasing, the amplitude. The oscillation amplitude was diminished dramatically when the measured non-transmitting element was physically clamped, but was only eliminated completely when the transmitting element was clamped. This confirmed that the physical vibration of the transmitting element resulted in the oscillations observed on the opposing corner element.

7.3.4 Effect of Air vs. Water Loading on Resonant Oscillation

This persistent oscillation in pulse-echo was observed in all A-series devices, with both water and air loading. The oscillation in air was observed by taking the FFT of the signal after the recovery of the receive amplifier while suspended out of the water tank. The water-loaded oscillation was then observed by submerging the surface of array into the water without a reflecting target in place. The frequency of oscillation in air and water for 14x14 2D array devices are given in Table 7.3 with transmit, receive, and impedance analyzer frequencies included for comparison.

Note that the oscillation frequency in air mirrors the impedance analyzer frequencies closely, indicating a strong correlation between the electrical response of the devices from the impedance analyzer measurements and the mechanical response observed in the

persistent oscillation. Coupled with the strong correlation between optical vibrometry measurements of the surface displacement in air, there is substantial evidence that this frequency is the natural vibrational frequency of the fundamental mode in air.

Table 7.3: Frequencies of pulse-echo persistent oscillation and optimal pulse-echo signal. Transmit, receive, and impedance analyzer frequencies are included for comparison. Note that the impedance analyzer frequencies are in air while transmit and receive are in water. (Oscillation frequency spectrum also included 10.0 and 10.4MHz components. 6.00MHz component is roughly 20dB larger).

				H2O	H2O	Air	Air	H2O	
Device	**t_{dev} (um)**	**W_{etch} (um)**	**L_{etch} (um)**	**f_{tx} (MHz)**	**f_{rx} (MHz)**	**$f_{imp\ an}$ (MHz)**	**PE Osc Freq (MHz)**	**PE Osc Freq (MHz)**	**PE Pulse Freq (MHz)**
A11_2D_40_90p_1	8.6	39	64	13.00	12.75	14.00	14.20	12.50	--
A11_2D_50_100p_1	8.6	50	77	9.40	10.00	6.10	6.00 *	4.2/4.68	--
A11_2D_65_150g_1	8.6	63	91	7.70	7.51	8.65	8.70	5.80	--
A11_2D_65_150p_1	8.6	63	91	7.00	6.91	9.50	9.60	--	--
A11_2D_75_150g_1	8.6	72	104	4.20	3.88	4.80	4.80/8.8	3.25	--
A11_2D_75_150p_1	8.6	72	104	4.20	3.89	4.90	4.85/8.5	3.25	--
A1_2D_175_9	8.1	78	103	5.40	5.17	6.76	6.80	4.45	5.60
A1_2D_150_12	8.1	78	103	5.60	5.40	6.82	6.90	4.70	5.65
A2_2D_175_12	8.1	65	96	6.20	6.14	8.00	8.00	5.10	6.00
A2_2D_150_9	8.1	65	96	--	--	--	8.65	5.70	7.00
A2_2D_150_10	8.1	65	96	--	--	--	8.80	5.80	7.10

For frequencies in water, we find that the pulse-echo signal frequency fits closely with the optimal transmit and receive frequencies, as expected, but the oscillation frequency falls roughly 15-20% below the optimal pulse-echo frequency. The contributing factors for this observation will be discussed in a later section.

A representative waveform from a 75µm element and FFTs of the oscillation in air and water for devices of varying size are shown in Figure 7.2. Note the downshift in frequency and decrease in amplitude of the oscillation from air to water loading for each device. The oscillation waveform shown includes recovery of the receive amplifier.

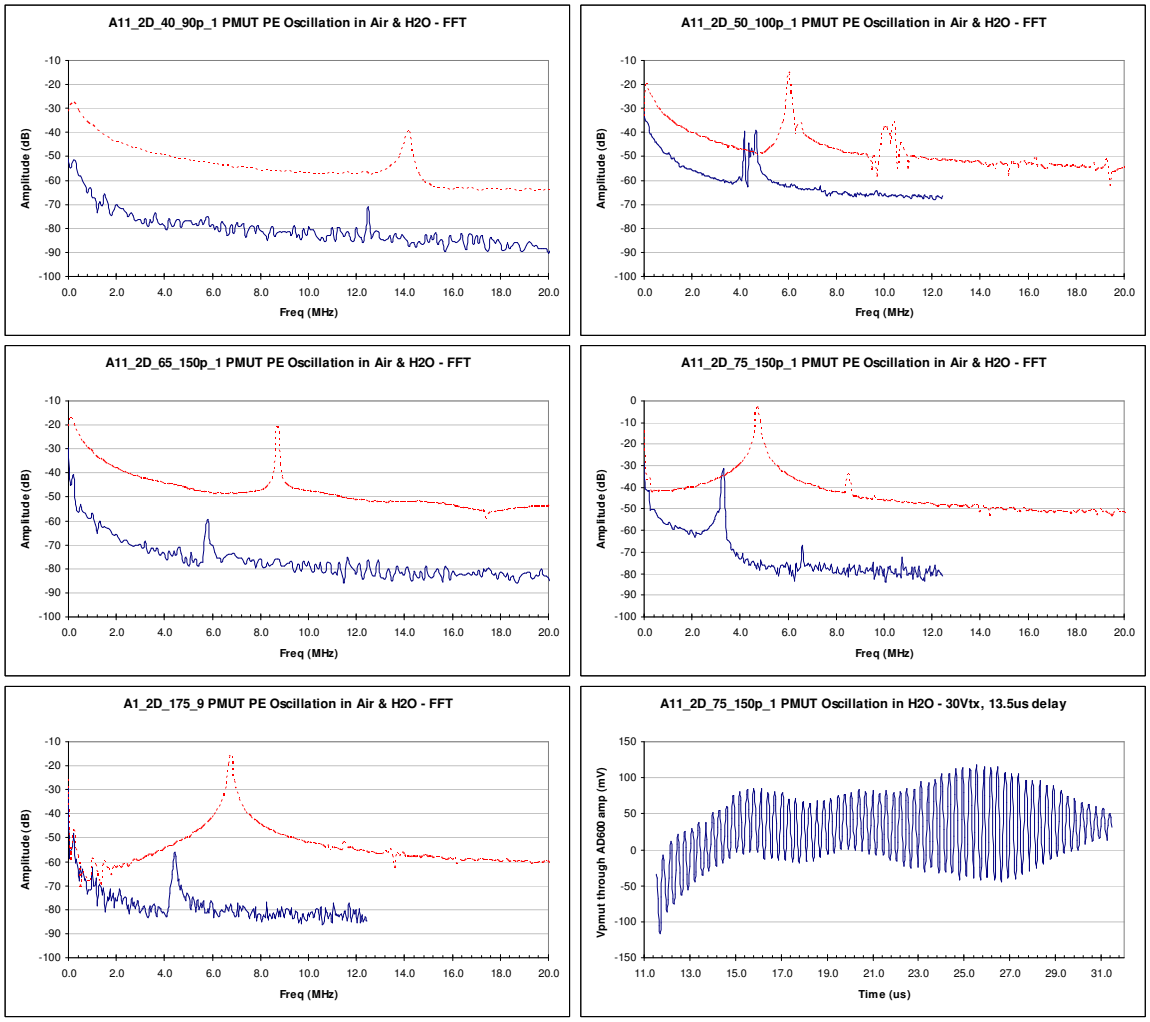

Figure 7.2: FFTs and a representative waveform of the persistent, non-propagating oscillation on the pMUTs in pulse-echo configuration in air and water. Dotted plots are response in air, solid plots are in water.

It is worth noting the multiple frequency peaks in the FFT of the oscillations in the A11_50 device and the A11_75 devices. For the A11_50 device in air, peaks exist at 6.0, 10.0, and 10.4MHz, while with water loading, only 4.2 and 4.68MHz frequency peaks appear. For the A11_75 device in air, peaks exist at 4.85 and 8.5/8.8MHz, while with water loading only the 3.25MHz frequency peak appears. These devices differ from most other devices which typically have a single frequency peak in the oscillation. All three of

these devices, A11_50p, A11_75p, and A11_75g, in particular, performed poorly as imaging arrays, with noticeably lower dynamic range and sensitivity. The appearance of multiple peaks in the oscillation frequency response gives indication of multiple modes of oscillation, possibly diverting more energy away from the propagating vibrational mode. The contributing factors to this aberrant behavior are currently unknown.

Referencing the time-domain oscillation observed in the optical vibrometry results (Figure 5.1 and 5.2), the timing of persistent oscillation waveform shown falls well within the duration of the surface displacement measured using optical methods.

7.3.5 Effect of Resonant Oscillation on Imaging Performance

The amplitude of the persistent oscillation across devices also provides indication of imaging performance. Table 7.4 shows the maximum measured oscillation amplitudes in air and water, with pulse-echo signal amplitudes provided when available.

Table 7.4: Persistent oscillation amplitudes in air and water for 14x14 pMUT single elements at $30V_{pp\text{-}tx}$. Pulse-echo signal amplitudes are provided for comparison when available.

					Air			H2O			
Device	**t_{dev} (um)**	**W_{etch} (um)**	**L_{etch} (um)**	**V_{tx} (V)**	**PE Osc Freq (MHz)**	**V_{osc} (mV)**		**PE Osc Freq (MHz)**	**V_{osc} (mV)**	**PE Pulse Freq (MHz)**	**V_{PE} (mV)**
A11_2D_40_90p_1	8.6	39	64	30.0	14.20	20		12.50	10	--	--
A11_2D_50_100p_1	8.6	50	77	30.0	6.00*	480		4.2/4.68	260	--	--
A11_2D_65_150g_1	8.6	63	91	30.0	8.70	480		5.80	10	--	--
A11_2D_65_150p_1	8.6	63	91	30.0	9.60	40		--	5	--	--
A11_2D_75_150g_1	8.6	72	104	30.0	4.80/8.7	3400		3.25	240	--	--
A11_2D_75_150p_1	8.6	72	104	30.0	4.85/8.7	1800		3.25	180	--	--
A1_2D_175_9	8.1	78	103	30.0	6.80	1030		4.45	16	5.60	60.0
A1_2D_150_12	8.1	78	103	30.0	6.90	1100		4.70	40	5.65	65.0
A2_2D_175_12	8.1	65	96	30.0	8.00	400		5.10	5	6.00	48.0
A2_2D_150_9	8.1	65	96	30.0	8.65	225		5.70	10	7.00	45.0
A2_2D_150_10	8.1	65	96	30.0	8.80	240		5.80	5	7.10	40.0

Note the significantly higher oscillation amplitudes of the A11 50μm and 75μm devices in comparison to the other devices. The devices that exhibited particularly high oscillation amplitudes were notably poorer in imaging performance with much lower signal to noise and a qualitative "haze" over the image field resulting in generally unusable B-modes.

For imaging applications, the narrow bandwidth of this fundamental resonant mode is a non-ideal characteristic for an imaging transducer. Not only has it been shown to negatively affect pulse-echo operation due to its long duration which limits the dynamic range for close targets, excitation of this resonant mode in the transmit waveform reduces axial resolution due to an increased pulse-length. For use as an imaging transducer, the pMUT elements must be driven off-resonance in such a way that will increase transmit pulse bandwidth and decrease persistent oscillation within the structure by limiting the resonant frequency component in the excitation while retaining a high transmit efficiency and receive sensitivity.

While the contributing factors to the oscillation amplitude are currently unknown, these observations suggest that minimizing the oscillation within the structure might significantly improve the dynamic range and signal-to-noise in imaging performance. Suggested methods to reduce the persistent oscillation and capitalize on off-resonance operation are proposed in the Discussion (§9.2.4).

7.3.6 Relevance of Resonant Oscillation in pMUT Vibrational Theory

The evidence from electrical, acoustic, and optical measurements indicates that the persistent oscillation is associated with significant deflection of the pMUT membrane and

is likely the fundamental resonant mode of free vibration of the plate. The fundamental resonance is typically the most easily modeled and studied vibrational mode, and errors are generally minimized compared to higher-order modes. Also, as the natural free vibration of the structure over the entire etched dimensions, the fewest assumptions need to be made regarding the boundary conditions for the resonant oscillation. This mode thus presents the simplest point from which to build a pMUT frequency theory. The additional considerations for higher-order operation or more complex boundary conditions (confined 1-1 mode) can then be built upon the foundation of fundamental free resonance.

The resonant oscillation frequencies will be modeled as a free vibration over the entire etched cavity dimensions. Resonant frequencies in air can be modeled to assess the boundary conditions in comparison to idealized clamped and simply-supported conditions. Composite plate material properties can be most easily evaluated from this mode as well. The effects of loading by water and forced, alternatively confined, or higher-order vibration for acoustic transmit and receive can be applied separately using the modeling results of the resonant mode.

7.4 Summary of pMUT Measured Frequencies

The pMUT frequencies measured using electrical, optical, and acoustic methods presented in the Experimental Methods chapters for 5x5 and 14x14 2D array single elements under both air and water loading are summarized in Table 7.5.

Table 7.5: Frequencies measured using electrical, optical, and acoustic methods for 5x5 and 14x14 2D pMUT arrays under air and water loading. Fields marked with -- designate measurements attempted but were unquantifiable.

			Air			H2O			
Device	t_{Si} (µm)	t_{PZT} (µm)	Imp. Analy. Freq (MHz)	PE Osc Freq - Air (MHz)	Polytec Freq - Air (MHz)	Tx Freq (MHz)	Rx Freq (MHz)	PE Osc Freq - H2O (MHz)	Polytec Freq - H2O (MHz)
A11_2D_40_90p_1	6.5	1.2	14.00	14.15		13.00	12.75	12.50	
A11_2D_50_100p_1	6.5	1.2	--	6.00/10.0		9.40	10.00	4.20/4.68	
A11_2D_65_150g_1	6.5	1.2	8.65	8.65		7.00	6.91	5.75	
A11_2D_65_150p_1	6.5	1.2	9.50	9.53		7.70	7.51	--	
A11_2D_75_150g_1	6.5	1.2	4.80	4.80/8.8		4.20	3.88	3.30	
A11_2D_75_150p_1	6.5	1.2	4.90	4.85/8.5		4.20	3.89	3.40	
A1_2D_175_9	6.0	1.2	6.76	6.75	6.75	5.40	5.17	4.50	5.3
A2_2D_175_12	6.0	1.2	8.00	7.90		6.20	6.14	5.10	
A1_2D_150_12	6.0	1.2	6.82	7.00		5.60	5.40	4.70	
Wg5 B5050_100A	6.0	1.1	12.70	12.40		10.90	10.98	--	
Wg6 B5050_100C	6.0	2.0	13.70	--		11.90	12.11	--	
Wg8 B5050_100D	11.0	1.0	10.65	10.80		11.00	11.07	--	
Wg9 B5050_100	11.0	2.0	12.78	--		12.60	11.96	--	
Wg12 B5050_100B	16.0	1.0	13.45	--		13.20	12.96	--	
Wg14 B5050_100	16.0	2.0	--	--		13.60	13.31	--	
Wg5 B7550_100A	6.0	1.1	8.86	9.00		7.70	7.28	--	
Wg6 B7550_84A	6.0	2.0	10.00	10.00		8.20	7.56	--	
Wg8 B7550_100C	11.0	1.0	9.11	8.30		8.40	7.78	--	
Wg9 B7550_100D	11.0	2.0	8.70	8.60		8.60	7.31	--	
Wg12 B7550_100A	16.0	1.0	9.75	9.75		9.10	8.21	--	
Wg12 B7550_100B	16.0	1.0	9.65	9.65		--	8.19	--	
Wg14 B7550_100A	16.0	2.0	10.90	11.00		8.60	8.56	--	
Wg5 B10050_100A	6.0	1.1	--	--		4.30	3.94	--	
Wg6 B10050_100C	6.0	2.0	--	--		5.20	4.61	--	
Wg8 B10050_100A	11.0	1.0	--	--		5.10	4.13	--	
Wg9 B10050_100C	11.0	2.0	--	--		4.80	4.10	--	
Wg12 B10050_100A	16.0	1.0	--	--		6.20	4.73	--	
Wg14 B10050_100A	16.0	2.0	--	--		6.40	4.92	--	
Wg5 B10050_100A	6.0	1.1	5.03	5.00		--	3.32	3.50	
Wg6 B10050_100C	6.0	2.0	5.83	5.85		--	3.94	--	
Wg8 B10050_100A	11.0	1.0	4.14	4.05		--	2.92	2.85	
Wg9 B10050_100C	11.0	2.0	4.45	4.45		--	3.23	3.35	
Wg12 B10050_100A	16.0	1.0	--	5.40		--	3.80	3.80	
Wg14 B10050_100A	16.0	2.0	6.07	6.10		--	4.16	--	
Wg5 B200100_100D	6.0	1.1	--	--		3.80	2.57/3.6	--	
Wg6 B200100_100B	6.0	2.0	--	--		4.30	4.52	--	
Wg8 B200100_100A	11.0	1.0	--	--	7.81	6.50	6.01	--	5.88
Wg9 B200100_100C	11.0	2.0	--	--		6.80	6.20	--	
Wg12 B200100_100B	16.0	1.0	--	--		8.40	--	--	
Wg14 B200100_100D	16.0	2.0	--	--		8.60	--	--	
Wg5 B200100_100D	6.0	1.1	--	--		--	1.40	--	
Wg6 B200100_100B	6.0	2.0	--	--		--	1.10	--	
Wg8 B200100_100A	11.0	1.0	--	--	2.63	--	1.53	--	1.73
Wg9 B200100_100C	11.0	2.0	--	--		--	1.51	--	
Wg12 B200100_100B	16.0	1.0	--	--		--	1.98	--	

Table 7.5 continued

Wg14 B200100_100D	16.0	2.0	--	--		--	2.05	--	
Wg5 B200100_100D	6.0	1.1	1.19	1.18		--	0.70	0.67	
Wg6 B200100_100B	6.0	2.0	1.39	1.38		--	0.80	0.82	
Wg8 B200100_100A	11.0	1.0	1.86	1.85	1.83	--	1.10	1.11	1.16
Wg9 B200100_100C	11.0	2.0	1.84	1.83		--	1.10	1.12	
Wg12 B200100_100B	16.0	1.0	2.49	2.50		--	1.98	1.63	
Wg14 B200100_100D	16.0	2.0	2.44	2.45		--	2.05	1.60	

In air, frequencies were obtained using the impedance analyzer and from measurement of the persistent oscillations remaining in the structure when the device was connected in a pulse-echo configuration (transmit and receive on the same element; discussed in detail in section §7.3). Under water loading, the persistent resonant oscillation measured using a pulse-echo configuration as well as acoustic transmit and receive frequencies are provided. Optical vibrometry measurements using the Polytec vibrometry system are shown for both loading conditions when available.

The impedance analyzer and resonant oscillation frequencies are in excellent agreement in air. Under water loading, the resonant oscillation frequency decreases as expected. The optical vibrometry frequencies are also in excellent agreement to the resonant oscillation frequency under both air and water loading. The acoustic transmit and receive frequencies in water are typically higher than the resonant oscillation frequency, with transmit being slightly higher than receive.

Recalling the different mode shapes observed using optical vibrometry (§5.3.2) and comparing to the measured frequencies of vibration, the 75µm devices operate in a fundamental 1-1 resonance mode while the 200µm device operated in a number of different modes shapes – 1-1, confined 1-1* (bounded by PZT or metal electrode layer),

mixed 2-1/1-2, 1-3, and 3-1 modes. Unfortunately, additional measurements with the optical vibrometer were unavailable.

The pMUT structures investigated here are believed to lie within a range where the relative thickness of the plate (thickness vs. lateral dimensions) plays an important role. The devices <75μm per side length are thick compared to the span and support primarily a fundamental 1-1 mode or confined fundamental mode. The larger devices begin to support additional higher-order modes as evidenced by the performance of the 100μm and 200μm devices measured using optical vibrometry and acoustic receive experiments.

The impedance analyzer measurements in air and the resonant oscillations measured in a pulse-echo configuration give the best indication of fundamental resonant free vibration behavior. Higher-order mode operation is best observed using optical vibrometry when available and acoustic receive measurements as an alternative. Multiple modes are observable using the acoustic receive experiments in the water tank which can highlight higher-order vibration as well as fundamental mode operation which is in good agreement with results from the other methods.

The measured frequencies from acoustic transmit and receive are typically higher than the resonant frequencies because the characterization of optimal acoustic frequencies includes consideration of the pulse-shape and bandwidth. Acoustic transmit, receive, and pulse-echo frequencies were evaluated on the basis of optimal imaging characteristics. Often, the resonant frequency is narrow-band with long pulse duration. In many cases the peak-to-peak amplitude is also smaller than when driven off-resonance. These characteristics of resonant vibration are non-ideal for imaging and the measured optimal

frequencies in transmit, receive, and pulse-echo are thus higher than the resonant frequency.

Acoustic transmit frequencies, in particular are typically higher still than the acoustic receive, resonant oscillation, and vibrometry frequencies. Acoustic transmission from the pMUT is a forced vibration which is dependent not only on the plate characteristics, but the forcing function as well. In this case the forcing function is the high-voltage excitation of the PZT layer which covers only a part of plate and, is itself, active only under the top signal electrode. Either the physical boundaries presented by the PZT film layer or the active electroded PZT yield smaller effective plate dimensions under acoustic transmission.

The subsequent analysis of pMUT vibrational frequencies will focus on the frequencies identified by the impedance analyzer, optical vibrometry, and resonant oscillations in pulse-echo mode as the fundamental free vibrational resonant frequency, f_{res}. Mindlin plate theory will be applied to model the frequency data based on the etch dimensions, thicknesses, and other plate properties. Acoustic transmit and other frequencies identified as the confined 1-1* mode will be investigated using alternative structural dimensions of the plate, such as the PZT film or electrode dimensions. The effect of compliant support in the boundary conditions will be treated as an augmentation of the frequency parameter in the frequency theory. Frequency change associated with water loading will be addressed as a frequency ratio coefficient as prescribed in the Methods (§6.4.2).

7.5 Mindlin Thick Plate Theory Applied to pMUT Free Resonant Vibration

7.5.1 Conventional CPT & Mindlin Plate Theories Applied to pMUT $f_{res,air}$

Comparison with the air-loaded resonant frequencies shows that conventional CPT and Mindlin theory are insufficient to fully describe the pMUT vibration. Figure 7.3 shows the comparison of measured Wg-series pMUT resonant frequencies to the CPT and Mindlin theories calculated for each wafer type using composite plates of the corresponding structure. The plots shown are plotted against the etched cavity length and use simply-supported or fully clamped edge conditions as labeled for the plate theory curves.

The measured resonant frequencies in Figure 7.3 are grouped closely by device size exhibiting little thickness dependence, contrary to what the CPT and Mindlin theory curves suggest. The theoretical curves show that the change in PZT thickness from 1μm to 2μm has a minimal effect on the theoretical frequency based on the groupings of curves with the same Si thickness.

Note that the frequency curves from Mindlin theory affect the devices with higher relative thickness more than the thinner devices. The position of the curves for Wg5/6 devices changes very little moving from CPT to Mindlin theory while the curves for Wg12/14, by contrast, are reduced more significantly. Also, this effect in the CCCC case is more prominent than in the SSSS case.

These curves show that the frequencies of the large, thin devices are moderately well-described by the conventional plate theories. However, the frequencies of the smaller devices are much lower than the conventional theories predict.

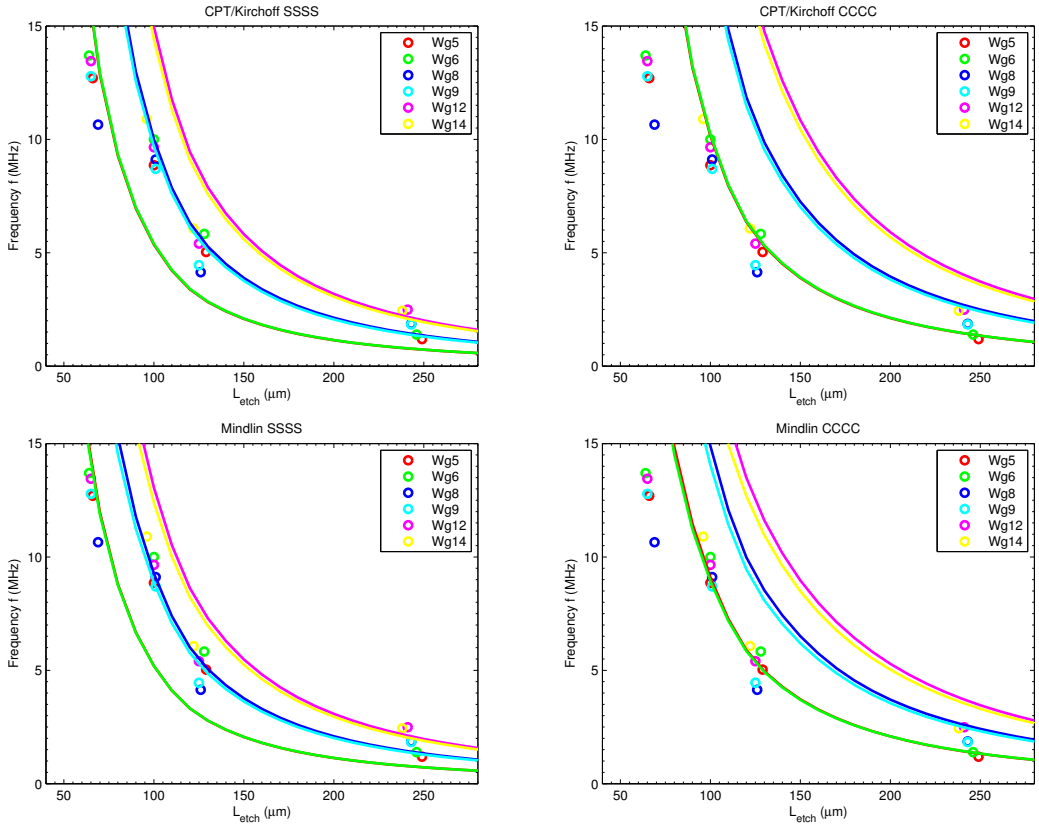

Figure 7.3: Measured pMUT resonant frequencies, $f_{res,air}$, compared to conventional plate theory frequencies calculated using devices of the same structure, plotted against device etched cavity length. CPT (top row) and Mindlin (bottom row) plate theories are considered with simply-supported (left column) and fully clamped (right column) edges. Theoretical curves are presented in the same color corresponding to the device type of the measured frequencies.

The Mindlin theory with CCCC boundary conditions describes the thinner Wg5/6 devices moderately well. However, as the relative thickness increases, the SSSS case appears to better describe the frequencies for the Wg8, 9, 12, and 14 devices as well as the 50μm Wg5/6 devices. This trend demonstrates that a spectrum of boundary

conditions is likely in play with pMUT vibration and is dependent on the relative thickness of the plate.

7.5.2 Generalized Analytical Method using pMUT $f_{res,air}$

The impedance analyzer frequencies were used as the resonant free vibration, $f_{res,air}$. When unavailable, the pulse-echo oscillation frequency in air was used as the two frequencies are in excellent agreement. For the analysis of the impedance analyzer frequencies, all devices are expected to operate in a fundamental mode.

Plotting the thickness-normalized frequency (f/t) vs. etch length (Fig. 7.4a), the frequencies of small devices (L<150μm) are grouped by Si thickness. Under CPT, the thickness-normalized frequencies should lie on top of each other. The grouping by thickness suggests additional factors that cause a decrease in frequency as relative thickness increases. If Mindlin-type effects (transverse shear deformation and rotational inertia) can be attributed to the thickness-dependent frequency decrease, the effects can be factored out using the proportionality of frequency parameters, λ^2, between CPT and Mindlin theory. The ratio of frequency parameters from Mindlin theory and CPT ($\lambda^2_{CPT}/\lambda^2_{Mindlin}$) shown in Fig. 7.4b is used as the compensation factor and is applied to the thickness-normalized frequency to produce the Mindlin-compensated frequencies shown in Fig. 7.4c. Values of λ^2 used here were calculated for fully-clamped (CCCC) conditions with the dimensions of the associated 5x5 pMUT devices.

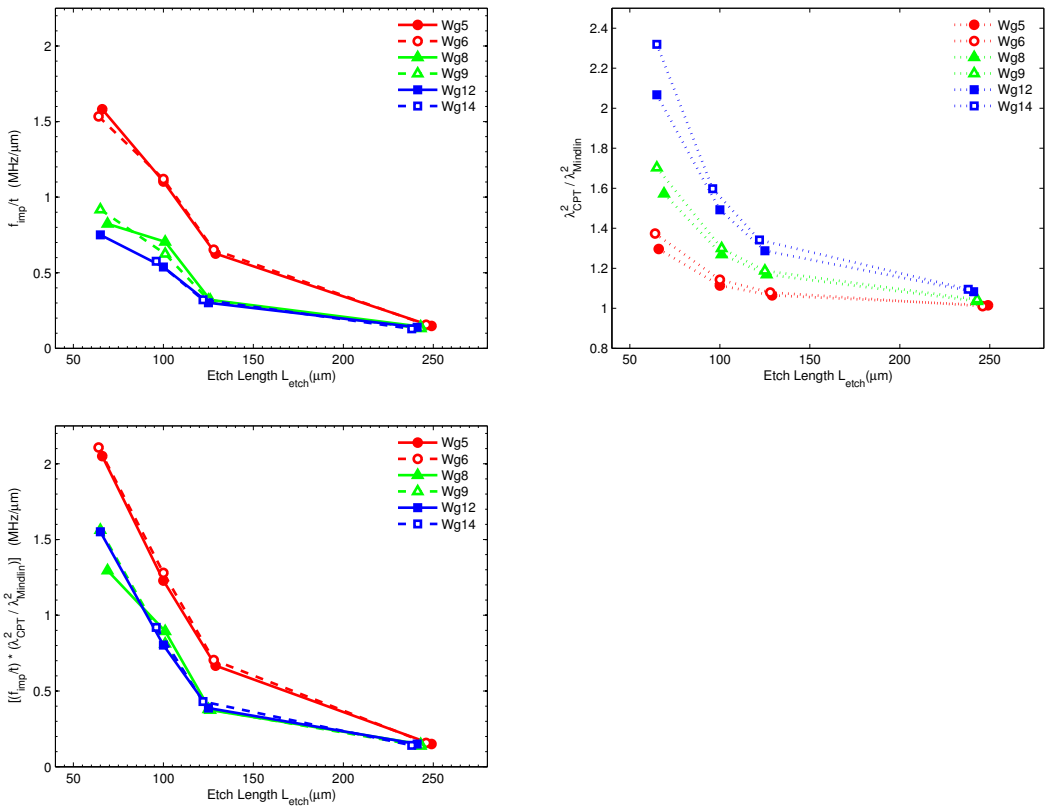

Figure 7.4: Mindlin-compensation of the resonant free vibration under air loading for 5x5 pMUT array devices. (top left, a) Uncompensated thickness-normalized frequency vs. etched length. (top right, b) Ratio of CPT to Mindlin λ^2 applied as Mindlin-compensation factors (bottom left, c) Mindlin-compensated thickness-normalized frequency vs. etched length.

The group separation by Si thickness is now diminished (as expected for CPT thin plates) and allows us to continue with a CPT-based analysis having extracted the relative thickness-dependent Mindlin effects. A CPT-based approach moving forward allows for a more straightforward comparison of effective λ^2 at a later point in the analysis.

Plotting the Mindlin-compensated thickness-normalized frequencies against $1/L^2$ as shown in Figure 7.5a, a roughly linear relationship exists between the two functions. Linear fits to the data can be made as shown in the figure with the intercept forced through the origin (describing the infinitesimal frequency of vibration for an infinitely

large plate). The linear fit is expressed in the form $y=mx+b=mx$ where y describes the thickness-normalized Mindlin-compensated frequency ($(f/t) * (\lambda^2_{CPT}/\lambda^2_{Mindlin})$) and x describes $1/L^2$. The intercept b, being forced through the origin, is 0 and the slope is given by constant m.

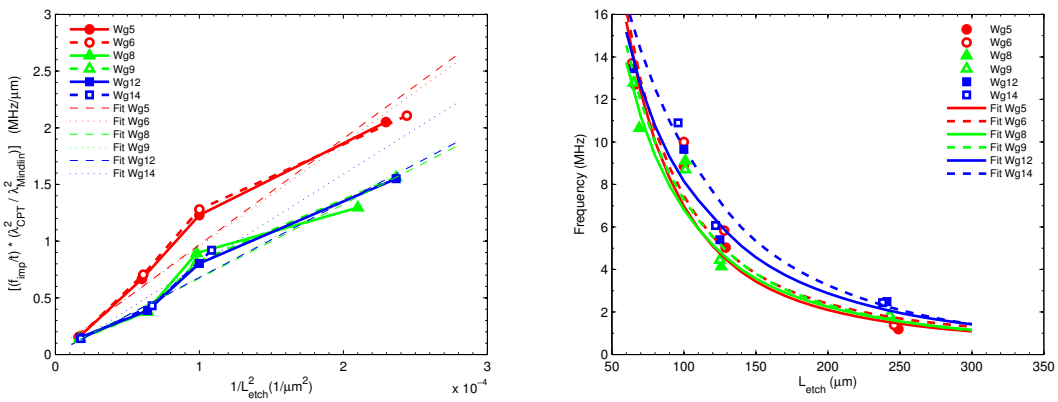

Figure 7.5: Curve-fitting to the Mindlin-compensated resonant free vibration frequencies under air loading for 5x5 pMUT array devices. (left, a) Mindlin-compensated thickness-normalized frequency vs $1/L_{etch}^2$ with linear fits to each device structure. (right, b) Linear fits from (a) rearranged to form theoretical curves in f vs. L plot with measured resonant frequencies included for comparison.

Recalling the general plate theory frequency equation,

$$\omega = \frac{\lambda_{mn}^2}{W^2}\sqrt{\frac{D}{\rho t}} = \frac{\lambda_{mn}^{*2}}{L^2}\sqrt{\frac{D}{\rho t}} = \frac{\lambda_{mn}^{*2}\, t}{L^2}\sqrt{\frac{E}{12\rho(1-\nu^2)}} \tag{7.1}$$

where $\lambda^{*2} = \lambda^2\phi^2$, $\phi = L/W$, λ^2 in CPT is dependent only on the aspect ratio $\phi=b/a$ and constant for all thicknesses while the quantity under the square root is a function of the plate material properties calculated from the thickness-fractions of the constitutive layers. The term under the square root, therefore, remains constant for a given pMUT laminate structure where the layer thicknesses are held the same. The slope m is thus equal to

$$m = \frac{\lambda_{CPT}^{*2}}{2\pi}\sqrt{\frac{E}{12(1-\nu^2)\rho}} \tag{7.2}$$

for devices of any length for each thickness structure. Slope values for the theoretical linear fits are given in Table 7.6.

Table 7.6: Theoretical fit values for Wg 5x5 pMUT fundamental resonant free vibration frequencies in air.

Device	t_{Si} (um)	t_{PZT} (um)	t_{dev} (um)	Linear Fit Slope, *m*
Wg5	6.0	1.1	8.0	9349
Wg6	6.0	2.0	8.9	9080
Wg8	11.0	1.0	13.0	6518
Wg9	11.0	2.0	13.9	6738
Wg12	16.0	1.0	18.0	6674
Wg14	16.0	2.0	18.9	7979

From these values and the measured pMUT thickness, the relationship between vibrational frequency and lateral dimensions can be described by plotting the frequency curves shown in Figure 7.5b.

The generalized model is shown to be in excellent agreement with the measured resonant frequencies, demonstrating that the $f \propto t/L^2$ relationship in plate theory holds true if appropriate values for *m* can be found. All points along these theoretical frequency curves assume constant λ^2_{CPT}, E, ρ, and v. Constant λ^2_{CPT} necessitates the same mode shape (fundamental 1-1 in Figure 7.5) and constant aspect ratios $\phi = b/a$. Note that the aspect ratio among the measured pMUT devices changes between different device sizes which would contribute to some error between the measured frequencies and the theoretical frequency curves.

Further analysis will proceed through two approaches. The two primary variables where uncertainty exists are E_{PZT} (and thus E_{comp}) and the boundary conditions described by λ^2. The first approach will hold the frequency parameters at idealized clamped or simply-supported values for each slope *m*. Values for an E_{comp} can be calculated and

compared to the theoretical layer-wise theories using a range of values for E_{PZT}. If the back-calculated E_{PZT} fit within a realistic range for PZT, the pMUT frequency theory can incorporate the new E_{PZT} value and utilize idealized boundary conditions. The E_{comp} should be constant-valued, independent of device lateral dimensions.

The second approach will hold E_{PZT} at a fixed value, solving for effective λ^2, with deviations from the idealized conditions attributed to compliant support. However, the effective λ^2 are expected to be a function of relative thickness and backing out of the generalized model with linear fitting will allow a more flexible analysis. Measured pMUT frequencies will be modeled using the full plate frequency equation rather than the slope m, solving for effective λ^2 using measured frequencies and plate dimensions and material properties.

7.5.3 Calculation of E_{comp} using Idealized Boundary Conditions

Values of E_{comp} will be calculated from the constant slope m from the previous section for each device thickness structure holding λ^2 at idealized clamped and simply-supported values. If E_{comp} is found to be constant-valued among all devices and compares favorably with values from layer-wise methods using realistic E_{PZT} values, the derived E_{comp} can be used in the subsequent development of pMUT frequency theory with idealized λ^2s.

Values of λ^2 and λ^{*2} for CPT are calculated for the 5x5 pMUT arrays using the etch dimensions. CPT values are used because the Mindlin effects have already been factored out using the λ^2 ratios. Aspect ratios, ϕ, vary less than 5% among pMUT wafers of the same size grouping. However, between different device size groups, the aspect ratio

varies by up to 69%, leading to significant difference between the frequency parameters of different sized devices. Devices with the same aspect ratio have constant-valued frequency parameters in CPT regardless of plate thickness.

Using the fitted slope, m, from the previous section along with the calculated λ^{*2}_{CPT} and composite density of the plate, an effective Young's modulus can be found by

$$E_{comp} = 12\rho_{comp}\left(1-\nu^2\right)\left(\frac{2\pi m}{\lambda^{*2}_{CPT}}\right)^2 \tag{7.3}$$

The composite densities used were calculated using the etch dimensions for all layers and the material properties provided in §7.2.2. Calculated values for the composite moduli from the linear fitting method are shown in Table 7.7.

Table 7.7: Calculated composite Young's moduli from curve-fitting method.

E_{comp}	50's	75's	100's	200's
Wg5	32.78	54.14	67.89	71.03
Wg6	33.88	52.77	70.51	78.21
Wg8	14.18	19.91	25.36	29.62
Wg9	18.59	23.05	31.01	35.27
Wg12	11.78	18.58	24.54	27.81
Wg14	16.57	28.23	34.51	41.59

A near-constant E_{comp} is expected for devices with the same layer-thickness structure, with minor variations associated with the incomplete coverage of the device cavity area by the PZT and metal layers above the device Si. Variation in the calculated E_{comp} from the curve-fitting method shown above for devices of the same thickness structure exhibit up to 60% decrease between 200μm and 50μm devices, much larger variation than expected from layer-wise calculated moduli.

The calculated composite moduli from the linear fitting method are up to 88% lower than those calculated from the layer-wise theories (Table 7.2) which range from 82-

116GPa. Note that for similarly-sized devices, the E_{comp} from the curve-fitting method decreases as the thickness increases, counter to the expected trend for increasing Si thickness and composition percentage. The Young's modulus for Si is 125GPa compared to the moduli in the range 10-86GPa for PZT films. As the PZT thickness is held at 1-2μm while the Si thickness is increased, the composite modulus should approach the higher Si modulus value.

The large variation in the E_{comp} calculated from the linear-fit method as well as values that fall well below those calculated using layer-wise theory are outside of the possible physical parameters of the constitutive material properties. While some variability and error is expected in the Young's modulus for PZT films resulting in a range of possible values for the composite modulus, there is very little physical relevance to the E_{comp} values derived through this method.

Comparing the measured fundamental resonant frequencies to the fitted theoretical frequency curves, the error falls within a maximum of 29%, with average error under 12%. The largest error values occur for the 75μm devices, while the 50μm and 200μm devices appear to be well described by the curve-fitting method.

The large errors between the measured and calculated frequencies for some devices combined with computed E_{comp} that are inconsistent with the possible physical material properties indicate that the linear fitting method using idealized λ^2 does not provide a complete description of pMUT vibration.

7.5.4 Calculation of λ^2 from Resonant Frequencies

Modification of the plate theory models to include compliant support will necessitate its introduction through the frequency parameter λ^2. From Equation 6.1, the frequency parameter can be calculated if the frequency of vibration, plate dimensions, thickness, Young's modulus, density, and Poisson's ratio are known. As the measured resonant frequencies are lower than those from clamped and simply-supported CPT and Mindlin plate theories, the effective frequency parameters will be lower than those prescribed for these ideal boundary conditions by. The degree to which the effective frequency parameters differ from idealized BCs in the conventional plate theories will be assessed here and will be shown in the following section to correlate to the effect of compliant support.

As previously discussed, the true dimensions of vibration have not been conclusively determined, though optical vibrometry has shown displacement of the device surface beyond the dimensions of the etched cavity. However, optical measurement of the enlarged dimensions was performed only on one device, and the dimensional trends observed for this device may not hold for all other devices. For this reason, the plate dimensions used in the following calculation and analysis of effective frequency parameters will be the etched cavity dimensions.

Similarly, because the Young's modulus of the PZT film has not been conclusively determined, a value of 10GPa, taken from the literature for similar PZT films, will be used in the subsequent calculations of the composite Young's modulus by Pister & Dong's method (see Background). Errors introduced from this assumption for E_{PZT} will affect all device models similarly.

Taking the fundamental resonance frequency in air measured by the impedance analyzer, the etched cavity width, total device thickness, and composite density and Young's modulus calculated from the layer-wise method, the effective frequency parameters λ^2_{eff} were determined for all Wg 5x5 pMUT devices using

$$\lambda^2_{eff} = 2\pi f W^2 \sqrt{\frac{\rho h}{D}} \tag{7.4}$$

Figure 7.6 shows the effective frequency parameters as a function of the non-dimensional *L/t*. The 5x5 pMUT array devices are separated in each plot by device size because the large changes in aspect ratio over the range of device sizes proved to be problematic in plotting the theoretical frequency parameters from CPT and Mindlin theory. Recalling from their defining equations in both conventional plate theories, the frequency parameters are a function of aspect ratios and thickness ratios, and not absolute dimensions. Frequency parameters are also independent of Young's modulus and other absolute plate properties. The aspect ratios used to calculate theoretical frequency parameters for each subplot were the mean values, held fixed, for each size class. Mean aspect ratios for Wg-series 50's, 75's, 100's, and 200's are 1.64, 1.44, 1.32, and 1.26, respectively.

These plots give an indication of the boundary conditions for each device group. The effective frequency parameters are expected to fall below the clamped Mindlin theory curve. The smaller, thicker devices tend to fall further below the theoretical CCCC Mindlin curve than the thinner devices, close to or even lower than the SSSS curve. Larger deviation from CCCC Mindlin theory indicates looser boundary constraints. For example, the 50μm devices all fall below both the CCCC and SSSS curves while the

200µm devices fall between them. This indicates that the larger devices tend to behave more like conventional clamped plates than do their smaller counterparts with much larger relative thickness.

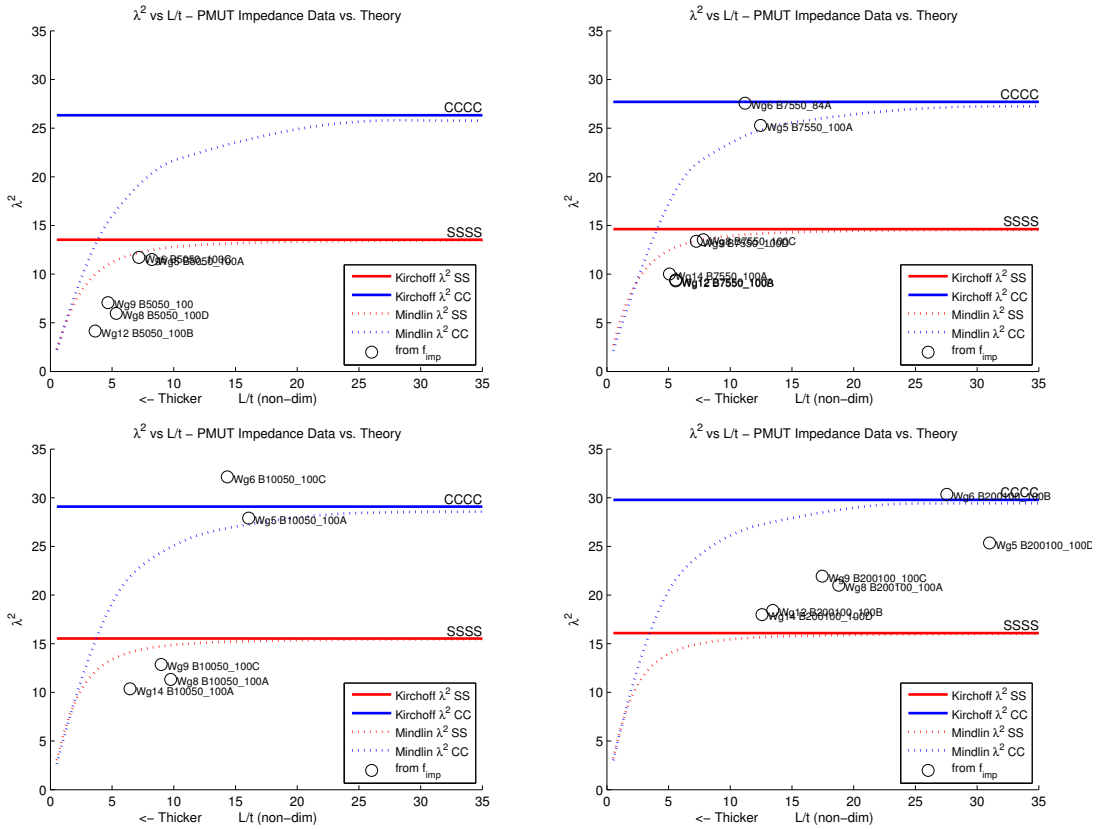

Figure 7.6: Fundamental mode λ^2 vs. *L/t* for Wg-series 5x5 pMUTs grouped by device size. (top left, a) 50's, (top right, b) 75's, (bottom left, c) 100's, (bottom right, d) 200's. λ^2 calculated from the measured resonant frequencies of pMUT devices (circles) are plotted against CPT (solid) and Mindlin (dotted) theories with CCCC (blue) and SSSS (red) boundary conditions.

Similarly, the effective frequency parameters can be plotted against theory grouped by their thickness structure. Figure 7.8 shows the effective frequency parameters calculated from the measured fundamental resonant frequencies of the Wg-series 5x5 pMUTs with the corresponding theoretical CPT and Mindlin frequency parameters for CCCC and SSSS conditions. Because the groupings now encompass devices over a

range of lateral dimensions and thus varying aspect ratios, the theoretical curves take into account the increasing ϕ as device size decreases. Interpolation on the Wg-series pMUT device sizes was used to determine the aspect ratios over the theoretical range, as shown in Figure 7.7.

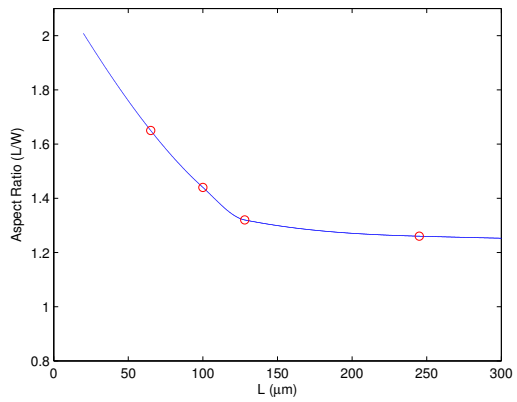

Figure 7.7: Interpolation of the aspect ratios of Wg-series devices (red) for use in theoretical calculations.

The resulting decrease in the theoretical λ^2 for smaller L is most apparent in the CPT curves which for fixed ϕ are typically constant.

Figure 7.8 shows trends similar to Figure 7.6. Thinner devices tend to have λ^2_{eff} closer to the CCCC theory than thicker devices (compare Wg5/6 to Wg12/14). Also, within each plot, where the device thicknesses are the same, the smaller devices tend to fall at or below the SSSS curve rather than between the CCCC and SSSS curves as the larger devices do.

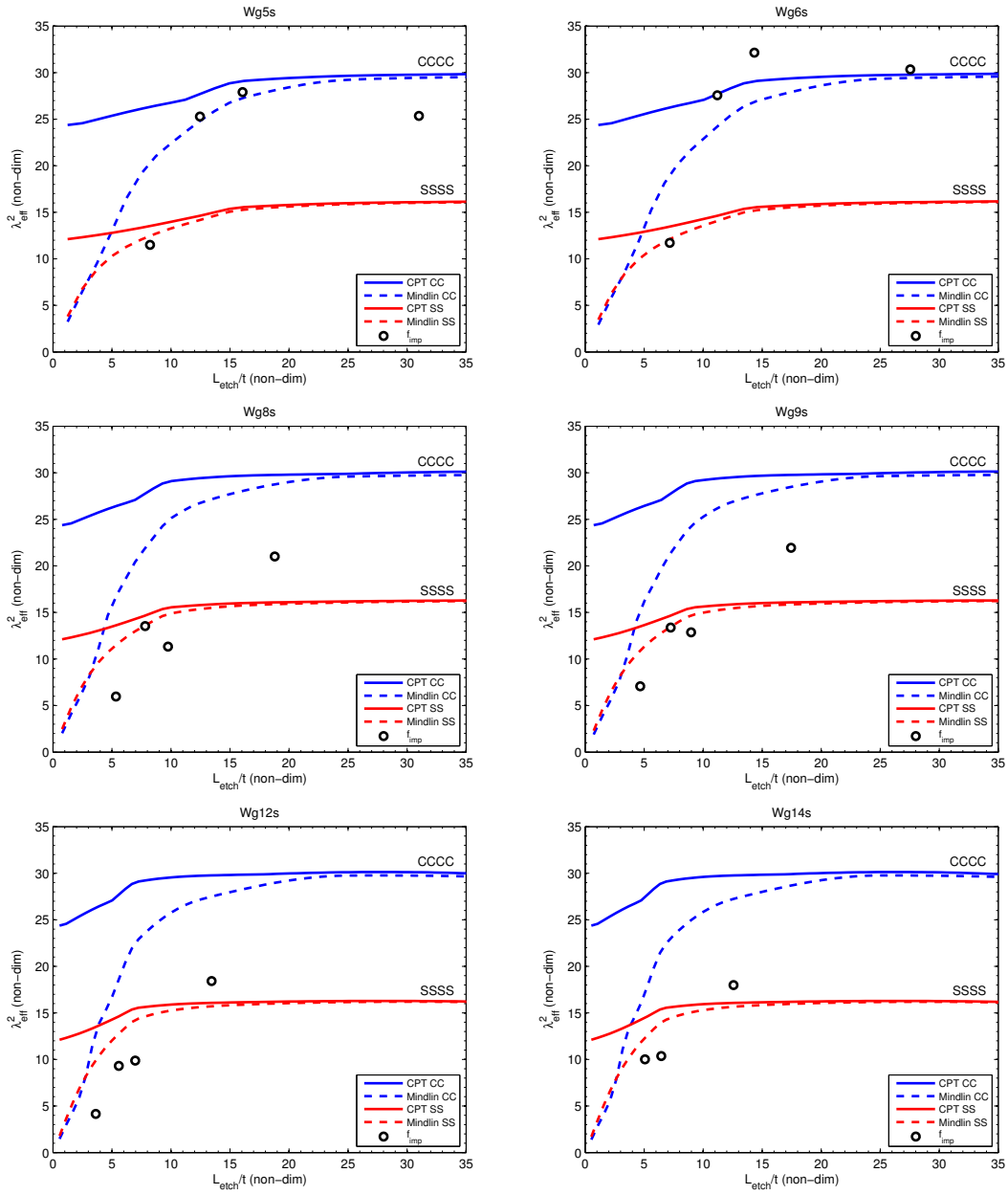

Figure 7.8: Fundamental mode λ^2 vs. *L/t* for Wg-series 5x5 pMUTs. λ^2 calculated from the measured resonant frequencies of pMUT devices (circles) are plotted against CPT (solid) and Mindlin (dotted) theories with CCCC (blue) and SSSS (red) boundary conditions. Plate theory λ^2's include interpolation based on variable pMUT *L/W* aspect ratios. Device structures for each subplot are as labeled.

To show how the effective frequency parameters for all devices compare in relation to each other, the λ^2_{eff} for all Wg-series and A-series pMUT arrays are plotted together in

Figure 7.9. CPT and Mindlin comparison curves for CCCC and SSSS conditions are provided, calculated using the properties of the thickest Wg14 device structure.

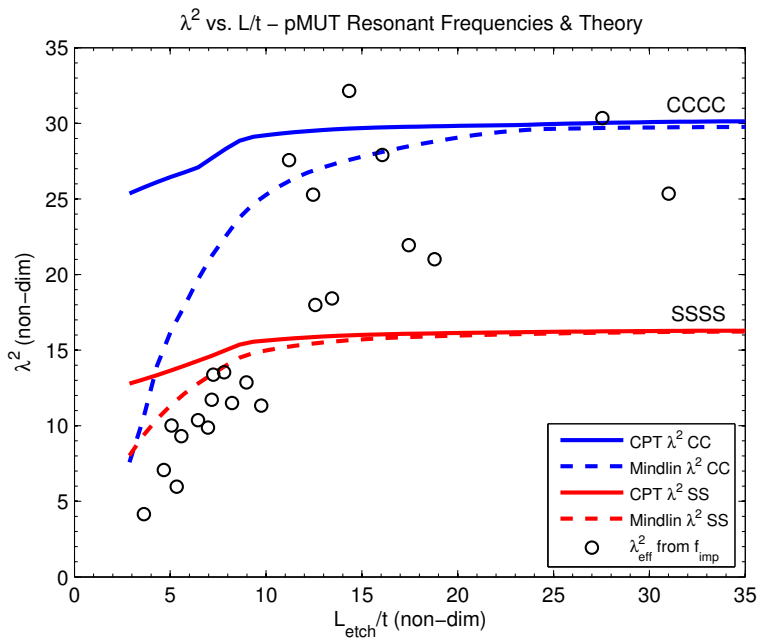

Figure 7.9: λ^2 vs. *L/t* for Wg-series 5x5 and A-series 14x14 pMUTs. λ^2 calculated from the measured resonant frequencies of pMUT devices (circles) are plotted against CPT (solid) and Mindlin (dotted) theories with CCCC (blue) and SSSS (red) boundary conditions. Plate theory λ^2's shown are calculated using Wg14 thickness and include interpolation based on variable pMUT *L/W* aspect ratios.

A quantitative description of the trend for λ^2_{eff} seen in Figure 7.9 would help to model the discrepancy from idealized clamped Mindlin theory and used for predictive pMUT frequency design.

Figures 7.6,7.8, and 7.9 show that the effective frequency parameter of small devices with large relative thickness fall below both the CCCC and SSSS Mindlin theories. As the relative thickness (*t/L*) decreases, the effective frequency parameter increases, falling between the SSSS and CCCC conditions, approaching the fully clamped condition as the relative thickness decreases. The degree by which the λ^2_{eff} deviate from the CCCC

Mindlin theory indicates a relaxation of the boundary constraints from the fully clamped condition. Optical vibrometry showed surface displacement over larger dimensions than the etched cavity which could be a result of looser boundary conditions. The relaxation of boundary conditions is likely the result of elastic or compliant edge support due to the uniform Si substrate that extends beyond the cavity dimensions across the surface of the device.

7.5.5 Compliant Support in pMUT Vibration

The deviation from theory observed in the effective frequency parameters calculated from the resonant frequencies of pMUTs in air is likely the result of compliant edge support due to the elasticity of the Si substrate layer which extends throughout the entirety of the pMUT array, beyond the etched cavity dimensions. While the compliance of Si is quite low, the dimensions of the pMUT devices likely play a role in increasing the effect of the material compliance at the boundaries of the plate.

As described in the Analytical Methods (§6.4.3), a fixed cantilever beam with compliant support experiences a decrease in the frequency of vibration from a rigidly supported beam by a degree linearly proportional to the thickness:length ratio. As the relative thickness increases, the frequency is expected to decrease as a result of the additional deformation of the structure caused by material compliance and shear/rotational forces at the edge. While similar forces are accounted for within the body of the plate in Mindlin theory, the use of idealized clamped and simply-supported boundary conditions does not include their effects at the edges. The material deformation due to the compliance of the boundary material result in a similar frequency decrease as

the relative thickness increases. While this decrease in frequency with thickness-span ratio may not necessarily remain linear for elastically restrained plates, some quantifiable decrease is expected.

Following the work of Xiang et al. [52], Gorman [68], and Zhou [69], the frequency decrease associated with elastic or compliant support is assessed through the frequency parameters. Taking the ratio of the effective frequency parameters from the measured pMUT resonant frequencies to the theoretical Mindlin CCCC frequency parameters for the same plate structure, we obtain a quantification of the frequency deviation from a rigidly supported plate due to compliance. Plotting this λ^2 ratio ($\lambda^2_{eff}/\lambda^2_{Mindlin,CCCC}$) against the relative thickness at the boundaries (t_{Si}/L_{etch}), we observe the expected frequency decrease due to support compliance with increased relative thickness, as shown in Figure 7.10.

Figure 7.10 shows that with the exception of the Wg5/6 75μm and 100μm devices, the λ^2 ratios follow a consistent decreasing trend with the thickness ratio. The decrease in λ^2 ratio with relative thickness is not purely linear, which is likely due to the mechanical confinement around the entirety of the plate (in contrast to a cantilever beam for which a linear relationship exists). The changing aspect ratios with etched length likely contribute to this nonlinearity and variance in the measured data as well.

Curves showing the relationship between Mindlin CCCC and other theoretical frequency parameters are provided as a reference. A constant value of 1 is provided to show where frequency parameters for a rigidly clamped Mindlin plate would lie. The dashed curve beginning at 1.0 and increasing above the Mindlin CCCC line shows how a rigidly clamped CPT/Kirchoff plate would behave with an increase in relative thickness.

The dotted curve beginning near 0.5 and increasing toward the Mindlin CCCC line shows how a simply-supported Mindlin plate would behave. Note that change in these curves do not indicate increase or decrease in the actual frequency parameters given by these theories, but that the ratio with respect to the rigidly clamped Mindlin plate changes.

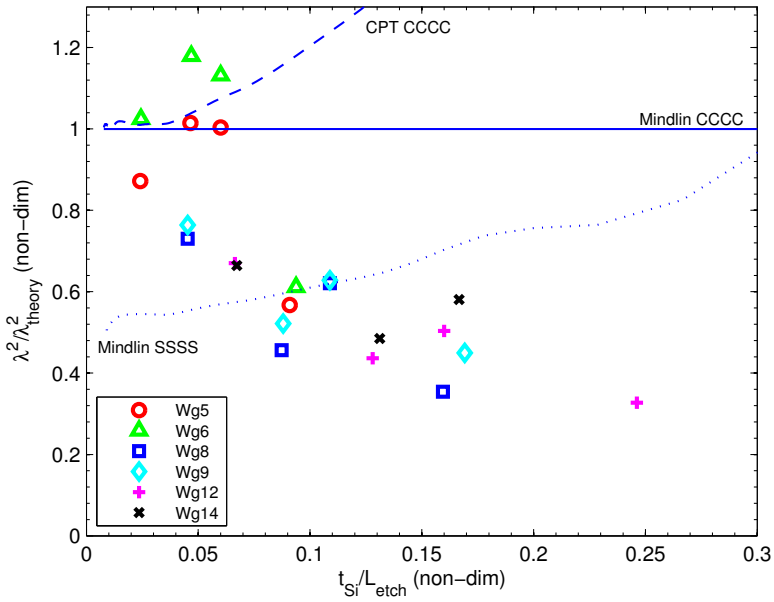

Figure 7.10: λ^2 ratio ($\lambda^2_{eff}/\lambda^2_{theory}$) vs. non-dimensional t/L for Wg-series 5x5 arrays. Effective frequency parameter calculated from measured resonant frequencies, theoretical frequency parameters determined from Mindlin theory for a CCCC plate. λ^2 ratio lines showing relationships between conventional plate theories and different boundary conditions are shown in blue. Ratios of CCCC Mindlin to CCCC Mindlin, SSSS Mindlin, and CCCC CPT/Kirchoff λ^2's are shown.

The position of the simply supported curve is provided because the SSSS condition carries some similarities to an elastically supported plate. Compared to a rigidly supported plate, the modal dimensions of the simply supported plate increase, similar to a plate on compliant support, yielding a decrease in the frequency of vibration as shown by the λ^2 ratio < 1.0.

To quantify the decreasing trend in λ^2 with relative thickness, the pMUT data was fit using polynomial regression curve-fitting tools. Linear and quadratic fits were taken on the data as a whole or in groups based on a structural aspect of device. Figure 7.11 shows four polynomial fits to the Wg-series pMUT data for $t_{Si}/L_{etch} < 0.25$. For three of these plots, the fit was forced through the point (0,1), as a thin plate is expected to closely follow the behavior of a rigidly supported plate described by conventional theory (Mindlin, in this case).

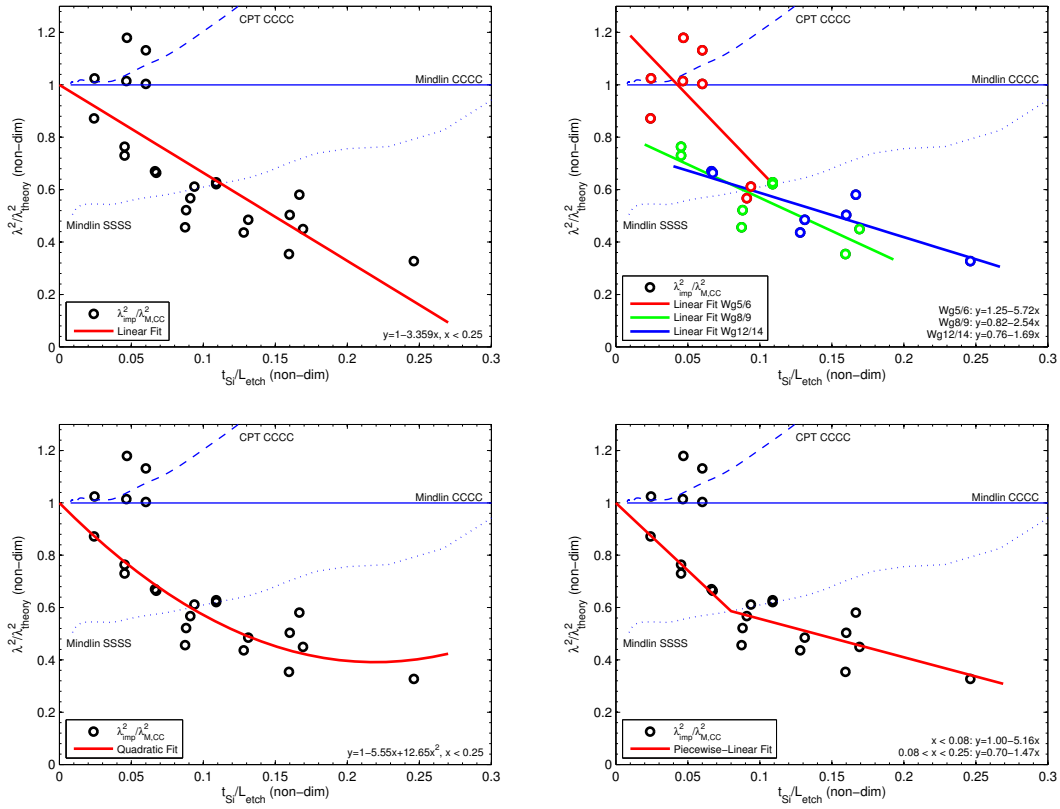

Figure 7.11: Fitting of λ^2 ratio ($\lambda^2_{eff}/\lambda^2_{theory}$) vs. non-dimensional t/L for Wg-series 5x5 arrays by four different methods. (top left) Linear fit, (top right) linear fit by device thickness groups, (bottom left) quadratic fit, (bottom right) piece-wise linear fit.

Because we have chosen to express the frequency decrease associated with compliant support through the frequency parameters, the fits to the λ^2 ratios can be treated as

models of the compliance, a function *C(t,L)* dependent on the Si thickness and device length.

The full-linear fit (upper left) takes a linear fit of the pMUT data as a whole. This linear fit was forced through the point (0,1). As the plot shows, the fit overestimates a large portion of the pMUT data. The linear fit takes the form

$$\frac{\lambda_{eff}^2}{\lambda_{M,CCCC}^2} = C(t,L) = 1 - 3.359\left(\frac{t_{Si}}{L_{etch}}\right) \quad \text{for } \frac{t_{Si}}{L_{etch}} < 0.25 \tag{7.5}$$

The quadratic fit (lower left) takes a quadratic fit of the pMUT data as a whole. This linear fit was forced through the point (0,1). This quadratic curve fits the data well. However, approaching *t/L*=0.25 the quadratic curve begins to turn back upwards with a positive slope which does match the behavior of the pMUT devices and is undesirable for use in a global analytical model. However, within the range 0<t/L<0.25 over which the quadratic fit is shown, the frequency-relative thickness relationship is well-modeled. The quadratic fit is given by

$$\frac{\lambda_{eff}^2}{\lambda_{M,CCCC}^2} = C(t,L) = 1 - 5.55\left(\frac{t_{Si}}{L_{etch}}\right) + 12.65\left(\frac{t_{Si}}{L_{etch}}\right)^2 \quad \text{for } \frac{t_{Si}}{L_{etch}} < 0.25 \tag{7.6}$$

The group-wise linear fit (upper right) takes the linear fit of the pMUT data in groups based on device structure, more specifically, by the Si thickness. This fitting method ignored the (1,0) constraint. Shown in different colors, the Wg5/6 (red), Wg8/9 (green), and Wg12/14 (blue) groupings fit each device group to a moderate degree. Again, the Wg5/6 75μm and 100μm devices deviate greatly from the general trend, causing the linear fit for this group to differ greatly from the other 2 devices groups. As a discontinuous fitting method, this fit is also not ideal for use in a global analytical

expression, but describes the effect of support compliance among different pMUT structures well. The group-wise linear fit is given by

$$\frac{\lambda_{eff}^2}{\lambda_{M,CCCC}^2} = C(t,L) = 1.245 - 5.716\left(\frac{t_{Si}}{L_{etch}}\right) \qquad \text{for } t_{Si}=5\mu\text{m}, \frac{t_{Si}}{L_{etch}} < 0.11$$

$$\frac{\lambda_{eff}^2}{\lambda_{M,CCCC}^2} = C(t,L) = 0.823 - 2.539\left(\frac{t_{Si}}{L_{etch}}\right) \qquad \text{for } t_{Si}=10\mu\text{m}, 0.02 < \frac{t_{Si}}{L_{etch}} < 0.20$$

$$\frac{\lambda_{eff}^2}{\lambda_{M,CCCC}^2} = C(t,L) = 0.757 - 1.691\left(\frac{t_{Si}}{L_{etch}}\right) \qquad \text{for } t_{Si}=15\mu\text{m}, 0.04 < \frac{t_{Si}}{L_{etch}} < 0.25$$

(7.7)

The piece-wise linear fit (bottom right) is a linear fit to the pMUT data in each of two domains, broken up at a specified point (t_{Si}/L_{etch}=0.08). This location was chosen at the point which would allow for the best fit to the pMUT data with larger relative thickness while maintaining an optimal fit to the data t/L<0.08. The linear fit of the first section was forced through the (0,1) constraint and continuity is maintained between the two sections. The piece-wise linear fit is given by

$$\frac{\lambda_{eff}^2}{\lambda_{M,CCCC}^2} = C(t,L) = 1 - 5.164\left(\frac{t_{Si}}{L_{etch}}\right) \qquad \text{for } \frac{t_{Si}}{L_{etch}} < 0.08$$

$$\frac{\lambda_{eff}^2}{\lambda_{M,CCCC}^2} = C(t,L) = 0.704 - 1.471\left(\frac{t_{Si}}{L_{etch}}\right) \qquad \text{for } 0.08 < \frac{t_{Si}}{L_{etch}} < 0.25 \qquad (7.8)$$

The coefficient of determination, R^2, gives an indication of the goodness of fit of a model, or how well the model approximates the real data points. Used with regression analysis, R^2 represents the proportion of variability in Y that may be attributed to some linear combination of the regressors in X. The R^2 typically falls in the range 0 to 1. An

R^2 value of 1 represents a perfect fit of the data while a value of 0 indicates a lack of correlation between the model and the data. The R^2 for each of the four compliance models is given in Table 7.8. R^2 values are also provided for the models recalculated without the Wg5/6 75 and 100μm devices.

Table 7.8: R^2 values calculated from λ^2 ratio residuals for different fit types (compliance models) for full pMUT data set and excluding Wg5/6, 75/100μm devices.

Fit Type	$R^2_{residuals}$	$R^2_{residuals}$ (w/o Wg5/6,75/100)
Linear	0.5924	0.3230
Quadratic	0.5523	0.7306
Piece-wise Linear	0.5363	0.7970
Group-wise Linear	0.7952	0.7498

The R^2 values provided in Table 7.8 show that while the group-wise linear model lacks global continuity between all device structures and does not model the expected behavior of thin plates (intercept at (0,1)), this model fits the observed data better than the other three models. However, recalling that the Wg5/6 75μm and 100μm devices behave much more like thin plates than those better described by Mindlin theory, we note that the observed values lie at or near the Mindlin and CPT CCCC condition and are not well-described by the compliance models. Creating a modified data set by excluding these devices from the fits and recalculating the R^2 for each model reveals that the quadratic and piece-wise linear models better describe the modified data set, joining the group-wise linear model with R^2 in the 0.73-0.80 range. The linear fit model remains a moderately poor fit to the observed data, with the R^2 decreasing with the modified data set.

While none of the compliance models perfectly describe the observed data, the remaining variance in the observed values may be the result of some of the factors previously described, including inaccuracies in the measurement of the etched

dimensions and an unknown Young's modulus of PZT. Future development and application of these compliance models will greatly benefit from a more detailed investigation into these factors.

7.5.6 Modified Mindlin Plate Theory with Compliant Support for pMUT Vibrational Frequencies

The compliance models discussed in the previous section may now be applied as a modification of the Mindlin plate frequency equation. As mentioned previously, the compliance will be introduced through an effective pMUT frequency parameter, λ^2_{pmut}, that is the product of the compliance model and the Mindlin CCCC frequency parameter such that

$$\lambda^2_{pmut} = C_{compliance}(t, L) \cdot \lambda^2_{M,CCCC} \tag{7.9}$$

The modified frequency equation for resonant vibration of pMUTs in air is then given as

$$f^t_{res,air} = \frac{1}{2\pi} \frac{\lambda^2_{pmut}}{W^2} \sqrt{\frac{D}{\rho h}} = C_{compliance}(t, L) * f^t_{Mindlin,CCCC} \tag{7.10}$$

Figure 7.12 shows the effective pMUT frequency parameter curves vs. *L/t* for the Wg-series devices, developed using the fit models described previously. The conventional Mindlin CCCC frequency parameter curves are also provided for reference.

The plotted λ^2_{pmut} show that inclusion of the *C(t,L)* compliance term provides a more accurate fit of the observed data than the Mindlin theory predicts, with the exception of the Wg5 75 and 100µm and Wg6 75, 100, and 200µm devices. From this standpoint, the quadratic and piece-wise linear fits model the observed data better than the other two fits.

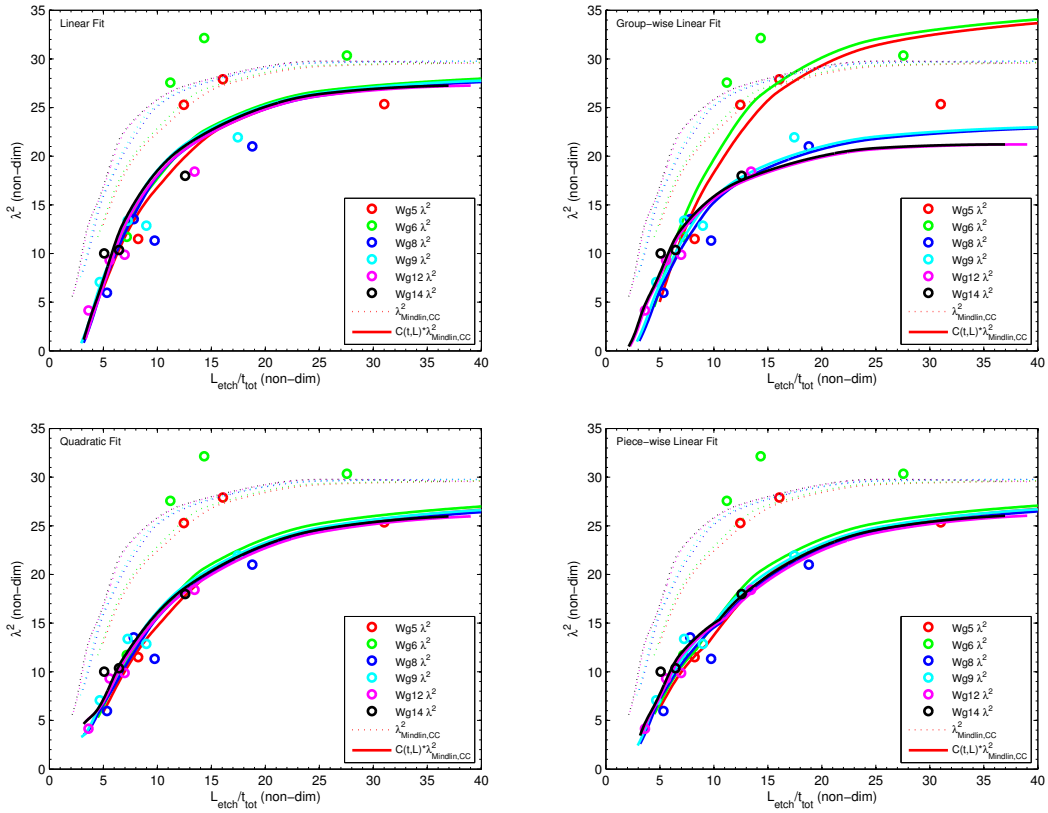

Figure 7.12: Modeled effective pMUT frequency parameter (λ^2_{pmut}) curves (solid) and observed pMUT data vs *L/t* for Wg-series devices. Mindlin CCCC $\lambda^2_{M,CCCC}$ curves are provided for comparison (dotted lines). Curve colors correspond to devices with similarly colored observed data points. (top left) Linear fit, (top right) group-wise linear fit, (bottom left) quadratic fit, (bottom right) piece-wise linear fit.

Evaluating the R^2 (Table 7.9) for the effective pMUT frequency parameters, we find that the compliance-modified frequency parameters fit the observed data better than the λ^2 ratios (Table 7.8). Excluding the observed values from the devices with small relative thickness, the R^2 values increase into the 0.92-0.94 range for the quadratic and piece-wise linear models.

Table 7.9: R^2 values of modified Mindlin frequency parameters with compliant support for pMUTs using four different fit models for compliance. Calculated for full pMUT data set and excluding Wg5/6, 75/100µm devices.

Compliance Fit Model	$R^2_{\lambda 2,eff}$	$R^2_{\lambda 2,eff}$ (w/o Wg5/6,75/100)
Linear	0.7792	0.7685
Quadratic	0.7447	0.9256
Piece-wise Linear	0.7329	0.9451
Group-wise Linear	0.8868	0.8240

Using the effective pMUT frequency parameters, the frequency equation (Eq. 7.10) for pMUTs based on a modified Mindlin plate theory with compliant support can be plotted against device etch length as shown in Figure 7.13.

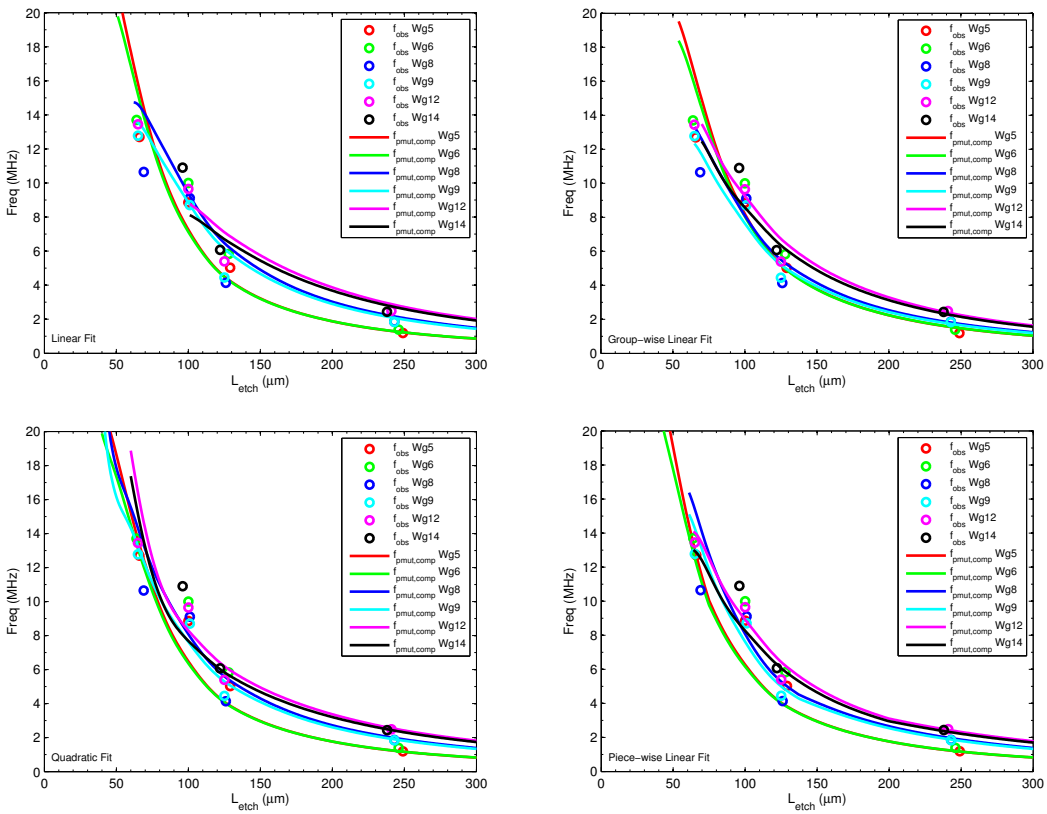

Figure 7.13: Frequency curves vs. etched length for theoretical Mindlin plates with compliant support modeled after Wg-series devices. Observed resonant frequency values included to show fit. (top left) Linear fit, (top right) group-wise linear fit, (bottom left) quadratic fit, (bottom right) piece-wise linear fit.

To show the theoretical frequency curves more clearly, the frequency can be plotted against L_{etch}/t_{Si} as shown in Figure 7.14.

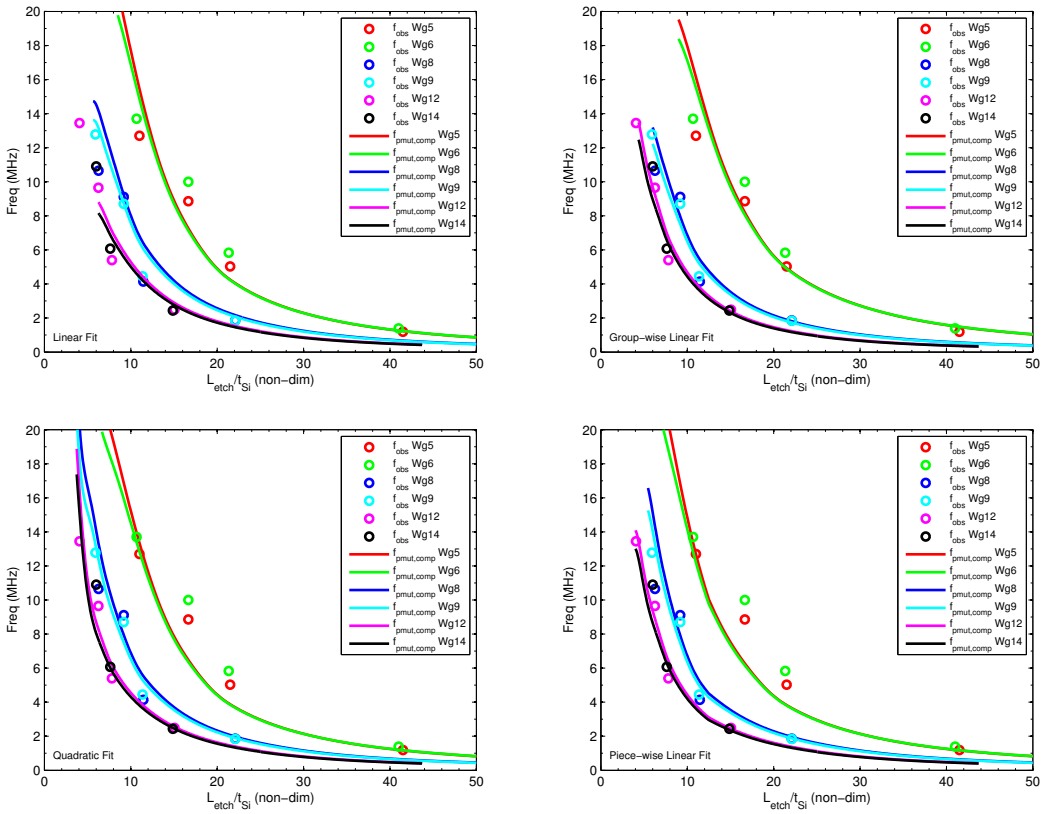

Figure 7.14: Frequency curves vs. *L/t* for theoretical Mindlin plates with compliant support modeled after Wg-series devices. Observed resonant frequency values included to show fit. (top left) Linear fit, (top right) group-wise linear fit, (bottom left) quadratic fit, (bottom right) piece-wise linear fit.

From Figures 7.13 and 7.14, the frequency equation for pMUTs based on a modified Mindlin plate theory with compliant support using each of the four compliance models are shown to fit the observed resonant frequencies well. The R^2 values (Table 7.10) of the theoretical pMUT frequency curves help to quantify their fit to the observed data.

Table 7.10: R^2 values of modified Mindlin frequency theory with compliant support for pMUTs using four different fit models for compliance. Calculated for full pMUT data set and excluding Wg5/6, 75/100μm devices.

Compliance Fit Model	R^2_{freq}	R^2_{freq} (w/o Wg5/6,75/100)
Linear	0.7519	0.7604
Quadratic	0.8510	0.9053
Piece-wise Linear	0.8641	0.9288
Group-wise Linear	0.8959	0.8979

The linear compliance model clearly lags behind the other three models appreciably. Overall, the modified pMUT frequency theory is shown to describe the measured resonant frequencies of real devices very well.

7.5.7 Application of the Modified pMUT Frequency Theory to New Devices

The modified pMUT frequency theory based on Mindlin plates with compliant support has been shown to describe the resonant frequencies of the Wg-series devices from which the model was derived. To demonstrate the efficacy of the theory as a predictive tool, the frequencies of devices from two subsequent wafer series will be assessed. The A-series 2D arrays have been discussed previously, with resonant frequencies presented in a previous section. Dimensions and resonant frequencies of the A- and C-series devices are provided in Table 7.11.

The C-series devices were the most recently fabricated and packaged pMUT arrays available at the time of this writing. Note that the C3 and C5 wafers were etched to yield 6.0 and 6.5μm Si similar to the A-series devices, the C1 wafer was etched to leave only 3.0μm Si, marking the thinnest pMUT 2D arrays to date. The resonant frequency behavior of the C-series devices was measured using only the impedance analyzer at the

time of this writing. While the A-series devices provide a broader range of lateral pMUT dimensions, the C-series devices push the lower limit of device thicknesses that have been assessed.

Table 7.11: Dimensions and resonant frequencies for A- and C-series devices.

Device	t_{Si} (µm)	t_{PZT} (µm)	t_{dev} (µm)	W_{etch} (µm)	L_{etch} (µm)	W_{PZT} (µm)	L_{PZT} (µm)	Imp. Analy. Freq (MHz)	PE Osc Freq - Air (MHz)
A11_2D_40_90p_1	6.5	1.2	8.6	39	64	52	47	14.00	14.15
A11_2D_50_100p_1	6.5	1.2	8.6	50	77	62	58	--	6.00
A11_2D_65_150g_1	6.5	1.2	8.6	63	91	76	73	8.65	8.65
A11_2D_65_150p_1	6.5	1.2	8.6	63	91	76	73	9.50	9.53
A11_2D_75_150g_1	6.5	1.2	8.6	72	104	87	83	4.80	4.80
A11_2D_75_150p_1	6.5	1.2	8.6	72	104	87	83	4.90	4.85
A1_2D_175_9	6.0	1.2	8.1	78	103	86	82	6.76	6.75
A2_2D_175_12	6.0	1.2	8.1	65	96	88	84	8.00	7.90
A1_2D_150_12	6.0	1.2	8.1	78	103	86	82	6.82	7.00
C1_75_16x32	3.0	1.2	5.1	80	110	92	85	3.85	--
C3_75_16x32	6.0	1.2	8.1	80	109	92	85	5.95	--
C5_75_16x32	6.5	1.2	8.6	79	111	92	85	6.60	--

Using Eq. 7.4 to calculate the effective frequency parameters, λ^2_{eff}, for the observed resonant frequencies, we can plot them against the relative thickness as shown in Figure 7.15. The Wg-series data are included (grayed) for comparison. The compliance models developed previously based on the Wg-series data are also shown.

Qualitatively, the A- and C-series data are reasonably modeled by the compliance fits shown, but are not perfectly described by any of the models. While the linear compliance model appears to yield the best fit to the effective frequency parameters of the A- and C-series devices, the variance of nearly all the A- and C-series data points (excluding A11 75µm) is very small.

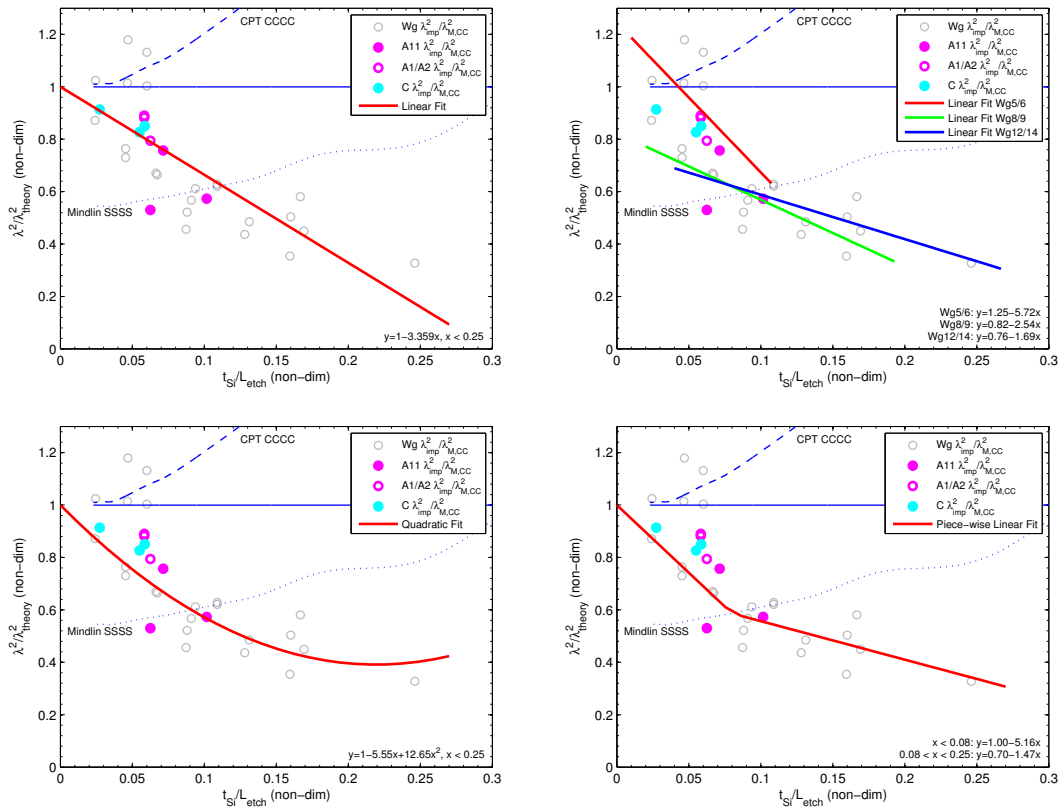

Figure 7.15: Calculated λ^2 ratios from A- and C-series device frequencies plotted as a function of relative thickness *t/L*. Wg-series observed data (grayed) and compliance models are provided for comparison. (top left) Linear fit, (top right) group-wise linear fit, (bottom left) quadratic fit, (bottom right) piece-wise linear fit.

It is worth noting that the A11 75µm devices that appear to be a statistical outlier from the rest of the data set performed particularly poorly as an imaging transducer with poor sensitivity and dynamic range. While perhaps not an indication of any causal relationship to a low λ^2_{eff}, both this device and the A11 50µm device are noted to have multiple frequency peaks in the oscillation FFT (see §7.3.5), high resonant oscillation amplitude remaining in the device in water, and distinctively poorer performance in pulse-echo imaging. The source of this aberrant behavior is currently unknown, though the marked departure from the expected response for pMUTs of such dimensions is noted.

The response of the A11 50μm device has been omitted from this analysis because impedance analyzer results were not available to validate either of the two frequencies identified from pulse-echo oscillation. The 4.8/4.9MHz frequency of the A11 75μm devices was selected for use in the analysis because the impedance analyzer results corroborate this frequency; however the 8.5 or 8.8MHz modes should be noted. The multi-mode responses of these two device types do raise some concerns to be investigated in more detail in the future.

Using the compliance models derived from the Wg-series devices to calculate $C(t,l)$, the effective pMUT frequency parameters, λ^2_{pmut}, and associated theoretical curves were calculated as shown in Figure 7.16.

The multiple curves shown of each color are the result of different aspect ratios and Si thicknesses within each group. From these plots, the quadratic and piece-wise compliance models appear to describe the frequencies of the A- and C-series pMUTs better than the other two.

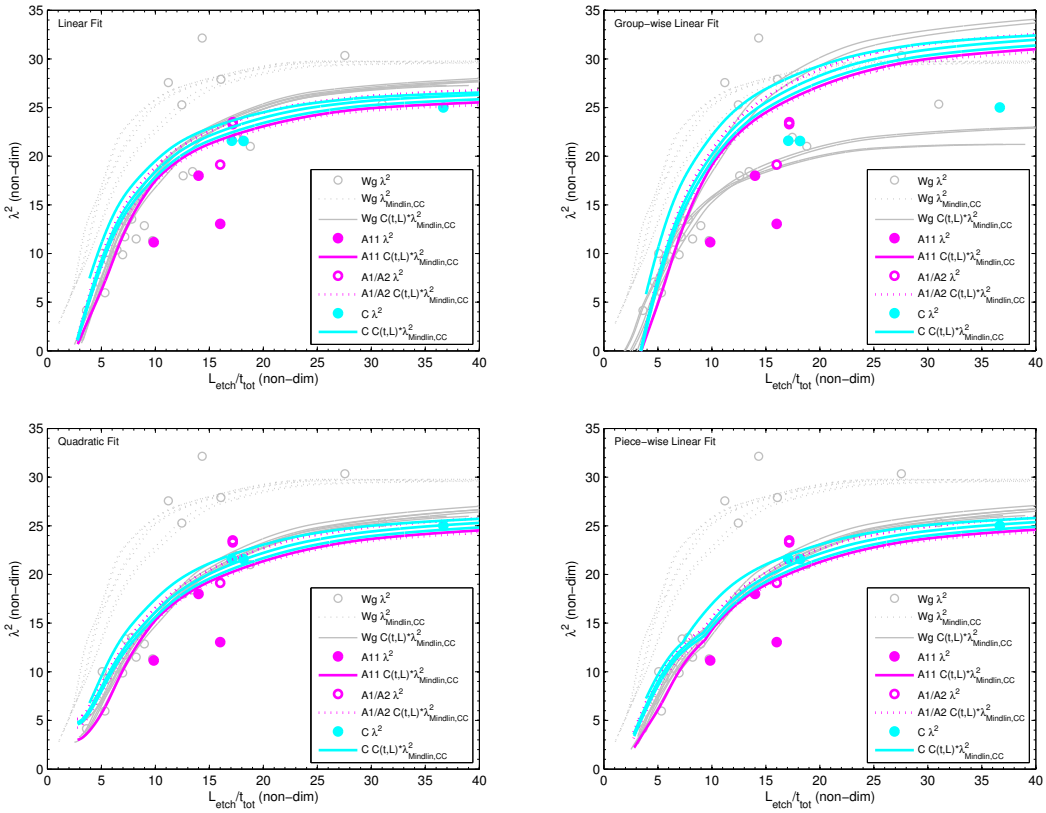

Figure 7.16: λ^2 vs. *L/t* for A- and C-series devices. Wg-series data and associated Mindlin and compliance-adjusted Mindlin frequency parameter curves are provided (grayed) for comparison. (top left) Linear fit, (top right) group-wise linear fit, (bottom left) quadratic fit, (bottom right) piece-wise linear fit.

Taking the effective pMUT frequency parameters and the modified pMUT frequency equation shown in Eq. 7.10, the frequency curves for each device group can be plotted as a function of device length, as shown in Figure 7.17.

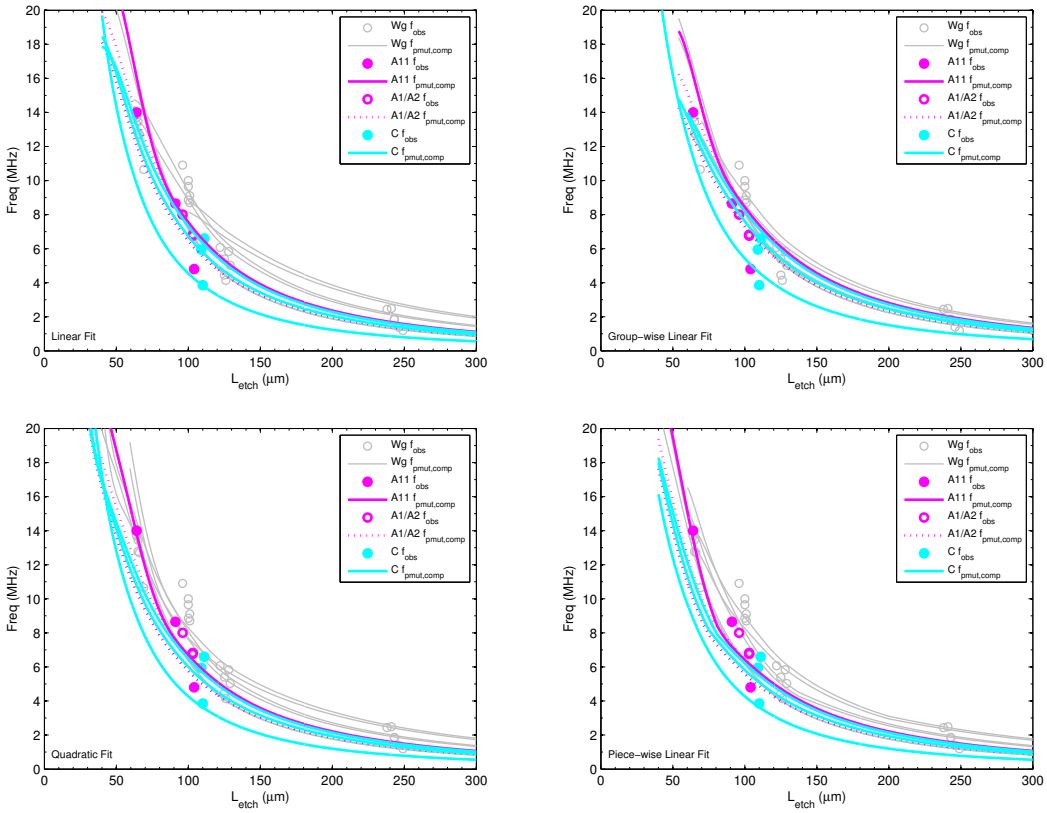

Figure 7.17: A- and C-series observed frequencies and pMUT frequency curves based on Mindlin plates with compliant support vs device length. Wg-series observed frequencies and associated curves are provided (grayed) for comparison. (top left) Linear fit, (top right) group-wise linear fit, (bottom left) quadratic fit, (bottom right) piece-wise linear fit.

In order to separate the different device thickness groups and highlight the role of relative thickness in frequency, the frequency curves can be plotted as a function of *L/t* as shown in Figure 7.18.

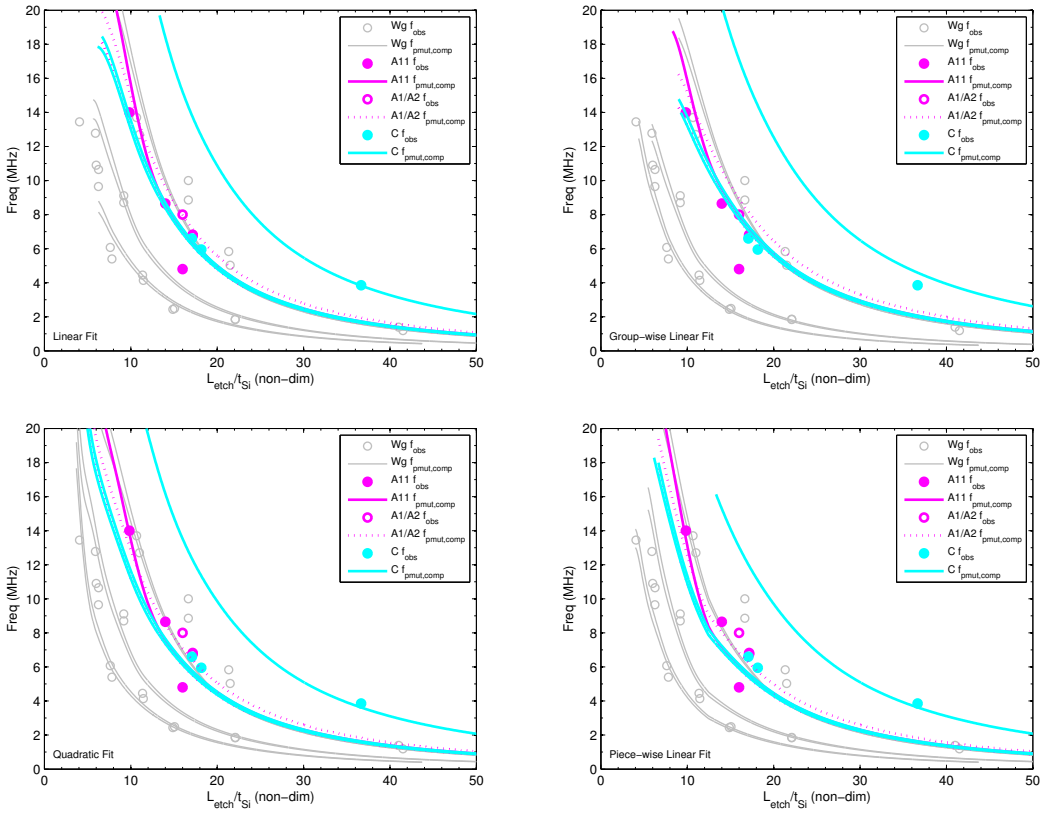

Figure 7.18: A- and C-series observed frequencies and pMUT frequency curves based on Mindlin plates with compliant support vs. device length/Si thickness. Wg-series observed frequencies and associated curves are provided (grayed) for comparison. (top left) Linear fit, (top right) group-wise linear fit, (bottom left) quadratic fit, (bottom right) piece-wise linear fit.

For a more quantitative view of how well the developed theory fits the observed A- and C-series devices, the R^2 for the fit residuals, λ^2_{eff} curves, and frequency theory curves are provided in Table 7.12.

From the R^2 values and the associated plots, it appears that frequencies predicted using the linear, quadratic, and piece-wise linear compliance models are in good agreement with the observed frequencies.

Table 7.12: R^2 from fit residuals, λ^2_{eff} curves, and frequency theory curves for A- and C-series pMUTs using linear, quadratic, piece-wise, and group-wise compliance models.

Compliance Fit Model	$R^2_{residuals,AC}$	$R^2_{\lambda 2,eff,AC}$	$R^2_{freq,AC}$
Linear	0.4093	0.7020	0.8412
Quadratic	0.1470	0.5322	0.8656
Piece-wise Linear	-0.0431	0.4286	0.8294
Group-wise Linear	-0.2876	0.3292	0.7281

While each compliance model has its own strengths and weaknesses, the quadratic model provides consistent results from the pMUT arrays tested thus far and is the suggested compliance model to be used within the range over which it is defined (t/L<0.27).

7.6 Summary

The methods described in this chapter have shown to provide an excellent model of the fundamental-mode vibrational frequencies in air. The resonant frequency in air is well-described by the analytical methods given.

Combining the equations for support compliance (Eq. 7.6, quadratic fit), and fully-clamped Mindlin frequencies (Eq. 7.1), we can express an expanded form of the general equation for pMUT fundamental-mode resonant frequencies in air (Eq. 7.10) as

$$f^{t}_{res,air} = \left[1 - 5.55\left(\frac{t_{Si}}{L_{etch}}\right) + 12.65\left(\frac{t_{Si}}{L_{etch}}\right)^2\right] * \frac{\lambda^2_{mn}(L_{etch}, W_{etch}, t_{tot})}{2\pi W^2_{etch}} \sqrt{\frac{E\, t_{tot}^{\ 2}}{12\rho(1-\nu^2)}} \qquad (7.11)$$

where length, width, and thickness dimensions are given by L, W, and t, respectively, ρ is the composite plate density, ν is the Poisson's ratio (~0.3), λ^2_{mn} is the frequency parameter taken from the interpolation of tabled values (dependent on L,W, and t), and E is the Young's modulus of the composite plate (from measurement or calculation from

composite plate flexural rigidity, D). The compliance term given is for the quadratic model, which for devices where $\frac{t_{Si}}{L_{etch}} < 0.25$ provides the most consistent results.

Chapter 8

pMUT Frequency Theory for Imaging Applications

8.1 Introduction

The pMUT frequency theory presented in the previous chapter establishes a method to identify the fundamental resonant frequency for the devices. Additional factors must be taken into consideration to determine optimal frequencies for imaging applications, shown in acoustic measurements to be up to 15-20% higher than the resonant frequency in water.

The resonant vibration is the natural free vibration of the pMUT plate. The transmit frequencies are, in contrast, electromechanically forced with a confined forcing function over the area where the PZT film is activated (electroded). The receive frequencies fall between the resonance and transmit frequencies and are an acoustically forced vibration in response to acoustic pressure waves which may generally be regarded as plane waves over the full device surface. However, in receive the pMUT membrane is, in part, freely vibrating, particularly following the duration of the incoming pressure wave. In this respect, the receive mode is likely to carry a larger component of the resonant frequency than the forced, off-resonance transmit mode. This serves to explain why the optimal acoustic receive frequency is typically lower than the transmit frequency and closer to resonance.

In both acoustic transmit and receive modes, however, surface structures such as PZT film and metal layers may introduce mechanical boundaries that alter the vibrational

behavior. The relationship between resonant and transmit/receive frequencies will be assessed using changes in the vibrational dimensions corresponding to physical pMUT component structures. Recalling that the optimal acoustic transmit and receive frequencies are a balance of near-resonance sensitivity and off-resonance bandwidth, the confined fundamental vibrational mode is expected to be higher than the measured acoustic frequencies. Optimal device characteristics for transmit efficiency and receive sensitivity will be discussed.

The effect of water-loading will also be considered as loading of the plate surface dampens and lowers the vibrational frequency. The equations for determining the frequency decrease associated with water-loading were presented in the Background and will be applied to the pMUT devices. The accuracy of the water-loading equations will be assessed.

8.2 Effect of Water Loading on pMUT Vibrational Frequency

An equation for the frequency decrease in the vibration of plates loaded on one side by water is provided by Greenspon [64, 65] and referenced by Leissa [51]. The equation is reproduced in Eq. 6.20 in the Background. This equation gives the frequency ratio of vibration in water vs. vacuum. For the purposes of this thesis, the air-loaded condition was treated as a reasonable approximation to the vacuum-loaded condition. The frequency ratio may be used to predict the expected water-loaded frequency for a vibrating plate from the known air-loaded response. The frequency ratio thus represents a correction factor, C_{H2O}, for use with frequencies in air.

The percent difference between water-loaded and vacuum-loaded plates can be calculated from the provided equation using the physical specifications of the pMUT devices. The water-loaded frequencies are expected to decrease by 7.8-42.5% from the air-loaded condition, depending on the boundary conditions selected. The minimum, maximum, and mean for the calculated water-load correction factors for the pMUT devices are given in Table 8.1.

Table 8.1: Statistics for calculated percent decrease in frequency due to water loading for pMUT device structures.

Statistic	SSSS	CCCC
Min	10.39%	7.86%
Mean	23.56%	19.01%
Max	42.53%	36.39%

The accuracy of the calculated water-correction factors can be evaluated by taking the frequencies measured using the impedance analyzer in air as the unloaded frequency compared to the measured resonant oscillation frequencies in water. The ratio of the resonant frequency in water and air can be compared to the calculated C_{H2O} as shown in Table 8.2. When available, the observed water-air frequency ratio is provided. However, the low amplitude of the resonant oscillation in water for many devices prohibited accurate measurement of the water-loaded frequency for these devices. Polytec frequencies in air and water are also provided for the two devices that were measured using optical methods. The percent difference between the observed and theoretical water-air frequency ratios is provided to quantify the accuracy of the water-loading model. The theoretical water-loaded resonant frequency is also calculated by taking the product of the observed resonant frequency in air and the theoretical water-loaded

frequency factor for fundamental 1-1 mode vibration over the full etched cavity for a fully clamped plate ($C_{H2O,CCCC}$), so that

$$f^{t*}_{res,H2O} = C_{H2O,CCCC} * f^{obs}_{res,air} \tag{8.1}$$

where the * identifies that the equation is formulated using observed frequency data.

Table 8.2: Calculated frequency factors (Eq. 6.20) for single-sided water loading in the vibration of A- and Wg-series devices. Calculated values are for (white) 1-1 mode, full etch dimensions, (green) confined 1-1 mode, etched width/PZT length, (orange) 3-1 mode, full etch dimensions. Water-air frequency ratios from measured pMUT data shown for comparison with percent error between observed and theoretical values. Theoretical resonant frequencies in water are given (pink) for fully clamped conditions, 1-1 mode over the full etched cavity.

	Air	H_2O							Theory
Device	$f_{res,air}$ (MHz)	$f_{res,H2O}$ (MHz)	f_{res} ratio (H2O/Air)	$f_{polytec}$ ratio (H2O/Air)	C_{H2O} Factor SSSS	C_{H2O} Factor CCCC	% Diff SS	% Diff CC	$f^{t*}_{res,H2O}$ (MHz)
A11_2D_40_90p_1	14.00	12.50	0.89		0.84	0.87	-6.9	-2.3	12.21
A11_2D_50_100p_1	6.00	4.68	0.78		0.81	0.85	3.2	8.0	5.09
A11_2D_65_150g_1	8.65	5.75	0.66		0.78	0.82	14.4	19.2	7.11
A11_2D_65_150p_1	9.50	--			0.78	0.82			7.81
A11_2D_75_150g_1	4.80	3.30	0.69		0.76	0.80	9.0	14.5	3.86
A11_2D_75_150p_1	4.90	3.40	0.69		0.76	0.80	8.1	13.7	3.94
A1_2D_175_9	6.76	4.50	0.67	0.79	0.74	0.79	10.5	16.1	5.37
A2_2D_175_12	8.00	5.10	0.64		0.76	0.81	16.7	21.6	6.50
A1_2D_150_12	6.82	4.70	0.69		0.74	0.79	7.3	13.2	5.41
Wg5 B5050_100A	12.70	--			0.82	0.86			10.97
Wg6 B5050_100C	13.70	--			0.85	0.89			12.12
Wg8 B5050_100D	10.65	--			0.85	0.88			9.42
Wg9 B5050_100	12.78	--			0.87	0.90			11.53
Wg12 B5050_100B	13.45	--			0.88	0.91			12.25
Wg14 B5050_100	--	--			0.90	0.92			
Wg5 B7550_100A	8.86	--			0.75	0.80			7.09
Wg6 B7550_84A	10.00	--			0.78	0.83			8.26
Wg8 B7550_100C	9.11	--			0.79	0.84			7.62
Wg9 B7550_100D	8.70	--			0.81	0.86			7.44
Wg12 B7550_100A	9.75	--			0.83	0.86			8.43
Wg12 B7550_100B	9.65	--			0.83	0.86			8.34
Wg14 B7550_100A	10.90	--			0.85	0.88			9.61
Wg5 B10050_100A	--	--			0.70	0.75			
Wg6 B10050_100C	--	--			0.73	0.78			
Wg8 B10050_100A	--	--			0.75	0.80			
Wg9 B10050_100C	--	--			0.78	0.82			
Wg12 B10050_100A	--	--			0.79	0.83			
Wg14 B10050_100A	--	--			0.81	0.85			
Wg5 B10050_100A	5.03	3.50	0.70		0.70	0.75	0.5	7.8	3.80
Wg6 B10050_100C	5.83	--			0.73	0.78			4.57
Wg8 B10050_100A	4.14	2.85	0.69		0.75	0.80	8.3	14.0	3.31

Table 8.2 continued

Wg9 B10050_100C	4.45	3.35	0.75		0.78	0.82	2.9	8.4	3.66
Wg12 B10050_100A	5.40	3.80	0.70		0.79	0.83	10.5	15.3	4.49
Wg14 B10050_100A	6.07	--			0.81	0.85			5.17
Wg5 B200100_100D	--	--			0.90	0.88			
Wg6 B200100_100B	--	--			0.92	0.90			
Wg8 B200100_100A	--	--		0.75	0.92	0.91			
Wg9 B200100_100C	--	--			0.93	0.92			
Wg12 B200100_100B	--	--			0.94	0.92			
Wg14 B200100_100D	--	--			0.95	0.93			
Wg5 B200100_100D	--	--			0.59	0.65			
Wg6 B200100_100B	--	--			0.62	0.68			
Wg8 B200100_100A	--	--		0.66	0.64	0.70			
Wg9 B200100_100C	--	--			0.67	0.73			
Wg12 B200100_100B	--	--			0.68	0.74			
Wg14 B200100_100D	--	--			0.71	0.76			
Wg5 B200100_100D	1.19	0.67	0.56		0.57	0.64	2.0	11.5	0.76
Wg6 B200100_100B	1.39	0.82	0.59		0.61	0.67	3.0	11.8	0.93
Wg8 B200100_100A	1.86	1.11	0.60	0.63	0.63	0.69	5.0	13.2	1.28
Wg9 B200100_100C	1.84	1.12	0.61		0.66	0.71	7.2	14.8	1.31
Wg12 B200100_100B	2.49	1.63	0.65		0.67	0.73	2.5	10.2	1.81
Wg14 B200100_100D	2.44	1.60	0.66		0.70	0.75	6.0	12.9	1.84

The data provided in Table 8.2 shows that the equation for the frequency decrease due to water loading describes the observed vibrational behavior to within 17% and 22% between the SSSS and CCCC formulations, respectively.

Equation 8.1 for $f^{t*}_{res,H2O}$ is thus useful in isolating and assessing the accuracy of the water-loading factor $C_{H2O,CCCC}$ without including the influences of the residuals or errors from modeling using the modified Mindlin frequency theory. By replacing the observed frequency data in Eq. 8.1 with the theoretical Mindlin frequency model for pMUTs in air, we can express the wholly theoretical frequency model for pMUT vibration in water as

$$f^{t}_{res,H2O} = C_{H2O,CCCC} * C_{compliance}(t,L) * f^{t}_{Mindlin,air} \tag{8.2}$$

Theoretical values calculated from the above equation will be explored in a later section as the water loading factor is the focus of this section and comparison of data from the two different media better quantify its accuracy.

Note that C_{H2O} is highly sensitive to the boundary dimensions and boundary conditions. A change of a few microns in dimensions can change the frequency factor by a few percent. The difference between frequency factors for clamped and simply supported boundary conditions is up to 10% over the range of pMUT structures. Recall that the λ_{eff} for the observed resonant frequencies reflect boundary conditions ranging from clamped to simply-supported to possibly even less constrained conditions. If the relationship between clamped and simply supported edge conditions in water-loaded frequency factors holds true for the less-constrained boundary conditions, the frequency factors would be even lower, yielding even lower theoretical frequencies. Therefore, the $f^{t*}_{res,H2O}$ provided in Table 8.2 and $f^{t}_{res,H2O}$ given in Eq. 8.2 represent an upper bound for the frequencies of pMUT resonance in water. Additional analyses may provide extended accuracy.

At present, the water-loading model using the clamped condition frequency factors for the theoretical frequency in water has been demonstrated to yield results within a few hundred kilohertz of the measured water-loaded resonant oscillation frequencies.

8.3 Optimal Acoustic Receive Frequencies for Imaging

The optimal receive frequencies will be considered first as these frequencies are more closely related to a full-plate fundamental mode vibration. The observed receive frequency in water (f_{rx}) is compared to the observed resonant frequency in air ($f_{res,air}$) and the theoretical resonant frequency in water ($f^{t*}_{res,H2O}$) in Table 8.3.

Table 8.3: Acoustic receive frequencies compared to calculated water-loaded resonant frequencies for A- and Wg-series devices. Theoretical resonant frequencies in water (pink) calculated from product of resonant frequency in air and water-loaded frequency factor for fully clamped conditions, 1-1 mode over the full etched cavity. Absolute and percent differences between observed f_{rx} and $f^{t*}_{res,H2O}$ are provided. Percent difference between observed $f_{res,H2O}$ and theoretical $f^{t*}_{res,H2O}$ are also provided for comparison when available.

	Air	H2O		Theory			
Device	$f_{res,air}$ (MHz)	f_{rx} (MHz)	C_{H2O} Factor CCCC	$f^{t*}_{res,H2O}$ (MHz)	Diff $f^{t*}_{res,H2O}$ vs. f_{rx} (MHz)	%Diff $f^{t*}_{res,H2O}$ vs. f_{rx} (%)	%Diff $f^{t*}_{res,H2O}$ vs. $f_{res,H2O}$ (%)
A11_2D_40_90p_1	14.00	12.75	0.87	12.21	-0.54	-4.43	-2.3
A11_2D_50_100p_1	10.00	10.00	0.85	8.48	-1.52	-17.93	8.0
A11_2D_65_150g_1	8.65	6.91	0.82	7.11	0.20	2.86	19.2
A11_2D_65_150p_1	9.50	7.51	0.82	7.81	0.30	3.87	
A11_2D_75_150g_1	4.80	3.88	0.80	3.86	-0.02	-0.54	14.5
A11_2D_75_150p_1	4.90	3.89	0.80	3.94	0.05	1.32	13.7
A1_2D_175_9	6.76	5.17	0.79	5.37	0.19	3.58	16.1
A2_2D_175_12	8.00	6.14	0.81	6.50	0.36	5.52	21.6
A1_2D_150_12	6.82	5.40	0.79	5.41	0.01	0.26	13.2
Wg5 B5050_100A	12.70	10.98	0.86	10.97	-0.01	-0.14	
Wg6 B5050_100C	13.70	12.11	0.89	12.12	0.02	0.14	
Wg8 B5050_100D	10.65	11.07	0.88	9.42	-1.65	-17.47	
Wg9 B5050_100	12.78	11.96	0.90	11.53	-0.43	-3.73	
Wg12 B5050_100B	13.45	12.96	0.91	12.25	-0.71	-5.78	
Wg14 B5050_100	--	13.31	0.92				
Wg5 B7550_100A	8.86	7.28	0.80	7.09	-0.19	-2.66	
Wg6 B7550_84A	10.00	7.56	0.83	8.26	0.70	8.42	
Wg8 B7550_100C	9.11	7.78	0.84	7.62	-0.16	-2.08	
Wg9 B7550_100D	8.70	7.31	0.86	7.44	0.13	1.69	
Wg12 B7550_100A	9.75	8.21	0.86	8.43	0.22	2.57	
Wg12 B7550_100B	9.65	8.19	0.86	8.34	0.15	1.81	
Wg14 B7550_100A	10.90	8.56	0.88	9.61	1.05	10.96	
Wg5 B10050_100A	5.03	3.94	0.75	3.80	-0.14	-3.81	
Wg6 B10050_100C	5.83	4.61	0.78	4.57	-0.04	-0.97	
Wg8 B10050_100A	4.14	4.13	0.80	3.31	-0.82	-24.70	
Wg9 B10050_100C	4.45	4.10	0.82	3.66	-0.44	-12.04	
Wg12 B10050_100A	5.40	4.73	0.83	4.49	-0.25	-5.49	
Wg14 B10050_100A	6.07	4.92	0.85	5.17	0.25	4.76	
Wg5 B10050_100A	5.03	3.32	0.75	3.80	0.47	12.46	7.8
Wg6 B10050_100C	5.83	3.94	0.78	4.57	0.62	13.62	
Wg8 B10050_100A	4.14	2.92	0.80	3.31	0.39	11.84	14.0
Wg9 B10050_100C	4.45	3.23	0.82	3.66	0.42	11.55	8.4
Wg12 B10050_100A	5.40	3.80	0.83	4.49	0.69	15.34	15.3
Wg14 B10050_100A	6.07	4.16	0.85	5.17	1.01	19.60	
Wg5 B200100_100D	1.19	0.70	0.64	0.76	0.06	7.51	11.5
Wg6 B200100_100B	1.39	0.80	0.67	0.93	0.13	13.97	11.8
Wg8 B200100_100A	1.86	1.10	0.69	1.28	0.18	14.02	13.2
Wg9 B200100_100C	1.84	1.10	0.71	1.31	0.21	16.32	14.8
Wg12 B200100_100B	2.49	1.98	0.73	1.81	-0.17	-9.10	10.2
Wg14 B200100_100D	2.44	2.05	0.75	1.84	-0.21	-11.62	12.9

Examining the absolute and percent difference between the observed frequencies and $f^{t*}_{res,H2O}$, we find that the optimal acoustic receive frequencies for devices with nominal size ≤75μm are well-modeled by $f^{t*}_{res,H2O}$ to less than 8.5% for all but three devices. In fact, for the devices where both acoustic receive and resonant oscillation frequencies in water are available, the f_{rx} is better described by the theoretical value (which is derived from the resonance in air).

For devices with nominal size of 200μm, only the fundamental frequency was considered (higher order modes will be discussed in a later section). Both f_{rx} and $f_{res,H2O}$ in water were well-modeled by the theoretical $f^{t*}_{res,H2O}$. The theoretical $f^{t*}_{res,H2O}$ fall within 200kHz (<16%) of both observed frequencies in water.

The 100μm devices present a particularly special case. While the 200μm devices operate with a clear distinction between fundamental and higher order modes in receive, the 100μm devices present two receive frequencies that are close to each other, within 1.1MHz (<29%). The higher frequency is not high enough to be considered a higher-order mode and little information is available to distinguish between what appear to be two fundamental mode f_{rx} frequencies when in water. With only one measured f_{res} frequency in air, it is somewhat unclear which f_{rx} frequency to use for comparison to the calculated $f^{t*}_{res,H2O}$. In Table 8.3, both f_{rx} frequencies for the 100μm devices are compared to the calculated $f^{t*}_{res,H2O}$. The theoretical frequency best describes the higher observed f_{rx} for the 5 and 15μm Si devices (<5%) while fitting the lower observed f_{rx} better for the 10μm Si devices (<12%).

This method of calculating $f^{t*}_{res,H2O}$ from the resonant frequency in air and the frequency factor from Greenspon's equation (Eq. 6.20) thus presents an excellent method of estimating the optimal acoustic receive frequency. The oscillation observed in a pulse-echo configuration is not always measurable in water. Additionally, this oscillation results in a degradation of image quality due to its long duration and inconsistent amplitude.

It should be noted that the distinct origins of f_{rx} and $f_{res,H2O}$ is significant in discerning their difference. The resonant oscillation in pulse-echo is the result of free vibration of the membrane following its response to a high-voltage transmit pulse. In air, little energy is expected to propagate into the medium, leaving most of the energy in the pMUT structure. In water, however, the oscillation may experience a slight downshift in frequency as a result of a significant portion of the energy propagated into the medium in addition to the effect of dampening by the water. This would serve to explain why the $f_{res,H2O}$ measured in water is lower than the calculated $f^{t*}_{res,H2O}$.

The receive frequency, on the other hand, is a free response to an incident acoustic plane wave. As such, the frequency is subject only to the effect of water loading. This provides a reasonable explanation for the calculated $f^{t*}_{res,H2O}$ approximating f_{rx} more closely than $f_{res,H2O}$.

For the determination of the optimal receive frequency for imaging applications, the analysis shows that we can forego calculating f_{rx} from a model of $f_{res,H2O}$. Instead, calculating $f^{t*}_{res,H2O}$ using the method described provides a direct approximation to f_{rx}.

Recalling that $f_{res,air}$ may be approximated using the compliance-modified Mindlin plate theory, the optimal receive frequency $f^{t}_{rx,H2O}$ may be modeled using the expression

$$f^{t}_{rx,H2O} = C^{full}_{H2O,CCCC} * C^{full}_{compliance}(t,L) * f^{t,full}_{Mindlin,air} \tag{8.3}$$

which is the same as the expression given in Eq. 8.2, though with the dimensions used to calculate each component specified to be the full etched cavity dimensions.

Plotting the theoretical receive frequencies, f^{t}_{rx}, using the Wg-series device dimensions, we find that the theoretical receive frequency curves describe the observed Wg- and A-series receive frequencies very well, as shown in Figure 8.1. Curves calculated using quadratic, piece-wise, and group-wise compliance models are shown. Curves for A-series device dimensions are omitted as the differences between them and the Wg5 devices are marginal.

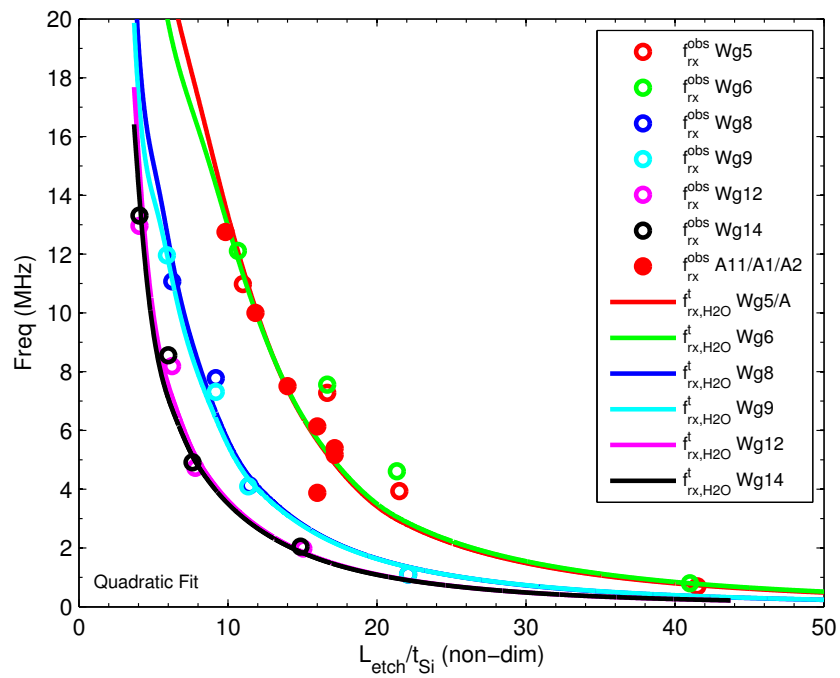

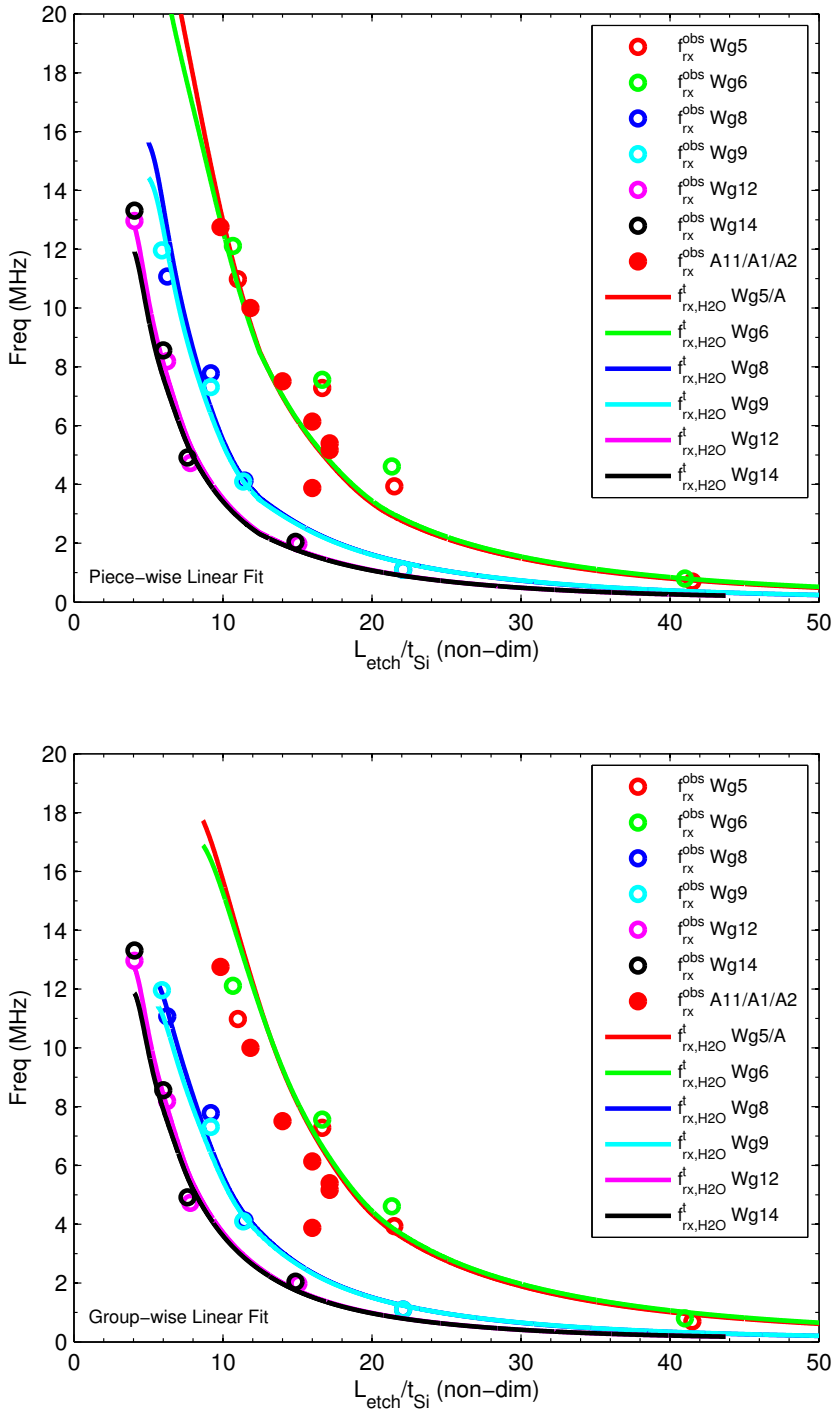

Figure 8.1: Theoretical and observed optimal acoustic receive frequencies in water for imaging applications. Theoretical f^{t}_{rx} calculated using quadratic (top), piece-wise (middle), and group-wise (bottom) compliance models.

Calculating the R^2 between the theoretical and observed receive frequencies using the different compliance models (Table 8.4), we see that the theoretical frequency calculated using the quadratic, piece-wise, and group-wise compliance models are an excellent fit to the observed data.

Table 8.4: R^2 values for theoretical and observed receive frequencies for Wg- and A-series devices.

Compliance Fit Model	$R^2_{freq,Rx}$
Linear	0.7167
Quadratic	0.9225
Piece-wise Linear	0.9173
Group-wise Linear	0.9040

These results demonstrate that an equation based on Mindlin plate theory and incorporating the effect of water loading and compliant support may be used to accurately predict f^t_{rx} using Equation 8.3. The receive frequency is a fundamental mode calculated using the full etch dimensions.

8.4 Optimal Acoustic Transmit Frequencies for Imaging

The optimal acoustic transmit frequencies have been shown to be up to 20% higher than the calculated fundamental resonant frequency. The electromechanical excitation over the confined active PZT area is likely a key contributing factor to this increased transmit frequency.

The theoretical Mindlin frequency is affected by changes in the dimensions of the plate. Changing only the plate length dimension and leaving density, flexural rigidity, thickness and plate width (etched width) the same, an increase of 1-18% is expected if the PZT length is used instead of the etched length and a change of 4-29% is expected if the electroded PZT length is used. The ratio between the confined vs. full dimension

theoretical frequencies can be compared to the ratio of the observed acoustic transmit vs. receive frequencies to assess if the decreased dimensions adequately explain the increase seen in acoustic transmit. Both ratios are given in Table 8.5.

Table 8.5: Calculated optimal acoustic transmit frequencies in water (compliance-modified Mindlin frequencies (f_M) with water loading) compared to observed values. f_M calculated using full etched cavity (full) and L_{PZT}-confined dimensions (conf). Quadratic, piece-wise, and group-wise compliance models based on the full etched cavity dimensions. Water-loading factors determined using full and confined dimensions. Highlighted theoretical frequencies (orange) identify the optimal compliance model for each set of devices.

	H2O	Obs	Theory	Quadratic		Piece-wise		Group-wise	
Device	**f_{tx} (MHz)**	**f_{tx}/f_{rx} Ratio**	**Conf / Full f_M Ratio**	**$f_{M,H2O}$ Full (MHz)**	**$f_{M,H2O}$ Conf (MHz)**	**$f_{M,H2O}$ Full (MHz)**	**$f_{M,H2O}$ Conf (MHz)**	**$f_{M,H2O}$ Full (MHz)**	**$f_{M,H2O}$ Conf (MHz)**
A11_2D_40_90p_1	13.00	1.02	1.16	12.08	14.21	11.82	13.91	14.16	16.66
A11_2D_50_100p_1	9.40	0.94	1.16	8.75	10.31	8.16	9.62	10.73	12.65
A11_2D_65_150g_1	7.00	1.01	1.14	6.28	7.28	5.93	6.87	7.86	9.11
A11_2D_65_150p_1	7.70	1.03	1.14	6.28	7.28	5.93	6.87	7.86	9.11
A11_2D_75_150g_1	4.20	1.08	1.14	5.11	5.95	4.93	5.74	6.46	7.52
A11_2D_75_150p_1	4.20	1.08	1.14	5.11	5.95	4.93	5.74	6.46	7.52
A1_2D_175_9	5.40	1.04	1.18	4.38	5.25	4.25	5.10	5.55	6.65
A2_2D_175_12	6.20	1.01	1.07	5.75	6.21	5.54	5.98	7.27	7.84
A1_2D_150_12	5.60	1.04	1.18	4.38	5.25	4.25	5.10	5.55	6.65
Wg5 B5050_100A	10.90	0.99	1.03	11.60	12.02	11.03	11.43	14.02	14.53
Wg6 B5050_100C	11.90	0.98	1.04	11.71	12.24	11.23	11.73	14.06	14.69
Wg8 B5050_100D	11.00	0.99	1.01	11.61	11.82	12.49	12.72	11.12	11.32
Wg9 B5050_100	12.60	1.05	1.00	10.85	10.89	11.68	11.72	10.09	10.13
Wg12 B5050_100B	13.20	1.02	0.94	14.99	14.12	12.81	12.07	12.76	12.02
Wg14 B5050_100	13.60	1.02	1.04	13.58	14.16	11.60	12.11	11.56	12.06
Wg5 B7550_100A	7.70	1.06	1.09	5.03	5.55	4.88	5.37	6.37	7.02
Wg6 B7550_84A	8.20	1.08	1.11	5.20	5.82	5.04	5.64	6.58	7.37
Wg8 B7550_100C	8.40	1.08	1.09	6.70	7.36	6.68	7.34	6.71	7.37
Wg9 B7550_100D	8.60	1.18	1.14	6.46	7.44	6.44	7.41	6.47	7.45
Wg12 B7550_100A	9.10	1.11	1.11	7.21	8.06	7.76	8.67	8.05	9.00
Wg12 B7550_100B	--		1.11	7.21	8.06	7.76	8.67	8.05	9.00
Wg14 B7550_100A	8.60	1.01	1.03	7.06	7.33	7.60	7.89	7.86	8.17
Wg5 B10050_100A	4.30	1.09	1.11	2.88	3.24	2.84	3.20	3.66	4.13
Wg6 B10050_100C	5.20	1.13	1.12	2.97	3.39	2.93	3.35	3.78	4.32
Wg8 B10050_100A	5.10	1.23	1.12	4.44	5.03	4.18	4.73	4.36	4.94
Wg9 B10050_100C	4.80	1.17	1.10	4.27	4.76	4.03	4.49	4.20	4.68
Wg12 B10050_100A	6.20	1.31	1.09	5.11	5.64	5.30	5.85	5.56	6.13
Wg14 B10050_100A	6.40	1.30	1.06	5.22	5.59	5.45	5.84	5.71	6.11
Wg5 B10050_100A	--		1.11	2.88	3.24	2.84	3.20	3.66	4.13
Wg6 B10050_100C	--		1.12	2.97	3.39	2.93	3.35	3.78	4.32
Wg8 B10050_100A	--		1.12	4.44	5.03	4.18	4.73	4.36	4.94
Wg9 B10050_100C	--		1.10	4.27	4.76	4.03	4.49	4.20	4.68
Wg12 B10050_100A	--		1.09	5.11	5.64	5.30	5.85	5.56	6.13
Wg14 B10050_100A	--		1.06	5.22	5.59	5.45	5.84	5.71	6.11

Additionally, theoretical acoustic transmit frequencies may be calculated from the product of the theoretical Mindlin frequency, water-loading factor, and a compliance model, such that

$$f^{t}_{tx,H2O} = C_{H2O,CCCC} * C_{compliance}(t,L) * f^{t}_{Mindlin,air} \tag{8.4}$$

Each of the elements on the right-hand side may be calculated using full or confined dimensions. For full dimensions, the full etched cavity dimensions were used. For confined dimensions, the etched width was used with the PZT length.

The compliance model for both theoretical frequency calculations used the full cavity dimensions because though the confined dimensions do present a different set of boundary conditions from the full cavity dimensions, the compliance for a confined suspended plate is not properly described by replacing the etched length with the PZT length. The compliance for the confined mode likely behaves in an entirely different way requiring separate study and derivation. Presently, the compliance for the full etched cavity will serve as an adequate approximation. Theoretical transmit frequencies using full and confined dimensions are shown in Table 8.5, calculated with quadratic, piece-wise, and group-wise compliance models.

The theoretical frequency results are in good agreement with the observed data. Using the quadratic and piece-wise compliance models provides the best approximation to the observed f_{tx} for all A-series and 50μm Wg-series devices. The theoretical frequencies employing the group-wise linear compliance model best described the observed f_{tx} for the 75 and 100μm Wg devices. The most appropriate models for transmit frequency determination are highlighted in orange.

The percent difference between observed and theoretical transmit frequencies is given in Table 8.6.

Table 8.6: Percent difference between calculated optimal acoustic transmit frequencies in water compared and observed values. Calculated transmit frequencies calculated using compliance-modified Mindlin frequencies with water loading. Mindlin frequencies calculated using full etched cavity (full) and L_{PZT}-confined dimensions (conf). Quadratic, piece-wise, and group-wise compliance models based on the full etched cavity dimensions. Water-loading factors determined using full and confined dimensions. Highlighted values (orange) identify the optimal compliance model for each set of devices.

	H2O	Obs	Theory	Quadratic		Piece-wise		Group-wise	
Device	**f_{tx} (MHz)**	**f_{tx}/f_{rx} Ratio**	**Conf / Full f_M Ratio**	**%Diff $f_{M,H2O}$ Full (%)**	**%Diff $f_{M,H2O}$ Conf (%)**	**%Diff $f_{M,H2O}$ Full (%)**	**%Diff $f_{M,H2O}$ Conf (%)**	**%Diff $f_{M,H2O}$ Full (%)**	**%Diff $f_{M,H2O}$ Conf (%)**
A11_2D_40_90p_1	13.00	1.02	1.16	-7.7	8.5	-10.0	6.5	8.2	21.9
A11_2D_50_100p_1	9.40	0.94	1.16	-7.4	8.8	-15.1	2.3	12.4	25.7
A11_2D_65_150g_1	7.00	1.01	1.14	-11.5	3.8	-18.0	-1.8	11.0	23.2
A11_2D_65_150p_1	7.70	1.03	1.14	-22.6	-5.8	-29.8	-12.0	2.1	15.5
A11_2D_75_150g_1	4.20	1.08	1.14	17.9	29.5	14.8	26.8	35.0	44.2
A11_2D_75_150p_1	4.20	1.08	1.14	17.9	29.5	14.8	26.8	35.0	44.2
A1_2D_175_9	5.40	1.04	1.18	-23.4	-2.9	-27.0	-5.9	2.7	18.8
A2_2D_175_12	6.20	1.01	1.07	-7.8	0.1	-11.8	-3.6	14.7	20.9
A1_2D_150_12	5.60	1.04	1.18	-27.9	-6.7	-31.7	-9.8	-1.0	15.8
Wg5 B5050_100A	10.90	0.99	1.03	6.0	9.3	1.2	4.6	22.3	25.0
Wg6 B5050_100C	11.90	0.98	1.04	-1.6	2.8	-6.0	-1.4	15.4	19.0
Wg8 B5050_100D	11.00	0.99	1.01	5.3	7.0	11.9	13.5	1.1	2.9
Wg9 B5050_100	12.60	1.05	1.00	-16.1	-15.7	-7.9	-7.5	-24.9	-24.4
Wg12 B5050_100B	13.20	1.02	0.94	11.9	6.5	-3.0	-9.4	-3.4	-9.8
Wg14 B5050_100	13.60	1.02	1.04	-0.2	4.0	-17.2	-12.3	-17.7	-12.8
Wg5 B7550_100A	7.70	1.06	1.09	-53.0	-38.9	-57.9	-43.4	-20.8	-9.7
Wg6 B7550_84A	8.20	1.08	1.11	-57.7	-40.8	-62.8	-45.4	-24.6	-11.2
Wg8 B7550_100C	8.40	1.08	1.09	-25.4	-14.1	-25.8	-14.4	-25.2	-13.9
Wg9 B7550_100D	8.60	1.18	1.14	-33.1	-15.7	-33.5	-16.0	-32.8	-15.5
Wg12 B7550_100A	9.10	1.11	1.11	-26.1	-12.9	-17.2	-4.9	-13.0	-1.1
Wg12 B7550_100B	--		1.11						
Wg14 B7550_100A	8.60	1.01	1.03	-21.9	-17.4	-13.2	-9.0	-9.4	-5.3
Wg5 B10050_100A	4.30	1.09	1.11	-49.5	-32.5	-51.3	-34.2	-17.4	-4.1
Wg6 B10050_100C	5.20	1.13	1.12	-75.0	-53.3	-77.2	-55.3	-37.5	-20.5
Wg8 B10050_100A	5.10	1.23	1.12	-14.8	-1.4	-22.0	-7.8	-16.8	-3.2
Wg9 B10050_100C	4.80	1.17	1.10	-12.4	-0.8	-19.2	-6.9	-14.2	-2.5
Wg12 B10050_100A	6.20	1.31	1.09	-21.4	-10.0	-16.9	-5.9	-11.6	-1.1
Wg14 B10050_100A	6.40	1.30	1.06	-22.6	-14.4	-17.4	-9.6	-12.2	-4.7
Wg5 B10050_100A	--		1.11						
Wg6 B10050_100C	--		1.12						
Wg8 B10050_100A	--		1.12						
Wg9 B10050_100C	--		1.10						
Wg12 B10050_100A	--		1.09						
Wg14 B10050_100A	--		1.06						

The highlighted values identify the optimal compliance model for each set of devices. All but three devices are described by the theoretical frequencies to within 16% of the observed acoustic transmit. We observe that the calculations using the confined vibrational dimensions describe the observed transmit frequencies better than those developed using the full etched dimensions. The theoretical transmit frequency is thus best given by the equation

$$f^{t}_{tx,H2O} = C^{confined}_{H2O,CCCC} * C^{full}_{compliance}(t,L) * f^{t,confined}_{Mindlin,air} \tag{8.5}$$

Plotting the theoretical transmit frequency curves and comparing to the observed transmit frequencies from Wg- and A-series devices (shown in Figure 8.2), we find that theoretical values describe the observed data very well.

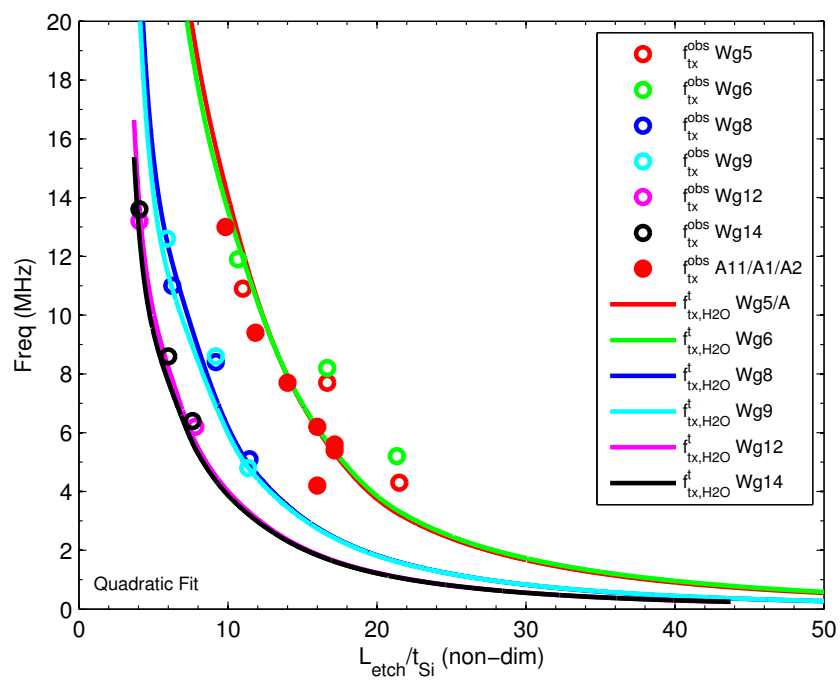

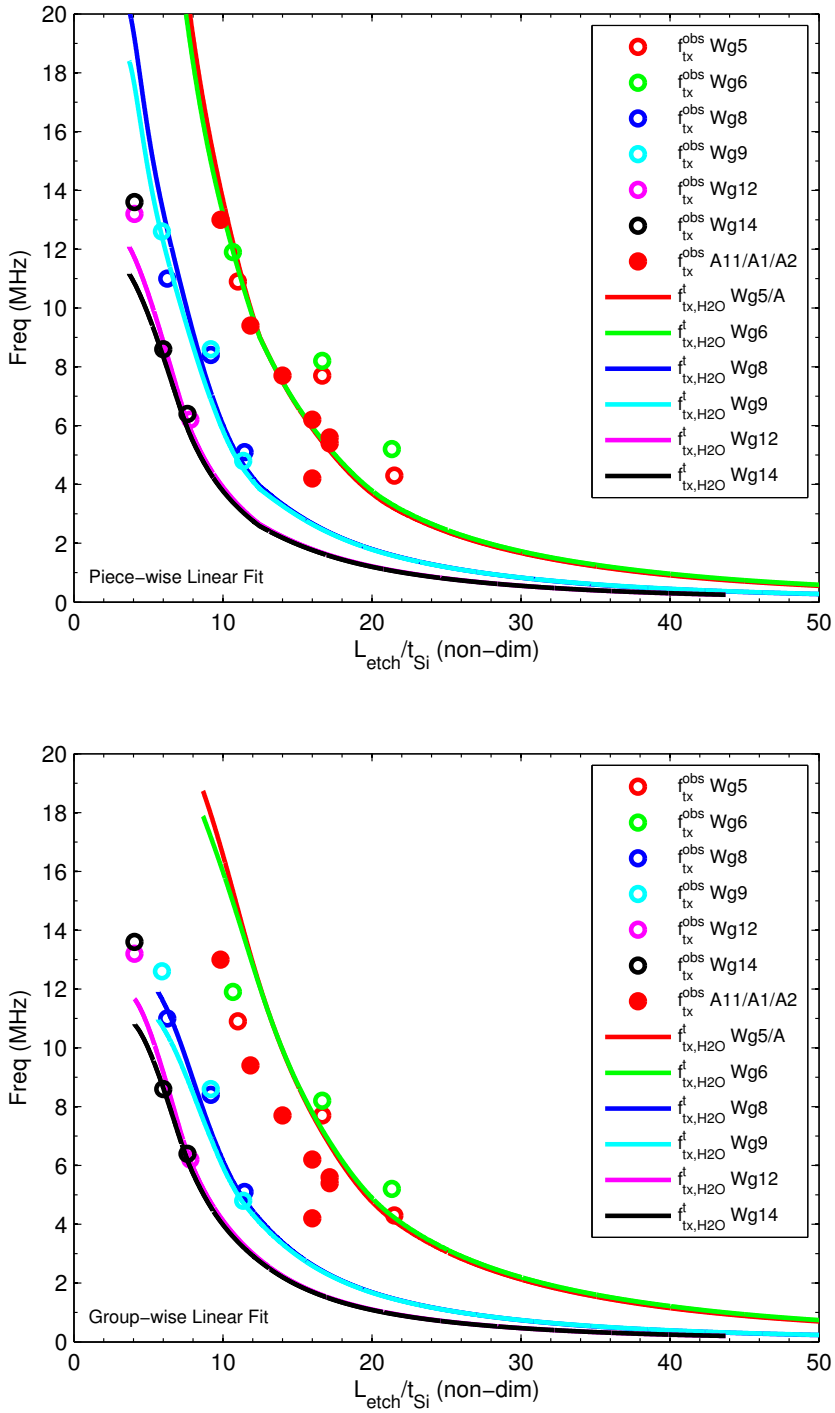

Figure 8.2: Theoretical and observed optimal acoustic transmit frequencies in water for imaging applications. Theoretical f^{t}_{tx} calculated using quadratic (top), piece-wise (middle), and group-wise (bottom) compliance models.

Calculating the R^2 between the theoretical and observed receive frequencies using the different compliance models (Table 8.7), we see that the theoretical frequency calculated using the quadratic, piece-wise, and group-wise compliance models are an excellent fit to the observed data.

Table 8.7: R^2 values for theoretical and observed transmit frequencies for Wg- and A-series devices.

Compliance Fit Model	$R^2_{freq,Tx}$
Linear	0.2730
Quadratic	0.8465
Piece-wise Linear	0.8509
Group-wise Linear	0.5990

These results demonstrate that an equation based on Mindlin plate theory and incorporating the effect of water loading and compliant support may be used to accurately predict f^t_{tx} using Equation 8.5. The transmit frequency is shown to be best described as a confined fundamental mode calculated using the etched width and the PZT length (smaller than the etched length) as the plate dimensions.

8.5 Higher Order Modes

The 200μm devices were shown by optical vibrometry to operate in a higher order mode in transmit. These higher-order modes were omitted in the modeling efforts presented previously, requiring separate treatment. The following analysis will focus on the modeling methods for this data set only. First, the changes to the theory required to model higher-order vibration will be considered. The higher-order frequencies observed using optical vibrometry in air and water will then be compared to the theory. Finally,

the higher-order acoustic transmit frequencies measured in the water tank will be compared to the theory.

Consider the general equation used to model the vibration of pMUTs in water

$$f_{H2O}^{t} = C_{H2O,CCCC}^{full/conf} * C_{compliance}^{full}(t,L) * f_{Mindlin,air}^{t,full/conf} \tag{8.6}$$

where the compliance term is calculated using the full etched dimensions while the Mindlin frequency in air and water-loading terms may be taken with either full or confined dimensions. Both the water-loading factor and the theoretical Mindlin frequency in air are well-defined for higher-order modes. In the latter component, the frequency increase is accounted for entirely in an increased frequency parameter. Computed tables of higher-order mode frequency parameters were adapted for use with pMUTs. Note that in the literature, the frequency parameters are given for mode *sequences* of increasing amplitude. However, the specific mode *shapes* (1-1,1-3,3-1,etc) are not always consistent with a single mode sequence number. The lowest mode sequence is always the fundamental 1-1 mode, however the order of the subsequent higher modes is dependent on the aspect ratio of the plate under consideration.

The compliance models developed previously are applicable for fundamental mode operation only. With only one device dimension set operating in a higher order mode, a substantive compliance model cannot be determined. For this reason, the compliance term will be omitted in parts of the following analysis. While it is likely that compliance of the edge supports impacts higher-order vibration, it is reasonable to favor omission of this term until a more comprehensive characterization of the compliance effects at higher-order modes is completed. The compliance factor from the fundamental mode will be

included in the analysis of optically observed frequencies, but will be omitted when the acoustic transmit frequencies are considered.

Additionally, the limited optical measurements available at present do not provide definitive evidence of full or confined vibrational dimensions. Both dimension sets will be considered in the following analysis.

Recalling the multiple higher-order mode frequencies observed using optical methods, 1-1, confined 1-1*, 1-2/2-1, 1-3 and 3-1 modes were observed in air and 1-1, confined 1-1*, and 3-1 modes were observed in water. Using the appropriate frequency parameters λ^2 for higher-order modes, the Mindlin frequencies were obtained for the Wg8 B200 physical specifications. Combinations of these higher-order Mindlin frequencies with compliance and water-loading factors yield possibilities for the theoretical higher-order vibration, given in Table 8.8 with observed frequencies from optical methods for comparison. Note that theoretical values for higher-order modes that include the compliance factor use the fundamental 1-1 mode compliance term and are italicised. The compliance for higher-order modes is expected to contribute less to decreasing the frequency of vibration than in the fundamental case, thus these values represent a lower-bound to the theoretical frequency.

Table 8.8 shows that the theoretical frequencies offer moderate approximation of the observed higher-order frequencies. The observed frequencies in air fall between the theoretical frequencies with and without compliance. In water, the theoretical 3-1 mode with compliance is within 6% of the observed frequency. Further development of the compliance modeling for higher-order modes will offer refinement and greater accuracy to this theory.

Table 8.8: Calculated higher-order frequencies for Wg8 B200 device specifications under air- and water-loading. Observed frequencies from optical vibrometry included for comparison.

			Air			H2O		
	Device	**Mode**	$f^{obs}_{optical}$ **(MHz)**	$f^{t}_{Mindlin}$ **(MHz)**	$f^{t}_{M} * C_{comp}$ **(MHz)**	$f^{obs}_{optical}$ **(MHz)**	$f^{t}_{M} * C_{H2O}$ **(MHz)**	$f^{t}_{M} * C_{H2O} * C_{comp}$ **(MHz)**
Full	Wg8 B200	1-1	1.83	2.46	1.74	1.16	1.69	1.20
		1-2	(5.47)	4.21	*2.98*	--	--	--
		2-1		5.39	*3.82*		--	--
		1-3	(5.69)	6.92	*4.90*	--	6.28	*4.45*
		3-1	(7.81)	9.63	*6.82*	(5.88)	8.74	*6.19*
Conf		1-1 *	2.63	2.75	1.91	1.73 2.79 3.21	1.93	1.33
		1-2 *	(5.47)	5.16	*3.57*	--	--	--
		2-1 *		5.62	*3.89*		--	--
		1-3 *	(5.69)	8.75	*6.05*	--	7.99	*5.52*
		3-1 *	(7.81)	9.84	*6.81*	(5.88)	8.98	*6.21*

* designates confined dimensions
() designate obs freq repeated in both full and confined modes
italics designate C_{comp} of 1-1 mode applied to higher-order modes [unconfirmed by experiment]

Next, consider the high-order acoustic transmit frequencies measured in the water tank. Table 8.9 presents the theoretical higher-order modes calculated using the specifications of the Wg-series 200µm devices. Both 1-3 and 3-1 modes are presented using full and confined dimensions. The observed higher-order transmit frequencies are provided for comparison.

Table 8.9: Theoretical Mindlin frequencies for 1-3 and 3-1 modes in comparison to observed acoustic transmit frequencies (shown to be higher-order from optical vibrometry). Theoretical frequencies are calculated for full and confined dimensions and include the decrease in frequency due to water loading. The effect of compliant support is not included.

		1-3		3-1	
Device	f^{obs}_{tx} **(MHz)**	$f^{t}_{H2O,full}$ **no compliance (MHz)**	$f^{t}_{H2O,conf}$ **no compliance (MHz)**	$f^{t}_{H2O,full}$ **no compliance (MHz)**	$f^{t}_{H2O,conf}$ **no compliance (MHz)**
Wg5 B200100_100D	3.80	3.24	4.13	4.51	4.64
Wg6 B200100_100B	4.30	3.22	4.10	4.48	4.61
Wg8 B200100_100A	6.50	6.28	7.98	8.74	8.98
Wg9 B200100_100C	6.80	6.02	7.65	8.38	8.61
Wg12 B200100_100B	8.40	9.77	12.41	13.60	13.95
Wg14 B200100_100D	8.60	9.90	12.56	13.78	14.12

While a theoretical frequency for each device may be found within Table 8.9, no consistent formulation is adequate in describing all of the 200μm devices. The 3-1 mode using confined dimensions fits the thinnest Wg5 and 6 devices well, but produces frequencies higher than the observed for thicker devices. With the addition of a compliance factor, it is expected that the theoretical 3-1 mode with confined dimensions will provide sufficient approximation of the higher-order vibration of pMUTs. Unfortunately, a wider range of device sizes and thicknesses capable of higher-order vibration must be evaluated in order to form an adequate compliance model to be applied here. However, the higher-order vibration of pMUTs has not been shown to produce promising imaging results, so continued exploration of higher-order frequency theory is unlikely to benefit the current imaging applications of pMUTs.

8.6 Summary

The methods described in this chapter have shown to provide excellent models of the fundamental-mode vibrational frequencies in water for imaging applications. The optimal acoustic transmit or receive frequencies in water are well-described by the analytical methods given. Expansion of these model equations into dimensional and material property terms can be used to guide the design of future pMUT devices.

Combining the equations for water-loading (Eq. 6.20), support compliance (Eq. 7.6, quadratic fit), and fully-clamped Mindlin frequencies (Eq. 7.1), we can express an expanded form of the general equation (Eq. 8.6, reproduced here) for pMUT fundamental-mode frequencies in water as shown in Eq. 8.7 and 8.8.

$$f^{t}_{H2O} = C^{full/conf}_{H2O,CCCC} * C^{full}_{compliance}(t,L) * f^{t,full/conf}_{Mindlin,air} \tag{8.6}$$

The equations for optimal acoustic transmit and receive are found by using the appropriate structural dimensions in Eq. 8.6, yielding either full or confined vibrational dimensions. For the optimal acoustic receive frequencies, the etched cavity length is used such that

$$f^{t}_{Rx,H2O} = \sqrt{\frac{1}{1+\left(\frac{\gamma_w}{\gamma}\right)\left(\frac{L_{etch}}{t_{tot}}\right)\left(\frac{C_{vm}}{2}\right)\left(\frac{A^2_{ij}}{B_{ij}}\right)}} * \left[1-5.55\left(\frac{t_{Si}}{L_{etch}}\right)+12.65\left(\frac{t_{Si}}{L_{etch}}\right)^2\right]$$
$$* \frac{\lambda^2_{mn}(L_{etch},W_{etch},t_{tot})}{2\pi W^2_{etch}}\sqrt{\frac{E\,t_{tot}^{\;2}}{12\rho(1-v^2)}} \tag{8.7}$$

where length, width, and thickness dimensions are given by *L, W,* and *t,* respectively, and subscripts describe specific structural dimensions.

In the water-loading term, γ_w/γ is the dimensionless ratio of the mass density of water to that of the plate, C_{vm} is a "virtual mass function" dependent on the plate aspect ratio, and *A* and *B* are mode-dependent coefficients given for mode *i-j* for the CC condition. In the Mindlin frequency term, ρ is the composite plate density, ν is the Poisson's ratio (~0.3), λ^2_{mn} is the frequency parameter taken from the interpolation of tabled values (dependent on *L*,*W*, and *t*), and *E* is the Young's modulus of the composite plate (from measurement or calculation from composite plate flexural rigidity, *D*). The compliance term given is for the quadratic model, which for devices where $\frac{t_{Si}}{L_{etch}} < 0.25$ provides the most consistent results.

For the optimal acoustic transmit frequencies, the PZT film length is used such that

$$f^{t}_{Tx,H2O} = \sqrt{\frac{1}{1+\left(\frac{\gamma_w}{\gamma}\right)\left(\frac{L_{PZT}}{t_{tot}}\right)\left(\frac{C_{vm}}{2}\right)\left(\frac{A^2_{ij}}{B_{ij}}\right)}} * \left[1-5.55\left(\frac{t_{Si}}{L_{etch}}\right)+12.65\left(\frac{t_{Si}}{L_{etch}}\right)^2\right]$$

$$* \frac{\lambda^2_{mn}(L_{PZT}, W_{etch}, t_{tot})}{2\pi W^2_{etch}} \sqrt{\frac{E\, t_{tot}{}^2}{12\rho(1-v^2)}}$$

(9.8)

These two equations constitute the predictive design theory desired for the frequency control of pMUTs. The selection of the appropriate equation to use is dependent on the intended application, though in general, using both the transmit and receive frequency equations in concert will help to establish both cavity and PZT film lateral dimensions. Careful selection of the relationship between cavity and PZT dimension will allow increased control of the frequency separation between transmit and receive operating points.

Chapter 9

Discussion

9.1 Application of the pMUT Frequency Theory

9.1.1 Transducer Design - Balancing Frequency, Efficiency, Sensitivity, and Physical Dimensions

The pMUT frequency theory presented has been shown to provide excellent quantitative description of the optimal fundamental-mode transmit and receive frequencies for imaging applications. However, the operating frequency is one of several aspects taken into consideration for the design of an ultrasound transducer. The physical dimensions, efficiency in transmit, and sensitivity in receive are just a few other parameters that require consideration in the design process.

The physical transducer dimensions in catheter-based imaging applications are extremely tight and must be strictly controlled. Taking the cabling and interconnect into consideration, the footprint of the transducer array must fit within an 8 or 10Fr catheter. Therefore, the element size and pitch must be carefully selected to permit the desired number of array elements within the allowable device footprint. Additionally, the thickness of the element must be neither too thin to cause mechanical failure nor too thick to prohibit flexure while remembering that the t/L relationship plays a significant role in the frequency and sensitivity of pMUTs.

Acoustic measurements have revealed that the transmit efficiency is higher for membrane thicknesses of 5-10μm while 15mm membranes experience a dampening of

transmit output and efficiency. This is particularly true for devices with smaller edge dimensions where the thickness to length is even greater. The relationship of transmit efficiency to length is somewhat inconsistent, though devices up to 75µm in nominal length fall within reasonable proximity of each other. Devices with 100 and 200µm lengths are typically poorer due to higher-order mode contributions. The recommended range of device dimensions to optimize transmit efficiency are those with <10µm thickness and <75µm length.

The receive sensitivity follows a more consistent trend, with sensitivity increasing with element length up to 100µm. This is likely an area effect, where the greater surface area is favored for the incident pressure to act upon. Devices with 200µm length were shown to have a diminished sensitivity compared to 100µm devices for 5 and 10µm thick elements. Thinner devices (5 and 10µm) also perform more favorably than thicker (15µm) devices with regard to receive sensitivity. The recommended device dimensions for optimal receive sensitivity are <10µm thickness and <100µm length while seeking as large an area per element as is feasible based on other criteria.

Choosing the design parameters of pMUT arrays for imaging applications requires a careful balance of all of these performance metrics. Before proceeding with the full design methodology, an educated approximation of the element dimensions and thickness will aid in applying the frequency design equations. The frequency plots and curves provided in the results and analysis may be used as a general guideline for device dimensions. A pre-selected aspect ratio to be held fixed throughout is recommended (preferably in the range 1.25-1.75), though it should be noted that the aspect ratios used

to develop the previously plotted frequency curves was variable with device size. If the equation for f_{tx} is used, a pre-selected L_{PZT}-L_{etch} ratio is recommended to simplify calculation.

The recommended design methodology then begins by selecting the target imaging frequency (transmit or receive) in water and choosing the appropriate corresponding frequency equation. Each term of the frequency equation can be expressed as a function of t and L, with $W=L/\phi$. If a desired t_{PZT} is chosen, then for any given t_{tot}, the frequency is dependent on L only. Plotting the frequency curve (Figure 9.1) for each t_{tot} against L or L/t, the appropriate L for the desired frequency can be found.

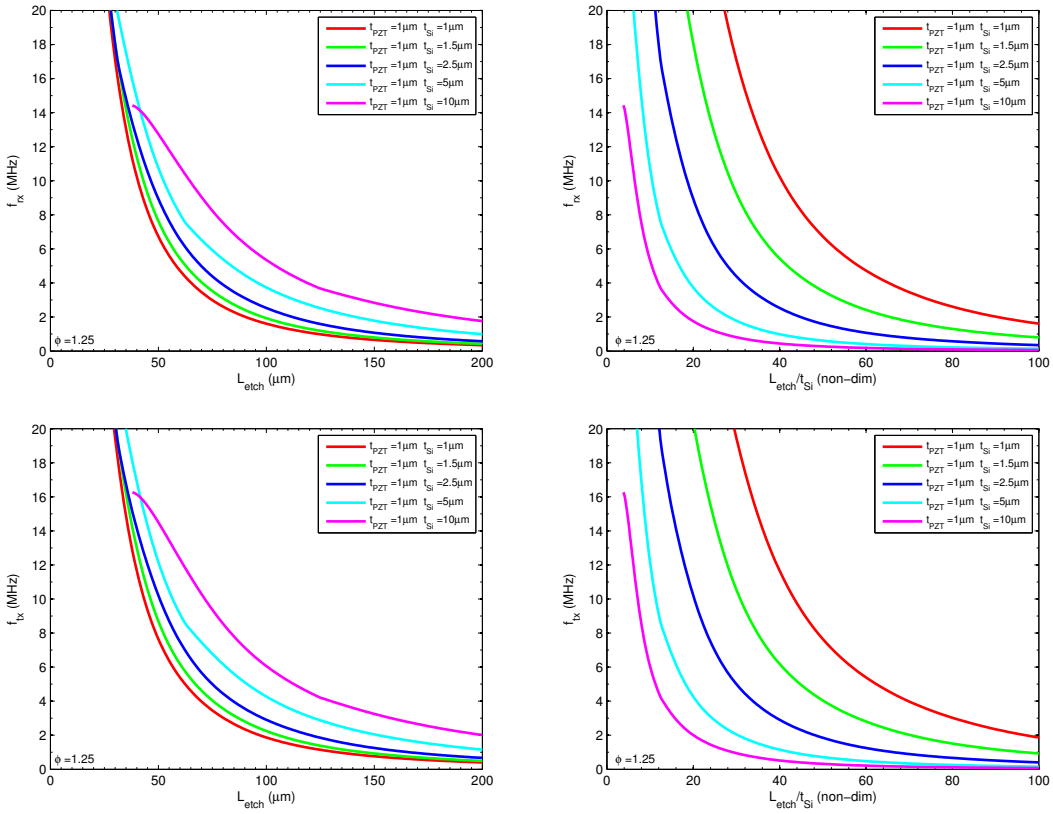

Figure 9.1: f_{rx} and f_{tx} frequency curves for multiple thicknesses with AR=1.25, t_{PZT}=1µm, $W_{PZT}=W_{etch}*1.05$, $L_{PZT}=L_{etch}*0.85$. (top left) f_{rx} vs. L_{etch}, (top right) f_{rx} vs. L_{etch}/t_{Si}, (bottom left) f_{tx} vs. L_{etch}, (bottom right) f_{tx} vs. L_{etch}/t_{Si}.

If the lateral dimensions are not within the constraints for the application, increasing the t_{tot} may help to bring the necessary L lower. However, lower and upper bounds do exist on the frequencies possible with a given L due to the feasibility of manufacturing very thin membranes (lower bound) or when the plate thickness is large enough to prohibit flexure. Also, the frequency equations given hold for plates with $t/L<0.27$. Therefore, not all frequencies will be available for any given element size, and it is to be expected that the dimensions required for higher frequencies (>12MHz) result in smaller device area and thus lower receive sensitivity.

Once the proper dimensions for the desired transmit or receive frequency are determined, the other frequency can be determined by adjusting the ratio of L_{PZT}:L_{etch}. The transmit and receive frequency gap is tunable by changing the short dimensions of the PZT to cover more or less of the cavity. Covering the entire cavity should leave both frequencies the same.

The frequency curves shown in Figure 9.1 exemplify calculated f_{rx} and f_{tx} for t_{Si}=1, 1.5, 2.5, 5, 10µm, t_{PZT}=1µm, AR=1.25, $W_{PZT}=W_{etch}*1.05$, $L_{PZT}=L_{etch}*0.85$. For a given frequency, by choosing the curve with the best t_{tot} to balance transmit efficiency and receive sensitivity, the appropriate L_{etch} can be found.

9.1.2 Limitations of the pMUT Frequency Theory

While the presented theory has been shown to provide predictive frequency results within 20% of the observed resonant frequencies of fabricated pMUTs, a number of constraints currently limit the effectiveness and accuracy of the model.

The primary limitation of the pMUT frequency theory is the empirical basis by which the constants for compliant support are derived. While founded on Mindlin plate theory and established based on a demonstrated principle of compliant edge support, the quantitative analysis of the compliant support is heavily dependent on the material properties of the membrane and substrate. The quantitative values used to describe the compliant boundary conditions have been developed from the observed frequencies of physical devices. Thus, the current theory is limited to membranes falling within the range of tested device dimensions, particularly the aspect ratio ($1.25<L/W<1.65$) and relative thickness ($t/L<0.27$).

The current theory is not only limited to these ranges, but has been developed assuming the relationship between the aspect ratio and relative thickness maintain the trends by which existing pMUTs have been made. Smaller devices (~50μm) fall on the larger side of the range of aspect ratios and are thus longer and more bar-like, while larger devices trend toward a more square-like aspect ratio. In order for the theory to account for both changing aspect ratios and variations in relative thickness, interpolation over the range of aspect ratios (Fig. 7.7) was employed to produce a comprehensive compliance model. Devices fabricated outside of this trend will likely be poorly modeled by the frequency theory currently presented.

9.2 Future Work

9.2.1 Measuring Composite E_{PMUT} or E_{PZT}

Determination of the elastic modulus of the deposited PZT is possible by constructing a cantilever unimorph structure with large length compared to the thickness. By measuring the resonant frequency of vibration and deflection of the cantilever in the presence of a known load, classical beam theory can be used to back-calculate the composite and PZT moduli given known values for the Si substrate and the dimensions of the beam. The use of a cantilever structure eases the theoretical calculation as the vibration of long, thin cantilevers relies on only a single fixed boundary which can be idealized as rigidly clamped, minimizing the effect of compliant support, and has been well-documented.

Using a plate structure introduces more complexity in the theoretical formulation, but if simplified geometries such as square or circular plates are used, some of the complexity can be avoided as such structures are well-documented. However, with suspended plates and membranes, there remains a degree of uncertainty in the size of the cavity below, which can be estimated by measuring test structures on the same wafer. The dimensions of cantilever structures, however, can be measured directly which reduces these uncertainties considerably.

9.2.2 Broader Range of Device Dimensions

The pMUT frequency theory was developed from empirical evidence covering a subset of the possible structural configurations and is thus limited in application to devices with similar dimensions. The current theory can be expanded to build a more

robust and descriptive theory by fabricating and testing devices over a comprehensive set of aspect ratios and relative thicknesses. Collecting empirical data over a wider range in both metrics will help separate the two variables and their independent effects on frequency and will improve the efficacy of the frequency theory by diminishing the need for interpolation and introducing greater accuracy in the compliance models.

9.2.3 Optical Vibrometry

Measurement of more pMUT devices using optical vibrometry will help elucidate many operating characteristics not observable using acoustic and electrical methods alone. The frequencies, mode shapes, vibrational dimensions, and crosstalk/coupling effects were measured for only two devices. Continued measurement and analysis using optical vibrometry can be used to develop a more comprehensive theory of operation.

Vibrational dimensions may differ depending on cavity sizes, layer thicknesses, or other device parameters. Higher-order mode shapes may be suppressed after a certain relative thickness is reached. The resonant oscillation frequency that travels throughout the array structure can be examined more closely. Other experiments with electrical crosstalk or mechanical coupling can be performed to study not just single element operation, but inter-element interactions as well.

9.2.4 Limiting Resonant Oscillation

The long-duration resonant oscillation has been shown to degrade dynamic range, bandwidth, and axial resolution. Driving the pMUTs off-resonance improves the bandwidth without sacrificing much transmit efficiency or receive sensitivity. However,

other methods of minimizing the resonant oscillation can be explored. Depositing dampening/absorptive material around the silicon die should reduce the oscillation amplitude, improving bandwidth and dynamic range. Thin matching layers deposited on the surface might help to couple energy out of the device silicon.

Fabrication of new device structures may also yield substantial benefits to pMUT imaging. The use of etched trenches in the device silicon between elements might limit the lateral propagation of mechanical energy. Different cavity geometries such as trapezoids or rhomboids might decrease lateral mechanical coupling as well. Many new structural possibilities exist and may yield breakthroughs in the performance of pMUTs for imaging.

9.3 Conclusions

The results presented in this dissertation prove that the frequency of vibration of pMUTs can be predictively modeled based on experimental data from various pMUT configurations. Acoustic and optical experimental methods, measurements, and results were presented from 2D pMUT arrays demonstrating their suitability for imaging in tissue and tissue-like phantoms. Moreover, the fundamental mode frequencies from resonant oscillation and optimal acoustic transmit and receive were analyzed. Comparison to conventional Mindlin theory showed that idealized clamped and simply-supported boundary conditions are insufficient to describe pMUT vibration. Models for compliant support were used to modify the boundary conditions in Mindlin theory. The modified Mindlin theory was applied to devices not included in the model development

to demonstrate the theory's predictive capability for pMUT resonant oscillation as well as optimal acoustic transmit and receive frequencies for imaging applications.

This modified Mindlin theory presents a predictive, quantitative description of pMUT vibration that had not been available previously. It is hoped that these results contribute to the ongoing development of pMUTs for forward-looking, catheter-based ultrasound imaging.

Appendix A

Vibration of Strings, Bars, and Plates

A.1 Vibration of Strings and Thin Bars

The approach and derivations provided in this section are adapted from Rossing and Fletcher [72].

A.1.1 Transverse Wave Equation for a String

By examining the net force on a string segment of length *ds* displaced by *dy* under tension *T* to form an angle θ, the net force dF is found to be the difference between the y components of T at the two ends of the segment.

$$dF_y = (T\sin\theta)_{x+dx} - (T\sin\theta)_x \tag{A.1}$$

Applying a Taylor's series expansion $f(x+dx) = f(x) + \frac{\partial f(x)}{\partial x}dx + \ldots$ to Tsin θ and keeping only first order terms,

$$dF_y = \frac{\partial(T\sin\theta)}{\partial x}dx \tag{A.2}$$

for small displacement y, sin θ can be replaced by tan θ=dy/dx, giving

$$dF_y = T\frac{\partial^2 y}{\partial x^2}dx \tag{A.3}$$

The mass of the segment, ds, is μds, so Newton's second law of motion becomes

$$T\frac{\partial^2 y}{\partial x^2}dx = (\mu ds)\frac{\partial^2 y}{\partial t^2} \tag{A.4}$$

Because dy is small, ds≈dx and writing c^2=T/μ, we find

$$\frac{\partial^2 y}{\partial t^2} = \frac{T}{\mu}\frac{\partial^2 y}{\partial x^2} = c^2 \frac{\partial^2 y}{\partial x^2} \tag{A.5}$$

where T is the tension in the string and μ is the mass per unit length.

A.1.2 Longitudinal Wave Equation for a String or Thin Bar

The equation of motion for longitudinal waves in a string or thin bar are found by applying Hooke's law for the stress and strain on a segment of the string. Taylor series expansion and differentiation can be used to find an expression for the net force acting on the segment and Newton's second law of motion is used to define the equation of motion,

$$\frac{\partial^2 w}{\partial t^2} = \frac{E}{\rho}\frac{\partial^2 w}{\partial x^2} = c_L^2 \frac{\partial^2 w}{\partial x^2} \tag{A.6}$$

where E is the Young's modulus in the string and ρ is the mass per unit volume. The longitudinal wave velocity is given by $c_L = \sqrt{E/\rho}$.

The normal modes of vibration for a structure with both ends fixed is then given by

$$f_n = n\frac{c}{2L} \qquad n=1, 2, 3, \ldots \tag{A.7}$$

A.2 Vibration of Bars

The approach and derivations provided in this section are adapted from Kinsler & Frey [73] and Rossing & Fletcher [72].

A.2.1 Bending Waves in a Bar

Transverse vibrations in bars and rods are somewhat similar to strings, however, frequency dependence on tension is more complicated. In fact, bars can vibrate under zero tension, with the elastic forces in the bar providing the restoring force in the force balance of the unit element.

The result of bending a unit segment of a bar produces stress and strain as a result of the elongation or compression on portions above or below the neutral axis. For a filament located at a distance z below the neutral axis, compression by an amount $d\phi$ produces a strain $z\, d\phi/dx$. The relationship between stress and strain for a material is given by the Young's modulus such that the force dF required to produce strain $z\, d\phi/dx$ is

$$dF = E\, dS\, z \frac{d\phi}{dx} \tag{A.8}$$

where dS is the cross-section of the filament and E is the Young's modulus.

The moment of this force about the neutral axis is $dM=[E\, dS\, z\, (d\phi/dx)]z$. The total moment over all filaments in the bar is thus

$$M = \int dM = E \frac{d\phi}{dx} \int z^2 dS \tag{A.9}$$

Defining a radius of gyration, K, for the cross-section such that

$$K^2 = \frac{1}{S} \int z^2 dS \tag{A.10}$$

the bending moment becomes

$$M = E \frac{d\phi}{dx} SK^2 \cong -ESK^2 \frac{\partial^2 y}{\partial x^2} \tag{A.11}$$

because $d\phi \cong -\left(\frac{\partial^2 y}{dx^2}\right)dx$ for small $d\phi$. For a rectangular cross-section, $K = h/\sqrt{12}$.

In order for the bar to remain in equilibrium, there must be shearing forces F with moment $F\,dx$ at the ends of the bar such that $F\,dx = dM$, giving

$$F = \frac{\partial M}{\partial x} = -ESK^2 \frac{\partial^3 y}{\partial x^3} \tag{A.12}$$

However, the shearing force is not constant, producing a net force $dF = (\partial F / \partial x)\,dx$ which causes an acceleration perpendicular to the axis of the bar. The equation of motion, then, becomes

$$\left(\frac{\partial F}{\partial x}\right)dx = (\rho\, S\, dx)\frac{\partial^2 y}{\partial t^2}$$

$$-ESK^2 \frac{\partial^4 y}{\partial x^4} = \rho\, S \frac{\partial^2 y}{\partial t^2}$$

$$\frac{\partial^2 y}{\partial t^2} = -\frac{EK^2}{\rho}\frac{\partial^4 y}{\partial x^4} \tag{A.13}$$

The displacement is then found to be

$$y = \cos(\omega t + \phi)\left[A\cosh\frac{\omega x}{v} + B\sinh\frac{\omega x}{v} + C\cos\frac{\omega x}{v} + D\sin\frac{\omega x}{v}\right] \tag{A.14}$$

where v is the wave velocity $v^2 = \omega K\sqrt{E/\rho} = \omega K c_L$ and the constants A, B, C, D can be found using the boundary conditions of the bar.

The vibrational frequencies can then be found by identifying the roots of the equations resulting from the displacement function above and the boundary conditions. Thorough solutions to common examples are given in the literature, with Kinsler & Frey

[73] and Rossing & Fletcher [72] giving excellent explanation and overview. The vibrational frequencies for 3 common examples are given below.

Simple support on both ends:

$$f_n = \frac{\pi c_L K}{2L^2} m^2 \qquad m=1, 2, 3, \ldots \tag{A.15}$$

Clamped on one end

$$f_n = \frac{\pi c_L K}{8L^2}\left[1.194^2, 2.988^2, 5^2, 7^2, \ldots, (2n-1)^2\right] \tag{A.16}$$

Free on both ends

$$f_n = \frac{\pi c_L K}{8L^2}\left[3.0112^2, 5^2, 7^2, 9^2, \ldots, (2n+1)^2\right] \tag{A.17}$$

A.2.2 Boundary Conditions for a Bar

Three simple boundary conditions for the ends of the bar commonly considered in vibration analysis are free (F), simply supported (SS), and clamped (C). At a free end, there is no torque and no shearing force, so the second and third derivatives of y are both zero. At a simply supported edge, there is no displacement and no torque, so y and its second derivative are both zero. At a clamped end, there is no displacement and no velocity, so y and its first derivative are zero.

Free $\partial^2 y/\partial x^2 = 0,\ \partial^3 y/\partial x^3 = 0$

Simply Supported $y = 0,\ \partial^2 y/\partial x^2 = 0$

Clamped $y = 0,\ \partial y/\partial x = 0$

Solutions to the equation of motion for bars with different boundary conditions can be found in the literature (Rossing & Fletcher provides a good overview).

A.2.3 Rotary Inertia and Shear Deformation in Thick Bars

Thus far, transverse motion of the bar has been considered due only to the bending moment or stiffness of the bar. This simplified condition is often called the Euler-Bernoulli beam. For long, thin bars or rods, this condition is sufficient. However for bars considered thick compared to their length, it is necessary to include the effects of the rotary inertia and shear stress, often called the Timoshenko beam.

As a beam bends, the elements of the beam rotate through some small angle. The rotary inertia is thus equivalent to an increase in mass and results in a slight lowering of the vibrational frequencies, particular for higher modes.

Shear forces tend to decrease the transverse deflection of the bar, thus also contributing to decreasing the frequency, particularly for higher order modes.

Overall, vibrational frequencies are decreased slightly for thick bars compared to thinner ones. As this research focuses on rectangular plates, the topic of thick bars will not be discussed further, except to say that the effects of shear deformation and rotary inertia influence plate vibration in similar ways.

A.3 Vibration of Rectangular Plates – Thin Plates

A.3.1 Waves in a Thin Plate

Like a bar, a plate can support longitudinal (compressional) waves, shear waves, torsional waves, or a bending wave [74]. Longitudinal, shear, and torsional waves, typically occur in structures that are large compared to the wavelength in all three dimensions. Longitudinal, shear, and torsional waves are capable of generating very little acoustic radiation compared to bending waves. Thus, bending waves are of the greatest relevance in the development of a vibrational frequency theory for pMUTs and are the only type that will be considered here.

A.3.2 Equation of Motion for a Thin Plate

The derivation of the differential equation governing the pure bending of plates under static transverse loading is presented in detail by Timoshenko [75], given by

$$\frac{Eh^3}{12(1-v^2)}\nabla^4 W(x,y) = q(x,y) \tag{A.18}$$

where $W(x,y)$ is the plate displacement, ρ is the volume density, v is Poisson's ratio, E is Young's modulus, h is the plate thickness, $q(x,y)$ is the applied static load, and $\nabla^4 = \nabla^2\nabla^2$, where ∇^2 is the Laplacian operator.

For free vibration of the plate, the loading, q, is equal to zero. However, an inertial force due to the motion of the plate must be accounted for and replaces the static loading.

The classical differential equation of motion for transverse displacement $W(x,y,t)$ of a plate by bending is [50]

$$\rho h \frac{\partial^2 W(x,y,t)}{\partial t^2} + \frac{Eh^3}{12(1-v^2)} \nabla^4 W(x,y,t) = 0 \tag{A.19}$$

where t is time. This equation can also be rewritten in the form (Leissa)

$$D\nabla^4 W + \rho h \frac{\partial^2 W}{\partial t^2} = 0 \tag{A.20}$$

where D is the flexural rigidity of the plate defined by

$$D = \frac{Eh^3}{12(1-v^2)} \tag{A.21}$$

We can choose to express the displacement $W(x,y,t)$ as the product of two functions, one involves spatial coordinates x and y while the other involves time t, such that $W(x,y,t) = W(x,y)\,T(t)$. Further, we select $T(t) = A \sin(\omega t + \alpha)$ where ω describes the frequency of oscillation (rad/sec) and α describes the phase of the time-varying vibration. The equation of motion then becomes

$$\nabla^4 W(x,y) - \frac{\omega^2 \rho h}{D} W(x,y) = 0 \tag{A.22}$$

which is now a function of the plate mode shape expression $W(x.y)$, the plate properties, and the circular frequency ω. Variation of the plate vibration in time is then described solely by ω.

The equation above governs the free vibration of all thin flat plates undergoing small amplitude vibration. Solutions to this differential equation that satisfy any prescribed boundary conditions will provide the necessary description of plate vibration that will be applied to pMUTs.

The expression of the equation of motion in dimensionless form allows advantageous scaling using a single solution set as will be shown later. Dimensionless spatial variables

ξ and η are presented where $\xi = x/a$ and $\eta = y/b$, and a and b are the dimensions of the plate. By appropriately multiplying or dividing the variables x and y by quantities a and b in the equation of motion and rearranging, a dimensionless form is obtained

$$\frac{\partial^4 W(\xi,\eta)}{\partial \eta^4} + 2\phi^2 \frac{\partial^4 W(\xi,\eta)}{\partial \xi^2 \partial \eta^2} + \phi^4 \frac{\partial^4 W(\xi,\eta)}{\partial \xi^4} - \phi^4 \lambda^4 W(\xi,\eta) = 0 \qquad \text{(A.23)}$$

where $\lambda^2 = \omega a^2 \sqrt{\rho h / D}$ and the plate aspect ratio is $\phi = b/a$.

Solutions to this differential equation will be presented by values of λ^2 that satisfy any prescribed plate boundary conditions for given aspect ratios and plate mode shapes and will provide the necessary description of plate vibration that will be applied to pMUTs. The frequency of oscillation can then be found using the plate properties – dimension a, thickness h, density ρ, and flexural rigidity D – through the expression

$$\omega = \frac{\lambda^2}{a^2} \sqrt{\frac{D}{\rho h}} \qquad \text{(A.24)}$$

A.3.3 Boundary Conditions

Three simple boundary conditions for the edges of a plate commonly considered in vibration analysis are free (F), simply supported (SS), and clamped (C). At a free end, there is no torque and no shearing force, so the second and third derivatives of the lateral spatial coordinate at the edge (x,y or ξ,η) are both zero. At a simply supported edge, there is no displacement and no torque, so the spatial coordinate and its second derivative are both zero. At a clamped end, there is no displacement and no velocity, so the spatial coordinate and its first derivative are zero.

For the study of pMUT vibration, the classical boundary conditions considered are simply supported and clamped as the constraints at the edges are confined to zero displacement. Expressions for the simply supported and clamped boundary conditions at the edge $x=a$ are given as an example below.

Simply Supported $$W(x,y) = \frac{\partial^2 W(x,y)}{\partial x^2} = 0\Big|_{x=a}$$

Clamped $$W(x,y) = \frac{\partial W(x,y)}{\partial x} = 0\Big|_{x=a}$$

A.3.4 Plates with Elastic Support

In the case of a plate supported by, or embedded in, a massless elastic medium, an addition stiffness term Kw is included into the equation of motion to produce

$$D\nabla^4 w + \rho h \frac{\partial^2 w}{\partial t^2} + Kw = 0 \tag{A.25}$$

where K is the stiffness of the foundation (or media) measured in units of force per unit length of deflection per unit area of contact. [51]

A.3.5 Frequency of Vibration under Classical Plate Theory

Numerous methods for the calculation of natural frequencies of an isotropic, rectangular plate are summarized by Leissa [51]. Gorman provides a clear summary of the classical plate theory for free vibration of rectangular plates [50] along with a presentation of natural frequencies for several classical boundary conditions. As mentioned previously, the natural frequency of vibration for a thin, isotropic plate with dimensions

a,b, thickness h, volume density ρ, plate flexural rigidity, D, and frequency parameter, λ^2 is given as

$$\omega = \frac{\lambda^2}{a^2}\sqrt{\frac{D}{\rho h}} \tag{A.26}$$

where the deflection is small relative to the plate thickness.

The remaining calculation of the frequency of vibration is continued in §6.2.1.

A.4 Vibration of Rectangular Plates – Thick Plates

A.4.1 Equation of Motion for a Thick Plate

The derivation of the equation of motion for a Mindlin plate using Hamilton's principle and variational principles is summarized by Rao [57]. The differential equation specifying Mindlin plate vibration is

$$\left(\nabla^2 - \frac{\rho}{kG}\partial_t^2\right)\left(D\nabla^2 - \frac{\rho h^3}{12}\partial_t^2\right)W + \rho h\partial_t^2 W = \left(1 - \frac{D}{kGh}\nabla^2 + \frac{\rho h^2}{12kG}\partial_t^2\right)q \tag{A.27}$$

where k is the shear correction factor and G is the shear modulus given by

$$k^2 = \frac{5}{6-\nu} \quad \text{and} \quad G = \frac{E}{2(1+\nu)} \tag{A.28}$$

For the free vibration of the rectangular Mindlin plate, the external force on the right hand side of the equation goes to zero and the equation of motion becomes

$$\left(\nabla^2 - \frac{\rho}{kG}\partial_t^2\right)\left(D\nabla^2 - \frac{\rho h^3}{12}\partial_t^2\right)W + \rho h\partial_t^2 W = 0 \tag{A.29}$$

In a process similar to that described for thin plate theory (see Appendix A.3), we can perform a separation of variables expressing the displacement $W(x,y,t)$ as the product of

two functions, one involving spatial coordinates x and y with the other involving time t, such that $W(x,y,t) = W(x,y)\,T(t)$. Further, we select $T(t) = A \sin \omega t$ where ω describes the frequency of oscillation (rad/sec).

The equation of motion then becomes

$$\left(\nabla^2 - \frac{\rho}{kG}\omega^2\right)\left(D\nabla^2 - \frac{\rho h^3}{12}\omega^2\right)W + \rho h \omega^2 W = 0 \qquad \text{(A.29)}$$

which is now a function of the plate mode shape expression $W(x.y)$, the plate properties, and the circular frequency ω. Variation of the plate vibration in time is then described solely by ω.

The equation above governs the free vibration of moderately thick rectangular plates. Solutions to this differential equation that satisfy any prescribed boundary conditions will provide the necessary description of plate vibration that will be applied to pMUTs.

A.4.2 Vibrational Frequencies of Rectangular Mindlin Plates

Determination of the natural frequency of vibration for Mindlin plates is approached in a manner similar to classical plate theory [57]. For simply supported conditions, an exact solution can be found by expressing the displacement function in the equation of motion as a series solution, the mn term being

$$W(x.y) = C_{mn} \sin\frac{m\pi x}{a} \sin\frac{n\pi y}{b} \qquad \text{(A.30)}$$

where a,b are the dimensions of the plate and m,n describe the mode shape. Substituting into the equation of motion, we obtain the frequency equation

$$\frac{\rho^2 h^3}{12kG}\omega^4 - \omega^2\left[\rho h + \left\{\left(\frac{m\pi}{a}\right)^2 + \left(\frac{n\pi}{b}\right)^2\right\}\left(\frac{\rho}{kG}D + \frac{\rho h^3}{12}\right)\right] + D\left\{\left(\frac{m\pi}{a}\right)^2 + \left(\frac{n\pi}{b}\right)^2\right\}^2 = 0$$

(A.31)

The remaining calculation of the frequency of vibration from the above equation of motion is continued in §6.3.2.

Bibliography

[1] D. E. Dausch, J. B. Castellucci, D. R. Chou, and O. T. von Ramm, "Piezoelectric Micromachined Ultrasound Transducer (pMUT) Arrays for 3D Imaging Probes," *2006 IEEE Ultrasonics Symposium, Vols 1-5, Proceedings*, pp. 934-937, 2006.

[2] D. E. Dausch, J. B. Castellucci, D. R. Chou, and O. T. von Ramm, "Theory and Operation of 2-D Array Piezoelectric Micromachined Ultrasound Transducers," *IEEE Transactions on Ultrasonics Ferroelectrics and Frequency Control*, vol. 55, pp. 2484-2492, 2008.

[3] D. E. Dausch, K. H. Gilchrist, J. B. Castellucci, D. R. Chou, and O. T. von Ramm, "Performance of flexure-mode pMUT 2D Arrays," *2007 IEEE Ultrasonics Symposium Proceedings, Vols 1-6*, pp. 1053-1056, 2007.

[4] K. Lindstrom and I. Edler, "The history of echocardiography," *Ultrasound in Medicine and Biology*, vol. 30, pp. 1565-1644, 2004.

[5] J. C. Somer, "Electronic Sector Scanning for Ultrasonic Diagnosis," *Ultrasonics*, vol. 6, 1968.

[6] O. T. Von Ramm and F. L. Thurstone, "Cardiac Imaging Using a Phased-Array Ultrasound System .1. System-Design," *Circulation*, vol. 53, pp. 258-262, 1976.

[7] C. L. Morgan, F. L. Thurstone, O. T. Von Ramm, W. S. Trought, and W. M. Clark, "Principles and Applications of a Dynamically Focused Phased-Array Real-Time Ultrasound System," *Journal of Clinical Ultrasound*, vol. 6, pp. 385-391, 1978.

[8] F. L. Thurstone and O. T. von Ramm, "Electronic beam steering for ultrasonic imaging," *Ultrasound in Medicine*, pp. 43-48, 1974.

[9] J. J. Wild and J. M. Reid, "Application of Echo-Ranging Techniques to the Determination of Structure of Biological Tissues," *Science*, vol. 115, pp. 226-230, 1952.

[10] A. Fenster, S. Tong, S. Sherebrin, D. B. Downey, and R. N. Rankin, "Three-dimensional ultrasound imaging," *Medical Imaging 1995 - Physics of Medical Imaging*, vol. 2432, pp. 176-184, 1995.

[11] A. Ghosh, N. C. Nanda, and G. Maurer, "3-Dimensional Reconstruction of Echocardiographic Images Using the Rotation Method," *Ultrasound in Medicine and Biology*, vol. 8, pp. 655-661, 1982.

[12] R. N. Rankin, A. Fenster, D. B. Downey, P. L. Munk, M. F. Levin, and A. D. Vellet, "3-Dimensional Sonographic Reconstruction - Techniques and Diagnostic Applications," *American Journal of Roentgenology*, vol. 161, pp. 695-702, 1993.

[13] F. L. Thurstone and O. T. Von Ramm, "A new ultrasound imaging technique employing two-dimensional electronic beam steering," *Acoustical Holography*, vol. 5, pp. 249-259, 1974.

[14] J. W. Hunt, M. Arditi, and F. S. Foster, "Ultrasound Transducers for Pulse-Echo Medical Imaging," *IEEE Transactions on Biomedical Engineering*, vol. 30, pp. 453-481, 1983.

[15] A. Safari and E. K. Akdogan, *Piezoelectric and acoustic materials for transducer applications*. New York: Springer, 2008.

[16] J. Curie and P. Curie, "Developpement par pression de l'eletricite polaire dans les cristaux hemiedres a faces enclinees," *Compt. Rend.*, vol. 91, pp. 383, 1880.

[17] T. L. Proulx, D. Tasker, and J. Bartlett-Roberto, "Advances in catheter-based ultrasound imaging - Intracardiac echocardiography and the ACUSON AcuNav (TM) ultrasound catheter," *2005 IEEE Ultrasonics Symposium, Vols 1-4*, pp. 669-678, 2005.

[18] K. L. Gentry, N. Sachedina, and S. W. Smith, "Catheter ultrasound phased-array transducers for thermal ablation: A feasibility study," *Ultrasonic Imaging*, vol. 27, pp. 89-100, 2005.

[19] K. L. Gentry and S. W. Smith, "Integrated catheter for 3-D intracardiac echo cardiography and ultrasound ablation," *IEEE Transactions on Ultrasonics Ferroelectrics and Frequency Control*, vol. 51, pp. 800-808, 2004.

[20] E. D. Light and S. W. Smith, "Two dimensional arrays for real time 3D intravascular ultrasound," *2003 IEEE Ultrasonics Symposium Proceedings, Vols 1 and 2*, pp. 877-880, 2003.

[21] E. D. Light, S. W. Smith, and J. F. Angle, "Advances in two dimensional arrays for real time 3D intravascular ultrasound," *2004 IEEE Ultrasonics Symposium, Vols 1-3*, pp. 790-793, 2004.

[22] S. W. Smith, W. Lee, K. L. Gentry, E. C. Pua, and E. D. Light, "Integrated interventional devices for real time 3D ultrasound imaging and therapy," *Therapeutic Ultrasound*, vol. 829, pp. 375-379, 2006.

[23] C. Daft, S. Calmes, D. da Graca, K. Patel, P. Wagner, and I. Ladabaum, "Microfabricated ultrasonic transducers monolithically integrated with high voltage electronics," *2004 IEEE Ultrasonics Symposium, Vols 1-3*, pp. 493-496, 2004.

[24] C. Daft, P. Wagner, B. Bymaster, S. Panda, K. Patel, and I. Ladabaum, "cMUTs and electronics for 2D and 3D imaging: Monolithic integration, in-handle chip sets and system implications," *2005 IEEE Ultrasonics Symposium, Vols 1-4*, pp. 467-478, 2005.

[25] I. O. Wygant, D. T. Yeh, X. F. Zhuang, S. Vaithilingam, A. Nikoozadeh, O. Oralkan, A. S. Ergun, G. G. Yaralioglu, and B. T. Khuri-Yakub, "Integrated ultrasound imaging systems based on capacitive micromachined ultrasonic transducer arrays," *2005 IEEE Sensors, Vols 1 and 2*, pp. 704-707, 2005.

[26] D. T. Yeh, O. Oralkan, I. O. Wygant, M. O'Donnell, and B. T. Khuri-Yakub, "3-D ultrasound imaging using a forward-looking CMUT ring array for intravascular/intracardiac applications," *IEEE Transactions on Ultrasonics Ferroelectrics and Frequency Control*, vol. 53, pp. 1202-1211, 2006.

[27] X. F. Zhuang, A. S. Ergun, Y. L. Huang, I. O. Wygant, O. Oralkan, and B. T. Khuri-Yakub, "Integration of trench-isolated through-wafer interconnects with 2d capacitive micromachined ultrasonic transducer arrays," *Sensors and Actuators a-Physical*, vol. 138, pp. 221-229, 2007.

[28] D. M. Mills, "Medical imaging with capacitive micromachined ultrasound transducer (cMUT) arrays," *2004 IEEE Ultrasonics Symposium, Vols 1-3*, pp. 384-390, 2004.

[29] O. Oralkan, A. S. Ergun, C. H. Cheng, J. A. Johnson, M. Karaman, T. H. Lee, and B. T. Khuri-Yakub, "Volumetric ultrasound Imaging using 2-D CMUT arrays," *IEEE Transactions on Ultrasonics Ferroelectrics and Frequency Control*, vol. 50, pp. 1581-1594, 2003.

[30] A. Caronti, G. Caliano, R. Carotenuto, A. Savoia, M. Pappalardo, E. Cianci, and V. Foglietti, "Capacitive micromachined ultrasonic transducer (CMUT) arrays for medical imaging," *Microelectronics Journal*, vol. 37, pp. 770-777, 2006.

[31] A. Nikoozadeh, I. O. Wygant, D. S. Linl, O. Oralkan, A. S. Ergun, K. Thomenius, A. Dentinger, D. Wildes, G. Akopyan, K. Shivkumar, A. Mahajan, D. N. Stephens, D. Sahn, and P. T. Khuri-Yakub, "Fully integrated CMUT-based forward-looking intracardiac imaging for electrophysiology," *2007 IEEE Ultrasonics Symposium Proceedings, Vols 1-6*, pp. 900-903, 2007.

[32] B. T. Khuri-Yakub and O. Oralkan, "Capacitive micromachined ultrasonic transducers for medical imaging and therapy," *Journal of Micromechanics and Microengineering*, vol. 21, 2011.

[33] I. O. Wygant, X. Zhuang, D. T. Yeh, O. Oralkan, A. S. Ergun, M. Karaman, and B. T. Khuri-Yakub, "Integration of 2D CMUT arrays with front-end electronics for volumetric ultrasound imaging," *IEEE Transactions on Ultrasonics Ferroelectrics and Frequency Control*, vol. 55, pp. 327-342, 2008.

[34] A. Bandyopadhyay, F. Akasheh, T. Myers, J. D. Fraser, and S. Bose, "Development of piezoelectric micromachined ultrasonic transducers," *Sensors and Actuators a-Physical*, vol. 111, pp. 275-287, 2004.

[35] J. J. Bernstein, S. L. Finberg, K. Houston, L. C. Niles, H. D. Chen, L. E. Cross, K. K. Li, and K. Udayakumar, "Micromachined high frequency ferroelectric sonar transducers," *IEEE Transactions on Ultrasonics Ferroelectrics and Frequency Control*, vol. 44, pp. 960-969, 1997.

[36] G. Percin and B. T. Khuri-Yakub, "Piezoelectrically actuated flextensional micromachined ultrasound transducers - II: Fabrication and experiments," *IEEE Transactions on Ultrasonics Ferroelectrics and Frequency Control*, vol. 49, pp. 585-595, 2002.

[37] S. H. Chang and Y. C. Tung, "Electro-elastic characteristics of asymmetric rectangular piezoelectric laminae," *IEEE Transactions on Ultrasonics Ferroelectrics and Frequency Control*, vol. 46, pp. 950-960, 1999.

[38] J. Cho, M. Anderson, R. Richards, D. Bahr, and C. Richards, "Optimization of electromechanical coupling for a thin-film PZT membrane: I. Modeling," *Journal of Micromechanics and Microengineering*, vol. 15, pp. 1797-1803, 2005.

[39] H. S. Choi, J. L. Ding, A. Bandyopadhyay, M. J. Anderson, and S. Bose, "Characterization and modeling of a piezoelectric micromachined ultrasonic transducer with a very large length/width aspect ratio," *Journal of Micromechanics and Microengineering*, vol. 18, 2008.

[40] P. C. Eccardt, P. Wagner, and S. Hansen, "Analytical Models for Micromachined Transducers - an Overview," *2006 IEEE Ultrasonics Symposium, Vols 1-5, Proceedings*, pp. 572-581, 2006.

[41] P. Muralt, N. Ledermann, J. Baborowski, A. Barzegar, S. Gentil, B. Belgacem, S. Petitgrand, A. Bosseboeuf, and N. Setter, "Piezoelectric micromachined ultrasonic transducers based on PZT thin films," *IEEE Transactions on Ultrasonics Ferroelectrics and Frequency Control*, vol. 52, pp. 2276-2288, 2005.

[42] G. Percin, "Plate equations for piezoelectrically actuated flexural mode ultrasound transducers," *IEEE Transactions on Ultrasonics Ferroelectrics and Frequency Control*, vol. 50, pp. 81-88, 2003.

[43] G. Percin and B. T. Khuri-Yakub, "Piezoelectrically actuated flextensional micromachined ultrasound transducers - I: Theory," *IEEE Transactions on Ultrasonics Ferroelectrics and Frequency Control*, vol. 49, pp. 573-584, 2002.

[44] G. Percin and B. T. Khuri-Yakub, "Piezoelectrically actuated flextensional micromachined ultrasound transducers," *Ultrasonics*, vol. 40, pp. 441-448, 2002.

[45] Z. H. Wang, J. M. Miao, and W. G. Zhu, "Micromachined ultrasonic transducers and arrays based on piezoelectric thick film," *Applied Physics a-Materials Science & Processing*, vol. 91, pp. 107-117, 2008.

[46] Z. H. Wang, N. G. Zhu, H. Zhu, J. M. Miao, C. Chao, C. L. Zhao, and O. K. Tan, "Fabrication and characterization of piezoelectric micromachined ultrasonic transducers with thick composite PZT films," *IEEE Transactions on Ultrasonics Ferroelectrics and Frequency Control*, vol. 52, pp. 2289-2297, 2005.

[47] L. Q. Yao, L. Lu, Z. H. Wang, W. G. Zhu, and Y. Dai, "Exact solution of multilayered piezoelectric diaphragms," *IEEE Transactions on Ultrasonics Ferroelectrics and Frequency Control*, vol. 50, pp. 1262-1271, 2003.

[48] D. E. Dausch, "Asymmetric 90 degrees domain switching in rainbow actuators," *Ferroelectrics*, vol. 210, pp. 31-45, 1998.

[49] O. T. von Ramm, S. W. Smith, and H. G. Pavy, "High-Speed Ultrasound Volumetric Imaging-System .2. Parallel Processing and Image Display," *IEEE Transactions on Ultrasonics Ferroelectrics and Frequency Control*, vol. 38, pp. 109-115, 1991.

[50] D. J. Gorman, *Free vibration analysis of rectangular plates*. New York: Elsevier, 1982.

[51] A. W. Leissa, *Vibration of plates*. Washington, DC: Scientific and Technical Information Division, National Aeronautics and Space Administration, 1969.

[52] Y. Xiang, K. M. Liew, and S. Kitipornchai, "Vibration analysis of rectangular mindlin plates resting on elastic edge supports," *Journal of Sound and Vibration*, vol. 204, pp. 1-16, 1997.

[53] R. D. Mindlin, "Influence of Rotatory Inertia and Shear on Flexural Motions of Isotropic, Elastic Plates," *Journal of Applied Mechanics-Transactions of the ASME*, vol. 18, pp. 31-38, 1951.

[54] R. D. Mindlin, A. Schachnow, and H. Deresiewicz, "Flexural vibrations of rectangular plates," *Journal of Applied Mechanics-Transactions of the ASME*, vol. 23, pp. 430-436, 1956.

[55] K. M. Liew, Y. Xiang, and S. Kitipornchai, "Research on Thick Plate Vibration - a Literature Survey," *Journal of Sound and Vibration*, vol. 180, pp. 163-176, 1995.

[56] C. M. Wang, K. H. Lee, and J. N. Reddy, *Shear deformable beams and plates : relationships with classical solutions*. Amsterdam; New York: Elsevier, 2000.

[57] J. S. Rao, *Dynamics of plates*. New York; New Delhi: Marcel Dekker; Narosa Pub. House, 1999.

[58] K. M. Liew, *Vibration of Mindlin plates : programming the p-version Ritz Method*. Amsterdam ; New York: Elsevier, 1998.

[59] K. M. Liew, Y. Xiang, and S. Kitipornchai, "Transverse Vibration of Thick Rectangular-Plates .1. Comprehensive Sets of Boundary-Conditions," *Computers & Structures*, vol. 49, pp. 1-29, 1993.

[60] Y. F. Xing and B. Liu, "Closed form solutions for free vibrations of rectangular Mindlin plates," *Acta Mechanica Sinica*, vol. 25, pp. 689-698, 2009.

[61] P. C. Chou, J. Carleone, and C. M. Hsu, "Elastic-Constants of Layered Media," *Journal of Composite Materials*, vol. 6, 1972.

[62] J. R. Vinson and R. L. Sierakowski, *The behavior of structures composed of composite materials*. Dordrecht ; Boston: Kluwer Academic Publishers, 2002.

[63] K. S. Pister and S. B. Dong, "Elastic bending of layered plates," *Proceeedings of the ASCE Journal of Engineering Mechanics*, vol. 84, pp. 1-10, 1959.

[64] J. Greenspon, "An approximate method for obtaining the frequencies, deflections, and stresses in sandwich and cross stiffened rectangular plates," *Tech Rep No. 1 (Nonr-3123(00)X), J.G. Eng. Res. Assoc*, 1960.

[65] J. Greenspon, "Vibrations of Cross-Stiffened and Sandwich Plates with Application to Underwater Sound Radiators," *Journal of the Acoustical Society of America*, vol. 33, 1961.

[66] M. J. Kobrinsky, E. R. Deutsch, and S. D. Senturia, "Effect of support compliance and residual stress on the shape of doubly supported surface-micromachined beams," *Journal of Microelectromechanical Systems*, vol. 9, pp. 361-369, 2000.

[67] R. E. Kielb, "Mechanical Vibrations-Cantilever beams – correction for compliant support," ME235 course notes, 2010.

[68] D. J. Gorman, "Free vibration analysis of Mindlin plates with uniform elastic edge support by the superposition method," *Journal of Sound and Vibration*, vol. 207, pp. 335-350, 1997.

[69] D. Zhou, "Vibrations of Mindlin rectangular plates with elastically restrained edges using static Timoshenko beam functions with the Rayleigh-Ritz method," *International Journal of Solids and Structures*, vol. 38, pp. 5565-5580, 2001.

[70] MEMSnet, "Material Database," MEMS and Nanotechnology Exchange, 2010.

[71] W. Tjhen, T. Tamagawa, C. P. Ye, C. C. Hsueh, P. Schiller, and D. L. Polla, "Properties of Piezoelectric Thin-Films for Micromechanical Devices and Systems," *IEEE Micro Electro Mechanical Systems*, pp. 114-119, 1991.

[72] T. D. Rossing and N. H. Fletcher, *Principles of vibration and sound*. New York: Springer-Verlag, 1995.

[73] L. E. Kinsler and A. R. Frey, *Fundamentals of acoustics*. New York: Wiley, 1950.

[74] L. Cremer and M. Heckl, *Structure-borne sound; structural vibrations and sound radiation at audio frequencies*: Berlin, New York, Springer-Verlag, 1973.

[75] S. Timoshenko and S. Woinowsky-Krieger, *Theory of plates and shells*: New York, McGraw-Hill, 1959.

Biography

Derrick Ren-yu Chou

Date of Birth: June 20th, 1981
Place of Birth: Norman, OK

Education

Duke University, Durham, North Carolina
Ph.D. candidate in Biomedical Engineering

Duke University, Durham, North Carolina
M.S. in Biomedical Engineering
Thesis: "Development of a laser scanning confocal microscope for analysis of tissue like scattering media"
Certificate in Photonics

Duke University, Durham, North Carolina
B.S. in Biomedical Engineering, Electrical Engineering, and Computer Science

Publications

D.R. Chou, J.B. Castellucci, D.E. Dausch, O.T. von Ramm, "Vibrational analysis of piezoelectric micromachined ultrasound transducers," *Polytec InFocus magazine - Optical Measurement Solutions*, iss. 1, 2010.

D.E. Dausch, J.B. Castellucci, D.R. Chou, O.T. von Ramm, "Theory and operation of 2-D array piezoelectric micromachined ultrasound transducers," *IEEE Transactions on Ultrasonics, Ferroelectrics, and Freq. Control*, vol. 55, 2008.

D.E. Dausch, K.H. Gilchrist, J.B. Castellucci, D.R. Chou, O.T. von Ramm, "Performance of flexure-mode pMUT 2D arrays," *2007 IEEE Ultrasonics Symposium*, 1053-1056, 2007.

D.E. Dausch, J.B. Castellucci, D.R. Chou, O.T. von Ramm, "Piezoelectric micromachined ultrasound transducer (pMUT) arrays for 3D imaging process," *Proc. IEEE Ultrasonics Symp.*, 930-933, 2006.

D.R. Chou, B.A. Bower, and A. Wax, "Low-cost, scalable laser scanning module for real-time reflectance and fluorescence confocal microscopy," *Applied Optics*, vol. 44, 2013-2018, 2005.

D.R. Chou, A. Wax, "Optical scattering of confocal laser scanning reflectance microscopy in turbid media," *2005 Conference on Lasers and Electro-Optics*, vol. 3, 1578-1580, 2005.

Memberships

Institute of Electrical and Electronics Engineers, *Student Member*